Karlsruher Institut für Technologie

Electrode Realisation and SiPM Characterisation for Dark Matter Search with XENONnT and XLZD

Zur Erlangung des akademischen Grades eines

Doktors der Naturwissenschaften (Dr. rer. nat.)

von der KIT-Fakultät für Physik
des Karlsruher Instituts für Technologie (KIT)

genehmigte

Dissertation

von

M. Sc. **Vera Hiu-Sze Wu**

aus Hongkong, SAR

Referentin:	Prof. Dr. Kathrin Valerius Insitut für Astroteilchenphysik Karlsruher Institut für Technologie
Korreferent:	Prof. Dr. Marc Schumann Physikalisches Institut Albert-Ludwigs-Universität Freiburg

Tag der mündlichen Prüfung: 13. Februar 2026

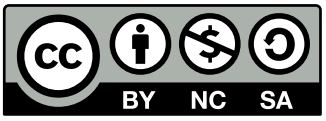

Erklärung der selbstständigen Anfertigung der Dissertationsschrift
Hiermit erkläre ich, dass ich die Dissertation mit dem Titel

Electrode Realisation and
SiPM Characterisation for
Dark Matter Search with
XENONnT and XLZD

selbstständig angefertigt, alle benutzten Hilfsmittel vollständig und genau angegeben und alles kenntlich gemacht habe, was aus Arbeiten anderer unverändert oder mit Abänderungen entnommen wurde.

Ich versichere außerdem, dass ich die Dissertation nur in diesem und keinem anderen Promotionsverfahren eingereicht habe und dass diesem Promotionsverfahren keine endgültig gescheiterten Promotionsverfahren vorausgegangen sind.

Karlsruhe, 05. Januar 2025

. . . . . .
(**Vera Hiu-Sze Wu**)

I dedicate this thesis to my beloved parents and sister.

致

家人

Abstract

Despite compelling evidence from cosmological and astrophysical observations for the existence of dark matter, its fundamental nature remains unknown. Dual-phase xenon time projection chambers (TPCs) are employed in direct detection experiments to search for one of the most popular dark matter candidates — weakly interactive massive particles (WIMPs). Owing to the extremely low interaction rates expected for WIMPs with ordinary matter, such experiments require exceptional sensitivity and ultra-low background. Examples include the currently operating XENONnT experiment and the proposed next-generation experiment, the XLZD project.

A key component of dual-phase xenon TPCs is the electric-field configuration in the detector and the electrodes used to generate it, which play a critical role in detector performance. This thesis presents contributions to the design, optimisation, quality control, and construction of the XENONnT upgrade electrodes. To support the evaluation of electrode performance and the resulting electric fields, an electrostatic field simulation framework based on the boundary element method (BEM) was implemented and is described herein.

This work focuses primarily on the realisation of the parallel-wire anode and the hexagonal etched-mesh cathode used in the XENONnT upgrade, both with a diameter of approximately $1.4\,\mathrm{m}$. Emphasis was placed on improving the mechanical stability and high-voltage performance of these electrodes through extensive testing and the application of complementary techniques. The experience gained from the XENONnT upgrade is summarised and used to derive recommendations for electrode design in the XLZD project, which targets electrodes with diameters of approximately 3 m. In addition, the feasibility of the parallel-wire electrode concept at the 3-meter scale required for XLZD was explored.

In addition to electrodes, photosensors are a key component of these detectors, as they record the light from the scintillation and ionisation signals produced in liquid xenon. This thesis also includes contributions to the testing of photosensors, specifically silicon photomultipliers (SiPMs), in liquid xenon for future-generation experiments. Measurements were performed with the NUXE-3 detector at the University of California, San Diego, using an array of 96 Hamamatsu VUV4 SiPMs to evaluate the feasibility of a novel TPC design. All SiPMs in the NUXE-3 detector were successfully commissioned and operated within this work, with measured photon gains consistent with values reported in the literature.

Zusammenfassung

Trotz überzeugender Hinweise aus kosmologischen und astrophysikalischen Beobachtungen auf die Existenz von Dunkler Materie ist ihre fundamentale Natur bis heute unbekannt. Xenonbasierte Zweiphasen-Driftkammern (engl. TPCs) werden in Experimenten zur direkten suche nach einem der am häufigsten untersuchten Kandidaten für Dunkle Materie, den schwach wechselwirkenden massiven Teilchen (engl. WIMPs), eingesetzt. Aufgrund der extrem niedrigen erwarteten Wechselwirkungsraten von WIMPs mit gewöhnlicher Materie erfordern solche Experimente eine außergewöhnlich hohe Sensitivität sowie ein extrem niedriges Untergrundniveau. Beispiele hierfür sind das derzeit in Betrieb befindliche Experiment XENONnT sowie das vorgeschlagene Experiment der nächsten Generation, das XLZD-Projekt.

Eine zentrale Komponente von Zweiphasenxenon-TPCs ist die elektrische Feldkonfiguration im Detektor sowie die Elektroden, mit denen dieses Feld erzeugt wird, da sie die Detektorleistung maßgeblich beeinflussen. Diese Dissertation präsentiert Beiträge zur Auslegung, Optimierung, Qualitätssicherung und Konstruktion der Upgrade-Elektroden von XENONnT. Zur Unterstützung der Bewertung der Funktionsfähigkeit der Elektroden und der daraus resultierenden elektrischen Felder wurde ein elektrostatisches Feldsimulationsframework auf Basis der Randelementmethode (engl. BEM) implementiert und in dieser Arbeit beschrieben.

Der Schwerpunkt dieser Arbeit liegt auf der Realisierung der Parallel-Draht-Anode sowie der hexagonalen geätzten Gitterkathode mit einem Durchmesser von $\sim 1,4\,\mathrm{m}$, die im Upgrade des XENONnT eingesetzt wurden. Besonderer Fokus wurde auf die Verbesserung der mechanischen Stabilität und der Hochspannungsfestigkeit dieser Elektroden gelegt, gestützt durch umfangreiche Tests und den Einsatz komplementärer Methoden. Die im Zuge des Upgrades gewonnenen Erfahrungen werden zusammengefasst und zur Ableitung von Empfehlungen für das Elektrodendesign mit einem Durchmesser von $\sim 3\,\mathrm{m}$ im XLZD-Projekt genutzt. Darüber hinaus wurde die Machbarkeit des Parallel-Draht-Elektrodenkonzepts im für XLZD erforderlichen 3-Meter-Maßstab untersucht.

Neben den Elektroden stellen Photosensoren eine weitere Schlüsselkomponente dieser Detektoren dar, da sie das in flüssigem Xenon erzeugte Szintillations- und Ionisationslicht registrieren. Diese Arbeit umfasst zudem Beiträge zur Untersuchung von Photosensoren, insbesondere von silicon photomultipliers (SiPMs), in Flüssigxenon für Experimente der nächsten Generation. Die Messungen wurden mit dem NUXE-3-Detektor an der University of California, San Diego, durchgeführt, wobei ein Array aus 96 Hamamatsu-VUV4-SiPMs verwendet wurde, um die Machbarkeit eines neuartigen TPC-Designs zu evaluieren. Alle SiPMs im NUXE-3-Detektor wurden im Rahmen dieser Arbeit erfolgreich in Betrieb genommen und betrieben, wobei die gemessenen Werte der Signalverstärkung mit den der Literaturwerten übereinstimmen.

Author's Contribution

The research presented in this thesis was conducted within large-scale experimental collaborations and involved contributions from many physicists and engineers. My contributions to the work described in this thesis are summarised below.

- Chapter 4: The benchmark tests comparing KEMField and COMSOL were performed in collaboration with Jan Behrens, Woosik Gil, and Ferenc Glück. I implemented and validated the XENONnT detector model in KEMField and carried out the associated simulations, benefitting from the discussions with Francesco Toschi and Ricardo Peres. Jan Behrens resolved several technical issues within KEMField that were essential for this work.

- Chapter 5: The wire test setup was constructed by Michael Schrank and Woosik Gil. I designed the test campaign, supervised the data collection performed by Wenjun Li, and conducted the data analysis. Mechanical simulations of the electrode frame were carried out by Klaus Müller and are included in the thesis for completeness. I performed all the electrostatic simulations presented in this chapter. I was also heavily involved in all the tests for quality improvement, quality assurance, as well as the assembly of the anode electrode in the cleanroom at Laboratori Nazionali del Gran Sasso (LNGS), assisted by with Klaus Eitel, Alexey Elykov, Melih Kara, Steffen Lichter, Klaus Müller, Sebastian Vetter, and others. The measurements after the test in the PANCAKE experiment were performed by Sebastian Lindemann, Tiffany Luce, and Alexey Elykov.

- Chapter 6: Mechanical simulations and the surface roughness measurements of the cathode were carried out by Klaus Müller and are included in the thesis for completeness. I performed all the electrostatic simulations presented in this chapter, along with the interpretations. I was also heavily involved in most of the tests for quality improvement, quality assurance, as well as the assembly of the cathode in the cleanroom at LNGS, assisted by Klaus Eitel, Alexey Elykov, Melih Kara, Steffen Lichter, Klaus Müller, Sebastian Vetter, and others. Sebastian Vetter developed the machine learning algorithm used for defect surveying. My contribution to this aspect was limited to visual inspection and minor input for labelling and comparisons; therefore, it is mentioned only briefly in this thesis. For the high-voltage tests, I prepared the complete experimental setup with assistance from Klaus Müller and others, acquired the test data, and performed the data analysis that informed subsequent testing decisions, as presented in this thesis. The measurements after the test in the PANCAKE experiment were performed by Sebastian Lindemann, Tiffany Luce, Alexey Elykov and Klaus Eitel.

- Chapter 5 and Chapter 6 contribute to the key results listed in [1], which I am listed as the corresponding author and also contributed substantially to the writing of the manuscript.

- Chapter 7: I performed data taking with the NUXE-3 detector and carried out the subsequent data analysis. The detector setup and connections to the readout systems were established by researchers at the University of California, San Diego, in particular Haiwen Xu, Jianyang Qi, Kaixuan Ni, Noah Hood, and Yue Ma, who also contributed to conceptual discussions and troubleshooting of the experimental setup.

Acknowledgements

During my four-year doctoral studies at the Institute for Astroparticle Physics at KIT, my experience was both fruitful and rewarding. There were moments of high and low, as well as periods of self-doubt, but the companionship, support, and encouragement from many people I met gave me the strength to endure these challenges with a smile. This work would not have been possible without them.

First of all, I would like to thank my supervisor, Prof. Dr. Kathrin Valerius, for allowing me to work in this field as a doctoral researcher and for being extremely supportive in many ways. I am immensely grateful for her support, patience, and tolerance. Together with Dr. Klaus Eitel, they provided me with valuable guidance, feedback, support, and understanding throughout my doctoral studies. I also thank Dr. Markus Steidl and Dr. Jan Behrens for their support and guidance during the early stage of my PhD. I am grateful to Dr. Francesco Toschi for his patient guidance, valuable feedback, and the many useful pieces of advice he provided during the later stage of my PhD.

I would also like to thank the many engineers and scientists who helped and guided me along the way, including Dr. Jan Behrens, Dr. Woosik Gil, Dr. Ferenc Glück, Dr. Markus Steidl, and Dr. Francesco Toschi, for their expertise in numerical simulations, as well as for many fruitful discussions. I am grateful to Michael Schrank for his expertise in cryogenics, and to Steffen Lichter and Klaus Müller for their mechanical engineering expertise. I thank Dr. Alexander Janson for his guidance on operating the microscopes and for his support in the laboratory. I would also like to thank Hendrik, Joerg, Monika, and Christian for their help and support during my laboratory work, as well as the safety officer Martin Mark for ensuring a safe working environment. It has been a great pleasure to work with all of you.

For the work on electrodes, I would like to thank the many members of the XENONnT collaboration whom I worked with. They demonstrated great dedication and passion and provided valuable discussions, including Prof. Kaixuan Ni, Prof. Dr. Marc Schumann, Prof. Dr. Uwe Oberlack, Dr. Klaus Eitel, Dr. Sebastian Lindemann, Dr. Petr Shagin, Dr. Alexey Elykov, Dr. Alexander Deisting, Dr. Andrew Stevens, Dr. Adam Brown, and many others. I would also like to thank Julia Müller, Tiffany Luce, Melih Kara, Yue Ma, and Sebastian Vetter for the time we worked together during the mock installations at Freiburg and KIT, and for making the electrode assembly process in the cleanroom more enjoyable.

I am deeply grateful for the support from the Karlsruhe House of Young Scientists for awarding me the Research Travel Grant, which supported my research visit to the University of California, San Diego. I would especially like to thank Ms. Schmoch for her understanding and for accommodating my circumstances. The exposure and experience gained during this visit were invaluable. I would like to thank Prof. Kaixuan Ni for hosting me in San Diego and for providing guidance on the project. In

addition, I thank Haiwen Xu, Yue Ma, Dr. Jianyang Qi, Dr. Zepeng Li, and Noah Hood for their patience and help in the laboratories, as well as for the useful feedback and discussions. I also extend my thanks to the friends I met in San Diego, Annika, Eric, Fabian, Isabel, Jai, and Sophie, who helped me cope with cultural shock and homesickness.

This work would not have been possible without the help of those who generously devoted their time to proofreading this thesis. I sincerely thank Dr. Yanina Biondi, Dr. Sukeerthi Dharani, Dr. Klaus Eitel, Dr. Ferenc Glück, Dr. Sharp Chim Yui Lo, and Dr. Francesco Toschi. I would also like to thank Sukee, Sharp, and Rufa (and 陳倩華, and Edward) for providing emotional support and companionship throughout the writing phase, which sustained me through the marathon of completing this thesis. I also thank Ms Knodel-Rupp for accommodating my needs when arranging the examinations.

I would also like to express my gratitude to my fellow group members. It has been an absolute pleasure to meet you all, and this journey has been more colourful and easier with your presence. I wish you all the best and every success. Thank you, Alexey, Alexis, Francesco T., Francesco P., Matthew, Melih K., Melih S., Sukee, Sebastian, Yanina, and everyone else. It is difficult to list everyone here, and I apologise if I have inadvertently missed anyone. The regular 11:45 lunch group and the occasional hangouts have also left me with many fond memories.

I would also like to take this special opportunity to thank my family for their unwavering love, encouragement, and support. 這些年遠赴海外求學，幸得現今科技之便，稍解鄉愁。然而與家人相隔千里，仍常感嘆無法隨時盡孝悌。每每回想往事，大則惦記家人以前為我各種的犧牲、包容、教導和支持，小則掛念家人的小習慣及喜好。也曾在想要放棄的時候，因為想起家人而選擇堅持下去。謝謝你們給我的所有，成為我最堅强的後盾。

Finally, a big thank you to my partner, Sharp, for always sharing my doubts and happiness, encouraging me, providing feedback when I needed it, and for the many trips to Karlsruhe. Your companionship made this journey easier. I look forward to moving on to the next stage of life with you.

Table of Contents

List of Tables

List of Figures

Abbreviations

$0\nu\beta\beta$	neutrinoless double beta decay
2D	two-dimensional
3D	three-dimensional
ADC	analog-to-digital converter
APD	avalanche photodiode
BBN	Big Bang nucleosynthesis
BiCGSTAB	Biconjugate Gradient Stabilised method
BC	boundary condition
BEM	boundary element method
BS	bottom screen
CAD	computer-aided design
CDM	cold dark matter
CMB	cosmic microwave background
CEνNS	coherent elastic neutrino-nucleus scattering
CFW	California Fine Wire
DAQ	data acquisition
DCR	dark count rate
EL	electroluminescence
ER	electronic recoil
FEM	finite element method
FFTM	fast Fourier transformation on multipoles
GAr	gaseous argon
GMRES	Generalised Minimum Residual method
GXe	gaseous xenon
HV	high voltage
HVFT	high-voltage feedthrough
JGU	Johannes Gutenberg University Mainz
KIT	Karlsruhe Institute of Technology
LCE	light collection efficiency
LNGS	Laboratori Nazionali del Gran Sasso
LXe	liquid xenon
NBrS	Neutral bremsstrahlung
NR	nuclear recoil
QA/QC	quality assurance and quality control
QE	quantum efficiency
ROI	region of interest
SD	spin-dependent
SEG	single electron gain
SI	spin-independent
SiPM	silicon photomultiplier
SM	Standard Model
SS	stainless steel
SPE	single photoelectron

PDE photon detection efficiency
PE photoelectron
PI photoionisation
PMT photomultiplier tube
PTFE polytetrafluoroethylene
PBH primordial black hole
TPC time projection chamber
UTS ultimate tensile strength
VUV vacuum ultraviolet
WIMP weakly interacting massive particle
XLZD XENON-LUX-ZEPLIN-DARWIN
YTS yield tensile strength

List of Symbols

d_w	wire diameter
d_l	leg width of etch mesh
D	diameter of the electrode
σ_S	thermal stress
E	Young's Modulus
α_{th}	coefficient of thermal expansion
ΔT	temperature difference
ρ_{ss}	density of SS316
F_{ax}	axial tension on the wire
L_0	undeformed length of the wire
ω_{el}	load from electrostatic force
ω_g	load from weight
ω_b	load from buoyancy
ω	total load from electrostatic force, weight and buoyancy
h_{max}	maximum sagging
N_{ph}	number of EL photons
N_e	number of electrons
E	magnitude of the E-field
p	operating pressure
α	first townsend coefficient
γ	second townsend coefficient
h_g	deflection under gravity only
h_o	deflection during operation
d_G	gap distance between electrodes
V_{bias}	SiPM bias voltage
V_{bd}	SiPM breakdown voltage
ΔV	SiPM overvoltage
R_Q	SiPM quenching resistance
C_j	junction capacitance
M	gain of SiPM
q_e	charge of an electron
R_{imp}	input impedance

Chapter 1

Searching for Dark Matter

As humanity pursues a deeper understanding of the physical world, it has become increasingly clear that our knowledge of the Universe remains incomplete, particularly regarding its composition. A wide range of astrophysical and cosmological observations indicate that the luminous matter constitutes only a small fraction of the total matter content of the Universe. A large, unseen component of the Universe is referred to as dark matter.

The term dark matter is, however, somewhat misleading. Unlike black holes, dark matter does not absorb light and is therefore not "dark" in the conventional sense, but rather optically invisible. Dark matter is, however, not only invisible, but its fundamental nature remains unknown. This lack of understanding has motivated extensive experimental efforts to identify dark matter as a new particle species.

The work presented in this thesis contributes to the worldwide experimental effort to directly detect dark matter, aiming to detect scattering between dark matter particles and known particles. This chapter begins by providing essential background on dark matter and the general experimental methods used to detect it. Chapter 2 introduces a current- and a next-generation direct dark matter search experiment that form the context of this thesis. They are the XENONnT experiment and the XLZD project, respectively.

In these detectors, the electric field and the electrodes that generate the electric field are essential to the operation and performance of the experiments. They are a central focus of this thesis. To establish the current state of electrode fabrication and associated challenges, Chapter 3 reviews the high-voltage performance and existing electrode designs in comparable experiments. Chapter 4 describes the electrostatic field simulation framework used to assess the electrodes by calculating the electric field they produce. Chapter 5 and Chapter 6 present details of the realisation of the XENONnT upgrade electrodes, with a focus on ensuring their structural integrity and high-voltage performance.

Beyond the electric-field configuration, photosensors are a critical component of these detectors. Chapter 7 presents a characterisation study of photosensors intended for future dark matter experiments. The studies presented in this thesis contribute to the advancement of detector technologies, thereby supporting ongoing efforts to shed light on the mystery of dark matter.

This chapter non-comprehensively summarises the primary evidence for the existence of dark matter and our current understanding of the topic. Interested readers are directed to more extensive reviews on the topic, such as [2–4].

1.1 Evidence for Dark Matter

There is substantial evidence for the existence of non-luminous matter across a wide range of observations, from large to small scales. On cosmological scales, measurements of the cosmic microwave background (CMB) provide strong constraints on the matter content of the Universe. On galaxy cluster scales, mass distributions inferred from gravitational lensing cannot be explained by the measured luminous matter alone; additional non-baryonic mass is required. On galactic scales, measurements of stellar rotation curves indicate the presence of a substantial non-luminous component within galaxies. Note that on even smaller scales, such as within the Solar System, the local dark matter density is insufficient to produce any observable effects on planetary motion [3].

While alternative theories may account for some observations, only the existence of dark matter provides a consistent explanation for all of them, as understood at the time of writing. The following section discusses in more detail how these observations support the existence of dark matter.

Cosmic Microwave Background

At the cosmological scale, which is the largest scale, the measurement of the CMB is one of the strongest pieces of evidence for the existence of dark matter and provides constraints on the abundance of dark matter together with the standard cosmological model, the Lambda cold dark matter model (ΛCDM). The model has 6 independent parameters, in which the dark energy or the cosmological constant, Λ, and the cold dark matter (CDM) component have been included in the energy density.

The CMB is the relic radiation from the early Universe, when the photons first decoupled with the hot plasma of matter at 3000 K [5]. The Universe then became optically transparent, and photons propagated freely and were cosmologically redshifted to 2.725 K [6], giving rise to the CMB we observe today.

Despite its high degree of isotropy, the temperature of the CMB exhibits anisotropies at the level of $\mathcal{O}(100\,\mu\mathrm{K})$, as measured with high precision by the Planck satellite [7] and shown in Figure 1.1 (left). These anisotropies originate from density fluctuations in the early Universe. The hot plasma was compressed into gravitational potential wells and counteracted by radiation pressure, leading to acoustic oscillations and temperature inhomogeneities. These oscillations were frozen at photon decoupling, after

which photons from regions at different temperatures propagated freely. The superposition of this radiation gives rise to the angular anisotropies observed in the CMB temperature map.

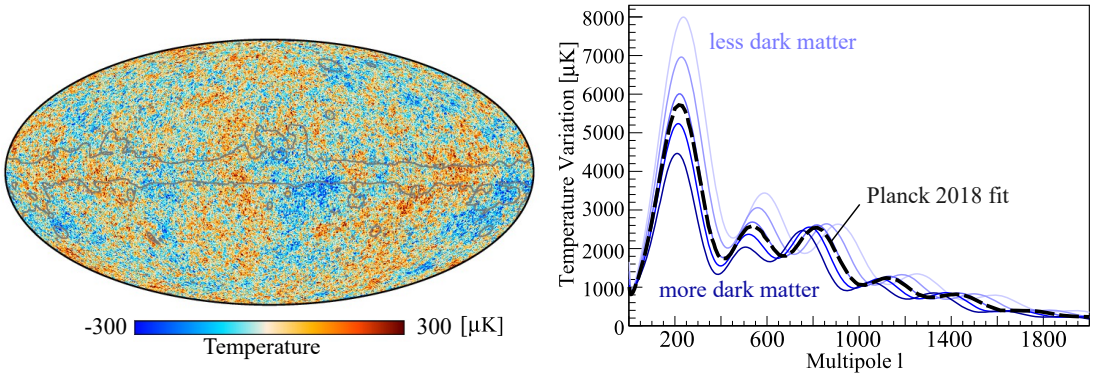

Figure 1.1: Left: the cosmic microwave background (CMB) map from the Planck satellite, with the galactic disk (grey line) removed and the average subtracted [7]. Right: Temperature power spectrum of the CMB. The black dashed line represents the best-fit ΛCDM model to the Planck 2018 data [7]. Blue lines show the ΛCDM model with the dark matter density varying between 0.11 and 0.43. Large (small) multipoles l correspond to small (large) angles on the galactic coordinates. The spectrum peaks at $l \sim 200$, corresponding to $\sim 1°$; while l at 1800 corresponds to $0.1°$. Figure adapted from [3].

As one may observe in Figure 1.1 (left), these anisotropies have a typical angular size, $\sim 1°$, on the map. More quantitatively, the profile can be decomposed into spherical harmonics, parametrised by the multipole l. Smaller l corresponds to a larger angular size, vice versa.

The power spectrum of the CMB can be well modelled by the ΛCDM model. Figure 1.1 (right, black dashed line) shows the overall best fit of the ΛCDM model to the power spectrum as a function of the multipole l to the data from the Planck satellite [7] shown on Figure 1.1 (left). The ΛCDM model prediction with varying dark matter content, while fixing all other parameters, is also shown in Figure 1.1 (right, blue solid lines). As can be seen in the figure, the position of the third peak is sensitive to the total amount of cold dark matter [3], Similarly, the position of the first peak is sensitive to the curvature of the universe, which was found to be a flat geometry of the current Universe [7], or that the total energy density $\Omega = \Omega_\Lambda + \Omega_{\text{matter}} + \Omega_{\text{radiation}} = 1$, where Ω, Ω_Λ, Ω_{matter} and $\Omega_{\text{radiation}}$ are the closure, dark energy density, matter density and radiation density parameters respectively. Among the matter density, $\Omega_{\text{matter}} \approx \Omega_{\text{baryon}} + \Omega_{\text{CDM}}$.

The composition of the Universe, determined by the data from the Planck satellite and the ΛCDM model, is summarised in Table 1.1. Note that $\Omega_{\text{radiation}}$ is $\sim 5 \times 10^{-5}$, which is negligible [8, Section 5.8]. Note also that among the baryonic matter, only 20% is luminous, the rest can be non-luminous gas or MAssive Compact Halo Objects (MACHOs), such as black holes and lonely planets [8, page 121].

In addition, the baryon density determined from the CMB and Big Bang nucleosynthesis (BBN) theory, which models the production of the lightest elements, predicts relic abundances that are in agreement with the observed abundances. This provides

Table 1.1: Measured values for the composition of energy density in the Universe.

Energy density	Ratio in total energy [7]	Ratio in Ω_{matter}
Ω_Λ	69%	
Ω_{baryon}	5%	16%
Ω_{CDM}	26%	84%

a strong constraint on the baryon density to be $\Omega_{\text{baryon}} \sim 5\%$ [9, 10]. To explain a flat Universe, the existence of non-baryonic dark matter is required [11].

Gravitational Lensing for Galaxy Clusters

Gravitational lensing is a powerful method for mapping non-luminous mass in the Universe. When a mass distribution lies along the line of sight, it deflects the path of light from background objects in accordance with General Relativity before the light reaches the observer. As a result, the foreground mass acts as a lens, distorting the observed image of the background source. The degree of this distortion depends on the mass distribution of the lens, the relative alignment of the lens and source, and the distances between the lens, the source and the observer.

Based on the strength and observability of these distortions, gravitational lensing is commonly classified into three regimes: strong lensing produces clearly visible effects such as highly distorted images or multiple images of the same background object. Weak lensing leads to subtle but coherent tangential distortions in the shapes of background galaxies that are not detectable for individual sources but must be inferred statistically. Microlensing is when the lensed images are too closely spaced to be resolved, resulting in a temporary increase in the apparent brightness of the background object as the lens passes through the line of sight.

Weak lensing is particularly effective for studying extended and relatively diffuse mass distributions. It has been widely used to measure the mass distribution of galaxy clusters and large-scale structure, and it provides strong evidence for the presence of dark matter.

A classic example of using weak gravitational lensing to infer mass that cannot be explained by only luminous matter is the Bullet Cluster (1E 0657–558), shown in Figure 1.2, which was formed by the collision of two galaxy clusters [12]. The hot plasma, which constitutes the dominant baryonic mass component of the system, was observed through X-ray imaging. The mass distribution of the cluster was reconstructed using weak gravitational lensing.

The overlaid maps show that the peaks of the mass distribution do not coincide with the dominant baryonic mass component contributed by the plasma. Instead, they roughly follow the distribution of galaxies in the cluster [12], which are effectively dissipationless during the collision, unlike the plasma. This spatial separation provides strong evidence that the dominant mass component in the system is non-dissipative, collisionless, and non-baryonic [12].

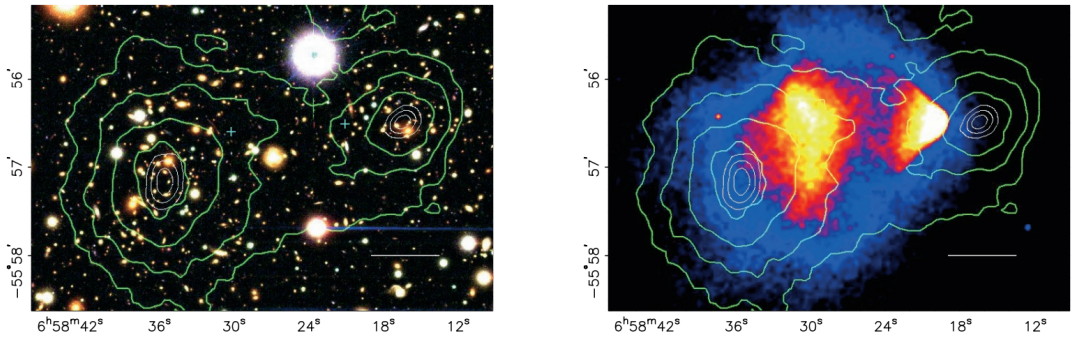

Figure 1.2: Mass distribution of the Bullet Cluster overlaid on optical and X-ray images. The green contours in both panels show the mass distribution reconstructed using weak gravitational lensing. Left: mass distribution overlaid on an optical image of the galaxies. Right: mass distribution overlaid on an X-ray image of the intracluster gas. Image from [12].

Rotational Curves for Galaxies

The time between collisions for stars in a galaxy is around 10^{-21} year, implying the stars are essentially collisionless in a galaxy and the gravitational interaction dominates their motion [13]. They, therefore, serve as a good tracer for the invisible mass in a galaxy.

From the standard Newtonian treatment, the circular velocity v_c of the stars is given by

$$v_c = \sqrt{\frac{GM}{r}}, \tag{1.1}$$

where M is the enclosed mass with radius less than r, G is the gravitational constant. If the mass of a galaxy were concentrated predominantly at its centre, similarly to the distribution of luminous matter, the circular velocity profile would be expected to follow $v_c \propto r^{-1/2}$. However, Vera Rubin's studies of the rotation curves of spiral galaxies since the 1970s revealed that their rotational velocities remain approximately constant at large radii [14, 15]. Numerous independent observations have since confirmed this behaviour [16, 17].

To have a flat profile for v_c, the enclosed mass should scale with radius, as can be seen from Equation 1.1. Therefore, the profile can be explained by a halo of spherically symmetric mass distributed in the galaxy and extending well beyond the visible galactic disk, with a density distribution roughly proportional to $\rho(r) \propto r^{-2}$. Examples of the rotation velocity profile of two spiral galaxies are shown in Figure 1.3, fitted with one of the commonly used dark matter halo density profile, namely the Navarro-Frenk-White (NFW) model with $\rho(r) \propto r^{-1}(1+r/r_s)^{-2}$, where r_s is a free parameter [18]. The examples illustrate that the baryonic mass contributions from the stellar disk and gas alone cannot explain the observed rotational velocities. In contrast, including a dark matter halo in the total mass distribution reproduces the measured rotation curves.

The observed flat rotational curves may also be explained by modifying Newtonian gravity at large distances. Modified Newtonian Dynamics (MOND), first proposed

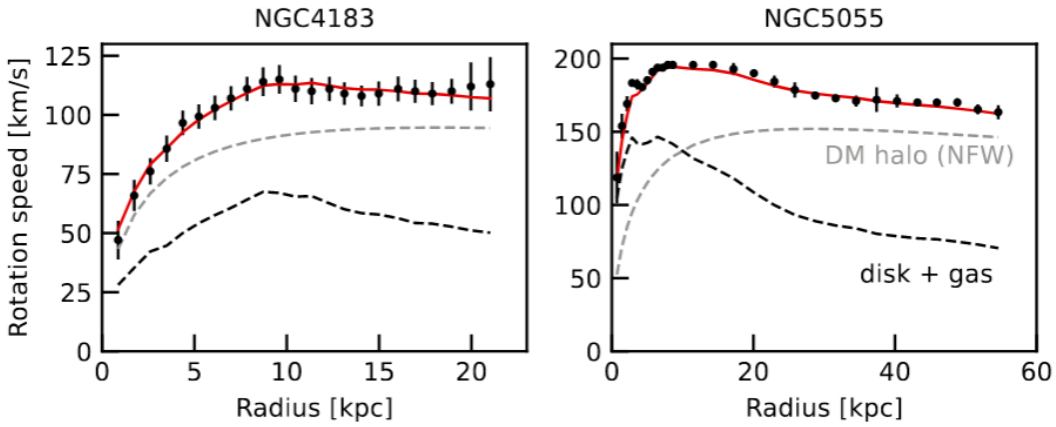

Figure 1.3: Examples of the measured rotational curve of spiral galaxies NGC4183 and NGC5055, along with the estimated profiles using different models. Black dots: data measured using the Spitzer telescope. Black-dashed line: expected profile using the density profile of only the baryonic component, namely the galactic disk and the gas in the galaxies. Grey-dashed line: fitted profile using the Navarro-Frenk-White (NFW) density dark matter halo model. Red line: total fit with the sum of the baryonic component and the dark matter halo component. Image taken from [19].

by Milgrom in 1982 [20], is a class of models developed to address this possibility. Although MOND successfully describes observations on the galactic scale, it cannot account for the observations at the cosmological scale, whereas dark matter can explain both large- and small-scale phenomena. As such, the presence of dark matter is favoured over modified theories of the gravitational force law [12].

1.2 Candidates of Dark Matter

Although a wide range of observations strongly indicate the presence of dark matter, its fundamental properties remain unresolved. To frame the discussion that follows, it is useful to first outline the basic criteria that viable dark matter candidates satisfy [2]:

- **Non-baryonic**: As discussed above, measurements of the CMB interpreted within the ΛCDM model, together with constraints from BBN and the observed abundances of light elements, consistently indicate that baryonic matter accounts for only about 5% of the total energy density of the Universe. Additional non-baryonic matter is therefore required to obtain a spatially flat Universe, as observed. Independent evidence for this non-baryonic component is provided by gravitational weak-lensing measurements, which have revealed the excess non-baryonic mass in galaxy clusters. While some treatments refer to invisible baryonic components as baryonic dark matter [8], such contributions constitute only a small fraction of the total energy density. Consequently, the remainder of this thesis focuses on non-baryonic dark matter, which makes up approximately 84% of the total matter content of the Universe.

- **Long-lived**: Dark matter already existed from the early Universe as we learned from the CMB, and still exist today in galaxies and galaxy clusters; its decay

lifetime should be comparable or longer than 13.8 Gyr, the age of the Universe [2].

- **Massive**: The candidate must carry mass and can interact via gravitational force.
- **Non-relativistic**: Viable dark matter candidates are expected to be non-relativistic ("cold" or "warm") rather than relativistic ("hot"). A large amount of hot dark matter would have erased density fluctuations in the early Universe, preventing the formation of the large-scale structure observed today.
- **Electrically neutral:** The absence of electromagnetic emission or absorption implies that dark matter particles must be electrically neutral or carry at most a very small charge.
- **Non dissipative:** Dark matter is required to interact only weakly with itself and with known particles, thereby preventing significant energy loss through radiation or collisions and enabling the formation of extended halo structures.

The possible mass range of dark matter spans many orders of magnitude, as shown in Figure 1.4. The lightest can be an ultra-light scalar field to particles. The upper bound for dark matter as a particle is given by the Planck scale, at which the particle collapses into a black hole by its own weight. For even higher mass, dark matter can be macroscopic objects, like Primordial Black Holes (PBHs) [21]. Note that PBHs are not included in the 5% baryonic matter budget, as they were produced before BBN [2, 3]. However, they are disfavoured as major contributors to the dark matter component by galactic and cosmological observations [22].

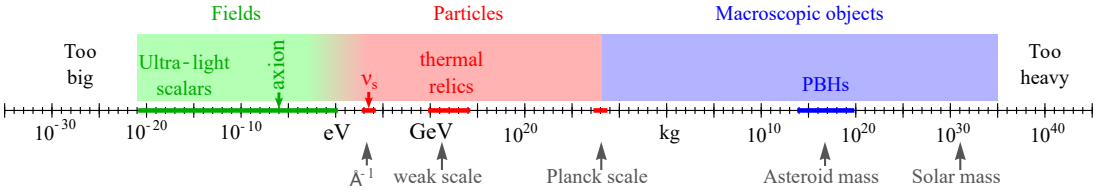

Figure 1.4: Mass range of dark matter candidates, such as the ultra-light scalars, axion, the sterile neutrino ν_s, and the primordial black holes (PBHs). The region for thermal relics that motivate weakly interacting massive particle (WIMP) is also marked. Various length scales are labelled in grey for the reader's reference. Figure adapted from [2].

1.2.1 The Standard Model

Concerning dark matter as particles, given the stated requirements, dark matter cannot be composed of Standard Model (SM) particles. As it should be non-baryonic, protons and neutrons are excluded. The requirement of long lifetimes rules out the bosons[1] and mesons. The absence of electromagnetic interactions further excludes charged leptons or photons.

Neutrinos satisfy several of the necessary conditions, as they are electrically neutral and weakly interacting. However, they cannot constitute the dominant component

[1] Gluon cannot be isolated due to quark confinement.

of dark matter. Neutrinos remained relativistic at the time of structure formation in the early Universe; therefore, they are disfavored [22]. In addition, their measured abundance masses in the Universe are far too small to account for the observed dark matter abundance [8].

In addition to the lack of a viable dark matter candidate, the SM faces several well-known theoretical limitations. These include the hierarchy problem, associated with the unnaturally small mass of the Higgs boson [23]; the strong CP problem, referring to the lack of observed CP violation in the strong interaction [23]; or the unresolved origin of neutrino masses [4]. These problems strongly motivate extensions of the SM, which naturally introduce new particles that can serve as dark matter candidates. Specifically, supersymmetry aims to resolve the hierarchy problem by providing supersymmetric partners of the SM particles, which differ in spin by 1/2, that can cancel the higher-order, divergent terms in the Higgs mass [24]. The theory provides WIMP candidates, such as neutralinos [4]. The Peccei–Quinn framework introduces a new field that, upon spontaneous symmetry breaking, gives rise to axions, possibly a dark matter candidate, and suppresses CP violation [25, 26]. The seesaw mechanism incorporates sterile neutrinos, which are potential dark matter candidates, to provide a small mass for the detected neutrinos [4].

Given the scope of this thesis, the remainder of this discussion is devoted to assessing the suitability of WIMPs as dark matter candidates.

1.2.2 Weakly Interactive Massive Particles (WIMPs)

In the hot plasma stage of the early Universe, dark matter particles constantly exchange energy with SM particles via elastic scattering, production, and annihilation; therefore, they were in thermal equilibrium. As the Universe expands, the number density of the dark matter particles reduces, so does the probability for them to annihilate into SM particles. At a certain point, the dark matter density stopped changing ("frozen out") into the *relic density*, the density that we measure today. The relic density depends on the annihilation cross section. If the cross section is assumed to be at the weak-scale, the freeze-out density aligns with the observed dark matter abundance of 26%, for the mass from a few GeV/c^2 to 100 TeV/c^2 [27]. Since there is no a priori reason why the two parameters are consistent, this agreement is called the "WIMP miracle" [4].

In addition to cosmological considerations, WIMPs are well motivated from a particle-physics perspective. As discussed above, supersymmetric extensions of the Standard Model naturally predict stable, weakly interacting particles such as the neutralino [2, 4]. The new particle can simultaneously address the dark matter and hierarchy problems of the SM, thereby contributing to its prominence as a leading WIMP candidate among other possibilities.

1.3 The Hunt for WIMPs

To investigate the properties of WIMPs or other dark matter candidates, dedicated experimental approaches have been developed. These searches are grouped into three categories: *direct detection*, *indirect detection*, and *collider searches*.

Direct detection experiments aim to observe the scattering of dark matter particles off SM particles, typically nuclei, in terrestrial detectors. Indirect searches look for signatures of dark matter annihilation or decay in astrophysical environments, such as excesses in gamma-ray fluxes. Such searches are sensitive to assumptions about the dark matter halo distribution and require precise modelling of astrophysical backgrounds. Collider searches probe the dark sector by colliding SM particles at high energies, potentially producing dark matter particles or their mediators, which are inferred from missing-energy signatures.

In the following, direct detection of WIMPs is discussed to narrow the scope of the discussion.

1.3.1 Interaction Rate for Direct Dark Matter Search

As WIMPs do not carry electric charge, they rarely interact with atomic electrons, so-called electronic recoil (ER). If they interact with SM particles, they are most likely to elastically scatter off and transfer the momentum to the atomic nucleus, called nuclear recoil (NR), which subsequently produces detectable signals [3].

Detectors detecting these signals are placed in underground laboratories to wait for the scattering with WIMPs, analogous to the traditional Chinese proverb, "守株待兔". *Taking only to the literal meaning, it means to stay under the tree for "free" rabbits to come and crash onto the tree, back in the days when hunting for food was still common. The higher the interaction rate, or the event rate from the perspective of the detectors, the faster the "hunt", which is important given the limited human lifespan.*

The event rate is proportional to the local dark matter number density $n = \rho_0/m_\chi$, where ρ_0 is the local DM density, and m_χ is the mass of the dark matter particle. The interaction rate is also proportional to the total number of target nuclei, $N = M/m_N$, where M is the total target mass in the detector and m_N is the nuclear mass. In addition, the event rate also depends on the velocity of the dark matter particle in the detectors' reference frame v, and the scattering cross section σ. The differential event rate can be expressed as [3]:

$$\frac{dR}{dE_{\text{NR}}} = nN \int_{v_{min}}^{v_{max}} \vec{v}\, f(\vec{v}) \frac{d\sigma}{dE_{\text{NR}}}\, d^3\vec{v}, \tag{1.2}$$

where E_{NR} is the deposited nuclear recoil energy, $f(v)$ is the normalised velocity distribution function in the detectors' reference frame.

Direct detection experiments can exploit the relative motion between the Solar System and the Milky Way. As the Solar System orbits the Galactic centre within the dark

matter halo, dark matter particles acquire a higher relative velocity with respect to detector target particles. This effect gives rise to the so-called "dark matter wind". For the distribution function, the Maxwell-Boltzmann velocity distribution with most probable speed at 220 km/s is commonly used [2, 3]. The minimum velocity v_{min} to induce a NR of energy E_{NR} [3]:

$$v_{min} = \sqrt{\frac{E_{\text{NR}} m_N}{2} \frac{1}{\mu^2}}, \tag{1.3}$$

where μ is the reduced mass of WIMP and the nucleus. The maximum velocity, $v_{\max}$, is set by the Galactic escape velocity, measured to be approximately 544 km/s, albeit with significant uncertainty [3, 22]. The local DM density $\rho \sim 0.3\,\text{GeV/c}^2/\text{cm}^3$, which has a large uncertainty of $\sim 50\%$ [3]. However, ground-based experiments tend to assume the same value of $0.3\,\text{GeV/c}^2/\text{cm}^3$ for the sake of comparisons.

Given the typical mass of a WIMP of $\mathcal{O}(100\,\text{GeV})$, and the relative velocity of ~ 220 km/s, the de Broglie wavelength is comparable to the typical size of a nucleus. The form factor $F(E_{\text{NR}})$ of the nucleus should be taken into account for the interaction cross section [3]. The cross section, which depends also on the velocity and the recoil energy, has the spin-dependent (SD) and the spin-independent (SI) components, written as [3]:

$$\frac{d\sigma}{dE_{\text{NR}}} = \frac{m_N}{2v^2\mu^2} \left(\sigma_{SI} F_{SI}^2(E_{\text{NR}}) + \sigma_{SD} F_{SD}^2(E_{\text{NR}})\right). \tag{1.4}$$

The spin-independent cross section is given by [3]:

$$\begin{aligned} \sigma_{SI} &= \sigma_n \frac{\mu^2}{\mu_n^2} \frac{(f_p Z + f_n(A-Z))^2}{f_n^2} \\ &= \sigma_n \frac{\mu^2}{\mu_n^2} A^2, \quad \text{if } f_p = f_n, \end{aligned} \tag{1.5}$$

where σ_n is the WIMP-nucleon cross section, μ_n is the reduced mass of WIMP and the nucleon, f_p and f_n are the coupling strength of WIMP to protons and neutrons respectively, A is the mass number, and Z is the atomic number [3]. In the second line, where $f_p = f_n$, the cross section $\sigma_{SI} \propto A^2$, meaning that the higher the mass number, the higher the event rate for spin-independent interactions. At the same time, due to the higher m_N, the minimum velocity v_{min} in Equation 1.3 also increases; in other words, the recoil energy E_{NR} is smaller to compensate. Therefore, to benefit from the increased cross section, the detector's energy threshold must be lowered.

If WIMP is fermionic, which couples to unpaired nuclear spins J, then the spin-dependent interaction becomes relevant, with the differential cross section given by [3]:

$$\frac{d\sigma_{SD}}{d|\vec{q}|^2} = \frac{8G_F^2}{\pi v^2} \left[a_p \langle S_p \rangle + a_n \langle S_n \rangle\right]^2 \frac{J+1}{J} \frac{S(|\vec{q}|)}{S(0)}, \tag{1.6}$$

where $\vec{q}$ is the momentum transfer, G_F is the Fermi constant, $a_{p,n}$ are the effective WIMP couplings to protons and neutrons, $\langle S_{p,n} \rangle$ are the expectation values of the total spin operators for protons and neutrons in the target nucleus, which are model-dependent [3, 22].

The important takeaway is that the SD component does not scale with A^2, but depending on the total nuclear spin J of the target nucleus and the spin-structure function $S(|\vec{q}|)$ [3]. Therefore, sensitivity for the SD interactions is isotope-specific. For example, ^{129}Xe and ^{131}Xe are sensitive to the spin-dependent WIMP-neutron interaction [3].

Going back to the original quest, to build an experiment sensitive to the rare WIMP SI interactions with a reasonably shorter exposure time (of the order of years), the optimal detector should have a high mass number A for which the spin-independent cross section scales quadratically, a high target mass M which give higher number of target nuclei N, a low energy threshold and an ultra-low background not to outgrow the potential signal, if exist. *With the hunting analogy, the hunter should go to a forest with thicker tree trunks to increase the chance of getting free "rabbits" as they crash onto the trees.*

1.3.2 Neutrino Fog as the Irreducible Background

The neutrino fog, defined in [28], refers to a gradual transition into the region with an irreducible neutrino background in WIMP searches, which also produces NR at a similar rate and energy spectrum. The neutrino background is mainly contributed by the ^{8}B neutrinos from the sun, the atmospheric neutrinos and the diffuse supernova background [3]. They interact with SM particle via coherent elastic neutrino-nucleus scattering, or CEνNS (pronounced as "sevens"), which has a similar spectrum as for WIMPs. At the same time, as with WIMPs, they cannot be effectively shielded against because of their low cross sections; thus, they constitute an irreducible background for WIMP searches.

There are ways to mitigate the neutrino fog, for example, by observing the annual modulation of the signal. The event rate has a dependence on the relative velocity between the DM particles and the detector on Earth, as shown in Equation 1.2. When the Earth is moving in the same (opposite) direction as the solar system around the Milky Way, the velocity is enhanced (reduced). This affects the event rate as shown in Figure 1.5. The figure also shows that the Solar System is currently moving toward the constellation Cygnus, meaning that the dark matter wind is blowing from that direction. In experiments sensitive to the directional information of incident DM particles, such as the CYGNO experiment [29], they can better distinguish the neutrino, especially from the sun, and the DM signals.

In addition to the annual modulation, sufficiently accurate modelling of neutrino fluxes across energy ranges may, in principle, enable statistical discrimination of a dark matter signal from neutrino-induced backgrounds. Nevertheless, achieving this discrimination requires large exposure, precise spectral measurements and reliable theoretical predictions of the neutrino energy spectrum [22].

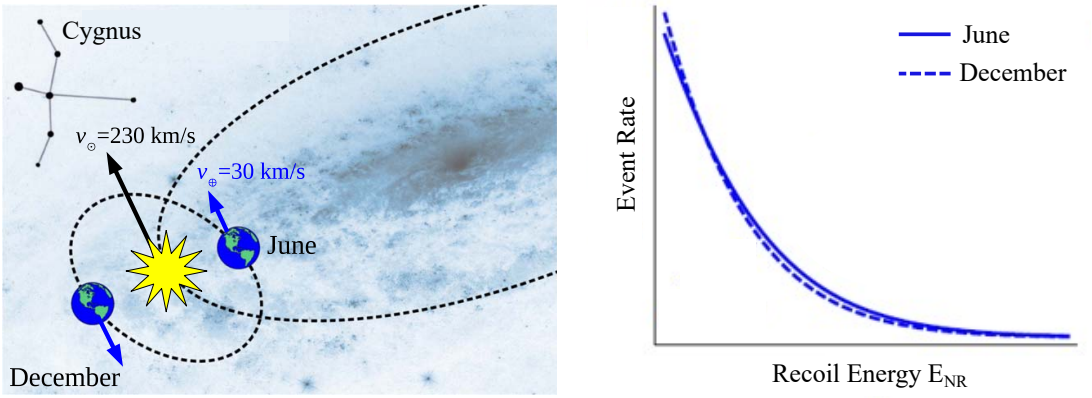

Figure 1.5: Annual modulation of the dark matter event rate. Left: Illustration (not to scale) of the motion of the Solar System within the Milky Way for different months, with constellation Cygnus shown for direction reference. Figure taken from [3]. Right: Dependence of the dark matter event rate on the recoil energy E_{NR} in June (solid line) or December (dashed line). Plot adapted from [22].

1.3.3 Experiments and Current Status

For the NR interaction, possibly coming from a WIMP, most of the deposited energy is transferred to heat, or phonons in solid materials. A smaller amount of the deposited energy is transferred to excitation or ionisation of the target atoms [3]. Experiments can detect one or more of these physical quanta, namely the scintillation photons, ionisation electrons or phonons, from the energy deposition, to understand the interaction type and energy. The detected signals for different experiments are summarised in Figure 1.6.

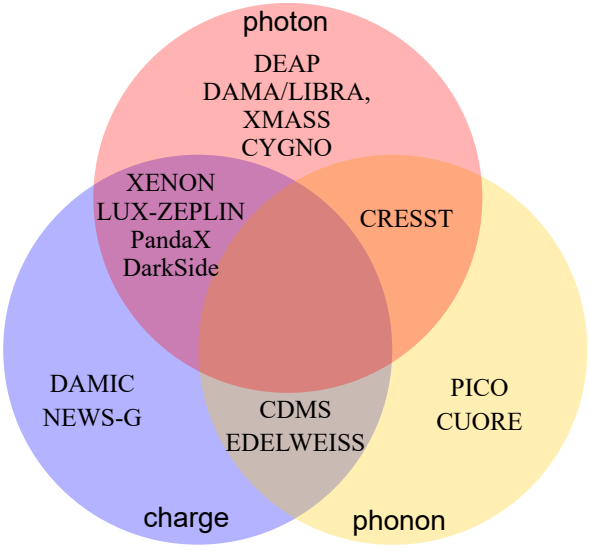

Figure 1.6: Overview of direct dark matter search detectors categorised by their detected signal(s), namely scillation photons, ionisation charge, phonons, or their combinations. The quanta are produced by the deposited recoil energy. Adapted from [30].

The experiments reconstruct interaction events from signals generated by the quanta. After properly removing and modelling the background events, the events potentially

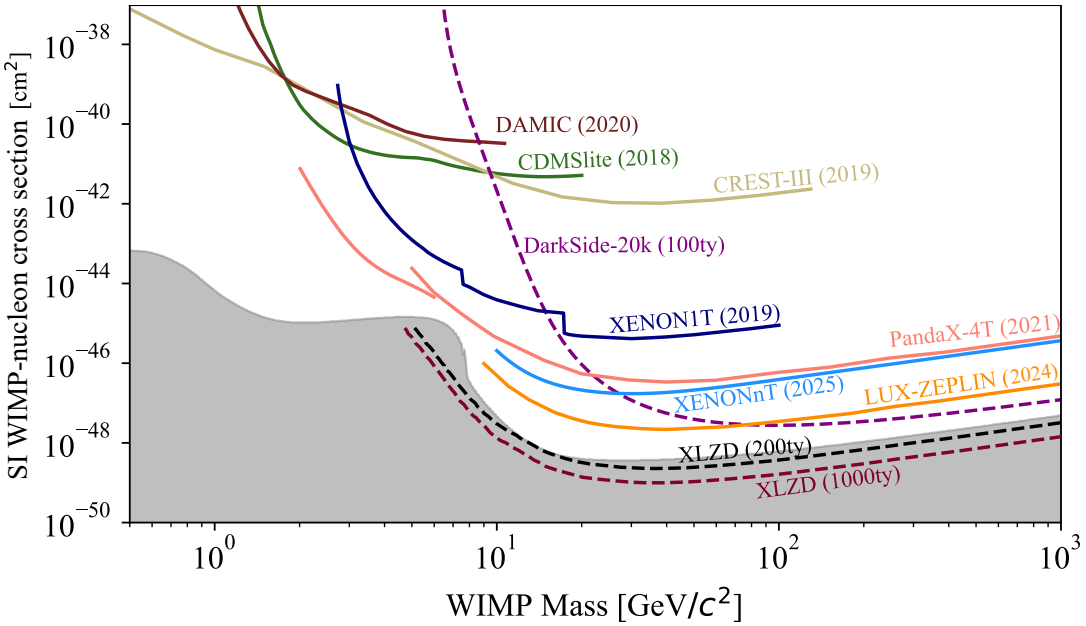

Figure 1.7: Upper limit on the SI WIMP-nucleon cross section over WIMP mass for different experiments. Solid lines indicate the 90% confidence limits, and dashed lines indicate the projected sensitivity. Figure produced using codes and literature values from the Python repository `dd_limit_plot` [31]. The neutrino fog for xenon shown is from [28].

caused by WIMP-nucleon scattering can be selected. Assuming a cross section and a certain WIMP mass, one can calculate the expected total number of WIMP events by integrating Equation 1.2 over the recoil energy spectrum above the detection threshold, multiplied by the exposure time. If the WIMP of each given mass has the assumed cross section, the number of WIMP-like events should match the expected number of events. However, if no WIMP-like events are observed, the experiment can set an exclusion limit on the parameter space of the cross section. The current status of the spin-independent WIMP-nucleon cross section parameter space is shown in Figure 1.7.

So far, neither WIMPs nor other dark matter candidates have been directly detected[2], including collider and indirect searches. As for direct searches for WIMPs, experiments continue to increase sensitivity and are slowly entering the neutrino background.

[2]The DAMA/LIBRA experiment claimed a 12 sigma discovery. However, the results have been in strong tension with other experiments [3, 22]

Chapter 2

Dark Matter Detection with Dual-phase Xenon Time Projection Chamber

In Chapter 1, dark matter as a new type of particle was motivated, with a major focus on the candidate WIMPs. Various detection methods and experiments for direct dark matter searches were introduced. Among these experiments, dual-phase time projection chamber (TPC) detects both the light and charge signals from energy deposition, as categorised in Figure 1.6. This type of detector was proposed in 1995 [32], and has been one of the most effective detector designs for the search for WIMP [33–36].

This chapter introduces the concept of dual-phase xenon TPC, on which the XENONnT experiment and the XLZD project are based. These experiments set the context for the remaining part of the thesis. In section 2.1, the working principle and the various components of the dual-phase xenon TPC are introduced, with the highlight on the indispensable role of the electrostatic field in the TPC. Section 2.2 introduces the XENONnT experiment with a highlight on the challenges of its electrodes. Section 2.3 introduces the XLZD experiment, which is the next-generation experiment planned by converging the efforts of the XENONnT and the LZ experiments, as well as the DARWIN R&D activities.

2.1 Dual-phase Xenon Time Projection Chamber (TPC)

Detecting rare events such as WIMP-nucleon interactions requires that the TPC detector be designed and optimised in the following ways: first, the interaction rate should be maximised to increase the likelihood of observing rare events, and the threshold of the recoil energy E_{nr} should be minimised (see also subsection 1.3.1). Secondly, the efficiency of signal collection, such as light and charge, should be maximised to increase the signal-to-noise ratio. Thirdly, the background should be suppressed as much as possible, using both active and passive background-removal techniques. The remaining discussion in this chapter centres around these three aspects.

2.1.1 Liquid Xenon as Target Material

Liquid xenon and argon are common choices of target materials for the dual-phase TPC for the search for dark matter [34, 35, 37, 38]. A larger target mass increases the interaction rate, as shown in Equation 1.2. Using a liquid target instead of a gaseous target enables a significantly more compact detector design while maintaining a large target mass. The density of liquid xenon (LXe)[1] can be much higher than that of gaseous xenon (GXe)[2], depending on the thermodynamic state variables. Solid xenon[3] has a density close to LXe, similarly for argon, therefore offering little advantage in terms of detector compactness. At the same time, a solid target is less scalable than a liquid or gaseous target due to the difficulty of maintaining crystal homogeneity and the long times required to grow large, uniform crystals. Thus, using the liquid phase as the primary target material is optimal for detector compactness, interaction rate, and scalability.

In terms of the interaction rate, xenon and argon have relatively high atomic masses compared to organic scintillators or lighter noble elements, leading to larger spin-independent cross sections, as shown in Equation 1.5. While xenon has more than three times the atomic mass of argon, its heavier nucleus makes xenon more sensitive to higher-mass WIMPs than argon from kinematic considerations. Therefore, experiments with the two target materials probe slightly different parameter spaces. Nevertheless, xenon experiments have demonstrated a lower recoil energy threshold by analysing only the amplified charge signals, enabling competitive results for light dark matter candidates [40, 41]. The amplification will be explained in Section 2.1.4.

In terms of signal collection, both pure argon and xenon are highly transparent to their own scintillation light, and electrons can drift over long distances in these media due to their low electron affinity [42]. Noble fluids are chemically inert and can therefore be efficiently purified in a continuous recirculation and purification system [43]. As a result, both the ionisation and scintillation signals are preserved as they propagate through the detector, before they are detected by the sensors. This property enable the scalability of such experiments without a significant loss in detection efficiency.

On the other hand, the scintillation light yield in xenon is the highest among noble liquids [44], and the average energy required to produce a quantum (called the W-value), either a photon or an electron, for xenon is lower in comparison to argon [42, 45–47]. In addition, the wavelength of the scintillation light for xenon at 175 nm [48] is detectable by commercial photosensors, while that for argon at $\sim$128 nm [49] usually requires wavelength-shifters which lead to reduction in efficiency and potentially increased background [38, 50, 51].

In terms of background, both argon and xenon have high stopping power due to their high atomic number and density [42], meaning outer detector volume can shield the inner volume from background radiation, a property known as *self-shielding*. To benefit from this, 3D position reconstruction is required to exclude events from the outer

[1] Density of liquid xenon at 177 K and 1.928 bar is 2859.8 kg/m^3 [39].
[2] Density of gaseous xenon at 177 K and 1.928 bar is 18.077 kg/m^3 [39].
[3] Density of solid xenon at melting point is $\sim$3400 kg/m^3.

detector volume. Such a technique will be discussed in subsection 2.1.6.

On the other hand, natural argon has an intrinsic radioactive background from cosmogenically activated ^{39}Ar, which is in the region of interest (ROI) for WIMP search[4]. Distillation columns have been employed to further deplete the ^{39}Ar concentration from underground argon [38]. In contrast, natural xenon has a small intrinsic background for WIMP search from the isotopes ^{124}Xe and ^{136}Xe, which have the half-lives at 1.1×10^{22} yr and 2.23×10^{21} yr respectively [52, 53]. In addition, the 8.9% of ^{136}Xe in natural xenon, which is an isotope that can undergo double beta decay, enabling an additional scientific channel, namely the search for neutrinoless double beta decay ($0\nu\beta\beta$) [53–55]. This hypothetical process beyond the SM requires neutrinos to be Majorana particles. In $0\nu\beta\beta$, the neutrino emitted at one decay vertex is absorbed as an antineutrino at the second vertex, such that the decay energy is shared only between the two emitted electrons, producing a monoenergetic signal [56].

There is also ongoing research on doping a bulk argon volume with a traceable amount of xenon, combining some advantages from both noble fluids [57]. As a final remark, experiments with different target materials are complementary and allow cross-validation of the results.

In the following sections, the discussion is centred on using xenon as the target material, but similar principles apply to argon-based detectors.

2.1.2 Signal Generation using Xenon

As mentioned before, an incoming particle transfers its energy to an atom in the liquid phase. The simplified mechanism of the energy deposition is illustrated in Figure 2.1 and described in detail in [58–61]. The recoiled atom may deposit energy to nearby xenon atoms either through excitation, ionisation, or elastic scattering (i.e. heat) [61]. The increase in heat via elastic scattering is not detectable in this type of detector[5]. With the transferred energy from the recoiled atom, the xenon atoms are either in the excited state, Xe^*, or an ionised state, Xe^+. The excited state Xe^* forms a singlet or a triplet state excimer, also known as the excited molecule Xe_2^*, which subsequently transitions back to the ground state and emits vacuum ultraviolet (VUV) scintillation photons. On the other hand, Xe^+ can form an ionised molecule, Xe_2^+, when combining with another xenon atom. It may recombine with an electron, becoming an excimer that decays and emits VUV light. In this process, the amount of light and electrons produced is called the *light yield* and *charge yield*, respectively.

As mentioned in subsection 1.3.1, incoming particles can interact with the xenon atoms via ER or NR. Background gamma rays and charged particles deposit energy via scattering with electrons in xenon atoms, i.e. the electronic recoil (ER). WIMPs, neutrons, or neutrinos via coherent elastic neutrino-nucleus scattering (CEνNS) deposit energy by scattering with the xenon nuclei, i.e. the nuclear recoil (NR).

[4] On a similar note, natural krypton has large activities of ^{81}Kr and ^{85}Kr, therefore not considered for rare-event searches [42].

[5] Detecting heat dissipation requires an ultra-low-temperature crystal detector, such as SuperCDMS [62], to suppress background thermal noise.

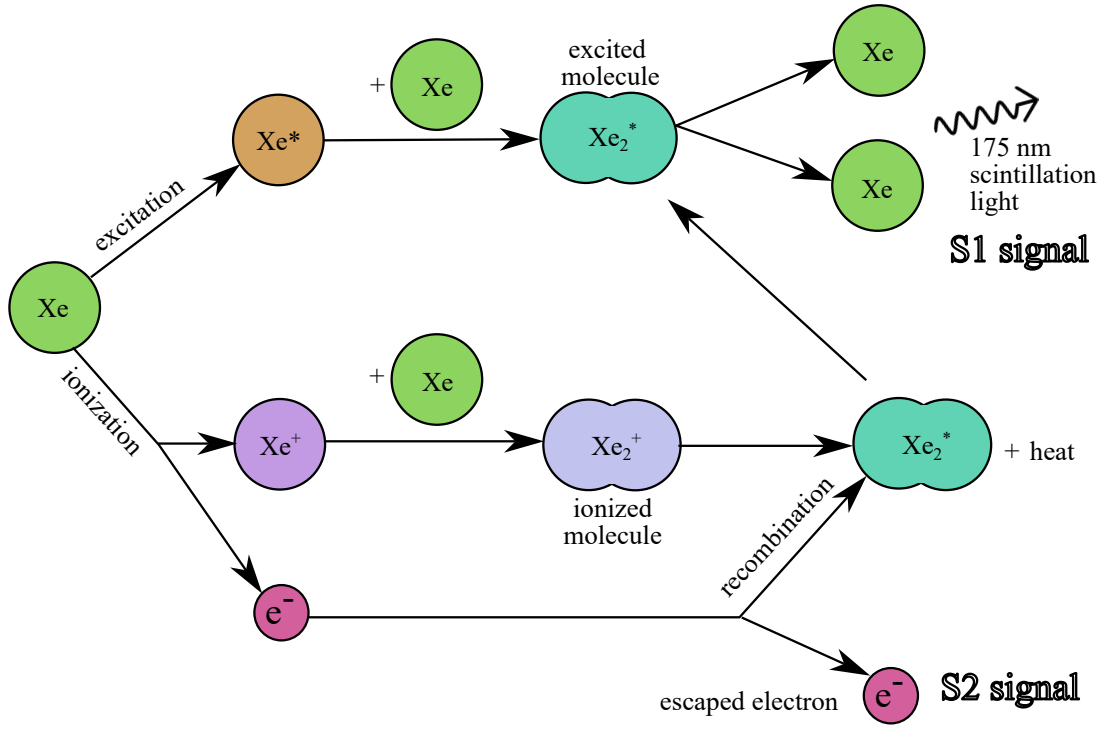

Figure 2.1: Simplified recoil energy deposition processes for a xenon atom. Figure inspired by [63].

The two types of interaction yield slightly different signal responses in the following aspects. Firstly, due to the difference in energy density, the NR has a higher ratio of singlet state (fast) emission than the triplet state (slow) emission [44]. However, since the lifetime for both singlet and triplet states is very short for xenon[6], the difference is difficult to use for discrimination, unlike the case for argon[7].

Secondly, the ratios of light yield to charge yield also depend on the incident particle type and energy, as well as the external electric field [44, 61, 65, 66]. The recoiled nuclei from NR, especially the ionised ones, lose a substantial amount of energy by elastic scattering (i.e. heat) with other xenon atoms, which is undetectable in the xenon TPC. In contrast, due to its small mass, the recoiled electron experiences minimal heat loss, resulting in a higher charge yield than in NR. In addition, the recombination process is faster for interaction with higher ionisation density or stopping power, such as those with NR and alpha particles. This further reduces the charge yield and increases the light yield for NR. When an external field is present, in this case, the drift field, the field can pull the electrons away before recombination happens, especially for ER.

In summary, the simultaneous detection of scintillation light and ionisation charge of xenon from an interaction enables effective discrimination between NR and ER events. Since WIMPs are expected to interact predominantly via nuclear recoils, while most background particles produce electronic recoils, ER/NR discrimination allows efficient rejection of background events, thereby enhancing the sensitivity of WIMP

[6]For liquid xenon, the lifetime for the singlet (triplet) state is 4.3 ± 0.6 ns (22.0 ± 2.0 ns) [64].

[7]For liquid argon, the lifetime for the singlet (triplet) state is 7.0 ± 1.0 ns (1600 ± 100 ns) [64]. The long lifetime of the triplet state enables the pulse-shape discrimination between interaction types.

searches. The following section introduces the dual-phase xenon TPC as a dark matter detector that can effectively measure both the charge and light signals upon interaction.

2.1.3 Working Principle

Dual-phase xenon TPC detectors for dark matter searches are usually built in a cylindrical geometry. A schematic diagram of the standard implementation of a dual-phase xenon TPC is shown in Figure 2.2 (left). As shown in the figure, LXe, as the target material, occupies most of the detector volume. In addition to the liquid phase, there is also a thin layer of GXe sitting on top, hence the name "dual-phase" TPC.

As can be seen in the figure, LXe as the target material occupies most of the detector volume with a thin layer of GXe on the top. This configuration is called "dual-phase" TPC as opposed to "single-phase" used in experiments such as XMASS [67] and NEXT-100 [68].

One of the most crucial components of the TPC is the electrostatic field within, which is primarily defined by three electrodes: the anode, gate, and cathode, shown in Figure 2.2, as well as the field cage surrounding the side of the detector (not shown). When a WIMP particle scatters with the xenon nucleus, the recoiled nucleus deposits energy to neighbouring atoms either by excitation or ionisation. The excited atoms emit the VUV scintillation light, which is the primary signal, usually referred to as "S1". At the same time, the free electrons from ionisation drift upwards and are extracted into the gaseous phase by the established electrostatic field in the detector. The electrostatic field in the gaseous phase is high, such that the accelerated electrons excite more xenon atoms in the gaseous phase to emit VUV light, which is labelled as the secondary signal or "S2". Since the S2 lights are induced by electrons, they are also called electroluminescence (EL).

The light from both the S1 and S2 is collected by photosensors located at the top and bottom of the detector, as shown in Figure 2.2 (left). The two signals can be distinguished by their characteristic pulse shapes. The lateral positions, x- and y-positions, of individual signals are reconstructed from the light distribution across the photosensor arrays, also called the hit pattern. With the knowledge of the electrostatic field configuration in the detector, the electron drift path can be estimated. This information enables correlation of the lateral positions of the two signals originating from the same interaction vertex, allowing the two signals to be paired. In addition, given the estimated drift path and drift velocity, the time difference between the paired S1 and S2 signals can be related to the interaction depth (z-position). This motivates the term "time projection chamber".

The volume bounded by the cathode and the gate electrodes is called the *active volume*, as only interactions within this region can produce both correlated S1 and S2 signals. A paired S1 and S2 signal within the active volume is defined as a reconstructed *event*, and the 3D position of an event can be determined as described above. Such 3D position information enables the rejection of background events that interact near the outer regions of the liquid xenon target, as noted in the previous section.

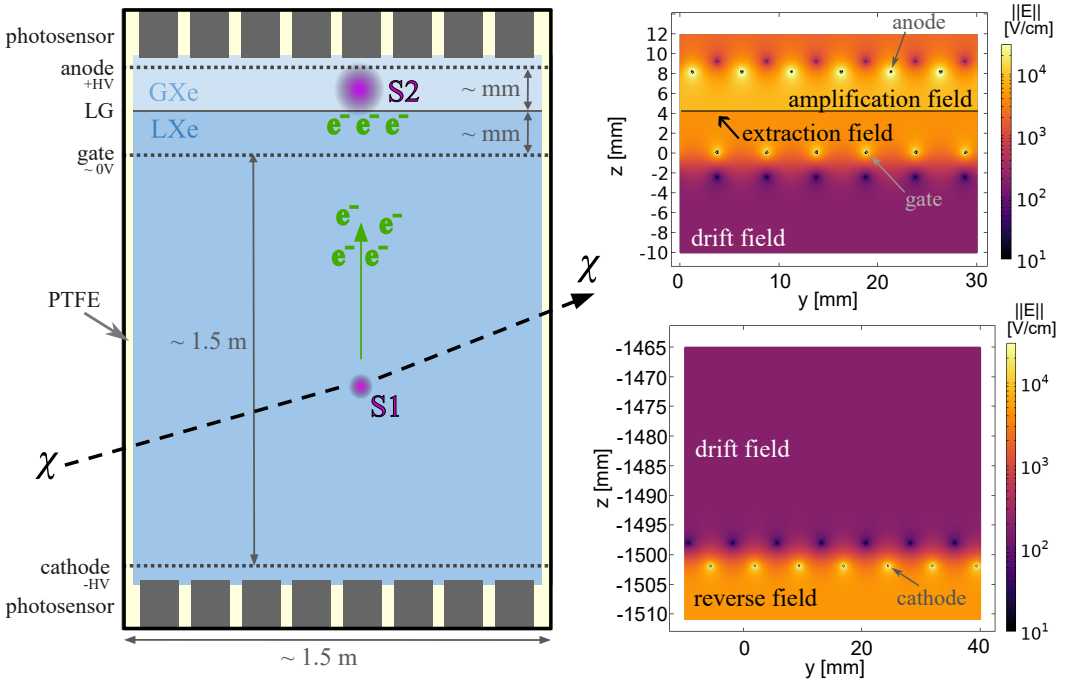

Figure 2.2: Left: side-view schematic diagram (not to scale) of the dual-phase time projection chamber (TPC) adapted from [1]. The provided dimensions are similar to the current generation experiments [35–37]. The horizontal dotted lines represent the electrodes, namely the anode, gate and cathode. The horizontal solid line indicates the liquid-gas (LG) interface located between the anode and the gate electrodes. The photosensors (grey boxes) and PTFE reflectors (pale yellow regions) are also shown. The black dashed arrow marks the path of a dark matter particle χ. The green arrow indicates the direction of electron drift. The primary and secondary signals are denoted S1 and S2, corresponding to the light and charge signals produced by energy deposition during interaction. Right: zoomed-in diagram of the region around the electrodes, with the colour map indicating the magnitude of the electrostatic field. The conventional names of the corresponding field regions are labelled. The small black circles represent the grid-like electrodes, as indicated. The local minima in the electric field map around the electrodes arise from the repulsion of electric field lines between electrode grids held at the same electric potential.

2.1.4 Electrostatic Field in TPC

As mentioned, the electrostatic field in the detector is responsible for projecting the z-position of the interaction onto the time axis and converting the charge signal into a light signal, which is crucial for the operation of the SiPMTPC. The field configuration can be further optimised to improve the detector's performance in terms of signal detection efficiency and background mitigation.

The electrostatic field is primarily established by the anode, gate, and cathode electrodes, as well as the field cage. The anode and the gate are typically a few millimetres apart, sandwiching the liquid-gas interface, while the cathode is situated at the bottom of the TPC. In addition to the three electrodes, conventional TPC detectors for dark matter experiments include two additional screening electrodes, which are biased at a potential close to that of the photosensors and shield them from strong external fields. However, their necessity is debatable [34] and does not affect the operation principle

of the dual-phase detector; hence, they are omitted from the remainder of the discussion.

Regarding nomenclature, the field regions are named according to their functionality, as shown in Figure 2.2 (right). The *drift field*, bounded by the gate and the cathode in the liquid phase, is responsible for drifting the electrons from the event vertex to the liquid-gas interface. The applied potentials at the gate, cathode, and field cage primarily define the field in this region. The strong *extraction field* at the liquid-gas interface enables electrons to overcome the potential barrier and be extracted into the gaseous phase. The *amplification field* in the gaseous phase is responsible for the amplification of the charge signals and converts them into an S2 light signal via EL. The extraction and amplification fields are primarily determined by the applied potentials at the anode and gate, as well as by the relative vertical position of the liquid-gas interface. In addition, the *reverse field* is present below the cathode, pointing downward and opposite to the direction of the drift field. Although it does not serve a specific purpose, its higher field strength relative to the drift field defines several important cathode design parameters and is therefore relevant.

Since the electrodes are within the field of view of the photosensors, they are designed with a grid-like geometry that allows a significant fraction of the scintillation light to pass through. Due to the grid-like structure, the electric field from one side of the electrode can penetrate to the other through the opening, in contrast to a solid-plate electrode. This effect is referred to as *field leakage*, also visible in Figure 2.2 (right). From the perspective of having a homogeneous detector response, the field leakage should be minimised. However, reducing field leakage generally compromises other electrode parameters, such as optical transparency. A more detailed discussion is presented in chapter 3. Apart from field leakage, there are optimisations or requirements specific to each field region, which are discussed in the following.

Drift Field

The drift field plays an important role in distinguishing NR from ER, thereby improving background rejection efficiency. As noted in the previous section, the recombination probability of free electrons and xenon ions depends on the electric field strength at the interaction site, which in turn affects the ratio of light to charge yield. The charge yield as a function of the light yield for simulated interactions at different drift field strengths is shown in Figure 2.3. The two populations in different colors correspond to ER and NR interactions, often referred to as the ER and NR band. A larger separation between the two populations results in stronger discrimination power and improved background rejection.

As shown in the figure, the ratio of light to charge yield for NR interactions exhibits only a weak dependence on the drift field strength due to their higher ionisation density, in contrast to ER interactions. At the higher drift field, the charge yield for ER events increases, as ionisation electrons are extracted more efficiently before recombination can occur. At lower drift fields, the two populations overlap more significantly, leading to degraded discrimination power. ER events that cannot be distinguished from NR events in the light and charge yield parameter space are referred to as ER

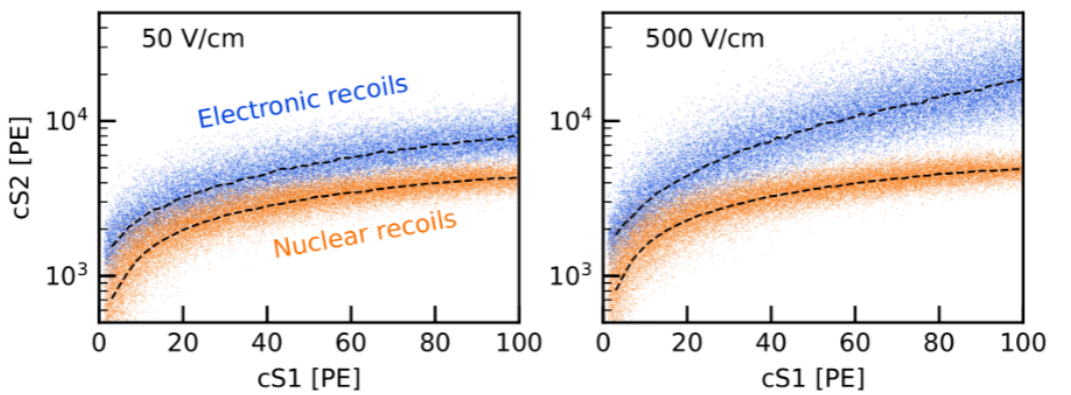

Figure 2.3: Simulated ER and NR band as a function of S1 signal. "cS1" and "cS2" refer to the S1 and S2 signals with the detector effects corrected. The field strength of the drift field is (left) 50 V/cm and (right) 500 V/cm, as labelled in the subplots. Taken from [19].

leakage.

Nevertheless, when detector effects and associated uncertainties are taken into account, it has been shown that higher drift fields do not necessarily lead to improved discrimination power or reduced ER leakage. Ref. [69] studied the dependence of ER leakage on the drift field, as shown in Figure 2.4. It was found that the optimal drift field lies in the range of $240-290$ V/cm. While the higher ER leakage at low drift field is expected, that at high drift field was potentially due to the uncertainty of the gain of the S1 and S2 signals, as well as the uncertainty of the field strength at interaction site. It is also noted in [69] that the result might differ with different detector thresholds, as seen in the same plot, where XENON100 reports a low ER leakage also at 100 V/cm.

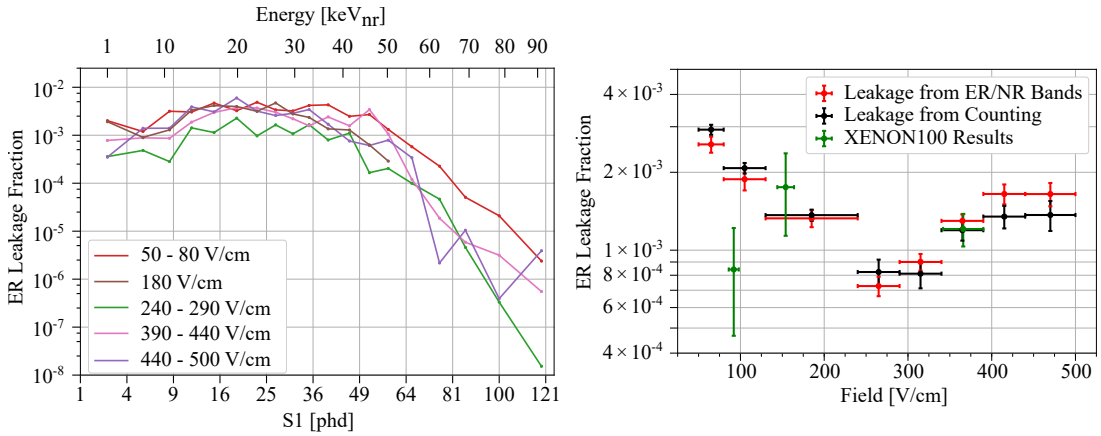

Figure 2.4: Left: Dependency of the ER leakage fraction on recoil energy and drift field. Right: integrated values for the events with 1–80 S1 photons detected (phd). Plots taken from [69].

In addition to the requirement for field strength, the drift field should also be optimised for spatial homogeneity. In the active volume with a non-homogeneous drift field, the electrons may drift laterally and collide with the sidewall. In such a case, the S1-S2 pairing will be impossible, thus reducing the active volume of the detector.

Also, a non-homogeneous drift field results in a non-uniform light and charge yield across the detector. This non-uniformity can, in principle, be corrected, given a good knowledge of the electrostatic field configuration in the detector; however, the uncertainty from the corrections degrades the discrimination power between ER and NR interactions, as suggested in [69].

The homogeneity of the drift field can be improved by implementing an array of *field shaping rings* behind the PTFE side reflector of the TPC, where the potential on the rings gradually decreases from the gate potential to the cathode potential [19, 70]. Since a perfectly homogeneous field is unattainable, accurate knowledge of the field configuration inside the TPC critical for correctly tracing the drift paths of the electrons in the TPC [19]. The information is provided by electrostatic field simulations, as discussed in chapter 4.

Extraction Field

As the free electrons reach the liquid-gas interface, the strong electric field at the interface enables electrons to overcome the potential barrier and be extracted into the gaseous phase. A fraction of these electrons is extracted into the gaseous phase, characterised by the *extraction efficiency*. The field strength at the liquid-gas interface governs the extraction efficiency. At the interface, due to the different dielectric constants between LXe and GXe, the electrostatic field has a discontinuity at the boundary, given as:

$$\begin{aligned} E_{\perp_g}\epsilon_g &= E_{\perp_l}\epsilon_l, \\ E_{\parallel_g} &= E_{\parallel_l}, \end{aligned} \tag{2.1}$$

where $E_\perp$ is the field perpendicular to the surface, $E_\parallel$ is the field parallel to the surface, ϵ is the dielectric constant, the subscripts g and l annotate the gaseous and liquid side of the interface. In the case of xenon, $\epsilon_{LXe} = 1.88$ [71, 72], and $\epsilon_{GXe} = 1.00127$ [71]. So the field in the gaseous phase is approximately twice as strong.

There is a strong indication that an extraction efficiency below 100% might result in trapped electrons being released in an uncontrolled manner, leading to delayed electron signals [73, 74]. These delayed signals might be misidentified as S2 signals and accidentally paired with an uncorrelated S1 signal. In addition, the release of an excessive number of uncontrolled electrons may saturate the photomultipliers (PMTs), thereby increasing the detector's downtime. Therefore, an extraction efficiency close to 100% is recommended.

The field strength at the liquid side of the interface, for which the extraction efficiency approach 100%, was found to be larger than 5 kV/cm[8] [75], or a higher value $>$7 kV/cm [76, 77]. In any case, to achieve a high electric field, the distance between the anode and the gate is typically very small, on the order of a few millimetres.

[8]Note that sometimes in the literature, the field in the gaseous phase is quoted instead [34, 75].

Amplification Field

As mentioned, the amplification field accelerates the extracted electrons until they collide with the xenon atoms. These collisions excite the xenon atoms, which subsequently emit VUV photons at 175 nm. This physical process is called electroluminescence (EL), and it is detected as the S2 signal. The amount of produced photons depends on the drift path L_d from the liquid-gas interface and the anode, as well as the field strength along the path. With a distance $L_d \sim 4\,\text{mm}$ and a potential difference between the gate and anode $\Delta V_{ag} \sim 7\,\text{kV}$, a single extracted electrons can generate a few hundred VUV photons close to the photosensor array at the top of the detector (see also Section 5.8), thus amplifying the charge signal.

The amplificator factor, or gain, was found to be linearly related to the reduced field (i.e., the field divided by the pressure) for a certain range of field [75, 78]. Meaning that even at 100% extraction efficiency, the higher the field, the higher the EL photon yield. The pressure dependence is related to the electron collisional mean free path. At low pressure, the electrons are more likely to accelerate for longer and gain more energy before a collision. If the reduced field is high enough, the electrons can gain enough energy to ionise xenon atoms[9]. Therefore, the aforementioned linearity between the number of electrons and EL yield holds until accelerated electrons begin to ionise additional electrons, producing an electron avalanche, also called electron multiplication [49, 75].

In general, the gain for the S2 signal should be large enough that the detection of a single electron from the interaction is feasible. Sensitivity down to a single electron allows an even lower recoil energy threshold for studies using only the S2 signal [40, 41]. At the same time, the amplification field should remain below the threshold for electron multiplication, as it could lead to electrical breakdowns that can damage detector components (see also section 5.8). Another constraint is that the EL signal should not saturate the photosensors, as it can complicate energy reconstruction or even damage the sensors. The S2 resolution should be as uniform as possible to avoid adding an uncertainty on the energy reconstruction of the event, as well as degrading the discrimination power [60].

The field in the EL region is fast-changing and complex due to the narrow gap between the anode, the interface, and the gate in the millimetre range, as well as the high field at the electrode surface in the sub-millimetre range. Therefore, knowledge of the field configuration in that region is crucial when designing and calibrating the signals, which will be discussed in more detail in chapter 4.

Typical Potentials on the Electrodes

To satisfy the requirements of the electric field configuration described above, the typical bias voltages applied to the electrodes can be summarised as follows. The distance between the cathode and gate electrodes depends on the detector size H, such that the cylindrical aspect ratio of the TPC remains approximately at unity [80]. The optimal drift field is assumed to be independent of H, so the potential difference between the

[9] The first ionisation energy for xenon is at 12 eV [79].

cathode and the gate scales with H. The gate electrode is typically grounded; thus, the cathode electrode should be at $V_{\text{cathode}} = -||\vec{E}_d|| \times H$, where E_d is the drift field at $\sim 100 - 500\,\text{V/cm}$, and H is the height of the detector. For the current generation experiments with $H \sim 1.5\,\text{m}$, the ideal V_{cathode} should be $\mathcal{O}(-10\,\text{kV})$. The presence of the field cage is essential for the field uniformity within the active volume.

The photosensor array below the cathode is typically positioned within a few centimetres of the cathode to minimise the volume of inactive liquid xenon, which is costly. PMTs are commonly used as photosensors in these experiments (see chapter 7) and typically operate at approximately −1.5 kV. In this case, the combination of the high potential difference between the PMT array and the cathode, as well as the small separation in between, gives rise to the strong reverse field observed below the cathode, as shown in Figure 2.2 (right).

The gap between the anode and the gate need not to be increased with detector size. To achieve the required high extraction field and the amplification field, the electrodes are typically separated by only a few millimetres. With the gate electrode grounded, the anode potential is typically below $+10\,\text{kV}$, optimised based on electrostatic field calculations, such as the one discussed in chapter 4.

2.1.5 Signal Detection Efficiency

To achieve high signal detection efficiency, the detector must maximise the collection of scintillation light from both the S1 and S2 signals. In addition, the number of the ionisation electrons produced at the interaction vertex should be preserved during drift until they are converted into the S2 photons.

The detector design should ensure that the photons produced either in the S1 or S2 signals can effectively reach the sensitive area of the photosensors, quantifies by the parameter light collection efficiency (LCE). To maximise light collection efficiency (LCE), the interior of the TPC chamber is covered by polytetrafluoroethylene (PTFE) (see the example in Figure 2.5), which is highly reflective for xenon VUV light with the reflectance at $> 97\%$ [81].

As mentioned, the electrodes, typically made of stainless steel (SS), are located within the field of view of the photosensors and generally have lower reflectivity than PTFE [82, 83]. To allow a large fraction of scintillation light to pass through, the electrodes are therefore designed with a grid-like geometry. The ratio of the open area to the total area of the electrode is defined as the transparency of an electrode. Purely from the perspective of LCE, the electrodes should be as transparent as possible. Other design considerations for the electrodes are discussed in Chapter 3.

In addition, the photosensors should be arranged to provide high coverage of the detector volume. High photon detection efficiency is also required to effectively capture the light signals. Commonly employed photosensors include PMTs [84] and silicon photomultipliers (SiPMs) [85], with their performance characterised by the quantum efficiency (QE) and photon detection efficiency (PDE), respectively. Extensive selection campaigns are typically carried out to identify the best-performing photosensors

with the highest efficiency [84–86]. Nevertheless, because the scintillation and electroluminescence light fall in the VUV range, the effective detection efficiency is generally limited to approximately 20–30%. A detailed discussion of the photosensors is provided in Chapter 7.

Although the light collection efficiency for S2 signals is less critical due to the large signal amplification in the EL region, achieving single-electron sensitivity remains important for low-energy searches. Therefore, it is essential to retain the ionisation electrons produced at the interaction vertex. To preserve the charge signal prior to its conversion into EL light, a homogeneous drift field is required to prevent electrons from drifting towards the PTFE walls, as discussed above. In addition, the electron extraction efficiency at the liquid-gas interface should be as close to 100% as possible.

In addition, xenon purity is another critical factor for retaining the charge signal during drifting. As the electrons drift through the detector, they can be trapped by or attach to electronegative impurities, thereby reducing the amount of S2 signal. The time before trapping is characterised by the parameter *electron lifetime*. Studies have shown that electrons trapped in the detector can be released at later times, producing delayed electron signals [73, 87]. In addition, impurities in the detector medium can emit electrons through photoionisation, further contributing to delayed electron signals [73]. Such delayed S2 signals can result in mispairing between S1 and S2 signals or contribute to the background in analyses that rely solely on S2 information.

To minimise the presence of impurities, the interior volume of the detector is evacuated to ultra-high vacuum before filling the TPC with xenon. Since detector materials constantly emmanate impurities through a process known as outgassing, continuous purification of the xenon target is required, along with the selection of materials with low outgassing rates when building the detector. The electron lifetime can also be monitored in the xenon purification loop using an additional module, known as a purity monitor [88], which enables calibrations and offline corrections to account for incomplete charge collection.

In addition to backgrounds originating from delayed electron emission, backgrounds from physical interactions and energy deposition must be suppressed, as they decrease sensitivity if not well modelled and can increase the deadtime of the data acquisition (DAQ) system. There are several background suppersion strategies, and the following section will discuss a number of these approaches in detail.

2.1.6 Background Mitigation

The background level is largely suppressed through a combination of passive shielding and active veto systems. First of all, the low-background, high-sensitivity dark matter experiments are also built in deep underground laboraties, as the overburden provides effective passive shielding against cosmic rays, more critically, the cosmic muons (see [3, Figure 9]). Excessive cosmic muon events could overwhelm the DAQ system, leading to deadtime. More critically, muon-induced neutrons can produce NR events, which cannot be distinguished from WIMP-induced events using ER–NR discrimination.

In the underground laboraties, the experiments are also equipped with veto system(s) wrapping around the TPC [89, 90]. They can detect the Cherenkov radiation from background gammas or the neutron events. These events are tagged by the veto system and removed from analysis. These systems can also act as passive shielding, as the water can effectively shield gammas and neutrons if they come from the outside of the detector.

The next layer of the nested detectors arrangement is the TPC. There are background sources from the detector materials, which cannot be shielded against. Before constructing the detector, materials should be carefully selected to minimise the amount of radioactive material remaining in the detector. Screening campaigns are usually carried out [91] for such purposes. The same applies to the electrodes inside the detector, as the combination of radioactivity and high field on the surface can create detectable charge signals [73].

Before operating the TPC, the electrode and other components should also minimise their exposure to air, as it contains ^{222}Rn [92]. Otherwise, the plate-out of ^{222}Rn daughters from the surfaces during the detector's operations contributes to the background for dark matter and $0\nu\beta\beta$ searches [93]. Experiments are also equipped with an active purification system and cryogenic distillation to remove radioactive isotopes, including radon and krypton [35, 93].

While the detector is operating, additional techniques can be used to remove background events at the analysis level. As mentioned, due to the high stopping power of LXe, the outer layer of the active volume shields the background from outside the detector, a property called *self-shielding*. Therefore, with the 3D position of the event, the events at this outer volume of xenon, which are most likely background events, can also be removed from the ROI. The r-component of the event's 3D position was provided by the hit pattern of the S2 signal, and the z-component can be reconstructed from the time difference between the S1 and S2 signals. This technique is commonly known as *fiducialisation*, and the remaining volume is called the *fiducial volume*. Dark matter particle or neutrinos can still penetrate the outer layer due to their low interaction cross-section. The $0\nu\beta\beta$ search is not affected either because the signal originates from within the detector.

In addition to the fiducial volume, background signals from gamma rays and beta decays can also be rejected by the NR-ER discrimination, as mentioned in subsection 2.1.4. Neutrons and CEνNS contribute to the NR background. While the veto system can remove the background from neutrinos, but not the CEνNS due to the low cross-section. Possible directions of mitigation against the CEνNS background was covered in subsection 1.3.2. Nevertheless, they remain the irreducible backgrounds for current-generation dark matter experiments [94]. Note that in some other studies, the ER events might be the signal and NR events become the background, such as the search for solar axions [95] or light dark matter [40]. Typically, ER events are much more frequent than NR events.

There are also background contributions from the electrodes, such as spurious light and charge emission, as well as high voltage (HV) breakdown [96, 97]. They are more

unpredictable and can be detrimental to the detector's operation, so it is important to understand them. Details will be discussed in section 3.2.

2.2 The XENONnT Experiment

The XENONnT experiment is located at Laboratori Nazionali del Gran Sasso (LNGS), which has 1400 m of rocks above the laboratory, to shield the muon flux by six orders of magnitude [98]. The dual-phase xenon TPC of XENONnT, shown in Figure 2.5, has the dimensions of ∼1400 mm in diameter and 1486 mm tall between the cathode and the gate, such that the active LXe mass is 5.9 tonnes. The top and bottom of the TPC are covered by a total of 494 PMTs, each with a round photocathode. For each array, a monolithic PTFE disk of 8 mm thick holds the PMTs in position, together with a thick copper disk positioned behind it. The PTFE disk also reflects the light that lands on the gap between the PMTs. In addition, PTFE pillars and panels (or called the PTFE side reflector), arranged into an icositetragon (24-gon) prism, cover the sides to maximise the LCE. Behind the PTFE side reflectors is the field cage system that improves the field uniformity inside the TPC [70]. The field cage elements include an array of field shaping wires, guard rings and resistor chain. The high-voltage feedthrough (HVFT) outside the field cage delivers negative bias voltage to the cathode from the top of the cryostat.

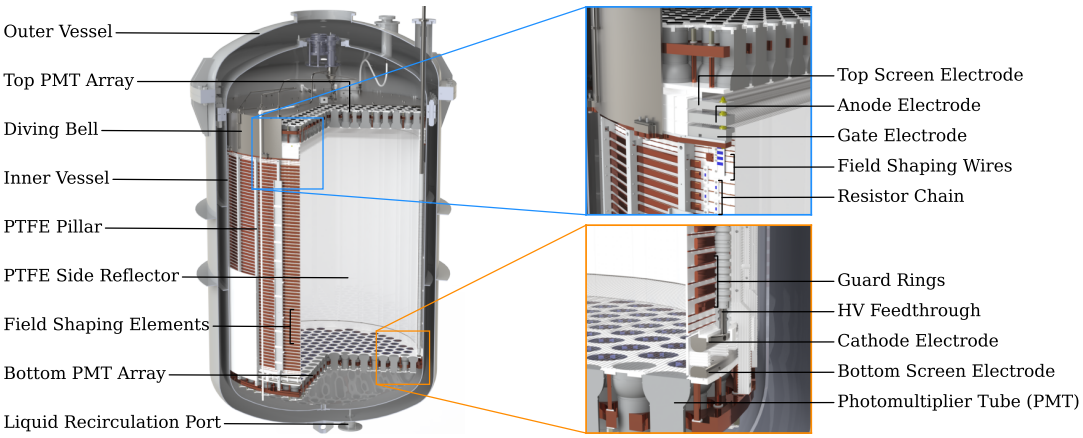

Figure 2.5: CAD drawing of the XENONnT TPC with the cryostat and the LXe/GXe piping. The top and bottom right panels zoom into the top and bottom grid regions, respectively. Image taken from [35], with minor adaptation.

A detailed overview of the instrumentation of the XENONnT experiment is provided by [35]. In this section, the introduction is restricted to facilitate comprehension of the remaining part of the thesis. The following is summarised mainly from [35].

The TPC is insulated by a cryostat with an inner and outer vessel. The LXe fills the inner vessel, and the liquid level is set by the diving bell over the top PMT array. The diving bell can move vertically to control the liquid level, which is then monitored by level meters located at different positions. The liquid levels were set at 4.9 mm or 5.1 mm, summarised later in Table 2.3.

To liquify xenon and regulate the temperature inside the cryostat, pulse tube refriger-

ators (PTR) provide the cooling power. A copper block is thermally coupled to the PTR. Then, a proportional-integral-derivative (PID) controller[10] regulates the temperature of the copper block via a heating element, which in turn stabilises the temperature and the vapour pressure in the cryostat. The nominal operating temperature and pressure are summarised in the table Table 2.1. These parameters are important when determining the EL signal and breakdown voltage of xenon.

Table 2.1: Nominal operating conditions [35].

Absolute pressure	1.9 bar
Temperature	175 K

Outside the TPC, the neutron and muon veto systems passively shield the cryostat and actively tag background events. The two veto systems are optically separated but use the same water in the water tank to detect the Cherenkov light. The 700 tonnes of deionised water in the water tank act both as a passive shield for external radiation and as part of the active veto system. The neutron veto, which encloses the volume 1 m away from the cryostat, is designed to tag the neutrons coming out of the TPC, since neutron events contribute to the NR background. As thermalised neutrons are captured in the water tank, the outgoing gamma rays accelerate electrons via Compton scattering, thereby producing Cherenkov light to tag neutron events. The water tank was later loaded with gadolinium to increase the capturing cross-section. The muon veto system outside the neutron veto has lower efficiency, but it is sufficient to detect muon-induced Cherenkov light.

XENONnT has demonstrated innovative techniques, such as the LXe purification system that can purify 4-16 tonnes of xenon per day; a high-flow radon removal plant to remove the unavoidable radon background continuously; a gadolinium-loaded neutron veto system; and a PMT quality assurance and quality control (QA/QC) campaign that ensures the quality of PMTs before installation [35, 84]. Many more technical aspects of the XENONnT experiments are omitted, such as the calibration sources and purification systems, as they are less relevant to this thesis.

2.2.1 Electrodes and Fields

There are three main electrodes in the XENONnT TPC, namely, the anode, the gate, and the cathode. Additionally, the top and the bottom screens are in place to protect the PMTs from the strong field. In the XENONnT experiment, the collection of the top screen, the anode and the gate is often referred to as the *top stack*, and the cathode and the bottom screen are grouped as the *bottom stack*, due to their vicinity and relevance to each other.

The electrodes consist mainly of parallel wires. The frames for all five electrodes were made of SS304, and the wires are made of SS316, motivated by the reduced amount of electron emission [96]. The geometrical parameters are summarised in Table 2.2. The vertical positions listed in the table were at the nominal operating

[10]Lakeshore Cryotronics, Cryogenic Temperature Controller Model 340. `https://www.lakeshore.com`

temperature, accounting for material shrinkage. Note that the distance between the parallel wire, or the *pitch* (Figure 3.1) is narrower for the top stack. The choice was partly to minimise the electrostatic force between the anode and the gate despite the lower optical transparency.

Table 2.2: Geometrical information of the electrodes for XENONnT. TS and BS refer to the top and bottom screens, respectively. All dimensions are in mm. Apart from the wire diameter, all numbers are rounded to the first decimal place. The frame height and width are simplified. The frame shape refers to the shape projected to the top view. The vertical positions refer to the positions at the bottom of the wires when the detector is at LXe temperature, assuming the wires are perfectly straight. The wire gap is measured from the bottom of the top entity to the top of the bottom entity. Remark(**): gap distance between the gate frame and the copper ring, which is grounded; the distance between the gate and the cathode frame is not meaningful.

Electrode	Frame Shape	Frame Height, Width	Frame Gap	Wire Diameter	Wire Pitch	Vertical Position	Wire Gap
TS	24-gon	15×31		0.216	5	$+36.0$	
			9.9				27.6
Anode	24-gon	18×31		0.216	5	$+8.1$	
			7.9				7.9
Gate	24-gon	20×31		0.216	5	0.0	
			4.9 **				1486.7
Cathode	circle	20×24		0.304	7.5	-1487.0	
			19.9				54.4
BS	circle	15×25		0.216	7.5	-1541.6	

As described in [19, Section 6.3], after a cool-down cycle, the wire deflection of the anode and gate wires increased by $2-3$ mm for the longest wires for each electrode. The minimum gap between the electrodes reduced from the target value of 7 mm to $\sim$3 mm. The continuous reduction in tension across the electrodes suggests the drop is due to relaxation of the electrode frame after the cold test. Subsequently, due to circumstances and to limit the deflection, wires of the diameter of 0.304 mm were added to each electrode perpendicular to the wire array: 4 below the anode electrode and 2 above the gate electrode.

Despite the limited deflection, the perpendicular wires create highly non-uniform fields in the S2 production region and non-uniform extraction efficiency [19]. These non-uniform, rapidly changing fields were challenging to mitigate at the data-analysis level [99].

In addition to the challenge posed by the deflection of the gate and anode electrodes, stable conditions cannot be achieved if the potential difference between the anode and the top screen exceeds 6 kV during commissioning. This limited the anode potential and thus the extraction field between the anode and the gate.

The cathode and bottom screen were also found to be short-circuited. It was probed that the resistance in between is around $10\,\Omega$, matching the resistance of meter-scale SS wire[11] [19]. Therefore, the short circuits are most likely caused by a broken wire connecting the bottom stack electrodes. Regardless of the cause, the bottom stack electrodes have been limited to the same potential. Since the bottom screen is 5 mm away from the bottom PMT array, a high bias voltage for the bottom stack could damage the PMTs.

The bias voltages of all the electrodes during stable operations are summarised in Table 2.3. The drift field was remain at $23.0^{+0.4}_{-0.3}$V/cm instead of 200 V/cm [35]. The extraction field was between 2.9 kV/cm and 3.7 kV/cm in LXe, depending on the non-uniform distance between the wire of the anode electrodes and the liquid surface caused by sagging [35]. The extraction efficiency dropped from the designed value of 96% [100], to $> 70\%$ around the perpendicular wires, and $\sim 53\%$ for the rest of the TPC [35].

Table 2.3: High-voltage configurations in different science runs (SRs). All voltage values are in kV. The liquid level is relative to the nominal position of the gate electrode wires.

	Top Screen	**Anode**	**Gate**	**Top Ring**	**Cathode**	**Bottom Screen**	**Liquid Level [mm]**
Designed	-1.5	6.5	-1.0	-0.95	-30	-1.5	4
SR0	-0.9	4.9	0.3	0.65	-2.75	-2.75	5.1
SR1	-0.9	4.9	0.3	0.65	-2.75	-2.75	5.1
SR2	-0.1	4.85	0.3	0.65	-2.75	-2.75	4.9

2.2.2 Current Status

Despite numerous challenges, the XENONnT experiment has achieved high sensitivity and set competitive limits across multiple scientific goals. The latest limit for WIMP from the XENONnT experiment is also visible in Figure 1.7 with 3.1-tonne$\times$year exposure [101]. Stringent limit of spin-independent WIMP-nucleon scattering cross-section was set above the WIMP mass of $10\,\mathrm{GeV/c^2}$, with the minimum at $1.7 \times 10^{-47}\,\mathrm{cm^2}$ at WIMP mass of $30\,\mathrm{GeV/c^2}$ at 90% confidence level. In addition, XENONnT recorded a 2.7σ indication of solar ^{8}B neutrinos through CEνNS [102], and placed limits on light dark matter [40, 103].

To further enhance the capabilities of the XENONnT experiments, various electrode upgrade options are proposed in section 3.4. The field configurations will be summarised in section 4.4. The realisation of the electrodes is discussed in chapter 5 and chapter 6.

[11] If taken the resistivity of 6.9×10^{-7}, it would require around 1 m of the cathode wire, or around 0.55 m of the bottom screen (BS) wire.

2.3 The XLZD Experiment and the 3-meter Scale Electrodes

The XENON-LUX-ZEPLIN-DARWIN (XLZD) project is a next-generation experiment, roughly twice the diameter and height of current-generation LXe dark matter experiments such as XENONnT. The project brings together three collaborations–XENONnT, LUX-ZEPLIN (LZ), and DARWIN–hence the name. The XENONnT and LZ experiments are the current-generation xenon dual-phase TPC experiments, with the upper limit on SI WIMP-nucleon cross section shown in Figure 1.7 [101, 104]. The DARWIN project was in the R&D phase and was planned with a similar geometric dimension to the XLZD project [105].

Ref. [34] provides a detailed overview of the baseline design of the XLZD experiment as well as areas for further R&D. In this section, the introduction of XLZD is restricted to facilitate comprehension of the remaining part of the thesis. The content was summarised mainly from [34].

The main goal of the XLZD experiment is to achieve a sensitivity for WIMP down to the neutrino fog, which is believed to be an irreducible background [28]. The target is to reach 3σ discovery potential at $3 \times 10^{-49}\,\mathrm{cm}^2$ at $40\,\mathrm{GeV/c}^2$ WIMP mass for SI WIMP-nucleon cross section with $1000\,\mathrm{tonne}\times\mathrm{year}$ exposure. The 90% confidence level upper limits with 200 and $1000\,\mathrm{tonne}\times\mathrm{year}$ exposure are shown in Figure 1.7. It is also sensitive to $0\nu\beta\beta$ in ^{136}Xe, with a half-life up to 5.7×10^{27} years, among many other possible scientific channels.

To achieve the goals, the baseline design for the XLZD TPC has a diameter of 2.98 m. The nominal height is 2.97 m in height with 60 tonnes of active xenon mass. The strategy for achieving the ambitious scientific goals is to design the TPC so that its height can be increased in stages. Specifically, the active mass would start from 40 tonnes, increase to 60 tonnes, and finally to 80 tonnes if the situation permits. This strategy enables improved risk and performance assessment at an earlier stage and provides time for xenon recuperation, while remaining competitive with respect to scientific goals.

Regarding the electrodes, there will be at least three: the anode, the gate, and the cathode. The screening electrodes, which are to protect the PMT arrays, are commonly used in TPCs, but their necessity might be arguable [34]. For example, the LZ and PandaX-4T experiment operates the detector without the top screen [106, 107]. Reducing the number of electrodes results in greater transparency and LCE, a lower radioactive background, and a lower risk of failure or malfunction.

The targeted drift field is around 250 V/cm, resulting in a cathode potential of around 70 kV. A robust solution for delivering the HV is also an active field of research. The extraction field in gas is targeted at $6-8\,\mathrm{kV/cm}$.

At present, there is no decision regarding the type of electrode for XLZD. It could be a parallel-wire, hexagonal etched mesh, woven-wire mesh, or another design, depend-

ing on both performance and feasibility. However, active R&D is undoubtedly needed to build the electrodes for XLZD. It would be increasingly challenging as the detector size increases.

As summarised in section 3.2 and suggested by [97, 108], the surface field requirement on future electrodes is even more stringent, to avoid early breakdown. Electrodes with a larger area are more likely to have asperities that can induce electrode backgrounds, and they are also more difficult to survey, detect, and repair. They require greater mechanical strength to support their own weight while maintaining good optical transparency and low radioactivity. Regardless of electrode type or design, they are becoming increasingly challenging to manufacture and fabricate due to their large size and fine-precision requirements. Last but not least, a robust and efficient QA/QC approach is paramount, as these electrodes must operate in ultra-sensitive experiments for years of uninterrupted operation.

2.4 Summary

At the beginning of this chapter, I listed three major design principles for a rare-event search experiment: maximise the event rate, maximise the signal-collection efficiency, and minimise the background level.

As explained, the choice for xenon as the target material is motivated by both physics and technological point of view. The enhanced event rate and sensitivity for WIMP detection and the possibility to search for $0\nu\beta\beta$. The many physical properties of xenon also benefit signal collection efficiency, and a low intrinsic background level.

The detection efficiency for the light signal is maximised by optimising the LCE of the detector and the QE of the photosensors. The charge signal is enhanced by a better purity level of LXe. The low background level is achieved primarily through passive shielding, an active veto system, careful material selection, fiducialisation, and ER-NR discrimination.

More importantly, throughout this brief overview, I highlighted the relevance of the electrostatic field and the electrodes for a successful operation of such dual-phase TPC detectors on various levels and aspects. To summarise, the electrodes are essential for the TPC in the following ways. First, they provide a uniform drift field for z-position reconstruction. Second, they provide the fields for extracting and amplifying the signal in the gaseous phase, enabling discrimination between ER and NR events. They thereby enable effective and critical techniques for classifying signals and backgrounds within the TPC.

The chapter also highlighted several targets on the electrostatic field configuration. First, we need to achieve a uniform drift field of 100 V/cm to 300 V/cm and an extraction field in liquid beyond 5 kV/cm for 100% extraction efficiency. Secondly, the combination of the anode and the gate should give a good S2 gain and fine S2 resolution. Although not explicitly stated before, the third target is that the field and the electrodes should remain stable for years of operation.

These simultaneous targets, together with the requirement of high detection efficiency and low background level, set stringent and challenging requirements for the electrodes. Primarily, they should provide uniform fields. Note that the field uniformity requirements are more stringent for the anode and the gate, due to the high field and the need for S2 resolution, while it is more relaxed for the cathode. In addition, all electrodes need to be electrically and mechanically robust (i.e., structurally intact). The latter infer that the electrodes should be strong and thick. But they also need to be as optically transparent and low radioactive as possible, limiting the amount of material. Last but not least, the fabrication should be feasible and realisable.

In the next chapter, these requirements are explored in more detail in the context of the various electrode designs.

Chapter 3

Electrodes for Dual-phase Xenon Time Projection Chambers

Given the purpose and requirements of the electrodes, the next question is how to build them. It is, in fact, not a trivial task to build the electrodes that meet all the requirements and targets, despite years of effort and experience. It will be even more challenging for future-generation experiments, where the electrodes are even larger. Therefore, it is of utmost importance to examine the feasible options and identify room for further R&D.

Electrodes consist of a highly transparent grid and a frame that supports the grid's structure, both typically made of SS. Commonly considered types of the grid include parallel-wire arrays, woven-wire meshes, unwoven-wire meshes, and hexagonal etched meshes [109, 110]. The configuration of a parallel-wire array and a woven-wire mesh is self-explanatory. The nonwoven-wire mesh consists of two layers of parallel-wire arrays arranged perpendicular to each other. The hexagonal etched mesh is produced by photochemical etching of a metallic sheet, such as a SS sheet. Photochemical etching is a subtractive manufacturing process that enables the fabrication of complex-patterned structures with high precision on thin sheets [111]. Typically, the anode and the gate use the same grid type to improve S2 response, whereas the cathode may use a different grid type.

Section 3.1 compares the mentioned grid types. Section 3.2 summarises some studies on the HV-related backgrounds for the experiments and HV-stability problems. This is followed by the concrete examples of electrodes from different experiments in Section 3.3. Finally, Section 3.4 introduces the electrode upgrade campaign for the XENONnT experiment.

3.1 Various Electrode Types

The schematic drawing of the top view of the different grids is illustrated in Figure 3.1. The geometry of these grids is mainly characterised by the pitch or opening, as well

as the cross-sectional length scale, i.e. wire diameter d_w or leg thickness d_l. The electrode size, usually characterised by the diameter D, is another important parameter.

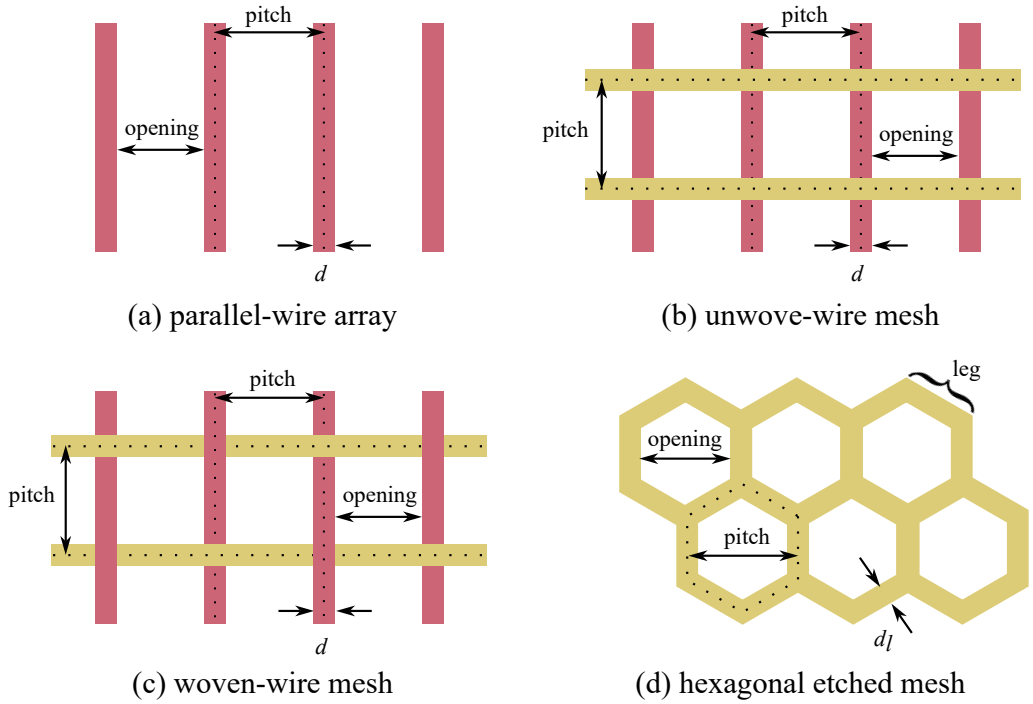

(a) parallel-wire array (b) unwove-wire mesh

(c) woven-wire mesh (d) hexagonal etched mesh

Figure 3.1: Schematic diagram of different types of grid configurations, viewed from top. (a) is a parallel-wire array, (b) is an unwoven-wire mesh, (c) is a woven-wire mesh, (d) is a hexagonal etched mesh. The wire meshes are characterised by their pitch/opening and wire diameter d_w. The etched mesh is characterised by the leg width d_l. Figure adapted from [60].

The field uniformity can be degraded in two ways. One contribution is electrode deflection, which has a larger effect on the anode and the gate because they are usually separated by a small gap. The electrodes deflect primarily due to their own weight and the electrostatic force between them. The deflection can be reduced by applying a higher tension to the grid, at the expense of the structural integrity. Another contribution is field leakage through the grid openings. The larger the opening, the greater the field leakage and thus the worse the field uniformity. In addition, since the opening changes the field, it also alters the electrostatic force and, consequently, the grid deflection; however, the relationship is not monotonic.

In general, due to the more homogeneous geometry, all types of meshes exhibit less field leakage than the parallel-wire array. Also, due to the one-directional load distribution, the unwoven-wire mesh [109] and the parallel-wire array tend to deflect more, including deflecting the support frame. The woven-wire mesh and the hexagonal mesh, on the contrary, distribute the mechanical load in all directions on the plane, such that a flat electrode with a uniform field might be more attainable.

A counterargument to the meshes is that they generally use more material, especially for etched meshes. Not only would that sacrifice radiopurity and transparency, but the increased weight also increases deflection despite the distributed load. The load due to the weight for meshes scales with D^2 for meshes, while that for parallel-wire

arrays scales with D. Note also that typically, cold-drawn SS wires possess greater material strength and better surface finish than cold-rolled or annealed SS sheets made from the same alloy [112, 113]. This difference arises from their respective production methods: wires are drawn, whereas sheets are rolled, resulting in different strains and hardnesses. Therefore, for future electrodes at a larger scale, the flatness and, more importantly, the structural integrity of the etched mesh might also be challenging to guarantee as naively assumed.

Concerning the EL region, studies suggest that a uniform mesh, such as an etched mesh or woven-wire mesh, would reduce the S2 resolution compared to a parallel-wire electrode [60, 109]. At the same time, the electron path for parallel-wire electrodes is also more well-defined than for meshes. This is because the alignment of the anode and gate grid affects the electron path, and thus the S2 signal size and width [60]. Alignment is difficult to control across mesh-type electrodes and is easier for parallel-wire grids.

When considering the local field at electrode surfaces, given the well-defined, round geometry of wires, parallel-wire arrays might be preferred. Wires are also easier to replace if there are observable imperfections, such as kinks, which can cause local field enhancement. On the other hand, meshes have higher surface field variations due to the crossing wires [110, Figure 4.6]. For nonwoven meshes, the gap between the two layers of parallel wires also creates non-uniform fields that are difficult to model and control [109]. Etched meshes can have unprofiled sharp corners and imperfections, such as spiky structures or protrusions, that may occur during manufacturing or handling. These imperfections can introduce high fields and background emission. At the same time, repairing defects in woven-wire or monolithic etched meshes is extremely challenging, if not impossible [110], which could restrict the scalability and practicality of these designs for future experiments.

On the other hand, fractures or breaks in parallel-wire grids or the bottom layer of the unwoven-wire grid would likely be detrimental to the operation of the TPC detector, as dangling wires can short-circuit nearby electrical components (see section 2.2). While woven-wire or hexagonal meshes will not pose a risk of short-circuiting nearby parts upon fracture, the high field around the fracture might still cause emission backgrounds or breakdown. This shows that the structural integrity of electrodes is important for all types of grids.

In terms of manufacturing feasibility, parallel-wire arrays might seem an easier option, due to the availability of long, high-quality wires with a diameter of $\mathcal{O}(100\,\mu\mathrm{m})$. However, as noted in [109], the common strategy of installing parallel-wire grids or unwoven-wire meshes has been challenging. As the wires are tensioned and manually mounted individually onto a frame, the frame deforms, making the process iterative, cumbersome, and error-prone. While an etched-mesh is more straightforward to assemble [107, 114], commercial vendors to date have not yet enabled the production of single-piece etched meshes beyond 1.5 m with an $\mathcal{O}(100\,\mu\mathrm{m})$ [114]. A custom-made woven-wire mesh at the scale of 1.5 m has been demonstrated [109]. However, the delivery at even larger sizes is unclear.

In addition, all types of grids share a common challenge: a 3-metre-scale monolithic frame that holds the grid is also difficult to manufacture and prone to failure (see subsection 5.2.2). The feasibility and robustness of composite frames, which have potentially more mechanically weak points than monolithic frames, have yet to be demonstrated.

It should be emphasised that this comparison serves only as an overview and is over-simplified. Ultimately, all aspects should be optimised together, including the geometry, material, and field for all electrodes, as these parameters are interrelated.

3.2 HV Performances of Electrodes in Xenon Experiments

Despite efforts to build high-quality electrodes, most XENON TPC experiments could not achieve their designed drift field [96], and some could not achieve the desired extraction efficiency of nearly 100%. Examples are shown in Figure 3.2. All TPCs listed here have an aspect ratio $\simeq 1$.

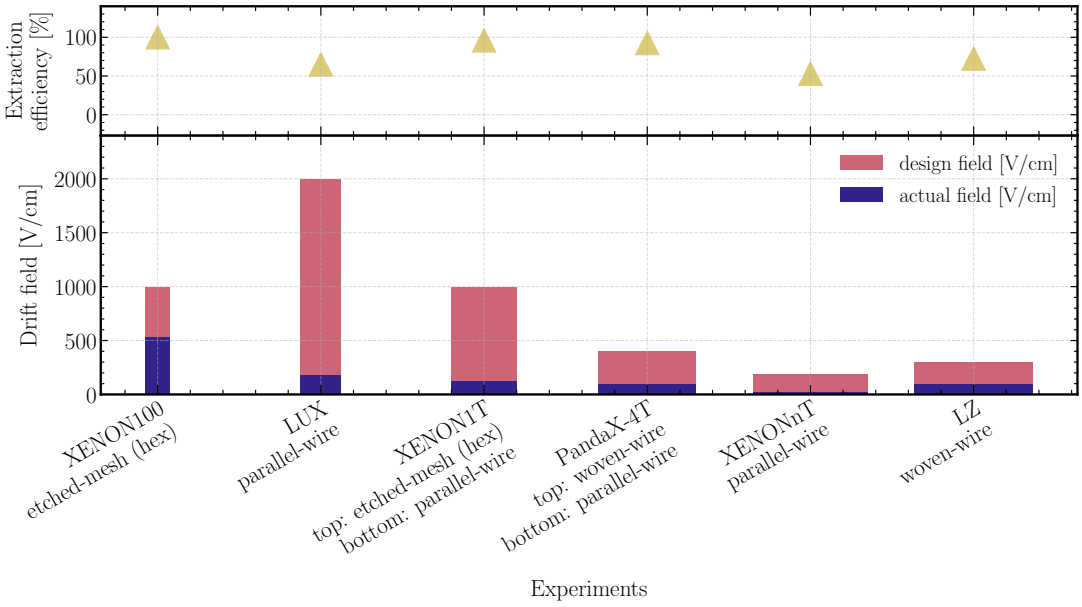

Figure 3.2: Designed vs actual field for different experiments. The designed extraction efficiency is assumed to be 100%. For the drift field, the width of the bars scales with the diameter of the electrodes D. The experiments are also ordered by diameter. This is only a simplified summary, as the experiments comprise multiple runs and campaigns with slightly different field configurations. The values for the actual field were obtained from the drift field used in their major WIMP analysis. The references for different experiments are as follows. XENON100: [115]; LUX: [116, 117] XENON1T: [118, 119]; PandaX-4T: [36, 120], XENONnT: [35], LZ: [104, 106];

Specifically, most experiments reported that they had to limit the bias voltage on the electrodes due to spurious light emission, charge emission, or HV instabilities [73, 104, 115, 118, 121]. The light and charge emission comes from the cathodic electrodes, namely both the cathode and the gate electrodes [87, 104, 122]. These spurious emissions, in case from the gate electrode, can be misidentified as the S2 signals, increase the chance of mis-pairing the S1 and S2 signals (also called the *accidental*

coincidences), impair the energy resolution due to inaccurate reconstruction [73], and compromise the low energy thresholds [96, 122]. In the following, these electrode emissions will be grouped as the *electrode backgrounds*.

In some cases, prominent spurious signals can disrupt the normal data-taking process, creating dead time in the detectors [73, 104]. Prominent charge emission, together with charge multiplication due to a high electrostatic field[1], might lead to HV instability or even breakdown, posing a danger to the experiment's operation. The rapid release of a large amount of energy might damage parts of the detectors [123], for example, saturating the photosensors or causing burn-through in the insulators.

Both the cathode and the gate are submerged in LXe, where the threshold of electroluminescence and charge multiplication was measured at around 400 kV/cm and 700 kV/cm, respectively, using thin wires [96, 124]. For these experiments, the surface field on the electrodes should remain below these thresholds when operating at their designed bias voltages [96]. Nevertheless, experiments with SS electrodes have measured these electrode backgrounds at substantially lower surface fields of around $40-65$ kV/cm, as summarised in [96, 121]. Therefore, there must be additional mechanisms involved that are causing the electrode backgrounds and HV instabilities.

The exact mechanisms causing light emission, charge emission, and HV instabilities are not yet well understood. Popular hypotheses include field enhancement due to positive ions, radioactivity, field enhancement due to dust or asperities on the electrodes, bubble nucleation, and corrosive products in the oxide layer [121, 122].

3.2.1 Photoionisation

The work function for SS is 4.3 eV. Due to the electron-affinity of LXe, SS submerged into LXe has a lower work function of 3.7 eV [96]. The VUV photons from xenon light have an energy of 7 eV, enough to cause photoionisation on the SS electrodes , resulting in delayed electron emission [73]. It was also verified that, in the presence of LXe, the photoionisation rate increases compared to the vacuum case [73]. Note that these signals correlated with the initial (or primary) S1 or S2 signal, and can be mitigated to some extent through specific analysis cuts.

3.2.2 Malter Effect

Another possible cause of electron emission is the Malter effect [73, 122, 125], which is the electron emission when positive ions accumulate on a thin insulating layer on the cathodic electrodes. Due to the insulating layer, the positive ions cannot be neutralised but accumulate on the surface, leading to an enhanced electric field. When the field is high enough, it can pull electrons over the potential barrier, inducing electron emission. In addition, the combination of the insulating layer, or the positive ions, might also alter the work function, favouring electron emission [122, 126]. Upon neutralisation, the energy from recombination on the surface might also induce secondary electron emission [73]. This phenomenon was also observed in wire chamber experiments [126, 127].

[1] See the subsection on "Amplification Field"

As the electrodes are submerged in LXe in the TPC, a thin oxide layer or a solid xenon layer[2] can be formed on the surface of the SS electrodes submerged in LXe [96, 122]. And the positive ions, originating from the interaction, drift towards the cathode. Therefore, with these two conditions, the premise for this hypothesis can be established.

However, [96] suggested that this might not be the dominating effect, at least for faint electron emission or single electron signals. This is because the mentioned processes should correlate with the ion concentration, meaning that for experiments above ground or during calibration, the electron emission rate should be higher. However, they do not observe this correlation. They also added that the ion rate in these low-background-sensitive experiments is much lower than that in wire chamber experiments with high luminosity.

Apart from the above explanations, other light and charge emission mechanisms do not correlate with the actual physical events.

3.2.3 Radioactivity

Radiogenic events can occur at the electrode surface, creating charged particles [92]. Such events might be due to ^{238}U and ^{232}Th in the bulk material or the plate-out of ^{222}Rn. Due to the presence of a strong field at the surface of electrodes, the light signal from the event is largely suppressed, creating electron-emission signals [73].

3.2.4 Corrosive Products in the Oxide Layer

An extensive campaign was conducted on various wire samples in LXe to measure the electrode background as fields increased [96]. Despite the use of ultrapolished fine wires, electron emissions were still recorded before the EL and charge multiplication threshold.

There are several observations. First, samples that underwent the acid and passivation process showed the most significant reduction in emission rates. The acid treatment, also called *pickling*, removed impurities and dissolved the iron surface, thereby increasing the wire's corrosion resistance. During the passivation process in a controlled environment, an impurity-free and smooth chromium oxide layer was formed, which is also more chemically stable than the iron surface. These samples The second observation was that electropolished samples also showed reduced electron emission rates, though not as significantly as those from the pickling and passivation treatment. Thirdly, wires made of SS316L showed a lower emission rate than those made of SS304 or SS302. It is known that SS316 and SS316L have better corrosion resistance compared to other stainless steel variations [128, 129]. Fourthly, a BeCu wire sample, which also has good corrosion resistance, showed the best HV stability and emissions. All these observations provide strong evidence that corrosion in the oxide layer can lead to spurious emission.

[2]By physisorption: formation of a solid layer due to Van der Waals attraction. This effect is strong with xenon, which has many outershell electrons [122].

The microphysical process leading to these observations is not yet known. The authors suggested that a possible microscopic explanation could be the resonant tunnelling effect. Regardless of the microphysical process, this result showed that surface treatment, specifically pickling and passivation, can reduce the rate of electron emissions, and that the use of SS316 is recommended over SS304 or SS302. Although BeCu showed the best performance, SS wires have better mechanical properties.

3.2.5 Bubble Nucleation and Field Emission

Regarding the prominent emissions, HV instability, and early breakdown, a popular hypothesis is that asperities, protrusions, and filaments enhance the field at the electrode surface [60, 96]. When the field is high enough, electrons may overcome the work function and be emitted from the electrode surface.

It was suggested that field emission on wires is relatively difficult to achieve, as a field enhancement factor of $\beta \sim 100 - 1000$ is required [96]. Estimating with Equation (1a) in [130], to reach the current of 1×10^{-16} A for an area of 0.1×0.1 mm and a work function of 3.7 eV, the enhanced field due to asperities have to be around $\mathcal{O}(1\,\mathrm{MV/cm})$. This is the typical local field needed for field emission [131]. Such an enhancement requires a very long, sharp geometry, which is unlikely to have been omitted in these carefully engineered experiments. In addition, the usual electropolishing procedure should smooth these substructures.

The bubble nucleation theory was also considered to explain the HV instabilities seen in experiments [97, 122]. Upon initial field emission, the generated heat causes a bubble to form and grow. Due to the different dielectric constants of GXe and LXe, the field inside the bubble is also enhanced by 1.2 [132]. At the same time, the dielectric strength of GXe is lower than that of LXe. As the bubble grows and the field is strong enough to allow charge multiplication, breakdown can easily occur[3]. Evidence for bubble nucleation initiating breakdown in LXe was observed by low-speed video [97]. The same theory was also used to explain earlier breakdown than predicted in liquid helium experiments [122].

3.2.6 Mitigation Strategies

Based on the above review, a few mitigation strategies should be implemented when building next-generation electrodes, specifically the cathode and gate, as these background emissions and HV instabilities impaired the TPC 's performance.

First, radioactivity on the grid should be kept to a minimum. The amount of material for the electrode grids is insignificant compared to the PMTs, the field cage, or the cryostats, so it may not significantly contribute to the overall radioactive background for the rare-event search. However, it was suggested that radiogenic events at the surface can contribute to electron emissions, thereby inducing delayed signals [73]. Therefore, the material used should be carefully screened and selected. Also, during

[3] According to [132], a secondary feedback effect is also necessary to initiate breakdown. See more in subsection 6.4.2

the final assembly, i.e., after all the cleaning procedures, the assembly time should be kept short to reduce the exposure to ^{222}Rn [110].

Secondly, pickling treatment and passivation showed promising and substantial improvements in the rate of electron emission [96], as mentioned above. The treatment procedure was documented in detail in [96]. In addition, electropolishing the electrode and using SS316 instead of SS304 were recommended, but not BeCu, due to other factors, such as mechanical strength [96].

Thirdly, the cleanliness of the electrode is also important, as attached filaments, dust, or insulating layers can also degrade the HV performance of the electrodes [96]. In addition to standard cleanroom assembly protocols, [107] employed an anti-ionising gun to reduce dust on the electrode.

Fourthly, there should be a systematic method for identifying and removing apserities, as they have been shown to promote early breakdowns. As electrodes become larger in future experiments, it becomes increasingly challenging to survey these asperities and imperfections and to repair them. Therefore, a systematic and efficient method is critical to the success of future electrodes, which will be discussed in chapter 6.

As a final remark, ref. [97, 123] reported the empirical relation between the stressed area A and breakdown field E_{max} with an inverse power law:

$$E_{max} = C \cdot A^{-p}, \tag{3.1}$$

where the coefficient C and the power p are determined empirically, and depend on the material and the treatment of the electrodes. The stressed area depends on the field, the gap distance, and the square of the electrode diameter D^2. Despite the exact mechanism not being fully confirmed, it is reasonable to assume the correlation is due to the number of asperities on the electrode surface, which likely scales with the grid area, leading to earlier HV instabilities. It was also suspected that larger capacitance promotes the earlier breakdown events [108], which can explain the dependency on the gap distance between the electrodes. In summary, this formula motivates a lower threshold for the surface field for the future electrodes at $\mathcal{O}(10)$ kV/cm [97].

3.3 Electrodes Realised in TPC Experiments

Currently, different collaborations have used electrodes such as variations of the parallel-wire electrodes [35, 133], etched-mesh electrodes [114, 115, 134], or a combination of both [118]. The use of woven-wire meshes has also been demonstrated [107, 109]. Additional novel designs include coated electrodes on a transparent substrate [38] or the introduction of supporting structures between electrodes. Note that the coated electrodes cannot be used as the gate electrode; the supported electrodes must still demonstrate good field uniformity and minimal charge-up or leakage current.

In the following, I describe in more detail the latest electrode designs from different experiments. This section will become largely relevant for the realisation of electrodes on a similar scale in chapter 5 and chapter 6.

3.3.1 PandaX-4T Electrodes

The PandaX-4T experiment is a dual-phase xenon TPC experiment (TPC diameter of $D{\approx}1.2$ m and a height of 1.2 m), with the main goal of searching for WIMPs [135]. This subsection was translated from [107, 136].

PandaX-4T chose woven-wire mesh for the anode, gate, and the BS, and a parallel-wire electrode for the cathode. The choice was partly justified by the argument that cathodic electrodes are more prone to discharges, and the parallel-wire array offers a smoother wire surface. A top screen is absent in this TPC design.

The SS woven-wire mesh was manufactured in China, with a pitch of 3 mm and a wire diameter of 0.19 mm. The name of the company was not reported. The mesh was tensioned on top of the SS electrode frame and glued to the frame with even application of epoxy (FT2850) (see Figure 31 in [136]). After around 24 hours, the epoxy was cured. Then, the mesh outside the electrode frame was cut away by wire cutters. The cutting points were spot-welded to remove sharp edges. A subsequent application of epoxy covered all locations with spot-welding to prevent breakdown.

The parallel-wire mesh has a slightly different procedure. First, the electrode frame was manufactured as an elliptical ring, so that after installing all the wires, it deforms into a circular shape. The frame geometry was predetermined using ANSYS simulations. Before installing the wires, the frame was pre-deformed. Then, all the wires were carefully placed on the electrode frame and tensioned by hanging precision weights at each end. Cross-referencing a similar procedure in [134], the electrode frame likely has grooves to ensure wire alignment. The wires are then fixed to the frame using epoxy and spot-welding, as with the woven-wire mesh.

3.3.2 LZ Electrodes

The LZ experiment is another dual-phase xenon TPC experiment, with the main goal of searching for WIMPs [104]. The details of production, handling, and tests of the LZ electrodes can be found in [109, 110] with a few details highlighted here.

The LZ electrodes have a diameter $D{\approx}1.5$ m and are all woven-wire meshes made of SS304 wires. The top screen is also absent in the LZ TPC design. The choice of using woven-wire meshes in motivated in [109, 110], similar to the arguments presented in the section 3.1.

Since a high-quality commercial woven-wire mesh was not available at the time of the work, LZ designed and produced the mesh using a custom-made loom and tools, unlike PandaX-4T, which purchased its woven meshes from vendors. Subsequently, the woven mesh was trimmed to fit the electrode frame and glued to the frame using epoxy[4]. Subsequently, an additional ring (the Glue Ring) was placed on top to cover the sharp edges from cutting. No spot-welding use was reported, as in the case of PandaX-4T. However, the unevenness of the Glue Ring exerts extra load onto part of the woven mesh, leading to damage and breaking the woven mesh [110]. The issue

[4]EP29LPSP from Master Bond

was mitigated by placing plastic beads in between the rings to protect the woven mesh and by paying close attention to the frame's overall flatness.

Other challenges were also reported in [110]. Firstly, there were global distortions of the square geometry during the production of the woven mesh (see Figure 4.17 of [110]). Additionally, it was also challenging to align the anode and the gate mesh. Both obstacles would increase the S2 smearing. Secondly, they noted that the mesh was hard to repair. If a defect is found on a wire, such as a broken wire, it is practically impossible to replace it without damaging the mesh.

3.3.3 NEXT-100 Experiment

The main goal for the NEXT-100 experiment is to search for a signal from the $0\nu\beta\beta$ decay. The use of high-pressure GXe[5] enables particle discrimination based on event tracks and topologies. The experiment completed its commissioning phase in 2024 and started operating the detector in high-pressure xenon [68].

Although the NEXT-100 experiment is a single-phase TPC, its electrode design, operation, and testing share similarities with those of dual-phase experiments. The content in this subsection highlights central elements from [114].

There are three electrodes for the NEXT-100 experiment. The anode and the gate set the electroluminescence region, while the gate and the cathode set the drift region. The electrodes have a diameter of $D{\approx}1.5\,\mathrm{m}$. They used a hexagonal etched mesh from a single SS316Ti sheet.

At first, the etched mesh was also found to be fragile. But through iterations with the manufacturing company, the NEXT-100 collaboration found that using thicker photoresist during photochemical etching and skipping the secondary etching step yielded a sturdy etched mesh with no broken legs at the same geometry and dimensions. Note that no electropolishing of the meshes after photochemical etching was reported.

The authors also explored the fabrication by combining partial semi-circular meshes. Both spot-welding and soldering the meshes together to form a full mesh were attempted. However, the joints were found to underperform and could not sustain the structure for long.

3.4 XENONnT Electrode Upgrade

For the cathode issue, which was presumably due to a broken wire, one possible fix is to remove the broken wire from the electrode. However, there is concern that after one cooling cycle, the wire cathode may become more fragile, potentially leading to more wires breaking. Therefore, we built a backup cathode to prevent such a situation.

As mentioned in subsection 2.2.1, there are several issues with the electrodes for the

[5]The operating pressure is at 13.5 bar [68]. The high pressure also suppresses HV breakdowns. In a dual phase TPC, the pressure is usually at $\sim$2 bar.

XENONnT TPC, which have not been operating at the designed and nominal field configurations. To improve the detector's performance, an upgrade was proposed and carried out over a 3-year program. This section will describe the proposals and the corresponding field configurations using the verified models and strategies for field simulations mentioned in the previous sections.

The upgrade of the electrodes mainly aims to achieve two goals. First, the perpendicular wires for the anode and the gate will be removed after the upgrade, as the highly non-uniform field has been challenging to mitigate. The field between the top screen and the anode will be reduced so the anode can achieve a higher potential. Secondly, the short circuit between the cathode and the bottom screen will be removed.

Therefore, the collaboration decided to build upgraded electrodes that can replace the installed electrodes when an upgrade is considered favourable. Therefore, from 2021 to 2024, we built a set of backup electrodes for XENONnT, including the anode, gate, and cathode, that can replace the installed electrodes when an upgrade is considered favourable. While learning from the experiences, we also considered devising a feasible electrode for the DARWIN electrodes.

A new anode, gate and cathode were built for the upgrade to replace the existing electrodes. Since the top and bottom screens are less critical to the detector's function and performance, and given limited information about the actual issues with the electrodes and limited resources, no replacement was built.

Regarding the new top stack, perpendicular wires were added to the anode and gate to reduce grid deflection, which was believed to be exacerbated by mechanical relaxation after a cooling cycle. To mitigate this, the stress in the new electrode frames was mechanically relaxed by annealing during manufacturing, and the target wire tension of the anode and the gate was increased to provide greater relaxation margins. The anode frame was also made thicker (height from 18 mm to 24 mm) to withstand the substantially increased wire tension. To reduce the field between the anode and the top screen, the top screen was proposed to be flipped, so the wires are at the top of the frame and farther from the anode.

Regarding the bottom stack, a new cathode grid was fabricated with a hexagonal etched mesh instead of a parallel-wire array. The choice of hexagonal etched mesh was intended to reduce the risk of wire breakage. The design and production of the mesh make it unsuitable for the anode and the gate, as discussed in subsection 4.4.1. The new frame was also mechanically relaxed. As mentioned, we know that the resistance between the cathode and the bottom screen is $\approx 10\,\Omega$. If the broken wire were on the bottom screen, the wire would be removed from the screen. In the worst-case scenario, if the top and bottom screens are found to be undesired after opening, the parallel-wire array on the frame will be removed entirely, leaving only their frames in the TPC.

To summarise, the following were proposed for the upgrade operation:

- Option I (best case scenario):

  - The new anode and gate wire tension increased to reduce sagging
  - The new anode frame has modifications to the geometry so that it can better withstand the force from wires (mostly the hole for HVFT is thickened and the height)
  - All the new frames (anode, gate, cathode) were mechanically relaxed before installation by annealing. The anode and cathode frames underwent another cold cycle.
  - Cathode change to hexagonal etched mesh with 4 mm welding seam along the centre.
  - Top Screen will be flipped during the upgrade operation.
- Option II:
  - All items in Option I
  - Remove one bottom screen wire
- Option III:
  - All items in Option I
  - Remove all wires in the top and bottom screens

The following studies in this thesis were conducted focusing on Option I, for which the field simulation model is more complex and the detector configuration is closest to the validated models, thereby enabling more robust verification of the newly implemented field simulation framework (chapter 4). During the upgrade operation, however, it was observed that the top and bottom screens contained multiple loose wires. As a result, it was decided to remove all wires from these screens, corresponding to Option III listed above. As demonstrated in section 4.4, the absence of the screens does not significantly affect the electric-field configuration or the relevant electrode-related parameters; therefore, it will not change the key conclusions of the thesis.

The purpose of the screens is to shield the PMTs from strong external electric fields; therefore, the screens are typically biased at voltages close to the PMT operating potentials. In the absence of the top screen, the top PMT array is exposed to the more positively biased anode electrode, effectively placing the PMTs at a more cathodic potential. It has been demonstrated by the LZ experiment that such a configuration does not significantly affect the operation of either the TPC or the top PMT array [104]. In the XENONnT experiment prior to the upgrade, the bottom screen was negatively biased at a potential approximately 1.25 kV lower than that of the bottom PMT array, with a gap of less than 5 mm. No significant degradation in PMT performance was observed under these conditions. Given that the distance between the cathode and the bottom PMTs exceeds 5 cm, the cathode is therefore expected to be biased at potentials of $\gtrsim$10 times without adversely affecting the bottom PMT array from the perspective of external electric fields. A detailed investigation of PMT performance under strong external electric fields is beyond the scope of this thesis.

3.5 Conclusion

For the optimal performance of the dual-phase TPC detector, the electrodes should fulfil the following requirements:

a Providing good field uniformity: minimum field leakage and minimum deflection
b Low radioactivity
c High transparency
d Minimum electrode-induced background
e Feasible to fabricate
f Robust: good structural integrity and HV stable

As explained, some of the requirements may be mutually exclusive. For example, a thicker electrode favours requirements (a) and (f), but not requirements (b) and (c). All these requirements may result in a complex solution that is difficult to fabricate. The increasing size also adds more challenges to meeting these requirements simultaneously. In addition, methods are needed to quantify the reliability and robustness of these electrodes and reduce the risk of failure during year-long operation at cryogenic temperatures.

Nevertheless, among all these requirements, structural integrity and HV stability are more critical, as malfunctions in either could be detrimental to the detector's operation. While field uniformity, radiopurity, and optical transparency are vital, they are more predictable and stable parameters. They can be pre-determined and possibly corrected during the data analysis. Therefore, this thesis is primarily focused on ensuring the structural integrity and HV stability during the design and fabrication, while assessing the feasibility of fabrication for future-generation electrodes.

Regarding electrode type, I focused on improving the parallel-wire and hexagonal etched-mesh electrodes. This choice is motivated by their performance, which has been proven effective in previous detectors, and by experience in fabrication and analysis gained through generations of experiments. On the other hand, both show limitations for future experiments involving increasing target volumes. From the comparison in section 3.1, we can see that parallel-wire grids have a lower, more well-defined surface field, and the grid itself is easier to scale up. However, they have a higher risk of structural failure and greater grid deformation. On the contrary, the hexagonal etched mesh likely has a higher and difficult-to-profile surface field, and the grid itself is harder to scale up. However, they have a lower risk of structural failure and grid deformation. Improvements or breakthroughs are needed in these areas to make the parallel-wire or hexagonal-mesh electrode a viable option for future detectors.

There are also specific requirements for each electrode. For the anode, the grid deflection requirement is the most stringent among all electrodes, as it strongly affects the S2 response. Similarly, the alignment between the anode and the gate electrodes also affects the width of the S2 signal. Then both the gate and the cathodes are cathodic electrodes, which can induce electrode backgrounds and trigger electrical breakdown. Therefore, their surface field and smoothness are also important quantities of interest for the electrode fabrication.

Apart from the importance of robust electrodes, the need to determine field configurations was also emphasised multiple times. This is important for designing and optimising field uniformity in the bulk volume (both LXe and GXe), as well as to determine certain electrode parameters, such as the surface field and the electrostatic

forces acting on the electrode grid. This leads to the discussion in the next chapter: the electrostatic field simulations.

Chapter 4

Electrostatic Field Simulation

Electrostatic field simulations are an essential tool for the TPC detector in various aspects. First, during the design phase of the experiment, the simulations were performed to optimise the field configuration and to determine appropriate bias voltages for the electrical components, primarily the electrodes and the field cage [19]. The resulting simulated field configuration enables accurate event reconstruction and the application of field-dependent corrections, as explained in chapter 2. In addition, the simulation also provides electrode-related parameters. The electrostatic force acting on the electrodes contributes to the deflection of the electrode grids, leading to an inhomogeneous field and systematic errors. The surface electric field on cathode electrodes is another important parameter concerning the electrode-induced backgrounds.

This chapter first introduces the tools used for the simulations in section 4.1. Results from simple case studies are presented in section 4.2 to explain the subtle differences between the simulations. Section 4.3 summarises the 3D field simulation model and verifications for the XENONnT geometry. Section 4.4 presents the results of applying the frameworks to the upgrade electrodes.

4.1 Simulation Framework

Owing to the geometric complexity of the TPC, the electrostatic field problem must be solved numerically. Several modelling approaches can be considered, including full 3D models, 2D axially symmetric models, and local 3D models. These approaches are often complementary rather than mutually exclusive.

Although a full 3D model may naively appear to be the most accurate option, it frequently entails significant compromises in computational efficiency and, indirectly, numerical accuracy. To improve efficiency, geometric symmetries should be exploited whenever present to reduce the problem size. In case the system possesses, or can be well approximated by, axial symmetry, the full 3D problem can be reduced to a 2D axially symmetric model. Such models are highly efficient, allow fine discretisation of the domain, yield accurate solutions, and are well-suited to performing optimisations

and parameter sweeps. For small structures that break axial symmetry, a focused 3D model with truncated simulation domains can be constructed and subsequently simulated. Such a model is referred to as the *local 3D model* in the remainder of this thesis. The boundary conditions (BCs) of the local 3D models can be derived from the corresponding 2D simulations or by symmetry planes. Despite their high accuracy, these local models are more prone to systematic errors because appropriate BCs are not always straightforward to impose. Full 3D models are useful for verifying the assumptions and results of the local 3D simulations.

Owing to the approximately cylindrical geometry of the TPC, 2D axially symmetric models were employed and found to provide accurate field descriptions in most regions of the detector [19]. Extended features that break this symmetry, such as perpendicular wires mentioned in subsection 2.2.1, are modelled by combining the 2D axially symmetric approach with local 3D simulations [19]. A global 3D model, on the other hand, can accommodate fully three-dimensional extended structures that are difficult to capture with either 2D axial or local 3D models, such as the central welded strip of the upgraded cathode discussed in section 4.4. In summary, all three modelling approaches are employed for the XENONnT field simulations, depending on the specific purpose. In the following sections, their results are compared and cross-verified.

After identifying the appropriate modelling approaches, suitable numerical methods were selected for each case. As explained in the following section (subsection 4.1.1), two numerical methods are considered: the finite element method (FEM) and the boundary element method (BEM). Based on these choices of numerical models and methods, the corresponding software packages were used for the simulations: the commercial COMSOL Multiphysics package (subsection 4.1.2) and the custom-developed KEMField software from the KATRIN collaboration (subsection 4.1.3). Due to their complementary strengths, limitations, and specialised features, both tools were used and cross-verified in this work.

4.1.1 Numerical Methods

Both FEM and BEM are numerical methods for solving partial differential equations, with FEM being more widely used in general applications [137, 138]. The main difference is that FEM solves the equations throughout the volumetric domain, whereas BEM solves problems that can be expressed as an integral over the domain boundaries, thereby reducing the spatial dimension and the number of discretisation elements [137]. In electrostatic field simulations, FEM computes the electric potential $V(\vec{r})$ within the volume, while BEM solves for the surface charge density $\sigma(\vec{r})$ on the boundaries, from which $V(\vec{r})$ can subsequently be evaluated at any arbitary point. In contrast, FEM requires discretisation of the entire volume, with potential values at arbitrary points obtained by interpolation.

In a TPC, the relevant geometrical features span several orders of magnitude. The electrodes consist of hundreds of sub-millimetre wires, whereas the bulk volume has a diameter and height on the order of 1 m. Accurate FEM solutions require fine discretisation in the vicinity of the wires, where the electric field varies rapidly. At the same time, typical element growth rates of 1.2–1.5 constrain how rapidly adjacent el-

ements may increase in size [139], since larger growth rates are known to result in slower convergence and degraded accuracy [140]. This constraint consequently limits the maximum element size in the bulk volume. While this scale disparity has a limited impact on 2D axisymmetric models and local 3D simulations due to the relatively small number of discretisation elements, full 3D FEM simulations become computationally expensive and challenging to scale to larger detector geometries. On the other hand, BEM with reduced dimensionality reduces the number of discretisation elements, making an accurate, efficient full 3D model more attainable.

Since drifting electrons do not contribute significantly to the electric field and no time-varying magnetic fields are present in the TPC, the bulk volume can be treated as source-free. Under these conditions, Maxwell's equations reduce to the Laplace equation:

$$\nabla \times \vec{E} = 0 \Rightarrow \vec{E} = -\nabla V \tag{4.1}$$

$$\nabla \cdot \vec{E} = \rho/\epsilon_0 = 0 \Rightarrow \nabla \cdot (-\nabla V) = -\nabla^2 V = 0 \tag{4.2}$$

where $\vec{E}$ is the electric field, V is the electric potential, ρ is the electric charge, and ϵ_0 is the permittivity of free space. In such a case, the solution in the entire domain is uniquely determined by the *boundary conditions* (BCs).

While FEM can handle the general case in which a volumetric charge density $\rho \neq 0$, BEM is restricted to problems that can be treated as source-free. In the special case where $\rho = 0$, BEM can therefore be applied. In FEM, the partial differential equations are solved directly within the volumetric domain subject to the imposed BCs. In contrast, for BEM, the governing partial differential equation is reformulated as an integral equation over the domain boundaries:

$$\begin{aligned} V(\vec{r}) &= \frac{1}{4\pi\epsilon_0} \oint_S \frac{\sigma(\vec{r}\,')}{\vec{r} - \vec{r}\,'} dS \\ \vec{E}(\vec{r}) &= \frac{1}{4\pi\epsilon_0} \oint_S \frac{\sigma(\vec{r}\,')(\vec{r} - \vec{r}\,')}{(\vec{r} - \vec{r}\,')^3} dS \end{aligned} \tag{4.3}$$

Given the electric potential (Dirichlet BC) or the electric field (Neumann BC) specified on the boundaries, the surface charge density $\sigma(\vec{r})$ can be determined either directly or iteratively. Once the surface charge distribution is known, the electric potential and electric field can be evaluated at arbitrary points in space, for example, by direct summation or through suitable numerical approximations. The implementation details are discussed further in subsection 4.1.3.

In summary, given the scale disparity in the geometry of the TPC, a full 3D simulation using FEM to solve Laplace's equation is computationally expensive to achieve accurate results. BEM can efficiently reduce computational cost and memory requirements by transitioning from 3D volumetric discretisation to 2D surface discretisation. This

makes BEM a compelling choice for the full 3D field simulation for large-scale TPC geometries. The downside for BEM is the large linear system of equations (subsection 4.1.3) that are not trivial to solve efficiently [141].

As discussed in the remaining sections, the 2D axially symmetric and local 3D models were simulated using FEM, although BEM could, in principle, also be applied. For the full 3D model of the TPC with diameters ~ 1.5 m, BEM was employed to improve computational efficiency while maintaining numerical accuracy. The simulation tools used for these models are discussed in the following sections.

4.1.2 COMSOL

COMSOL Multiphysics® [142] is a commercial multiphysics simulation software that supports a wide range of physical models as well as their mutual coupling. Its FEM-based electrostatics module (`es`) is well established and available for both two- and three-dimensional geometries. The software provides comprehensive tools for setting up numerical simulations, including the definition and import of geometries, assignment of material properties, and customisable discretisation. A graphical user interface enables intuitive interaction with complex geometries and facilitates efficient model development.

Several functionalities are particularly useful for TPC electrostatic simulations and have been extensively employed in this thesis. Imported geometries can be modified using so-called "virtual operations", which remove unnecessary geometrical details and improve suitability for numerical simulation. For example, screws and screw holes in the imported CAD model of the electrode frame do not significantly affect the overall field configuration but are computationally expensive to discretise, and were therefore removed using these operations.

Regarding BCs, COMSOL offers numerous options, including prescribed charge, electric potentials or fields, symmetry conditions, analytical functions, and interpolated data. Symmetry conditions can significantly reduce the size of the simulation domain. Analytical functions or interpolated data are particularly useful for defining BCs in the local 3D simulations, whose values can be obtained from full 2D or 3D models.

COMSOL also provides built-in features, such as optimisation and parameter sweeps, that complement the simulation framework. In particular, the optimisation node enables automised tuning of parameters (e.g., electrode potentials) by optimising a user-defined objective function (e.g., minimising the field inhomogeneity). Parameter sweeps are useful for systematic comparisons between different configurations (Appendix C).

In addition, COMSOL includes post-processing tools for analysing and exporting simulation results, and various derived quantities can be evaluated directly. These include the electrostatic force acting on the electrodes, which is directly related to electrode deformation, and the maximum surface electric field, a critical parameter for evaluating electrode-induced backgrounds. Both quantities are particularly relevant for the assessment of the XENONnT upgrade electrodes (section 4.4). Further details of

the COMSOL features mentioned here are discussed in the context of their specific applications.

For the application, the COMSOL FEM electrostatic module is used for both the 2D axisymmetric model and the local 3D models in this thesis, due to the wide range of functionalities COMSOL offers. Although COMSOL introduced a BEM-based electrostatics module, preliminary tests with `version 5.4` revealed unphysical kinks in the calculated field strength when compared to the results for the same geometry obtained using a 3D FEM model with COMSOL or a 3D BEM using KEMField (subsection 4.1.3). The field calculation was also found to be computationally expensive and to require substantial memory. It was not pursued further in this work, but the method remains promising and is worth revisiting in future studies using the updated version of COMSOL.

4.1.3 KEMField

As mentioned, the XENONnT TPC consists of a large bulk volume with fine wires, whose dimensions span several orders of magnitude. The KATRIN experiment [143], which is an experiment dedicated to measuring the electron neutrino mass, encountered a similar situation. In the KATRIN main spectrometer, there is a large vacuum chamber with fine wires, whose dimensions span orders of magnitude. This poses challenges for the standard finite element method (FEM) in electro- and magnetostatic calculations.

For this reason, a custom-made, C++-based software, Kassiopeia, was developed for the KATRIN experiment [144]. It can simulate a system with specific geometry and potentials, evaluate the electromagnetic field for a given system, and propagate charged particles within the domain (vacuum). The software was developed with a modular design, in which one of its submodules, KEMField, was used for electromagnetic-field simulation. KEMField employs the boundary element method (BEM) for simulation. This common challenge between the KATRIN and XENONnT experiments naturally motivates the use of KEMField for the full 3D simulation of the TPC.

In the BEM implementation in KEMField, all the surfaces are discretised into triangles, rectangles or 1D line elements [145]. BCs are imposed on each of the discretised geometrical entities. Then, using numerical solvers, the charge density on each mesh element is determined to ensure that the potential or electric field on all elements satisfies the imposed BCs within the specified tolerance.

One type of BC is to specify the potential, known as a Dirichlet BC. With the discretisation of the boundaries, this results in a system of linear equations, in the form

of $A\mathbf{x} = \mathbf{b}$ to be solved [141, Equation 3.52–3.54, 3.56], where:

$$\begin{aligned} A_{ij} &= \int_{u_i} \frac{du_i}{4\pi\epsilon_0 |\vec{y}_j - \vec{r}\,'|}, \\ x_i &= \sigma_i, \\ b_j &= V(\vec{y}_j). \end{aligned} \tag{4.4}$$

In the equations, i and j denote the index of the discretisation surface elements, u_i represents the differential surface elements, σ_i represents a constant charge density over the surface element u_i, $\vec{r}\,'$ denotes the position on the surface and $\vec{y}$ denotes the position of the centroids of the discretisation elements u_i given by $\vec{y}_i = \int_{u_i} \vec{r}\,' \, du_i$.

Another BC implemented in KEMField is for the dielectric materials, which defines a ratio of dielectric constant on the surfaces, that is, the Neumann BC:

$$\epsilon^+ E_\perp^+ = \epsilon^- E_\perp^- \tag{4.5}$$

where the superscript $+$ $(-)$ represents the position just above (below) the element i, ϵ_i is the dielectric constant, and $E_\perp$ is the field at the centre of the element perpendicular to the surface. With the discretisation of the boundaries, the system of linear equations to be solved becomes [141, Equation 3.71–3.73]:

$$\begin{aligned} A_{ij} &= \frac{1}{\epsilon_0} \left[\frac{1}{2}\delta_{ij} + (1 - \delta_{ij}) \left(\frac{\epsilon^+ - \epsilon^-}{\epsilon^- + \epsilon^+} \right) \int_{u_j} \frac{\hat{n}(\vec{y}_i) \cdot (\vec{y}_i - \vec{r}\,') du_j}{4\pi |\vec{y}_i - \vec{r}\,'|^3} \right], \\ x_i &= \sigma_i, \\ b_i &= 0, \end{aligned} \tag{4.6}$$

where δ_{ij} is the Kronecker delta, $\hat{n}(r)$ represents the normal unit vector at the centroid.

In a simulation, both BCs can be employed for different entities. Usually, the metallic surfaces are considered as perfect conductors by imposing the Dirichlet conditions, and all of the linear insulating surfaces are imposed with the Neumann conditions [141].

To solve the linear system in Equation 4.4 and Equation 4.6, KEMField implemented iterative solvers, namely the Robin-Hood solve [145, 146] and Krylov solvers [141]. Previous attempts to simulate the TPC geometry in KEMField used the Robin-Hood solver [59, 147]. The solver aims to reach an equipotential surface, in the case of the Dirichlet BC, by redistributing charges among elements in each iteration. More details of the implementation in KEMField can be found in [148, Section 3.4.3]. The advantage of the Robin-Hood method is that it can be highly parallelised and benefit from a GPU architecture [59]. The memory usage scales with $\mathcal{O}(N)$ while the arithmetic operation scales with $\mathcal{O}(N^2)$, where N is the number of elements [141]. Details of the algorithm and implementation can be found in [141, Chapter 4].

In Krylov methods, an n-th order Krylov (sub)space is defined as

$$\mathcal{K}_n(A, \mathbf{y}) := \text{span}\{\mathbf{y}, A\mathbf{y}, A^2\mathbf{y}, ..., A^{n-1}\mathbf{y}\}, \tag{4.7}$$

where $\mathbf{y}$ is some non-zero vector [149]. Some special features of the Krylov subspace have been proven [149]. First, there exists a positive integer ν, such that the dimension of the Krylov space $\mathcal{K}_n$ cannot go beyond ν. Secondly, let $\mathbf{x}_*$ be the solution of $A\mathbf{x} = \mathbf{b}$, $\mathbf{x}_0$ be the initial guess for $\mathbf{x}$, and $\mathbf{r}_0 := \mathbf{b} - A\mathbf{x}_0$ be the initial residual. Then, it was proved that $\mathbf{x}_* \in \mathbf{x}_0 + \mathcal{K}_\nu(A, \mathbf{r}_0)$. Subsequently, Krylov-space solvers generally aim to generate a sequence of approximate solutions $\mathbf{x}_n \in \mathbf{x}_0 + \mathcal{K}_n(A, \mathbf{r}_0)$ such that the residual $\mathbf{r}_n \in \mathcal{K}_{n+1}(A, \mathbf{r}_0)$ is close to a zero vector within the set tolerance [149]. In addition, preconditioning, a transformation known in linear systems of equations, is often applied with Krylov methods to improve convergence rates [149]. Naively, the preconditioner transforms the system of equations so that the transformed $\mathbf{x}$ is less sensitive to changes or errors in $\mathbf{b}$.

Algorithms in the Krylov method family, such as restarted Generalised Minimum Residual method (GMRES) and Biconjugate Gradient Stabilised method (BiCGSTAB), with preconditioning options, are available in KEMField. Details of the methods and the implementation can be found in [141]. Note that GMRES guarantees convergence in less than N iterations for a non-singular system of equations with dimension N. However, the required memory increases with each iteration, posing a high demand on the machine. To address this problem, in KEMField, the Krylov subspace basis vector is discarded after a specified number of iterations. This implementation is called restarted GMRES (GMRES(n)) and no longer guarantees convergence [141]. On the other hand, BiCGSTAB has a small, fixed memory requirement but may result in poor convergence, if it converges at all [141].

The memory and arithmetic scaling of these methods are summarised in Table 4.1. For Krylov methods, the scaling depends on the number of iterations k, which, in the worst case, may diverge to infinity; however, in most cases it is smaller than N [141]. In the remaining sections, I will focus on GMRES, which exhibits good convergence for the TPC geometry implemented in this work. The convergence was also significantly faster than using the Robin-Hood solver with 4 K40 GPUs or 2 A100 GPUs.

Table 4.1: Scaling properties of different algorithms [141]. The number of iterations $k > 1$.

Method	Memory Scaling	Arithmetic Scaling
Robin-Hood	$\mathcal{O}(N)$	$\mathcal{O}(N^2)$
(Preconditioned) GMRES	$\mathcal{O}(kN)$ to $\mathcal{O}(N^2)$	$\mathcal{O}(kN)$ to $\mathcal{O}(N^3)$
(Preconditioned) BiCGSTAB	$\mathcal{O}(kN)$ to $\mathcal{O}(N^2)$	$\mathcal{O}(kN)$ to ∞

After the charge density is calculated by the solver, the electric field can be calculated at arbitrary points. Due to the long-range Coulomb force, evaluating the electric field can be computationally demanding and scales linearly with the number of elements. In KEMField, the electric field can be calculated by direct summation, which is slow but robust, or by a special version of fast Fourier transformation on multipoles (FFTM) [141], which approximates the far-field using multipole expansion [148, section 3.4.5.3]. The implementation significantly accelerated the field calculation process.

Concerning the boundary discretisations, basic geometries, such as cylinder and torus are provided by another module of Kassiopeia, called *KGeoBag*. Discretised external geometry can also be imported into KEMField for calculation.

The simulation framework used in the remaining sections is summarised in Table 4.2.

Model	Method	Tool
2D axisymmetric model	FEM	COMSOL
local 3D model	FEM	COMSOL
full 3D model	BEM	KEMField

Table 4.2: Simulation frameworks for the XENONnT TPC.

To ensure the reliability of the simulation models, both verification and validation should be performed. In the context of numerical modelling, verification concerns the correctness of the numerical solution of the governing equations, while validation concerns the appropriateness of those equations for describing the underlying physical phenomena. The verification process involves checking for errors in the solver implementation, discretisation, and BCs. To achieve this, the thesis compares the computed numerical solutions with analytical solutions and benchmark results. The different numerical models are also cross-compared. Discretisation errors are additionally assessed by performing the same simulations with various discretisation element sizes, a process known as mesh refinement. The computed solutions were also compared with XENONnT experimentally derived quantities.

4.2 Case Studies

The performance of the simulation frameworks was evaluated using simple test cases for which analytical solutions are available. These cases enable the identification of subtle differences between software implementations and the verification of the correctness of numerical models. The quantity of interests, such as charge and electrostatic forces, from the Krylov solver in KEMField, COMSOL and analytical solution. The solved potential and electrostatic field Robin-Hood solver in KEMField was already tested and compared, thus not the focus of this section [59].

4.2.1 Parallel-plate Capacitor

The parallel-plate capacitor is an importnat case for understanding the differences between the two simulation software, as the electrodes in the TPC are essentially capacitors with a dielectric material between them. In this simple case, the COMSOL simulation uses a 2D axisymmetric model. The KEMField model simulation uses a 3D model, although an axisymmetric model is also available in KEMField.

The parallel capacitor consisted of two separate conductive plates and a cylindrical outer shell enclosing them. The simulation model was defined with the parameters listed in Table 4.3. The dimensions of the plate and the applied potentials were selected to approximate the anode-gate electrode configuration in XENONnT. The shell dimension was set to 30 times the plate separation. In COMSOL, the material of the

shell medium was set to either air or LXe. In KEMField, the material of the medium cannot be specified. The simulation geometry and the electric potential of the domain from the COMSOL simulation are shown in Figure 4.1.

Table 4.3: Geometrical and electrical parameters for both the COMSOL and KEMField simulation.

Parameter	Value
Plate radius	685 [mm]
Plate thickness	0.216 [mm]
Plate separation	7.784 [mm]
Shell height (COMSOL)	233.52 [mm]
Shell radius (COMSOL)	233.52 [mm]
Anode voltage	4900 [V]
Cathode voltage	299.89 [V]

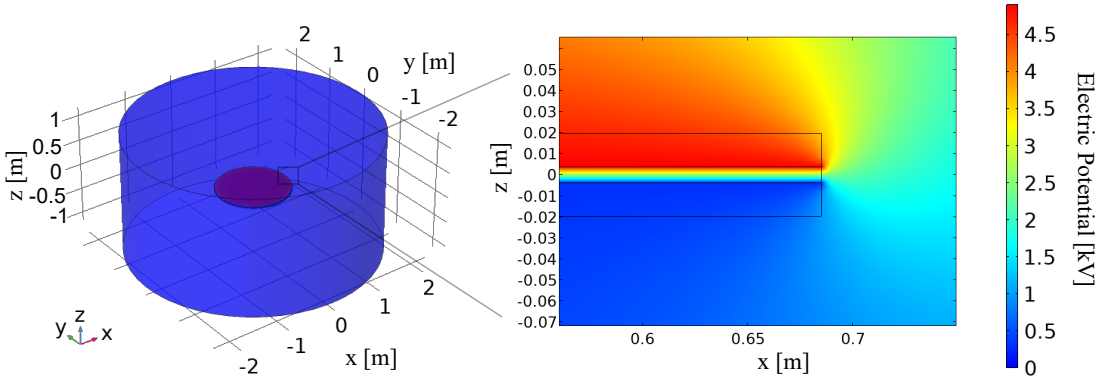

Figure 4.1: Simulation domain of the parallel-plate capacitor using COMSOL. The colour bar indicates the electric potential common to both plots. Left: 3D render by revolving the 2D solution. Right: 2D close-up at the edge of the plates.

The shell defines the finite simulation domain, which is necessary for FEM models, but not for BEM models. When the shell is not present in KEMField, the potential at infinity is set to $V = 0\,\mathrm{V}$ [150]. To reproduce this behaviour in COMSOL, a large grounded shell was introduced. The shell was grounded because KEMField does not support floating-potential BCs, whereas COMSOL does. This distinction between the two frameworks does not affect the TPC simulation, as the TPC cryostat is grounded in all cases.

The total charge on the electrode surfaces, computed using different software, is tabulated in Table 4.4, with the electrodes submerged either in air or in LXe. For the total charge calculated by COMSOL, both the built-in expression `es.Q0_{terminal name}` as well as a line integral of the charge density are listed for reference. The case of the shell in floating potential is also listed for comparison. Both the discretisations in COMSOL and KEMField were refined to minimise discretisation error while maintaining a reasonable simulation time. For comparison, the result from another simulation package (elcd3_3) was quoted [150].

In the COMSOL model, in which the shell potential was floating, there was no external reference potential defined, in contrast to KEMField. In other words, the COMSOL

Table 4.4: Charge on the surface of the electrodes computed by different software.

	Charge on anode [μC]	Charge on cathode [μC]
in Air		
external software elcd3_3 [150]	7.985	-7.857
KEMField (GMRES)	7.982	-7.855
COMSOL (grounded shell): `es.Q0`	8.013	-7.842
COMSOL (grounded shell): line integral	8.003	-7.835
COMSOL (floating shell): `es.Q0`	7.938	-7.938
in LXe		
KEMField (GMRES)	7.982	-7.855
COMSOL (grounded shell)	15.06	-14.74

model was equivalent to the case where both the anode and the cathode have the same potential (at $\pm 2300\,\mathrm{V}$). Therefore, by charge conservation, the charge on the anode and the cathode are identical as expected. However, with the grounded shell, the reference potential on the shell broke the symmetry, resulting in a slightly different charge distribution on the electrodes, as also observed in other simulations.

In the case of a dielectric material (LXe) filling the gap between the electrodes, the stored charge in the capacitor increases with the dielectric constant of the material. Still, the electric field between the electrodes remains constant, set by the potential difference between them.

In KEMField, the dielectric constant of the domain(s) is not explicitly specified, unlike in COMSOL. In the single-phase configuration, Neumann BCs cannot be imposed either. As a result, the BCs imposed in any medium are identical, thereby necessarily leading to an identical amount of charges on the electrodes both in air or in LXe. From this, it follows that the charge computed in KEMField corresponds to the sum of the free charge on the conductive materials and the bound charge associated with the dielectric materials that share the exact boundaries.

For COMSOL, materials are specified for each domain. From the results, the charge on the electrodes submerged in LXe was increased by the dielectric constant $\epsilon_{LXe} = 1.88$ [71, 72], implying that the built-in expression `es.Q0` calculates only the free charge on the electrodes. This yields results that differ from those of KEMField; thus, the charge cannot be used for comparisons between software, especially when there is more than one medium with different dielectric constants between the electrodes, without an analytical prediction.

4.2.2 Parallel-wire Capacitor

The parallel wire case consists of two parallel wires with length $L = 1\,\mathrm{m}$. The simulation model was defined with the parameters listed in Table 4.5.

Table 4.5: Geometrical and electrical parameters for both the COMSOL and KEMField simulation.

Parameter	Value
Wire diameter	0.3 mm
Wire length	1000 mm
Wire pitch (separation centre-to-centre)	10.3 mm
Shell radius (COMSOL)	5000 mm
Anode voltage	−500 V
Cathode voltage	500 V

For KEMField, the cylindrical geometry provided by KGeoBag was used and discretised with 200 elements along the axial direction and 72 elements along the azimuthal direction. Two 2D COMSOL models were tested, namely a planar model and an axisymmetric model.

For the axisymmetric model, the wire array was approximated by two toroidal rings with major radii $r = \{0.5, 1.0, 1.5\}$ m and a minor radius of 0.15 mm. The rings were separated by the wire pitch along the z-axis, which corresponds to the axis of rotation. While it is not possible to simulate parallel wires exactly in an axisymmetric model, increasing the major radius r improves the approximation to a parallel-wire system. The charge and force were subsequently divided by $2\pi r$, yielding consistent results for the different values of r. The results from the analytical calculation and different simulations are shown in Table 4.6, which are in good agreement.

Table 4.6: Results of the parallel-wire capacitor simulation. The capacitance was calculated by $\pi\epsilon_0/\cosh^{-1}(S/D)$ =6.57 × 10^{-12} C.

Quantity	Analytical Calculation [150]	KEMField (Krylov)	COMSOL (2D planar)	COMSOL (2D axial)
No. of cross-sectional mesh		72	160	160
Charge Q [nC]	$C \times \Delta V = 6.57$	6.59	6.58	6.58[nC/m]
Force on cathode F [$\times 10^{-5}$N]	$Q^2 \cdot E(r = S) = 7.54$	7.50	7.55	7.54 [N/m]

A subtlety arises when computing electrostatic forces on wires using KEMField. First, the charge distribution was computed for the full simulation. Then, to evaluate the force on a wire, the field acting on each surface element is calculated by excluding the contributions from the charges on the same wire. Otherwise, an unphysical self-force would be introduced. In reality, this self-force is internally balanced by the mechanical structure of the wire and should therefore not be included. For large geometries, the discussed procedure of manually setting the charge to zero and summing the resulting fields directly for each element becomes computationally expensive.

A faster implementation of KEMField has been proposed, in which the charge distribution is duplicated, the charges on the entity of interest are set to zero, and the built-in

force calculation is then applied. However, this approach is not further explored in this thesis.

By contrast, the force evaluation in COMSOL is straightforward: the electrostatics module provides a built-in `force calculation terminal` that can be directly evaluated in the `Result` node. As demonstrated by this example, the 2D models yield a force on the wires that is consistent with the analytical calculation and the KEMField result. Note that in other geometries, such as hexagonal-mesh electrodes, the 2D axisymmetric model cannot be applied.

4.3 Field Calculation for XENONnT

The 2D axisymmetric COMSOL model, as well as the local 3D model for the perpendicular wires, has been extensively studied and compared with data [19] and has since been adopted in the XENONnT analysis pipeline. For the full 3D KEMField simulation, the XENONnT TPC geometry before the electrode upgrade (section 2.2) was implemented and compared with those from the 2D axisymmetric model. In the following, the 2D axisymmetric model and the implementation of the full 3D model are described in detail. Discussion of the local 3D models is postponed to later sections, where the relevant context is provided.

4.3.1 2D Axisymmetric Model

The 2D axisymmetric model developed in [19] is shown in Figure 4.2. Although the XENONnT TPC geometry (Figure 2.5) is approximately axisymmetric, it is not exactly so. While the 2D axisymmetric model captures most of the features of the TPC, it deviates from the real geometry in several respects. In this 2D model, wires are represented as concentric rings rather than parallel wires, and the PMTs are similarly approximated by axisymmetric structures. As a consequence, the electric field near the central axis ($r = 0$) cannot be accurately reproduced. Perpendicular wires are also not included. Furthermore, inherently non-axisymmetric components, such as the HVFT or the polygonal electrode frames of the top stack, cannot be modelled within a 2D framework.

Despite these discrepancies, the 2D model has shown good agreement with the data in the drift region [19]. Subsequently, it was used to impose BCs for local 3D simulations, for example, for the field near perpendicular wires [19]. Local 3D simulations allow much finer meshing in the region of interest, enabling detailed studies and more accurate results. However, they remain limited for extended, non-axisymmetric structures, such as the HVFT, or near the electrode frame, where BCs are more difficult to impose. Thus, while the combined 2D–3D framework is effective, a full 3D model remains necessary for comprehensive verification.

Note that in [19], it was shown that the agreement with data improved when a non-zero charge distribution was imposed on the PTFE side reflector. However, this effect is not implemented in the full 3D simulation, as explained in the following section.

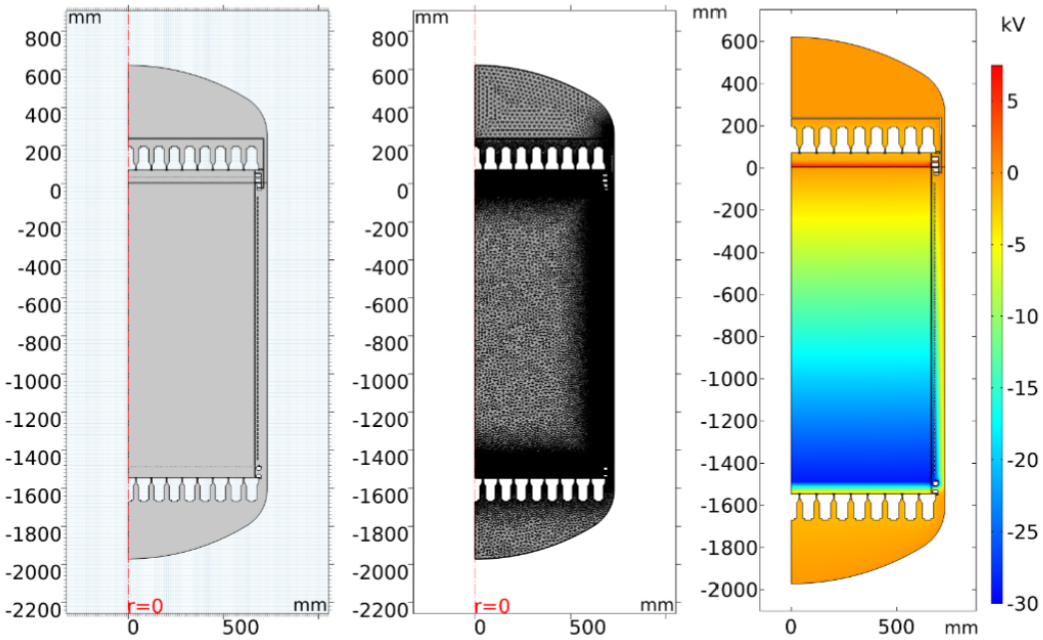

Figure 4.2: COMSOL 2D axisymmetric model for the field simulation of XENONnT. Left: geometrical implementation. Middle: discretisation elements. Right: potential throughout the detector. Image taken from [19].

4.3.2 Full 3D Model

For the full 3D model, most of the relevant components to the electric field in the TPC was implemented for the full 3D simulation using the KEMField package, namely the electrodes and the screens, the liquid-gas interface, the field cage, the simplified version of the PMTs, and other periphery entities such as the HVFT for the cathode, some grounded conductors around the TPC to further improve the field uniformity, and the inner vessel of the cryostat. The PTFE insulators were, however, not implemented due to a convergence problem. Given that the dielectric constant of PTFE (2.0 – 2.1 [151]) is close to that of LXe (1.88 [71]), the absence of the PTFE side reflector is not expected to affect the result significantly (subsection 4.3.3).

The model-building process for the full 3D field simulation used a C++ plugin that interfaces with the Kassiopeia software, which involved defining the geometry, discretising it into elements, specifying the BCs, and configuring solver parameters. As part of the general workflow, complex geometries, such as electrode frames and perpendicular wires, were discretised into triangular elements in COMSOL and imported into KEMField. Compared with the native geometry builder in Kassiopeia, named KGeoBag, COMSOL offers greater control over geometry definition, operations to simplify CAD drawings, and customisable discretisation with fine meshing in specific regions. It is therefore highly efficient for complex geometries. Only the wire-like structures far from the region of interest were discretised into the native discretisation elements (rectangles and 1D line elements) from KGeoBag, as these discretisation elements cannot be imported.

Since BEM tends to exhibit instabilities and divergent results when intersecting ele-

ments or boundaries are present, attentions were paid to avoid crossing boundaries. Also, connecting parts (e.g., the anode frame, the parallel wires, and the perpendicular wires) were discretised together in COMSOL, ensuring that the boundaries of the discretisation elements were mutually consistent.

For the BCs, all conductors were set to the Dirichlet BC, either grounded or with a bias voltage according to the SR0 configuration listed in Table 2.3. The liquid-gas interface was set to the Neumann BC.

While building the TPC model, the simulation and its components were also checked and verified across multiple aspects. First, the total charge on the boundaries should cancel out. Therefore, the charge on the dielectric surface and the conductor was evaluated to ensure they cancelled out and remained close to zero. Secondly, the field in the bulk volume was compared to the COMSOL 2D model, including also the discontinuity at the liquid-to-gas interface. Lastly, the electric field inside the conductor was monitored, which should theoretically be zero. Due to the discretisation error, this field was not exactly zero and approached zero as the discretisation was refined. This can be an indicator of significant discretisation errors for the conductors in the model.

Electrodes and Screens

The electrodes before the upgrade consisted of electrode frames and a few hundred *parallel wires* with the diameter of 0.216 mm or 0.304 mm. For the anode and the gate, there are additionally 2 and 4 *perpendicular wires*, respectively.

The CAD drawings of the frames for all five electrodes, including the two screening electrodes, were simplified and discretised in COMSOL before being imported into KEMField. For the cathode and the screen electrode grids, the accuracy of the field near the parallel wires is less critical than for the anode and the gate. To reduce computational cost, the parallel wires were modelled and discretised as 1D line elements, which are native to KEMField and KGeoBag. In practice, to avoid intersections between discretisation elements, the grids for these electrodes are slightly offset from the electrode frame.

The anode and gate were more finely discretised to improve the accuracy of the electric field in the region between them, which is particularly important given the small gap, the high field strength, and its role in defining the S2 signal. Therefore, the parallel-wire array, the perpendicular wires, and the frame from the CAD drawing were built together and discretised in COMSOL. The union operations in COMSOL ensure that no boundaries or elements overlap or cross.

The parallel wires were discretised into 4 elements along their cross-sectional surfaces. An attempt was made to refine the element size by doubling the elements around the wire for all the parallel wires, but the simulation did not converge to the correct results (subsection 4.3.3). The total charge on the conductors was yielding at $\mathcal{O}(10^{-14}\,\mathrm{C})$, compared to the case of $\mathcal{O}(10^{-6}\,\mathrm{C})$ in the correctly converged cases, and the field map was showing unphysical values. Therefore, the unrefined discretisation

was kept for the anode and the gate. The 6 perpendicular wires and the nearby parallel wires were, however, finely meshed to resolve wire crossings.

Liquid-to-gas Interface

In COMSOL, each domain was assigned a material with the specified dielectric constant, thereby affecting the field configurations. In KEMField, the material properties are not specified; only the dielectric-constant ratio between the two materials is set at the boundary, which is the liquid-gas interface in this case. The interface was simulated as a disk and was imposed with the Neumann BC, with the ratio of 1.88 [71].

Originally, the disk geometry from KGeoBag was used. The discretisation uses a polar-coordinate mesh, in which the user can specify the number of elements in the radial and azimuthal directions. Such discretisation necessarily leads to certain elements having a high aspect ratio, as shown in Figure 4.3. Aspect ratio is a common indicator of mesh quality. High aspect ratio generally leads to large numerical errors and a longer time for convergence.

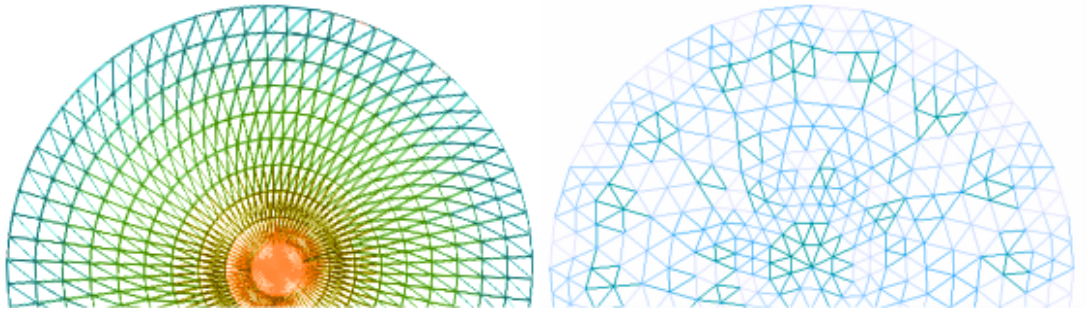

Figure 4.3: Discretisation elements of part of the disk geometry. Colour scales with the aspect ratio, where light blue is closest to 1 and preferable. Red has a higher aspect ratio with highly skewed elements, which is not preferred. Left: elements from KGeoBag. Right: elements from COMSOL.

To circumvent both problems, the disk was discretised in COMSOL. The normal vector is defined to point in the positive z-direction. With the use of free triangles in COMSOL for the discretisation, the aspect ratio for all the elements also improved, as shown in Figure 4.3.

Field Cage: Field Shaping Rings and Guards

Details of the construction and design of the field cage can be found in [19, 70]. The field cage consists of an inner and outer array of oxygen-free high-conductivity (OFHC, 99.99%) copper rings along the sides of the TPC, outside the PTFE wall. Their potentials were set by potential dividers so that the potential decreases gradually from the gate to the cathode, thereby improving field uniformity between the gate and the cathode. The field-shaping rings were designed to be in contact with the PTFE side reflector to remove the charge deposited on it, thereby avoiding field distortion [70]. The field cage comprises 71 smaller internal field-shaping rings and 64 larger outer rings (later termed field guards), arranged in two alternating layers, except at the top and bottom. The diameter of a ring is 2 mm and the length of $\sim$4 m.

Unlike in COMSOL, KEMField does not impose a zero field inside the conductor because the volumetric domain is not material-specific. To achieve a zero field inside the conductor, the charge should be allowed to migrate so that it cancels the external field. In KEMField, the charge distribution is constant on an element [141]. Therefore, the field can be reduced to near zero with finer meshing. While this may not necessarily affect the field outside the conductor, it can serve as a useful indicator of large discretisation errors.

The field-shaping rings were constructed using the KGeoBag torus geometry, which was discretised into rectangular elements. The poloidal number of elements, that is, the number of elements around the cross-sectional plane, was chosen at 10. The choice was made because the reduction in the field began to flatten out as the number of elements increased. The toroidal number of elements was set to 200, such that the aspect ratio was less than 100. Simulations of rings with aspect ratios greater than 100 required increasing computational time per element. On the other hand, simulations with small aspect ratios require a large number of elements, making them computationally expensive. Details of the refinement study are provided in Appendix A.

The cross-section of the field guards is approximately oval and cannot be simulated using the same geometric construction as that of the field-shaping rings. They were built and discretised in COMSOL and imported into KEMField. The vertical field strength across the field guards was also compared with the COMSOL simulation, yielding consistent results.

Others

To simplify the calculations, the PMT was only implemented as a plain disk, as the top and bottom screen shielded most of the field from the PMT array [147, Figure 3.11]. Note that this may not hold for the field configuration after the upgrade.

The HVFT, the grounding sleeve around the HVFT, the grounded bell on top of the top PMT array, and the copper ring near the gate electrodes are constructed and discretised together to avoid cross-boundary effects. They were imported into KEMField separately to set separate BCs. For these structures, no systematic mesh-refinement study was conducted because they are farther from the TPC.

The PTFE side reflector comprises a PTFE panel and pillars located within the field cage, as mentioned. However, the PTFE side reflector was excluded from the KEMField 3D model because the simulation did not converge, despite careful checks of the boundaries to ensure no crossings. That being said, the dielectric constant of PTFE (2.0 – 2.1 [151]) is close to that of LXe (1.88 [71]), therefore, the absence of the PTFE side reflector is not expected to affect the result significantly.

On the other hand, there is evidence that the PTFE side reflector of the XENONnT experiment presents a surface charge that affects the electric field within the TPC [19, 70]. However, a BC with a specified surface charge is not available in KEMField. This is one of the most significant limitations of the current KEMField model for the XENONnT experiment.

Lastly, the inner cryostat was included in the model. Since the field contribution from the inner vessel is shielded by the inner components, the implementation of the exact geometry is less critical. The geometry was extracted from the 2D axisymmetric simulation, revolved by 360 degrees, and partitioned at the liquid-gas interface to account for the connecting boundaries. The constructed geometry was discretised in COMSOL before importing into KEMField.

Final Configurations

To summarise, the final geometrical configuration of the simulation model is tabulated in Table 4.7. The minimum (maximum) element size is 0.00219432 (1421.78) mm^2 at the anode (bell). The minimum (maximum) aspect ratio is 1.2 (65.5) at the liquid-to-gas interface (top screen). Concerning the solver, the tolerance was set at 10^{-6}, with 50 iterations before restarts. Further details on the Krylov solver settings are provided in Appendix B.

Table 4.7: Configurations for the KEMField full 3D model. GND stands for ground. The meshing type starting with "KG" is the entity from KGeoBag in Kassiopeia. The boundary conditions for the field-shaping rings and the field guards are unspecified, as each entity has a different potential.

Part	Meshing type	No. of elements	Boundary Condition
Inner vessel	COMSOL triangles	422,984	GND
Bell + HVFT sleeve + copper ring	COMSOL triangles	47,053	GND
HVFT (cylinder)	KGeoBag rectangle	960	−30 kV
PMT (disk)	COMSOL triangles	$2 \times 83{,}106$	−1.3 kV
Top screen	KGeoBag 1D line	26,500	−0.9 kV
Top screen frame	COMSOL triangles	81,178	−0.9 kV
Anode (wires + frame)	COMSOL triangles	602,586	+4.95 kV
Liquid-to-gas interface	COMSOL triangles	660,476	1.88
Gate (wires + frame)	COMSOL triangles	509,228	−0.9 kV
Field shaping rings	KGeoBag rectangle	$71 \times 2{,}000$	Dirichlet
Field guards	COMSOL triangles	$64 \times 1{,}2910$	Dirichlet
Cathode	KGeoBag 1D line	18,200	−2.75 kV
Cathode frame	COMSOL triangles	106,358	−2.75 kV
Bottom screen	KGeoBag 1D line	18,200	−1.3 kV
Bottom screen frame	COMSOL triangles	126,362	−1.3 kV
Total no. of elements		3,883,189	

4.3.3 Simulation Result

For the KEMField computation of the full 3D simulation, the charge-distribution calculation 3,883,189 on three K40 GPUs required 7.8 hours. The total charge, which

is ideally zero, amounted to 2.24×10^{-12} C, with -3.29×10^{-6} C on the dielectric surfaces and 3.29×10^{-6} C on the conductors. The 2D axisymmetric model of COMSOL with 4,714,800 discretisation elements takes ~ 7 minutes to compute the solution on an AMD Ryzen 5 5625U processor with 6 cores.

To generate electrostatic field maps from the full 3D model for comparison and further studies, the electrostatic field was evaluated on a grid using FFTM. A fine resolution grid across the entire TPC volume will require substantial memory to load and analyse. To improve computational efficiency and reduce memory usage, field maps at different resolutions are generated. In the bulk region, where the field is more uniform, a 3D 5 mm grid was used to evaluate the field and potentials. For the top and bottom parts of the TPC near the electrodes, where the field is less uniform and exhibits large gradients, a grid spacing of 1 mm was used.

The field strength *map* in the TPC from both the KEMField 3D model and the COMSOL 2D model on the y-z plane, as well as the relative difference between the two maps, are shown in Figure 4.4. The parallel wires on the electrodes point into the page. The HVFT is visible on the right side of the KEMField y-z map, which cannot be simulated by either a 2D axial or a local 3D simulation. The COMSOL 2D axisymmetric map was mirrored for comparison and is shown on the y-axis instead of the r-axis. The KEMField map is evaluated on a uniform grid, whereas the COMSOL FEM model is evaluated at the centroids of the discretised mesh, which is irregularly distributed. The COMSOL map was interpolated into the KEMField grid for a fair comparison and shown in the figures.

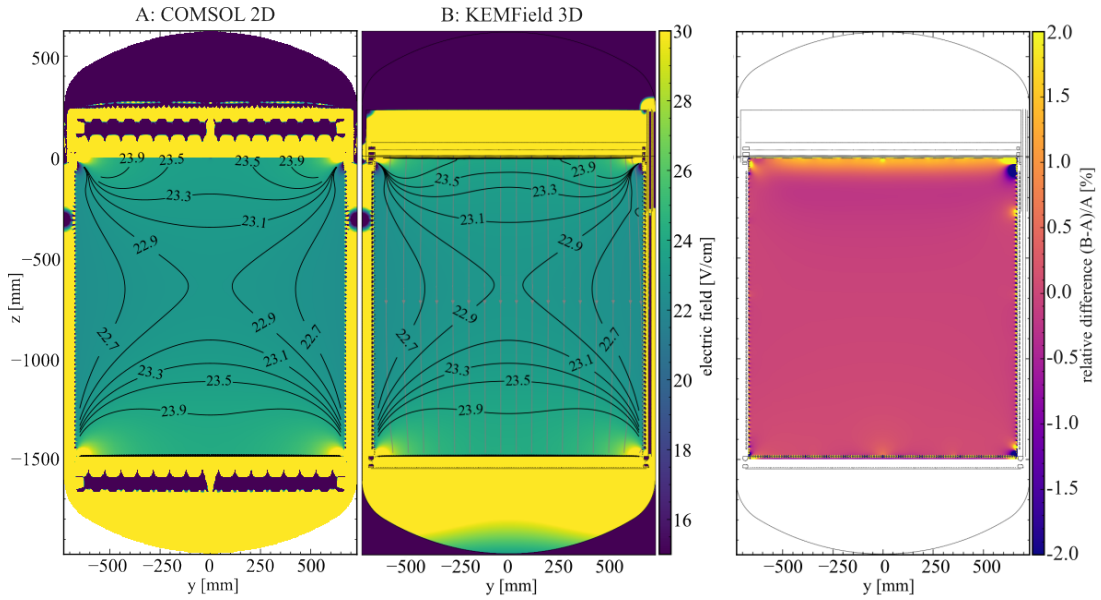

Figure 4.4: 2D field maps overlay with the geometry from the KEMField simulation for reference. The field strength contours are shown as black lines. Left: the mirrored COMSOL 2D map, and then mapped to the y-z coordinate. Middle: the sliced KEMField 3D map in the y-z cut plane through $x = 0$. The field lines are also shown in grey. Right: relative difference between the two maps in the active volume.

The relative difference between the maps in the active volume or the drift field region is less than 2% for most of the space. This is in agreement with the estimated system-

atic error of 1% for the COMSOL 2D map [19, Section 4.2.2]. At around $y = 0$ mm, it is expected to exhibit larger deviations due to the misrepresentation of the concentric wires in the 2D axial model. Note also that the effect from the HVFT is limited, as most are shielded by the field cage.

Drift Field

The field strength of the drift field along the vertical axis (z in Figure 4.4) of the TPC is shown in Figure 4.5. The results from KEMField and COMSOL 2D field are sampled along a set of vertical lines, named the *cut lines*, parallel in the y-direction (the side without HVFT) or r-direction, respectively, $\in [10, 610]$ mm in 50 mm step.

For the result from KEMField, the line from the side with the HVFT ($y > 0$ in Figure 4.4) does not show a significant difference with that on the side without the HVFT ($y < 0$), thus not shown. The band for the KEMField shows the maximum and minimum field strengths recorded along these parallel lines from the KEMField field map.

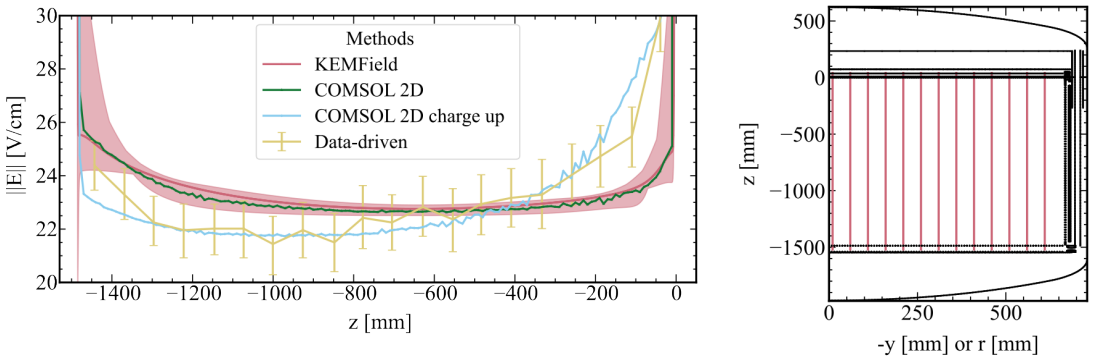

Figure 4.5: Left: averaged drift field from different models with SR0 configuration in Table 2.3. The solid lines represent the average values up to $r = 610$ mm. Data points from the data-driven field map were retrieved from [19]. Right: TPC geometry, where the lines indicate the position at which the field in the left plot was evaluated.

As shown in Figure 4.5, the average field values obtained from the COMSOL 2D model exhibit only minor deviations from the KEMField results. This indicates that the 3D structures included in the full 3D model do not significantly affect the validity of the 2D axisymmetric approximation. Additionally, the discrepancy between the 2D and 3D models is substantially smaller than the effect of charge accumulation on the PTFE panels, indicating that other detector effects dominate the uncertainties arising from the simulation models.

The field strength was also estimated from XENONnT calibration data [19] and is shown in Figure 4.5 for comparison. The data-driven field was estimated from the ratio of the two S1 peaks from ^{83m}Kr ER events, corresponding to the 32.2 keV and 9.4 keV electron transitions [152]. The ratio entails information about the field, owing to the field dependence of the recoil's light and charge yields. The data-driven field estimate shows the best agreement with the 2D COMSOL simulation that includes charge-up effects on the PTFE side reflector. This supports the conclusion that the deviation between the data-driven field and the nominal 2D COMSOL model arises

from wall charge-up effects, rather than from limitations in the geometric fidelity of the 2D axisymmetric model.

Extraction Field

The extraction field 1 µm below the liquid phase is shown in Figure 4.6 (right). The field distortion from the perpendicular wires is visible. The liquid-phase extraction field, starting from the centre of the surface and extending across the wires, is shown in the same figure (left), as well as the COMSOL counterpart. For the KEMField result, it was a synthetic case where the wires at the centre have more elements than the other wires, so as to study the effect of discretisation error.

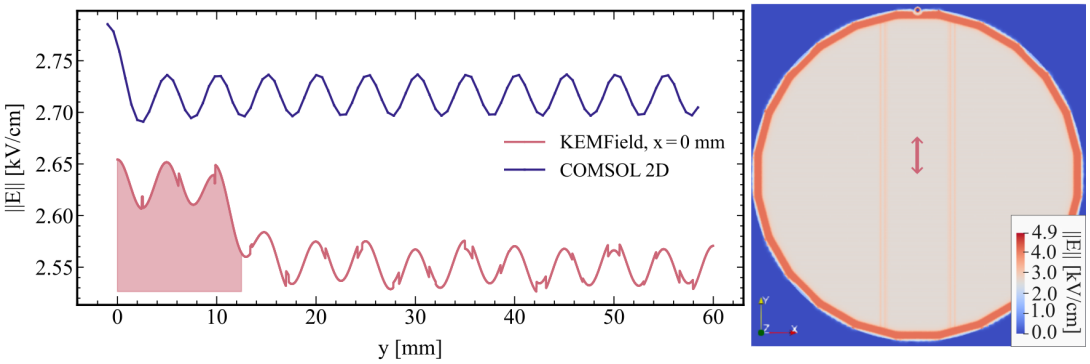

Figure 4.6: Extraction field from different simulations. The extraction field is the field strength in LXe 1 µm below the LXe surface. Left: 1D extraction field at $x = 0$ computed by KEMField and COMSOL 2D axisymmetric model. For the shown KEMField result, 5 parallel wires at the centre (shaded) were refined 5 times more than the other wires. Right: 2D extraction field map from KEMField. The pink arrow indicates the position at which the field in the left plot was evaluated.

In general, the extracted field from KEMField is lower than that obtained from COMSOL. This is likely due to the fewer elements around the wire than in the 2D simulation, as argued below. While the 2D simulation had 32 elements along the cross-sectional edge, the 3D simulation had 4 elements along the cross-sectional surface. For a refined discretisation for the 3D simulation with 8 elements along the cross-sectional surface of each wire, non-convergent results were obtained.

While refinement was not feasible, to understand the effects from the discretisation error, only the central 5 parallel wires (shaded) of the anode, and 6 wires of the gate were refined 5 times and had 20 elements around each wire; other wires had 4 elements. The difference in field strength between the non-refined wires and the COMSOL 2D model is approximately 7With the refined meshing, the field strength is higher and becomes closer to the COMSOL result. This is a strong indication that the reduced field strength was due to discretisation error.

In addition, the KEMField results show a discontinuous profile for both FFTM and direct-field calculations; only the FFTM result is shown in the figure. It may be due to discretisation errors on the liquid xenon surface, even though the surface was finely discretised.

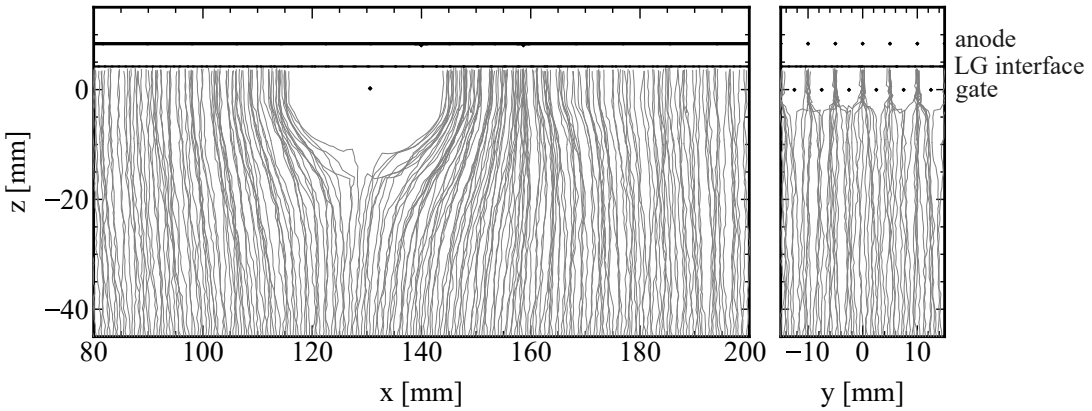

Figure 4.7: Projected electron propagation path around the perpendicular wires computed using PyCOMes onto x-z plane (left) and y-z plane (right). The geometry from KEMField at $y = 0$ is drawn in black solid time for reference. "LG surface" stands for the liquid-gas interface.

Perpendicular Wires

Concerning the extended object in the TPC, namely the perpendicular wires, the 2D axisymmetric model cannot properly account for these structures. A local 3D simulation was used [19], in which the BCs at the top and bottom boundaries of the domain were taken from the COMSOL 2D axial model, while the sides were set as the symmetry planes. With this technique, however, the validity of the symmetries exploited by the local simulation is reduced when the domain is near the electrode frames.

Since the field inside the detector cannot be measured directly, an alternative method for evaluating the simulation results is the electron distribution after propagation. Electrons are simulated and propagated in the generated field maps using a Python package, PyCOMes [153]. The package was developed to handle COMSOL output files and to track electron drift in the liquid xenon target [19]. The package also includes the drift speed and diffusion models from the literature to simulate the longitudinal and transverse spread of the produced electron cloud. It was extended to handle also the output from the 3D map from KEMField. The electron distribution provides a clearer understanding of the field's effect on the electron's trajectory and affects the position of S2 relative to the event vertex. The electron position at the liquid surface can be used as a proxy for the reconstructed S2 position.

While Figure 4.6 shows the effect of the perpendicular wires on the extraction field from KEMField, the electron propagation was done to further quantify the effect of the field distortion, as shown in Figure 4.7. PyCOMes interpolated the field maps from KEMField and performed charge propagation until the liquid level. With the coarse field map with 5 mm resolution, the electrons were propagated from $z = -45$ mm until $z = -10$ mm, then the fine field map with 1 mm resolution was used to propagate the electrons until $z = 4$ mm. The starting z-position was chosen such that the effect from the field distortion is insignificant, and it was consistent with other simulations for comparison.

Due to field distortion near the electrodes, electrons flow around the electrode wires.

As the electron approaches the parallel wires, starting from ∼5 mm below the gate at $z = 0$ mm, the paths split between the wires and reach the liquid-gas interface. This is named the *focusing effect*. The perpendicular wire above the gate produces a significant and non-periodic field distortion that extends 20 mm below the gate. These effects have also been observed using local 3D COMSOL [19] and full 3D KEMField simulation [147]. The full 3D KEMField simulation from this work yields consistent electron paths.

Furthermore, a 1D projection of the distribution of the electron position on the liquid surface along the x-axis is shown in Figure 4.8. The result from KEMField from this work is in good agreement with the local 3D simulation from COMSOL. Comparing with the previous full 3D KEMField simulation [147], the distribution is also closer to XENONnT data, obtained by the S2 signal projection from the ^{83m}Kr calibration, despite still having a significant mismatch as in the case for the local 3D simulation.

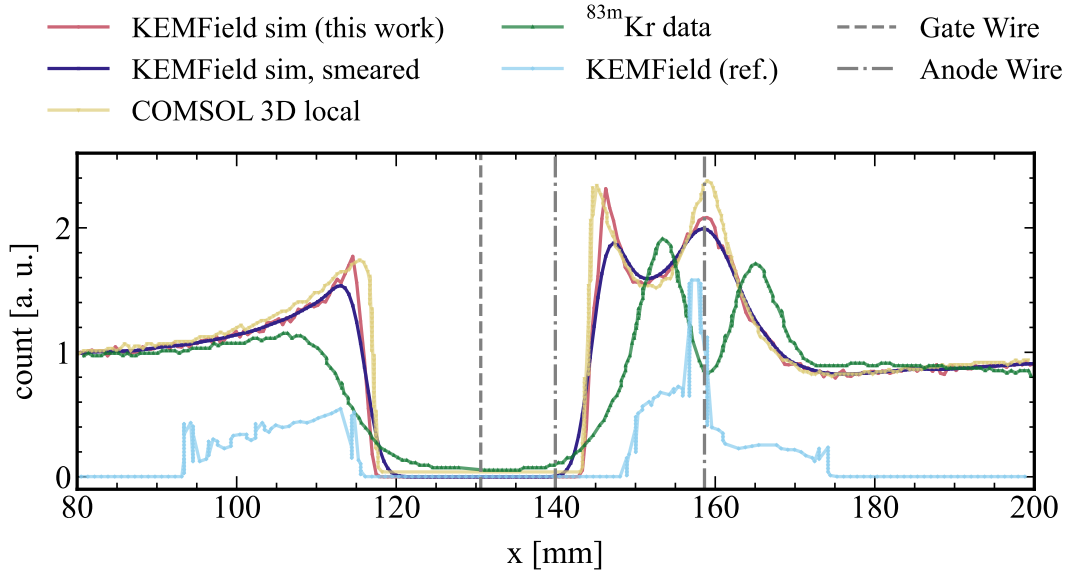

Figure 4.8: 1D projection of the distribution of the electron position on the liquid surface along the x-axis. The plot for "KEMField sim, smeared" was the result from KEMField, smoothed by 3σ Gaussian function. The plot for "COMSOL 3D local" and "^{83m}Kr" data were taken from [19]. The plot for "KEMField (ref.)" was taken from [147], which was a full 3D XENONnT simulation, but using an older version of KEMField and with the Robin-Hood solver.

The mismatch with data for both the local and full 3D simulations suggests additional effects that were not accounted for in this study, such as the shadowing effect from the wires (more discussion in section 5.8), or the position reconstruction of the S2 signal. Nevertheless, this comparison cross-verifies that the mismatch does not originate from the 3D local simulation.

HVFT

For the HVFT, a local 3D simulation was performed to verify that the electric field between the HVFT and the field cage remains below breakdown thresholds [19, Figure 4.5]. However, because the HVFT extends along the full length of the TPC, its

potential impact on the global field configuration cannot be fully captured by either a 2D axially symmetric model or a local 3D simulation. As discussed previously and shown in Figure 4.4, the resulting field leakage from the HVFT into the TPC is expected to be limited.

To confirm, electrons were simulated and propagated using the same method described above, starting at $z = -1450\,\text{mm}$, i.e., with a long drift path on which the HVFT field distortion has the largest impact on the electron trajectory. Result is shown in Figure 4.9. The effect does not extend into $y < 600\,\text{mm}$. . Additionally, it indicates that HVFT is not the most concerning 3D feature in the experiment.

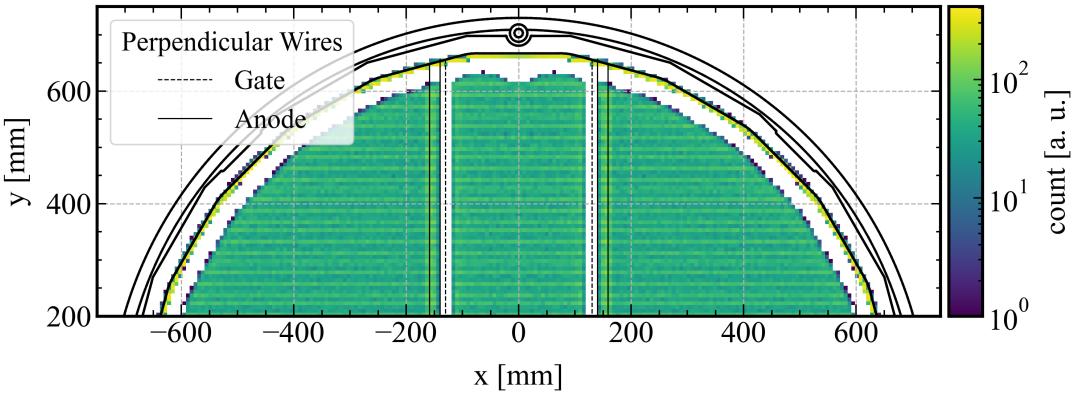

Figure 4.9: Eletrons propagate from $z = -1450\,\text{mm}$ from the side with HVFT. Mirrored at $x = 0$ for better visualisation. The projected geometry of the simulation model is shown in black solid lines, without the parallel wires. The perpendicular wires are indicated.

4.3.4 Discussions

The simulation results from KEMField are in good agreement with COMSOL 2D and local 3D FEM simulations. This indicates that, firstly, the 2D axial symmetry is a good approximation to the XENONnT TPC geometry, despite the presence of the parallel wires, perpendicular wires or the HVFT. This is also believed to hold for the next-generation detector, which has an even smaller surface-to-volume ratio. Secondly, the models with different software, namely KEMField and COMSOL and different methods, are cross-verified, thereby increasing confidence in the correct implementation of the simulation models as well as the absence of systematic effects due to a particular solver or software. The results are also compared with experimentally derived quantities. At the same time, several limitations on the full 3D model for the TPC have been identified.

First, the largest limitation is the lack of a charge BC. As shown in [19] and Figure 4.5, the difference introduced by the wall charge-up is significant on the overall drift field, and it can better match the simulation data. However, such a BC is absent in KEMField and not trivial to implement for the Krylov solver. One possible workaround is to impose a Dirichlet BC on a plane based on the results of a 2D simulation, which yields a wiggling potential due to the field cage. Each entity in KEField can have only one potential value; the PTFE panel must be divided into small segments to assign the varying BCs.

On a related note, the TPC design exhibits mirror symmetries that should be exploited to reduce simulation size, particularly for future-generation experiments. While this feature is available in COMSOL by imposing a symmetry plane or a zero-charge BC, neither is available in KEMField.

Secondly, the non-convergence limits the refinement of the discretisation on the parallel-wire electrode, thereby introducing a non-negligible error in the extracted field. Compared to the finely meshed 2D model, the difference is 7% (Figure 4.6). As mentioned, with the restart GMRES scheme for the Krylov method, the convergence is not guaranteed. Robin-Hood solver also suffers from a divergence issue when implementing the TPC geometry.

Thirdly, in both the 2D COMSOL and 3D KEMField models, the deflection of the electrode grids has been neglected. Local 3D simulations and data-driven methods have been used to estimate anode deflection. This adds systematic uncertainty to the results. In the future, one should use multiphysics coupling in COMSOL between electrostatic and structural mechanics simulations; however, this limitation also applies to the COMSOL 2D axial model when used without structural modelling.

Given these considerations, the strategy adopted in the remaining part of the chapter is as follows: the COMSOL 2D axial model is used for faster field optimisation; COMSOL 3D models are used to study local effects from non-axisymmetric geometric objects; and KEMField 3D simulations are employed to evaluate extended structures that are difficult to capture with the FEM simulations (such as the HVFT or welded strips), at the cost of reduced accuracy in local or surface-field estimates, and to verify the results from local 3D simulation.

4.4 Field Configuration after Upgrade

In the following sections, the simulation models used for the XENONnT experiment before the upgrade were extended to examine new field configurations after the upgrade under nominal conditions. The upgrade changes were incorporated into the 2D axial and full 3D simulations. With the updated global field simulation, the BCs for a local three-dimensional (3D) field simulation was approximated.

As the detector has been upgraded and is in the commissioning phase at the time of this work, there are uncertainties regarding its constraints and performance. To narrow the scope of the study, the liquid level and the potentials at the anode, gate, and cathode were set to the nominal values listed in Table 2.3. The absence of wall charge-up is also assumed for further study of the detector's field configuration following the upgrade.

Three upgrade options were introduced in section 3.4, and the electrode design optimisations presented in chapter 5 and chapter 6 were initially based on Option I. However, upon opening and inspecting the detector, the top and bottom screening electrodes were found to be in poor condition, with substantially reduced wire tension. As a result, Option III was adopted for the electrode upgrade, resulting in the removal of

the wire electrodes from the top and bottom screens. The major difference between Option I and III is that the parallel wires on the top and bottom screens are absent in Option III. In this case, the PMTs are exposed to a high external field, the effect of which is outside the scope of this thesis. It will be shown that the difference has a limited impact on the electric fields between the main electrodes (subsection 4.4.2). Consequently, the optimisation results presented here mostly focus on Option I.

4.4.1 Field Uniformity from the Central Welded Strip

A monolithic electrode at the size of ~ 1.5 m with submillimetre-scale fine structures is not readily commercially available. To overcome this challenge, we laser-weld two half-meshes to form a robust, high-quality mesh chapter 6. The edge for laser welding is thicker ($\sim$2 mm each) to facilitate the welding process. More details can be found in chapter 6.

The S2 signals are sensitive to the field inhomogeneity between the anode and the gate, as shown in subsection 4.3.3, the effect of perpendicular wires before the upgrade. Therefore, the design with the central welded strip is not the most suitable candidate for the anode and the gate electrodes. Therefore, the design was only considered for the cathode electrode. The effect of the central welded strip on the drift field is studied in the following.

The 2D axial-field simulation is not accurate at $r = 0$, and the structure is also extended in one direction, so that axisymmetry is no longer valid. To study the effect of the 4 mm welded strip on the field homogeneity, both a full 3D KEMField and a local 3D COMSOL simulation were performed.

For the KEMField implementation, since the hexagonal geometry is computationally expensive to simulate, the geometry was simplified by using a wire grid class from KGeoBag together with an imported plate geometry (4 mm width) placed on top of the wire grid to represent the welded strip along the $y-$axis, as shown in Figure 4.10.

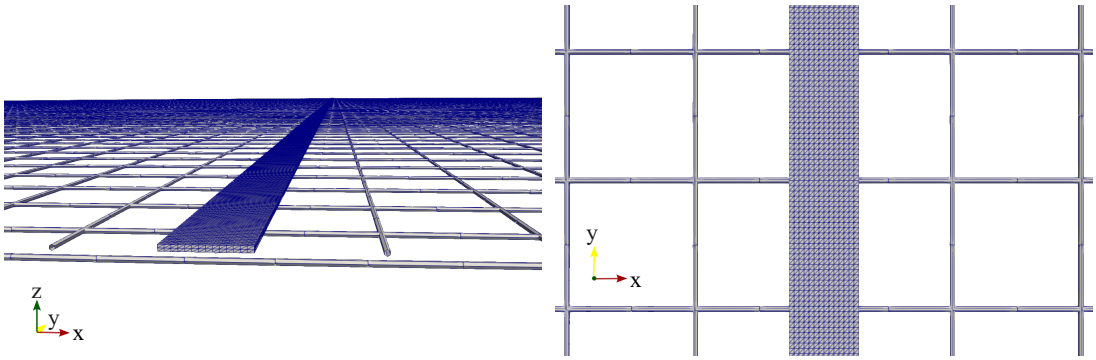

Figure 4.10: Geometry of the upgrade cathode implemented in KEMField. The discretisation elements are marked in blue solid lines.

The resulting field strength above the cathode, measured along a set of lines perpendicular to the central welded strip and parallel in $z-$direction, is shown in Figure 4.11. The plot shows the field enhancement caused by the welded strip, although this inhomogeneity diminishes at greater distances from the cathode. The effect of the elec-

trode frame is also visible on the outer edge of the detector ($|x| > 0.5\,\mathrm{m}$). Starting from $z \sim 4\,\mathrm{mm}$ above the cathode, the field enhancement due to the welding is smaller than that caused by the welded strip.

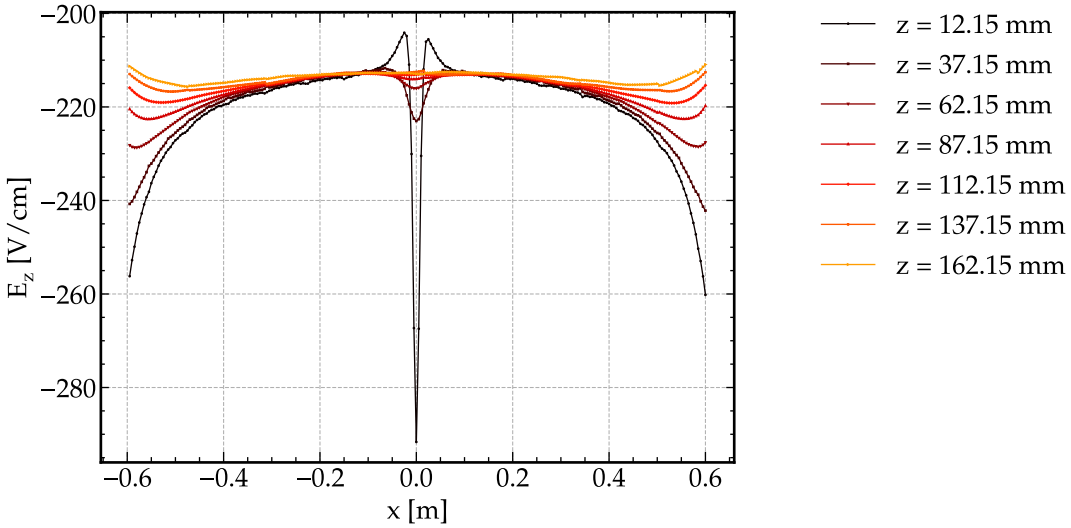

Figure 4.11: Field strength E_z computed by KEMField at various distances above the cathode on the line perpendicular to the cathode. The welding is at x =0 m. The variation dies out as the distance increases.

Since the geometry implemented in KEMField did not exactly match the upgraded cathode design, a COMSOL local 3D simulation with the truncated upgrade cathode was performed and compared with the full 3D results. It utilised the accurate mesh geometry from the computer-aided design (CAD) drawing, along with a smaller domain around the welded strip and a finer discretisation. The zoomed-in simulation domain is shown in Figure 4.12 (left).

In the previously mentioned local 3D simulations, the BCs were taken from the 2D simulation, which is invalid in this case. Therefore, the field at the top and bottom boundaries was taken from the KEMField simulation, at the z-position where the field was found to be more uniform. The domain was extended in the x-direction with $x \in [-40, 40]$ mm, such that the inhomogeneous field due to the welded strip is sufficiently small. Then, zero-charged BCs were imposed on the lateral boundaries, meaning the simulation domain was infinitely repeating.

To evaluate the results of both simulations, an array of lines in the z-direction was defined, each perpendicular to the welded strip at $y = 0$ and $x \in [-40, 40]$ mm. The normalised standard deviation of the field magnitude along these lines was used as the metric for field homogeneity. In comparison, the same calculation was performed for parallel wires without the central welded strip. The result is shown in Figure 4.12 (right) against the distance from the top surface of the cathode in the z-direction. The results from both the full 3D and local 3D simulations are generally in good agreement. The imposed BCs from the global simulation to the edge of the local simulation domain faithfully reproduced the bulk field behaviour. The different geometry of the upgrade cathode implemented in KEMField had no significant effect in the region of interest.

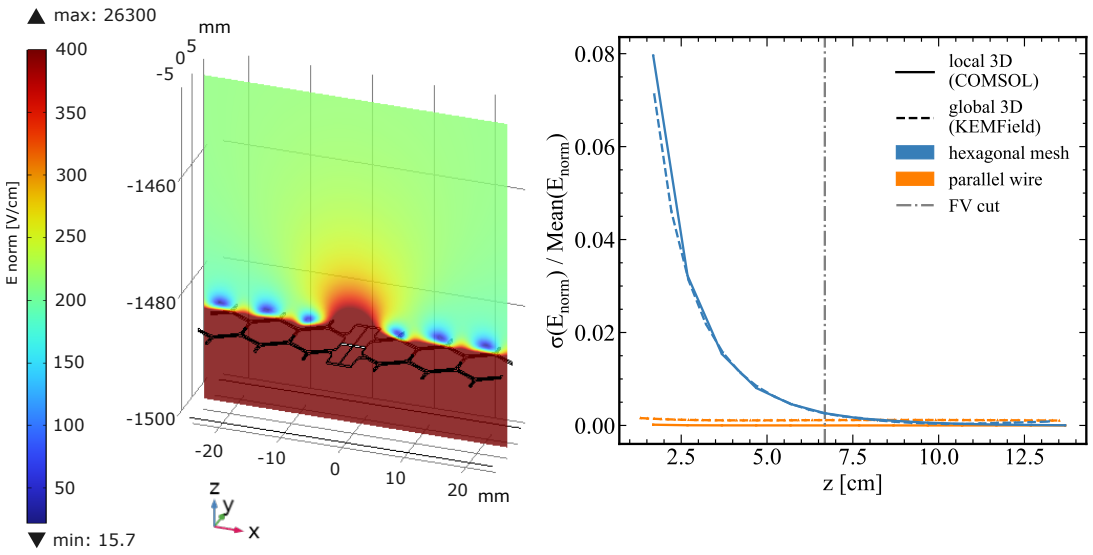

Figure 4.12: Left: close-up of the result of the local 3D simulation with COMSOL. The welded strip is along the y-direction. The E_{norm} field on the x-z plane at $y = 0$ is also shown by the colour map. Right: the standard deviation of E_{norm} for $x \in [-40, 40]$ mm normalised by the mean field at the same z-distance from the cathode. Results from both the local 3D (solid line) and global 3D (dashed line) simulations from COMSOL and KEMField are shown. The colour indicates the electrode configuration, with a hexagonal mesh cathode in blue and a parallel wire cathode in orange. The fiducial volume (FV) cut from the previous XENONnT analysis [99] is also indicated by the dashed-dotted line. Events to the right of the FV cut were accepted. The field inhomogeneity due to the welded strip vanishes from about 7.5 cm above the cathode.

Compared with the parallel-wire case, the case with the welded strip exhibits a larger field deviation, as expected. The closer it is to the cathode, the greater the field inhomogeneity. However, the breakeven point is approximately 7.5 cm above the cathode, comparable to the previous XENONnT fiducial volume [99], which is acceptable. Therefore, the hexagonal etched mesh with a central welding strip can be used as the upgrade cathode. Note that for future applications, the width of the strip may possibly be made narrower, which will further reduce the field inhomogeneity caused by the welded strip.

4.4.2 Surface Field and Electrostatic Force

As explained in chapter 3, other important parameters for the electrodes are the surface field and the load from the electrostatic force acting on the electrodes, which induces deflection on the electrodes.

As discussed in subsection 4.2.2, KEMField cannot efficiently calculate the electrostatic force acting on an entity, so the COMSOL FEM model was used. For the wire electrodes, from the 2D model, the force is calculated from the force acting on one of the concentric wires and then divided by $2\pi r$ of the wire to obtain the load per unit length, where r is the distance between the centre of the wire and the centre of the TPC. As shown in subsection 4.2.2, this method yields consistent results with 3D simulations. Additionally, the surface field on the wire was obtained by the built-in evaluation node in COMSOL of the maximum value in the selected domain around

the wires.

To simplify the calculation, the cathode welding and mesh were treated separately. For estimating the surface field on the cathode welding, a rectangular feature of 4 mm width at r ∼200 mm was introduced in the 2D model. Although this representation does not exactly reproduce the true geometry, it is sufficient for evaluating the surface field. The welding corners were rounded with a radius equal to one-tenth of the cathode thickness, which is a conservative choice for the rounded edge. The electrostatic force on the welded strip was not estimated, because the mechanical simulations described in subsection 6.1.2 only assumed a uniformly distributed load, and the contribution is expected to be small as it contributes to only 4% of the coverage of the entire mesh. Moreover, the welded structures are expected to be sufficiently robust that the additional electrostatic forces do not significantly affect their mechanical stability.

To model the electrostatic force acting on the cathode mesh, a simplified local 3D simulation was employed. The CAD drawing of the hexagonal etched mesh was truncated to a minimal rectangular unit cell corresponding to the repeating element of the hexagonal mesh pattern. The lateral boundaries were defined as symmetry planes to represent an infinitely repeating structure. The top and bottom BCs were taken from the 2D axially symmetric model, which specifies the drift and reverse electric fields.

The electrostatic force was evaluated using the built-in force calculation in COMSOL, and the resulting total force was normalised by the area of the unit cell to obtain the electrostatic load per unit area. This load was then used as input for the mechanical simulation described in subsection 6.1.2.

Since the actual potential on the cathode highly depends on the HV stability during the commissioning phase and the actual operation, a dependence of the surface field and the load per unit length or unit area on the cathode potential is shown in Figure 4.13. The potential across the electrodes was set at the designed value specified in Table 2.3. Both the case for Option I (with screens) and the case for Option III (without screens) are shown. As expected, the gate and the anode have limited dependence on the cathode potential.

A few observations can be made from the plot. First, the plot demonstrates that the local surface field on the cathode scales linearly with the applied potential. This is also true for other electrodes. Secondly, the absence of the screen reduces both the surface field and the load as expected. Thirdly, as discussed in section 3.2, the surface field of the cathodic electrodes, that is, the gate and the cathode, should be kept low, ideally below 50 kV/cm [96, 109, 121]. The surface field on the cathode and the gate from Figure 4.13 was calculated to have a field below 50 kV/cm.

Despite the bulk field above the central welded strip being enhanced, the surface field is lower compared to the legs of the mesh, because the geometry is more extended. The exact value of the maximum field on the mesh legs highly depends on edge rounding. The rounding at the edge was set to one-tenth of the mesh thickness. Although the exact cathode surface profile could not be determined, Figure 6.3 indicates that a

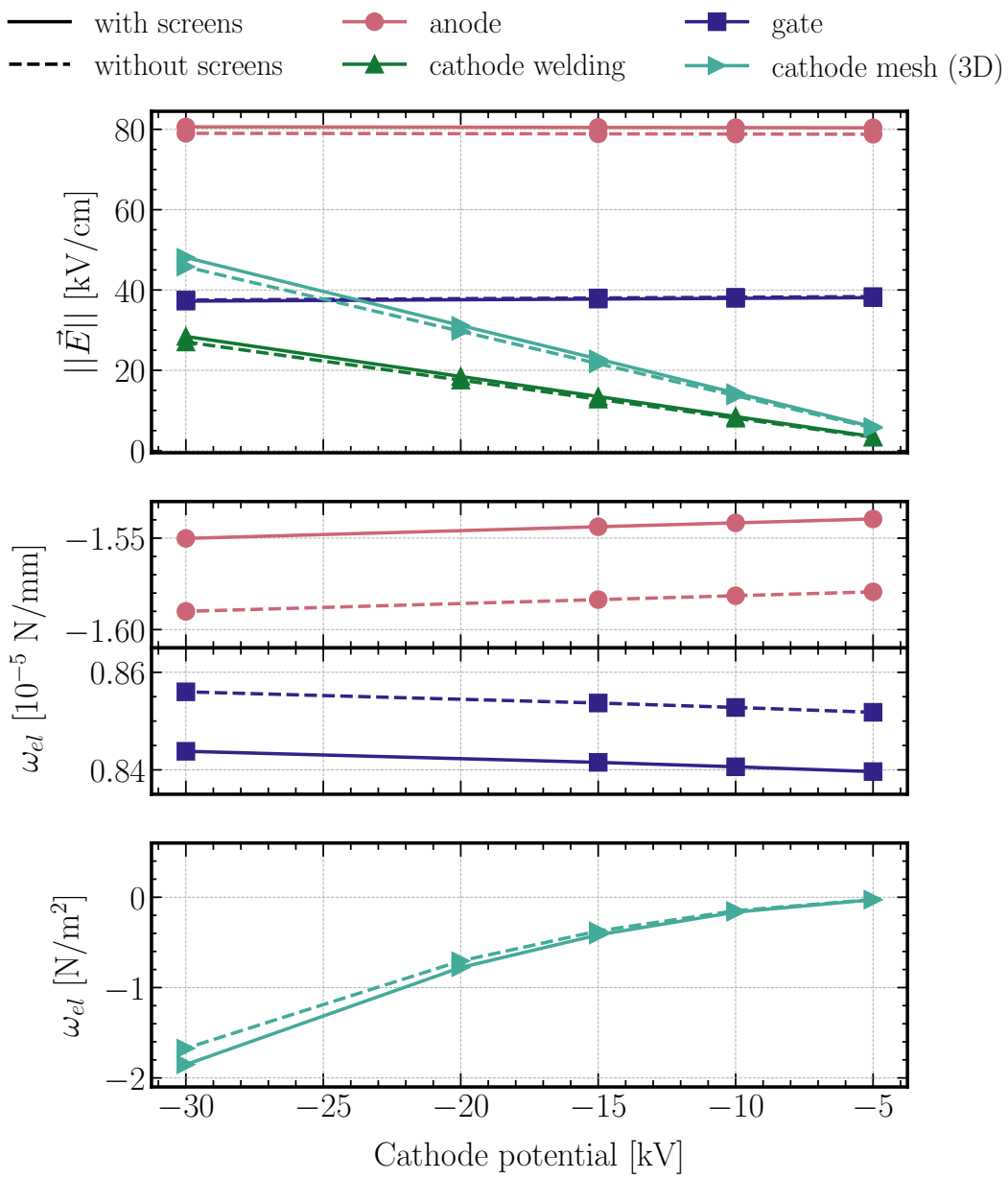

Figure 4.13: Dependence of the surface field and the load per unit length or unit area on the cathode potential. Top: maximum surface field strength of the electrodes. Middle: load per unit length of the wire electrodes. Bottom: load per unit area of the hexagonal mesh cathode.

30 µm rounding radius is likely a conservative estimate: this corresponds to a surface field below 50 kV/cm.

The sign convention adopted for the load defines a negative value as pointing downward, in the same direction as gravity. The electrostatic load acting on the gate is approximately half of that on the anode. This difference arises because the dielectric constant leads to an electric field around the anode that is roughly twice as strong as that around the gate. It is worth noting that an electrostatic load results in grid deflection, which in turn increases the local electric field strength and thus further enhances the load. This positive feedback mechanism was not taken into account in the results shown in this plot. However, for small deflections, the effect of this feedback

is expected to be minor.

4.5 Conclusion and Outlook

There are inherent limitations in numerical modelling when attempting to replicate real-world systems.

Concerning various modelling schemes, while local 3D models offer improved discretisation and therefore higher accuracy, they can yield incorrect results if BCs are not applied correctly, which is not always straightforward. The global 3D model, implemented with KEMField and BEM, while sacrificing local accuracy, provides a valuable tool for verifying local 3D simulations or for studying configurations where the 2D axial symmetry approximation breaks down. This hierarchical modelling strategy is commonly employed in numerical simulations that span wide ranges of length scales, such as in meteorology.

At the technical level, KEMField offers several advantages over COMSOL for large-scale TPC field simulations. For example, it includes the FFTM solver, which enables extremely fast field evaluations once the charge distribution is computed. KEMField is also customisable and open-source, allowing all computed quantities to be directly inspected and verified within the code. In contrast, COMSOL is commercial software that operates as a black box for certain internal computations. On the other hand, KEMField also has important limitations. Most importantly, the charge BCs are not supported, which prevents the exploitation of geometric symmetries and the study of field distortions due to PTFE side reflector charge-up. Refined discretisation was occasionally constrained by convergence issues.

Overall, the different modelling approaches are complementary. Together, they provide a flexible and robust simulation framework for the XENONnT detector geometry. The models with different software are established, cross-verified and compared with the data, increasing confidence in the correct implementation of the simulation models as well as the absence of systematic effects due to a particular solver or software. These simulation models will also be employed in the subsequent chapters to study upgraded electrode designs and related detector effects.

Looking ahead to future-generation experiments, such as XLZD, a similar multi-tiered approach can be adopted, combining models of varying accuracy and computational efficiency. Additionally, alternative tools, such as the BEM module in COMSOL, may be explored to further enhance simulation capabilities and the versatility of the model.

Chapter 5

Parallel-wire Electrodes

From section 2.1, we can see the importance of electrodes and their effect on the signal. From there, we learned the criteria needed for the electrodes. In chapter 3, an overview of different types of electrode designs was presented and extended to the latest developments in electrodes across various experiments and observations, specifically regarding HV stability and electrode backgrounds. In subsection 2.2.1, section 3.4, and section 4.4, details specific to the XENONnT current and upgrade electrodes were introduced, which set the context for this and the next chapter. Note that this chapter and the next chapter are complementary to [1].

In particular, this chapter focuses on developing a parallel-wire electrode to enhance the anode, with particular attention to improving structural integrity and the assembly procedure. While both the anode and the gate were made as parallel-wire electrodes, the anode has a more stringent requirement than the gate. Therefore, the discussion is centred around the anode without loss of generality. The next chapter focuses on building a hexagonal-mesh electrode for upgrading the cathode, with emphasis on HV performance.

While the concepts and motivations behind this and the next chapter are relevant for the next-generation detector, namely the XLZD experiment, the actual work was performed on the upgrade electrodes for XENONnT, with a diameter of 1.4 m. Experiences and insights were obtained and summarised from the production of these XENONnT electrodes for future electrodes for XLZD (i.e., around 3.0 m).

The parallel-wire anode electrode in discussion consists of 265 SS fine wires, mounted parallel to each other onto an icositetragon SS frame. Wires were bent by 90° into holes with a diameter of 2.1 mm on both ends. Then, copper pins were pressed into holes on both ends. Since copper is a softer material compared to SS, the copper deformed into the shape that could securely clamp the wires in place without damaging them. Grooves stemmed out from the holes to align and hold the wires in position. To maintain the field homogeneity, the separation between the centres of wires (a.k.a pitch) is the same across the whole electrode, at 5 mm.

In the remaining chapter, I will discuss first the wire (section 5.1), then the frame of the electrode (section 5.2), followed by the assembly method (section 5.3). These sections include simulation, tests, and mitigation for a major manufacturing fault. Afterwards, the QA/QC measures and the final assembly was summarised, with a comparison to the gate electrode (section 5.4, section 5.5, and section 5.6). Finally, this chapter is concluded with the lessons learned for the XLZD experiment (section 5.7).

5.1 Wires

As summarised in section 3.1, one of the most detrimental problems to avoid for the parallel-wire electrode is wire breakage during the operation of the detector. This could be induced by mechanically overloading the wires or by an HV breakdown. To prevent the latter case, the wires were carefully observed before installation to avoid kinks. The edges of the electrodes were also covered by insulators. On the other hand, since the anode is not cathodic, it is less prone to inducing breakdown. Therefore, the remaining problem is the mechanical sturdiness and the structural integrity of the whole electrode system. More importantly, the wires must withstand the load and tension applied to them to prevent breakage.

Secondly, as argued in section 2.1, the deflection (hogging or sagging) of the wires should be reduced until the marginal benefit is at the expense of the permanent deformation of the wire and the increasing thickness of the wire. This is because the wire deflection directly affects the gain and the signal shape of the S2 signal, as explained in section 2.1. Specifically for the case of the anode in XENONnT, it was required to target the deflection of 0.5 mm during operation. The stringent requirement was chosen such that there could be some extra room for additional deflection for relaxation after cooling cycles.

As the wires are mounted onto the frame, they naturally deflect under their own weight, as well as the electrostatic force and the buoyancy during operation. To limit the deflection to 0.5 mm, thicker and stronger wires that can withstand a higher axial tension should be used. In addition to the loads and the high axial tension, the wire also has to withstand the thermal stress during the cool down of xenon to the liquid phase at around 177 K. On the other hand, in terms of LCE, the thinner the wire, the better. This motivates a dedicated study to select a thin and robust wire that can withstand the loads and meet the deflection requirement.

5.1.1 Choice of Wire Material

The wire candidates are listed in Table 5.1. SS316 or SS316L was considered due to the better resilience to electron emission [96] (see also section 3.2). In general, SS316 and SS316L have similar properties, while SS316L has a lower carbon content. Another major difference is the corrosion resistance after welding [128, 129], which is irrelevant in our application, as no welding on the wire is needed. In the case of PandaX-4T, where spot welding was used to fix the wire, this should be taken into account, and dedicated tests should be performed.

Table 5.1: Datasheet information for the candidates of the wire tests. The measurements of ultimate tensile strength and yield tensile strength are presumably taken at room temperature.

Manufacturer	Diameter [mm]	Material (AISI)	UTS [MPa]	YTS at 0.2% offset [MPa]
California Fine Wire (CFW)[154]	0.216	316 annealed	884	725
Vogelsang [155]	0.212	316 semi-hard	1000-1200	N.A.
Dahmen [156]	0.221	316L full-hard	1916.5	1528.5

5.1.2 Wire Deflection and Axial Tension

Loads on Wires during Operation

During the operation of the TPC, the weight of the wires, the electrostatic force, and the buoyancy force are the major contributors to the deflection of the wires. The weight and the buoyancy force are uniform along the wire. The load from the weight per unit length, ω_g, was calculated by

$$\omega_g = \rho_{ss}\pi r^2 \times g, \tag{5.1}$$

where ρ_{ss} is the density of SS, taken as 8000 kg/m^3 for SS316 [112, 157, Fig. 2], r is the cross-sectional radius of the wire, g is the standard gravity, taken as –9.81 m/s^2. The load from buoyancy per unit length, ω_b, was calculated by

$$\omega_b = -\rho_f \times g \times \pi r^2, \tag{5.2}$$

where ρ_f is the density of the fluid, either LXe or GXe. Assuming the operating temperature is at around 177 K and 1.928 bar at saturation, the density of GXe and LXe is 18.077 kg/m^3 and 2859.8 kg/m^3 respectively [39].

For the electrostatic force per unit length, ω_{el}, it was estimated from a two-dimensional (2D) axisymmetric model mentioned in subsection 4.3.1. In the COMSOL model, a force calculation node was added to the wires at three radial positions r away from the centre. Since it was an axial-symmetric model, the length of the wires was $2\pi r$. The average value of the total electrostatic force on the wires, divided by the length of the wire, results in the load per unit length. As demonstrated in subsection 4.2.2, this method of force calculation in the 2D axisymmetric model yields results consistent with those obtained from a 3D simulation and from analytical calculation.

For reference, the respective values for the anode and the gate are listed in Table 5.2, for the wire with a diameter of 0.216 mm. Note that the loads depend on the wire diameter. The total load per unit length acting on the anode wires in this case is -1.84×10^{-5} N/mm.

An accurate estimation of the mechanical load induced by electrostatic forces requires a coupled electrostatic–mechanical simulation, which is left for future work. First, the more the wire deflects, the higher the electrostatic force, which might further increase the deflection. This is called the feedback effect. Secondly, the relative difference in the deflection between nearby wires changes the field and thus the electrostatic force

Table 5.2: Load on the anode and the gate assuming the wire diameter is 0.216 mm and the load is uniform across the electrode. Negative denotes pointing downwards.

Type of Load	Load on Anode [N/mm]	Load on Gate [N/mm]
Weight (ω_g)	-2.88×10^{-6}	-2.88×10^{-6}
Electrostatic (ω_{el})	-1.56×10^{-5}	$+8.47 \times 10^{-6}$
Buoyancy (ω_b)	$+6.51 \times 10^{-9}$	$+1.03 \times 10^{-6}$
TOTAL [N/mm]	-1.84×10^{-5}	$+6.62 \times 10^{-6}$

on the wire. Thirdly, since the anode and the gate are typically within $\mathcal{O}(10\,\mathrm{mm})$, and are under a strong electric field with a dielectric boundary in between, the effect from the gate and the liquid surface might affect the deflection on the anode. Fourthly, the load per unit length is non-uniform along the wires as assumed in the simplified model, as shown in [158].

Regarding the feedback effect, it was shown in [110, Section 4.4.2] that with a small deflection, the prediction between a simple model and their non-linear model is similar. While both models assume a constant electrostatic force on the wire, the former one ignores the feedback effect. For simplicity, we are using the simplified model for the moment, given the stringent deflection requirement.

Axial Tension on Wire

To limit the maximum deflection under the aforementioned loads, axial tensions were applied to each wire during assembly to compensate for the load. As mentioned, if assuming the load is uniform on the wire, the wire deflects into a catenary profile [110, 159]:

$$z(x) = \frac{F_{ax}}{\omega}\left[\cosh\left(\frac{x\omega}{F_{ax}}\right) - \cosh\left(\frac{L_0\omega}{2F_{ax}}\right)\right], \tag{5.3}$$

where $z(x)$ is the z-direction profile as a function of position x, F_{ax} is the axial tension on the wire, ω is the total load per unit length for each wire, and L_0 is the undeformed length of the wire between supports.

Consider the longest wire where the deflection is the most prominent, L_0 is 1340.4 mm. With the load at $\mathcal{O}(1 \times 10^{-6}\,\mathrm{N/mm})$ and the typical F_{ax} at around 5 N, the higher order terms of $\cosh$ can be disregarded. At the center of the wire, i.e., $x = 0$, we can relate the wire deflection and the axial tensions F_{ax} on the wires:

$$F_{ax} = \frac{(\omega_g + \omega_{el} + \omega_b)L_0^2}{8h_{\max}} \tag{5.4}$$

where ω_g, ω_{el}, and ω_b are given in Table 5.2. $h_{\max}$ is the maximum deflection. Another treatment considered also the finite Young's modulus for the wire [19], giving the results in $< 0.2\%$ difference.

From Equation 5.4, the axial tension to reach 0.5 mm deflection, F_{ax} has to be greater than 8.26 N for the longest wire. To leave some safety margin, 8.6 N was chosen

during the design phase. Also, in principle, the tension is proportional to L_0^2. However, we limit ourselves to 4 different tension values to reduce human error during the assembly process, ranging from 3.2 N to 8.6 N.

Maximum Stress on the Wires

There are several contributions to the stress on the wire at different stages. First of all, when installing the wires to the frame, each wire was loosely inserted into a hole, bending in 90°. Then, a copper pin was inserted and deformed to fix the wire with friction. This stress is non-linear and highly geometry- and method-dependent, and therefore not estimated.

After installation, the major contribution to the stress is from the aforementioned axial tension, ranging from 3.2 N to 8.6 N, that keeps the wires from deflection. Then, when filling the TPC with LXe at ∼177 K, the electrode frame cools down slower than the wire due to their surface-to-volume ratios, inducing thermal stress on the wire:

$$\sigma_S = E\alpha_{th}\Delta T, \tag{5.5}$$

where σ_S is the thermal stress, E is the Young's Modulus, α_{th} is the coefficient of thermal expansion, ΔT is the temperature difference. The formula is independent of the geometry. Assuming the maximum temperature difference of 25 K, the Young's modules to be around 200 GPa between 175 K and 293 K [160], and the coefficient of thermal expansion is 1.5×10^{-5} [160], the thermal stress is 75 MPa. That is ∼2.75 N for the wire diameter of 0.216 mm.

During the operation, there is no longer thermal stress, but the electrostatic force acting on the wires. Its contribution, together with the gravitational load, amounted to only ∼0.02 N. Therefore, the maximum stress on the longest wires with a diameter of 0.216 mm is estimated to be at 11.35 N, given by the axial tension and the thermal stress.

5.1.3 Wire Strength at Different Temperatures

The main purpose of this test was primarily to determine the appropriate wire candidate that can survive the stated maximum stress, as well as the 90° bend from the copper pin fixation. Secondly, there was a hint that the strength of the wire changes with temperature [109], while more measurements were needed to confirm the dependence.

Thirdly, due to the slight difference in thermal expansion coefficients between copper and SS, it was unclear whether the fixation strength would change after a cooling cycle. The expected shrinkage in diameter of the copper pins is ∼3.9 µm using the thermal coefficient of 1.6×10^{-5} [161, Table 4] and the diameter of the pin of 2.1 mm. Note that the amount of shrinkage is much smaller than their fabrication tolerance of 50 µm. The corresponding change for the holes in the SS frame is ∼3.7 µm. The minor shrinkages are not expected to have a macroscopic effect. However, their impact on the mechanical sturdiness of the fixation at cold temperatures and after cooling cycles is to be verified.

Given the above motivations, a custom-made *tensile test* setup, as shown in Figure 5.1, was built to accommodate different measurements compared to the standard tensile test facility. We performed tensile tests with the wire candidates, summarised in Table 5.1, at 5 temperatures from room temperature down to 200 K to search for suitable wire candidates that can withstand the stresses reliably at low temperatures. We also performed the same test with an electrode frame mock-up and the copper pin fixation (later referred to as *the copper pin fixation*) to see the additional effects due to the fixation itself.

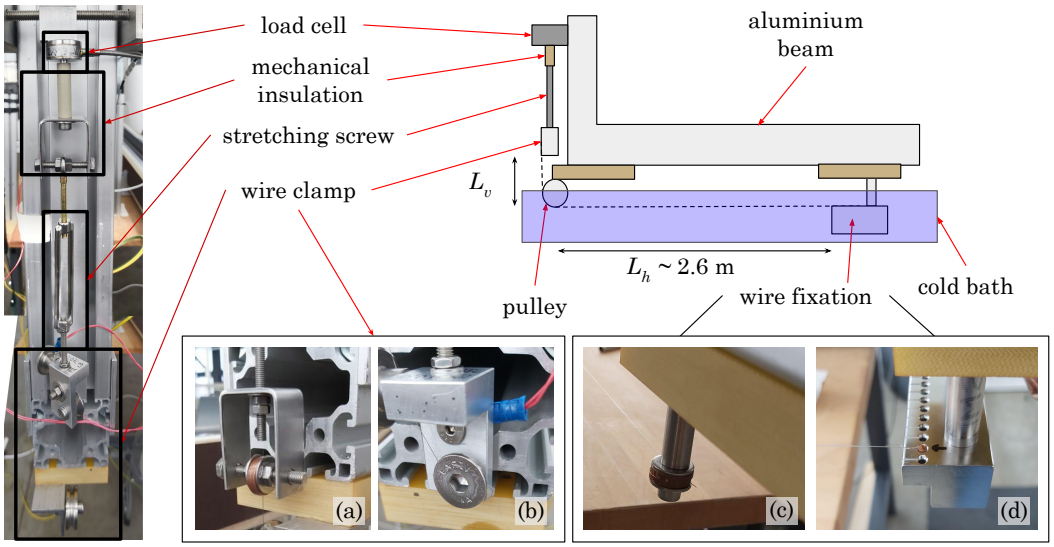

Figure 5.1: Drawings and photos of the wire test setup. The schematic drawing (top right) shows the setup when loaded into the cold bath. The L-shaped aluminium beam profile is supported externally outside the cold bath, which is not indicated in the drawing. The dashed line indicates the wire sample. L_v and L_h represent the vertical and horizontal length of the wire, measured from the centre of the pulley. The photo on the left is a composite image from two photographs to illustrate the vertical part of the setup. It consists of the Fixation V to fix the wire sample, a stretching screw to manually increase the strain of the wire sample, a load cell measuring the axial tension on the wire sample, and the mechanical insulation that decouples the movement of the stretching screw and the load cell. Fixation V is either (a) copper gaskets or (b) a screw clamp. The wire passed through the pulley to enter the horizontal part of the setup and was fixed by Fixation H, which is either (c) copper gaskets or (d) a copper pin with the mock-up of the electrode frame segment.

Experimental Setup

The setup contains an L-shaped aluminium beam profile, where the wire sample was mounted along the profile through a pulley, as shown in the schematic diagram in Figure 5.1. A wire fixation, either with a copper gasket or the copper pin fixation, fixed the wire to the end of the horizontal part of the setup, named as *Fixation H* in the remaining part. They are shown in Figure 5.1 (c) and (d) respectively. The wire passed through the pulley and was fixed at the other end to the vertical part by another fixation, named *Fixation V*. The length of the horizontal part and the vertical part of the wire is around 2.6 m and $\mathcal{O}(10\,\mathrm{cm})$ respectively, and they varied and were measured for each measurement. For Fixation V, we either used copper gaskets or

a screw clamp, shown in Figure 5.1 (a) and (b) respectively. We expected the two fixation methods to induce slightly different systematic errors, but we did not observe significant differences between the results. The Fixation V was attached to a screw system, which was used to stretch the wire sample in the axial direction. The screw was then indirectly attached to a 200-N load cell, which measures the axial force of the whole system, effectively of the wire sample, as the other components are far less ductile. The load cell was calibrated from time to time between measurements using standard weights hanging from pulleys.

As described at the beginning of the chapter, to install the wire, the wire first passes through the hole of the frame mock-up with a 90° bend. The position of the wire was guided by the groove in front of the hole. Then, a copper pin was inserted into the same hole. During the initial testing phase, the wires often broke at the tip of the groove, later referred to as the *groove tip*, during the pin insertion due to the sharp edges. To mitigate this, we manually ground the groove tip with grinding cords. The difference is shown in Figure 5.2. After the grinding, the wires did not break during the pin insertion. For future electrode design, this should be taken into account to achieve a smoother or rounded groove tip, ensuring that the feature is produced right from the manufacturing phase.

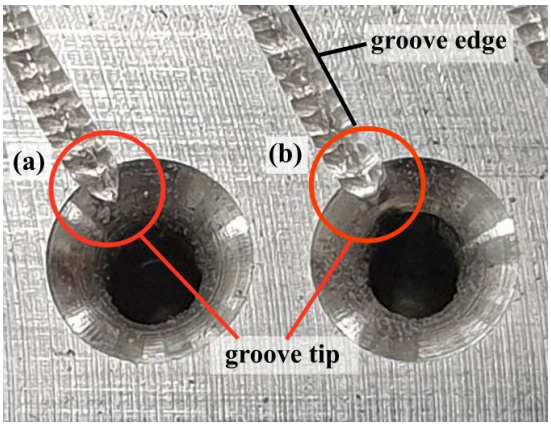

Figure 5.2: Difference before and after grinding the tip of the groove, named the groove tip, enclosed by the red circles. Circles (a) and (b) indicate the groove tips before and after grinding, respectively. (b) shows a clear edge at the end of the groove compared to (a). The side edge of the groove is also indicated by the black straight line, named the groove edge.

For each measurement, we first mounted a wire sample onto the aluminium frame outside the bath. Then, the cold bath was prepared by adding dry ice to a bath of ethanol inside the partially thermal-isolated bath. The liquid level covered approximately half of the pulley, as indicated by a marker. As the temperature reached the desired value, we positioned the whole aluminium frame so that the horizontal part of the wire was completely immersed in the cold bath. One temperature sensor, which we were using PT100, is sitting at the end of the bath to monitor the temperature T_{bath}. Another PT100 (T_{dip}) is attached to the horizontal aluminium beam and is around the middle of the wire sample. A DAQ module from National Instruments [162] at the rate of 50 Hz continuously read out the measurement from the load cell and the temperature sensors during a measurement. Then we turned the screw in steps by 1/4 of a turn while the stress was recorded by the load cell. Note that the wire samples and the load

cell did not rotate together. Since the threads on the screw are at equal distances, we afterwards determined the change in strain for each step, as well as the corresponding stress value.

In addition, for the copper pin fixation, we did an additional tensile test after the system underwent a thermal cycle down to 200 K. We cooled down the setup for around 1 minute until T_{dip} almost stabilised around 200 K. Then, we took out the setup for warming up until T_{dip} went back to room temperature before the tensile test. In case of a significant thermal relaxation between the copper pin fixation, the wire, and the electrode frame, there might be more room for the wires to wiggle. In such a case, the wire could slip through, and the YTS and UTS were expected to be reduced. In other words, the reduction in YTS and UTS, if any, would be caused by the relaxation of internal tension and stress, but not due to thermal shrinkage.

The Stress-Strain Curve

For each measurement, we obtained a continuous record of the tension measurement as we changed the length of the wire, as shown in the inset of Figure 5.3. To obtain the strain, $\Delta L/L$, we determined ΔL, which is the change in length, and L, which is the initial length of the wire sample. Given the diameter of the thread pitch, we could determine ΔL for the 1/4-turn, specifically steps of 0.25 mm or 0.4 mm in our tests. The initial wire length $L = L_H + L_W$, as labelled in Figure 5.1. To compute the stress, we converted the measured voltages from the load cell to forces with the average load cell calibration values. The wire diameter was measured at several positions using a micrometre, and the average value was used to obtain the stress. As a result, each measurement was processed into a stress-strain curve, as shown in Figure 5.3.

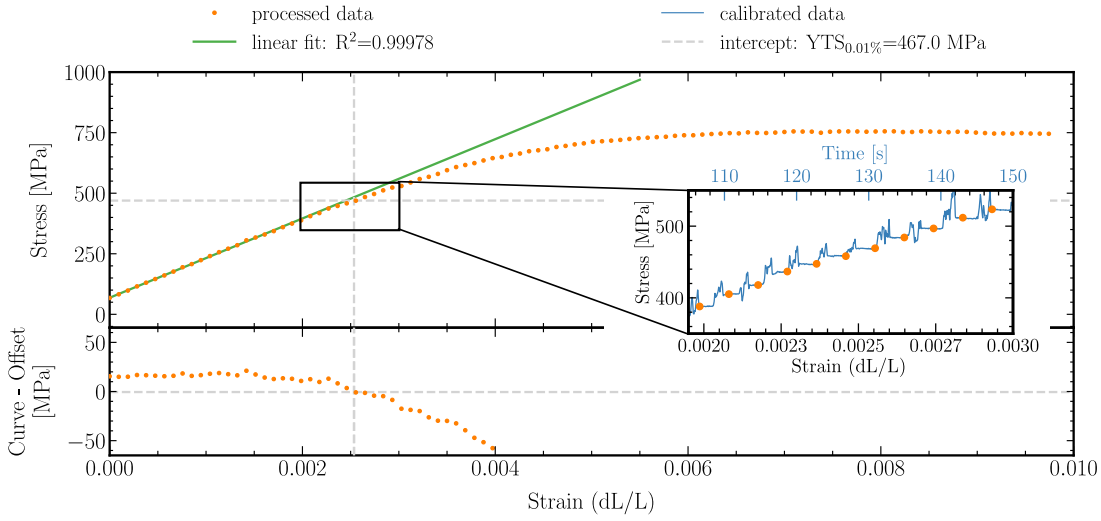

Figure 5.3: Example for the stress-strain curve from the data. The blue line in the inset plot is the calibrated raw data. The orange dots are the stress and strain values obtained from the raw data. Note that the time and the strain axis are not exactly one-to-one corresponding, and they are manually scaled for illustration purposes. The upper plot showed the stress-strain curve with the linear fit in the green line. The lower plot showed the stress-strain curve, subtracting the linear fit shifted by 0.01%. The grey dashed line indicates the interception points, where the y-value gives the yield tensile strength (YTS) at 0.01% offset.

According to the standard tensile test, the linear part of the stress-strain curve is defined as the elastic range of a material. A linear function can be fitted to the elastic range, where the slope is defined as the Young's Modulus. The YTS is defined as the stress at which the material starts to deform permanently. The value can be estimated by the intersection point between the stress-strain curve and the linear fit shifted by a certain amount. The conventional shift, or offset, is 0.2%, measuring the stress where the material is permanently deformed by 0.2%. In other words, the sample underwent an additional 0.2% deformation beyond the elastic deformation, which is irreversible. To further avoid the risk of permanently deforming the wire to a large degree, we set a more stringent requirement with an offset of 0.01% instead. The standard offset of 0.2% was used to cross-check with datasheet values.

For the linear fit, the first few points were usually off the straight line because the wire was slightly under-tensioned. Therefore, different fitting ranges were used, and only those with the R-square > 0.99 were considered in the final results. The line was then shifted by a 0.01% offset to the right, so that the intersection point between the fit and the stress-strain curve determines the YTS at 0.01% offset of the sample. The resulting YTS and Young's modulus were the mean value from the different fit ranges, while the fitting error is the standard error from the different fit ranges.

Results and Discussion

The resulting YTS at 0.01% offset for all the measurements at different temperatures is shown in Figure 5.4. The temperature was the average value recorded by the two PT100 sensors inside the bath. The error bound is the maximum and minimum recorded temperature measured by the sensors throughout each measurement. The error for YTS consists solely of the fitting error. For the California Fine Wire (CFW) sample at room temperature, we took 5 data points, and the statistical error is around 10%. It was, however, not shown in the plot due to the limited statistics. The maximum stress acting on the wire is also shown in the same plot for comparison. Since the value has a minor dependence on the diameter of the wire, only the one for 0.216 mm-diameter is shown, which is the diameter for CFW.

The error in ΔL is < 0.05mm, which is negligible compared to $L \sim 2600$m, so it was not considered. Since the vertical part of the wire was not submerged in the cold bath, this added an error to the initial total length. It was checked, and it was insignificant when determining the YTS.

Another systematic error comes from the friction of the pulley. In the ideal case, the change in strain on the vertical part of the setup should transfer exactly to the change in strain of the horizontal part. Consider the rolling friction coefficient for steel at room temperature is 0.002 [163]. The value might be higher at lower temperatures [164]. However, no value measurement exists at 200 K. If taking the value at room temperature and considering the tension at 30 N, the normal force acting from the wire to the pulley is $\sim$6 N, resulting in the frictional force of 0.012 N, which is 0.04% of the tension on the wire. Therefore, this effect on the measurement was also smaller than the fitting error.

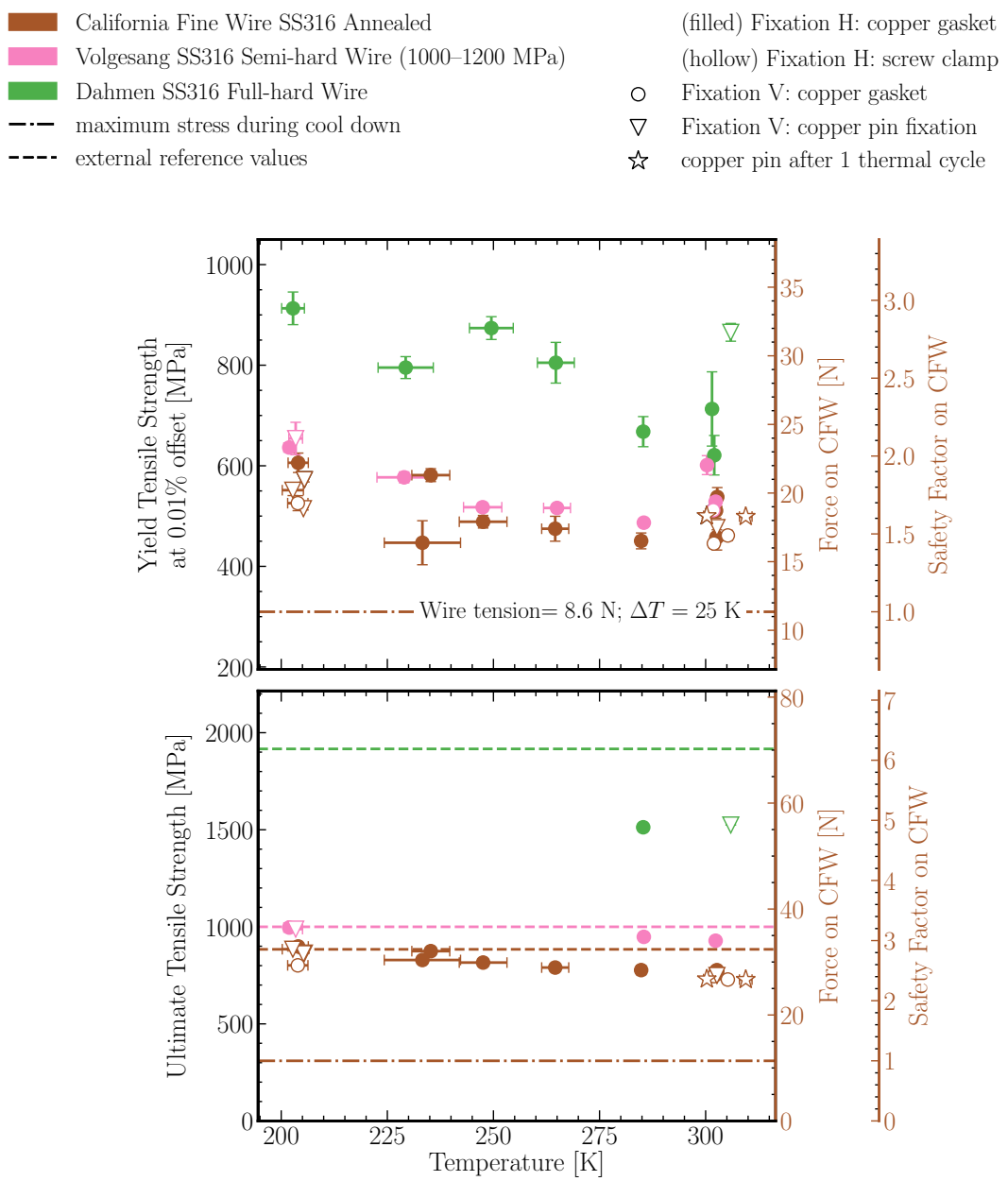

Figure 5.4: Results from the tensile tests at various temperatures. The top plot shows the yield strength at 0.01% offset, meaning the wire undergoes 0.01% additional deformation beyond elastic deformation. The bottom plot shows the ultimate tensile strength of the sample. Dashed lines in the bottom plot: the UTS values from the data sheet, as shown in Table 5.1. Dash-dotted line on both plots: the maximum stress on a 1340.4 mm wire, including the stress due to tensioning and thermal shrinkage when cooling down the TPC. The temperature gradient was assumed at 25 K, which is very attainable. The first left axes on both plots indicate the conversion to force acting on the CFW sample. The second left axes on both plots indicate the safety factor away from the maximum stress on the CFW wire. The filled and hollow points represent different Fixation V shown in Figure 5.1. Circle: tests in which the Fixation H is the copper gasket clamped the wire. Inverted-triangle points: tests with the copper pin fixation, where the wire was bent by 90°. Star points: tests with the copper pin fixation, and went through a thermal cycle.

From our results, all wire samples tested can withstand their maximum stress, caused by the axial tension and the thermal stress, with less than 0.01% plastic deformation. Specifically, the maximum stress for CFW is 11.35 N, indicated by the dash-dotted line in Figure 5.1. Compared to the estimated maximum stress, the average safety factor for CFW until deformation is 1.6 ± 0.2, with the minimum at 1.4. Subsequently, under the gravitational, electrostatic, and buoyancy forces, the deflection would be less than 0.5 mm for the anode electrode.

Additionally, as the temperature decreased to 200 K, we observed a slight increasing trend in the YTS at a 0.01% offset, as suggested in [109], with correlation coefficients ranging from -0.62 to -0.68 for all wire candidates. The YTS at a 0.01% offset with copper pin fixation differs by less than 5% compared to the copper gasket fixation, regardless of whether the system underwent a thermal cycle. From this result, we can infer that the copper pin fixation can reliably hold the wire in place in cold conditions and after the cooling cycle.

We validated the measurement by comparing the YTS at 0.2% offset, the UTS, and the Young's Modulus to the datasheet values, as shown in Figure 5.5. Concerning the YTS of CFW, the mean value we measured at room temperature is consistent with the datasheet value, being 744 ± 12MPa and 725 MPa respectively. The error is the standard deviation of the measurements to account for systematics between configurations. Note that the datasheet value was obtained directly from the spool specifications, and the value differed between batches. [165] reported the general YTS at 0.2% for annealed SS316 at 241 MPa, which also differs from the actual values of the particular batch we tested. For the Dahmen wire, the operating range of the setup was not enough to compute the 0.2% offset at room temperature. And there is no datasheet value for the Vogelsang sample to compare with.

For the UTS comparison, the datasheet values were presumably measured at room temperature, and they are systematically higher than the measured values. A hint can be seen in Figure 5.3, that as the wire sample entered the plastic region, the force decreased between steps of changing the strain. The effect grew stronger as the wire deformed more, as we observed (not shown). It can be understood as a physical process that, as the wire enters plastic deformation, part of the wire stretches more to compensate for the overloading tension, such that the tension drops. This could mean that first, the strain was underestimated, and second, the wire was continuously losing the applied tension between each step, resulting in a lower measure UTS. Compared to a standard measurement, an automatic device continuously increases the length at a definite strain rate or stress rate based on DIN EN ISO 6892. Slower strain rate can result in a lower UTS measured [166]. This can explain the incompatible result from the industrial measurements. Nevertheless, it is important to note that this systematic effect on the strain and UTS in plastic deformation was not expected to affect the result in the YTS, also demonstrated in Figure 5.3 (right). This is because the stress should start to deviate from the linearity at the strength regardless of the strain. And the reduction in tension was the strongest during plastic deformation.

While the measured YTS is in good agreement with the value from the datasheet, the measured Young's Modulus is also systematically lower than the value listed in

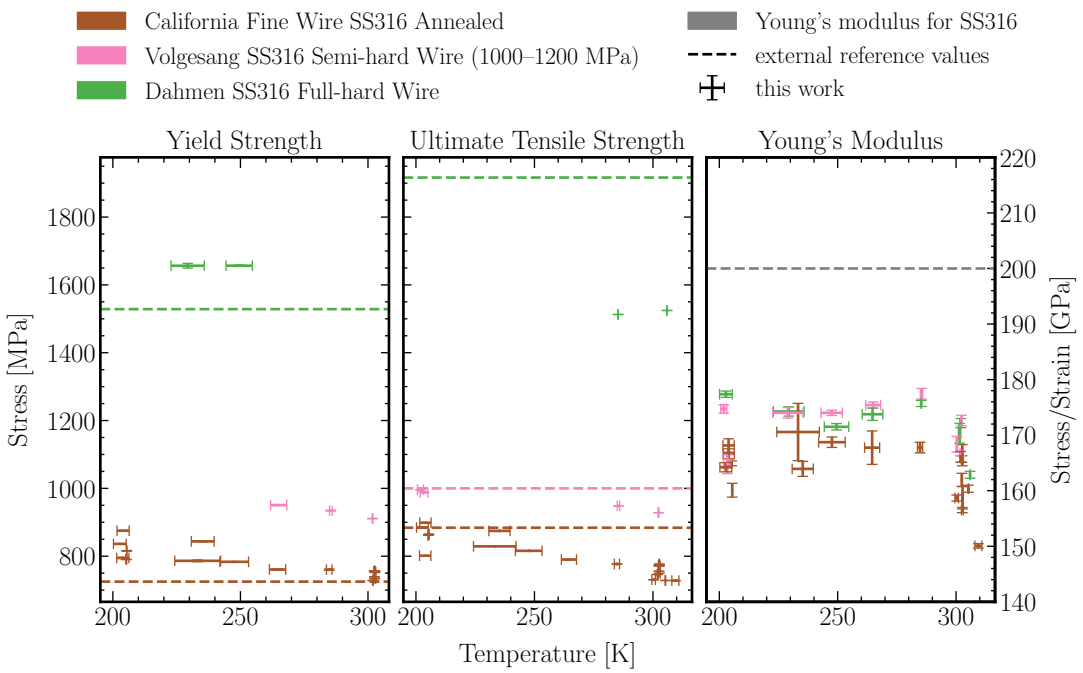

Figure 5.5: Comparison between the measured values and the datasheet values. Left shows the measured yield tensile strength (YTS) at 0.2% offset, and right shows the ultimate tensile strength (UTS). The dashed lines are the datasheet values. The points are the measured values using the same set of data as in Figure 5.4, but at 0.2% offset. Some data points were missing as they were out of range.

[160]. This may imply that the strain was underestimated by around 17% compared to the industrial standard. While the exact reason remained unclear, it does not affect the measurement of the strength of the wire with a similar argument in the previous paragraph.

Conclusion

From the test, we concluded that the relaxation and thermal shrinkage do not significantly reduce the strength of the copper pin fixation. We also concluded that all tested wire samples could, in principle, withstand the stress from axial tension and the stress due to temperature difference.

There are additional metrics to consider when selecting suitable candidates for the parallel wire electrode. Other collaborators checked the surface smoothness and discharges at high voltage, but they were not decisive factors between the Volgesang semi-hard wire and the CFW wire samples. When comparing SS316 and SS316L, the major difference is the corrosion resistance after welding [128, 129], which is irrelevant in our application, as no welding on the wire is needed.

Regarding the mechanical performance, the Dahmen full-hard wire breaks during installation with the 90° bend and copper pin insertion. Although its YTS is higher, hard wire is generally more brittle than soft wire. Annealed SS, on the other hand, exhibits enhanced ductility among the three samples, providing a longer range of plastic deformation before fracture. This property is crucial for preventing wire breakage, which

Table 5.3: Useful mechanical parameters for the CFW in the anode electrode.

Quantity (symbol)	Taken from	Value or conversion
CFW parameters		
Wire diameter (d)	datasheet	0.216 mm
Cross-sectional area (A_w)	$\pi d^2/4$	$3.664\,35 \times 10^{-8}$ m^2
Min. YTS at 0.01% offset (YTS$_{min}$)	Figure 5.4	445 ± 9 MPa $=$ 16.31 N
UTS	datasheet	884 MPa $=$ 32.39 N
Detector parameters		
Thermal stress (σ_S) at ΔT =25 K	Equation 5.5	75 MPa = 2.75 N
Longest initial wire length (L_0)	CAD drawing	1340.4 mm
Total load (ω)	Table 5.2	-1.84×10^{-5} N/mm
Force from the load	ωL_0	0.02 N = 0.5 MPa
Option I		
Axial tension (F_{ax})	consideration	8.61 N = 235 MPa
Maximum stress on wire (S_{tot})	$F_{ax}/A_w+\sigma_S$	310 MPa = 11.36 N
Safety factor for plastic deformation	YTS$_{min}/S_{tot}$	1.44
Safety factor for breaking	UTS$/S_{tot}$	2.85
Expected wire deflection (h_{max})	Equation 5.4	0.48 mm downward
Option II		
Axial tension (F_{ax})	consideration	9.20 N = 251 MPa
Maximum stress on wire (S_{tot})	$F_{ax}/A_w+\sigma_S$	326 MPa = 11.95 N
Safety factor for plastic deformation	YTS$_{min}/S_{tot}$	1.37
Safety factor for breaking	UTS$/S_{tot}$	2.71
Expected wire deflection (h_{max})	Equation 5.4	0.45 mm downward

could result in electrode short-circuiting or sparking at high voltages. Therefore, we subsequently used the CFW sample for the remaining tests and assembly.

5.2 Electrode Frame

The geometry of this electrode largely follows the XENONnT electrode design [19, 35]. The frame is a icositetragon (24-gon) with the inner diameters of around 1.33 m. The frame comprises an annealed SS316 slab with a YTS of about 240 MPa. The choice of material is again based on corrosion resistance and reduced electron emission compared to SS304 [96, 110]. Annealed SS, meaning the SS sample was heated in the oven during the manufacturing process to reduce the internal tension stored during machining. This was expected to reduce the relaxation after the cooling cycle, as such a relaxation can reduce wire tension, thus increasing the wire deflection. It was later found that only annealing was not enough to prevent the loss in tension due to the cooling cycle. More discussion on this can be found in section 5.6.

5.2.1 Improving the Mechanical Sturdiness of the Electrode Frame

Since the axial tension on the wires was substantially increased from around 4 N to 8.6 N, the wires exert greater stress on the electrode frame compared to the previous design. This created a weak point in the electrode frame, thereby compromising

the structural integrity of the overall electrode. The challenge was that the room for changing the electrode frame design was limited and constrained by other components of the detector. Therefore, a dedicated mechanical simulation on the electrode frame was performed to locate the weak points and only strengthen those regions to improve the sturdiness of the frame. In addition, the deformation of the electrode frame with the 265 wires was calculated, as the deformation has to be within the tolerances of the detector to maximise the fiducial volume.

For this, we used ANSYS Workbench 2021 for the finite element analysis (FEA). Instead of having 265×3 force components as the input, the forces on each polygon section were combined into a single force vector to simplify the calculation. To further increase the computational efficiency, we applied mirror symmetry along the horizontal axis in Figure 5.8. The simulation setup ended up with 12 input forces for the FEA.

To evaluate the component stresses on the electrode frame, the von Mises stress criterion was applied, which is commonly used for ductile materials such as steel. The multiaxial stress state in the real component was represented by an equivalent uniaxial stress, providing a comparable measure of material stress. This equivalent stress value can then be compared to the material's yield tensile strength (YTS) to assess the risk of material failure.

With iterations of the simulation, the geometry of the electrode frame was altered to better withstand the increased axial tension from the wires. The height of the SS frame increased from the original 18 mm (XENONnT design before upgrade) to 24 mm. In addition, the width varies along the circumference from 30.975 mm to 33.975 mm. The semi-circular hole where the high-voltage feedthrough would pass through was also thickened in width.

The final maximum stress was 98.6 MPa, where the cross-section is the smallest. Compared to the mentioned YTS of the material, the safety factor against permanent plastic deformation is 2.4 times. In addition, given the load of the wire tension, the ring deforms outward by a total of 4.41 mm in the direction perpendicular to the wires. Parallel to the direction of the wires, the ring deformed inward by 4.44 mm in diameter. This deformation is later compared to the measurement in subsection 5.4.1. After the optimisation, the frame was then manufactured by Mühlbauer Parts & System (MPS) [167].

5.2.2 Major Manufacturing Fault

An error occurred during the manufacturing process of the anode frame. The manufactured anode frame possessed visible physical imperfections and deviations from the original design, as shown in Figure 5.6. Since the anode frame is thicker in height compared to the previous design, the holes were machined from both sides. Part of the problem was due to the unstable frame when machining, which could explain the edge on the inner wall.

From a quick test, we found that some wires could not be properly fixed due to the

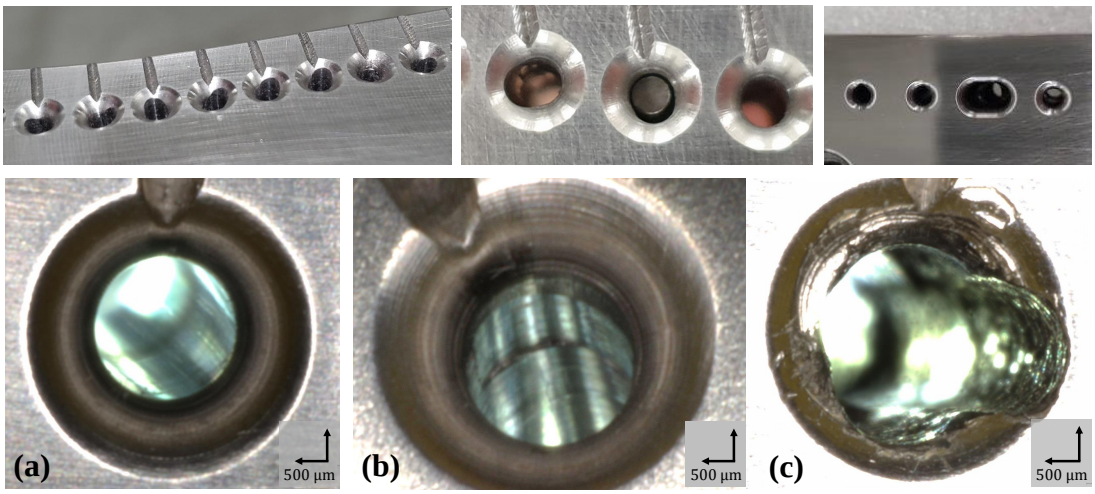

Figure 5.6: Top panel: Examples of physical flaws and deviations from the intended geometry on both sides of the electrode frame, resulting from manufacturing process errors. Bottom panel: Close-up images of the pin holes. (a) A hole with a smooth inner surface, deemed to be of good quality. (b) A hole with an edge on the inner wall, which could potentially damage the inserted wire. (c) A damaged hole with distorted geometry and a hazardous surface exposed to a high-field region. The open surfaces of similar holes were later manually polished, but the inner wall surfaces remained untreated.

elongated or enlarged holes. Some wires were broken during the pin insertion process, unlike the test mentioned in subsection 5.1.3, which used a segment sample of the frame with the same design. With the monolithic nature of the electrode frame, it is challenging to repair or remanufacture the frame. This should be taken into account for future generation detectors, which have twice the diameter of the frame.

Three solutions were implemented to mitigate the situation. First, the rough surfaces exposed to high voltage——i.e., those not located within the pin holes—were locally and manually polished using sandpaper and grinding cords.

Second, the entire frame underwent an additional electropolishing to further smooth sharp edges and rough surfaces. It is also found that electropolishing reduces the chance of breakdown [96].

Thirdly, we produced copper pins (OFHC, 99.99% Cu) in five different geometries and diameters so that at least one could hold the wires in place. The primary geometric difference among the pins was the presence or absence of a head (see Figure 5.7). In most cases, the elongated holes had a smaller diameter or a more favourable geometry on the opposite side of the frame due to the two-sided machining process. As a result, headless pins could penetrate deeper into the hole, thereby providing effective wire retention.

It was expected that the absence of a head should also reduce the electrostatic field around the pin, as the head has a sharper geometry. A 3D local field simulation was performed to confirm the effect of the pins on the field (Appendix C). The result showed that the field above the copper pin head for the pin with head (Pin H-) was

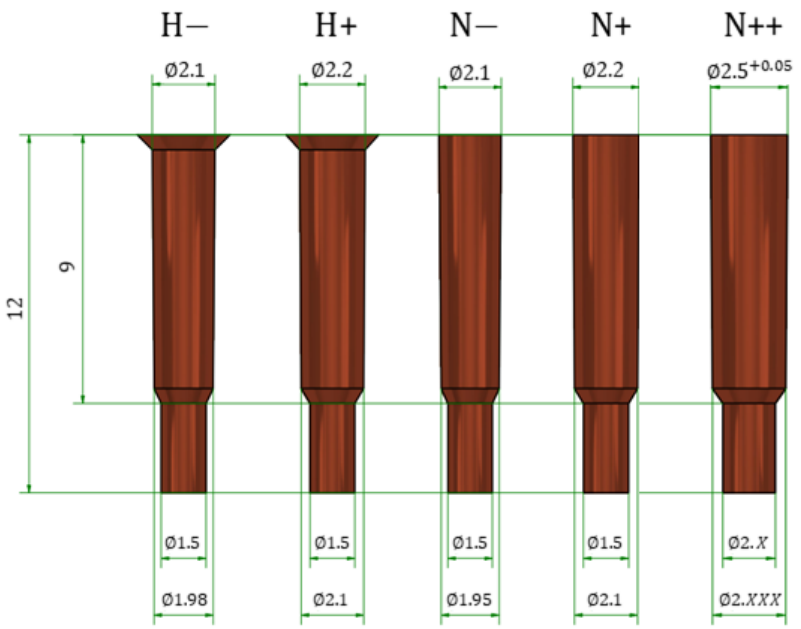

Figure 5.7: Different types of pins used for the anode electrode. All dimensions are in mm. Pins labelled "H" have a head, while those labelled "N" do not. The clipping parts of the pin, which exerted most of the force to fix the wire in place, were approximately 9 mm in length and had a conical shape. The "++", "+" and "-" signs indicate the maximum diameter of the clipping part of the pin to be 2.5, 2.2 and 2.1 mm respectively. The remaining part of the pin, which had a thinner diameter, was the extension that held the pin in place right before the insertion process.

around 4 kV/cm higher than the case with the "headless" pin (Pin N-). Therefore, from an electrostatic perspective, headless pins are more favourable.

From this focused local simulation, it was also shown that the side edge of the wire groove, hereafter referred to as the *groove edge*, and the wires exhibited the highest field magnitude. In other words, the groove edge is the limiting factor of achieving a low electrostatic field in this design, but not the pins. Nevertheless, the actual value is likely lower than the simulated value due to additional rounding from electropolishing. These regions are also fully covered by the PTFE insulation to suppress the likelihood of breakdown. Nevertheless, for next-generation electrodes, these groove edges should be designed with rounded or filleted profiles to reduce the local field.

5.3 Assembly Procedure

As pointed out in [92, 109, 110, 168], the previous common strategy of mounting parallel wires onto the electrode frame was a challenging and iterative process. On the other hand, the shorter the assembly time, the better, to limit the exposure of the wires to ^{222}Rn in air. Otherwise, the plate-out of ^{222}Rn daughters from the wire surfaces during operations would contribute to the radioactive background [92].

The challenge was due to the coupling between the elastic SS frame and the many SS

wires, in this case, 265 of them. This makes the system a non-linear complex system, for which an iterative process is typically required. Additionally, the non-uniform load from the parallel wires caused the frame to deform anisotropically. According to the internal experience of the previous wire installations, the frame was first externally deformed. Throughout the wire installation, the frame's shape was constantly monitored and re-shaped accordingly so that the wire tensions could stay at the desired values. For an even larger electrode, a new installation method is needed to reduce the installation steps and time needed for a full assembly, as well as human error and inaccuracy during the process.

In this work, we developed a new set of tools and procedures for a robust parallel-wire electrode installation, as shown in Figure 5.8. Essentially, we deformed the electrode frame to the final equilibrium shape before mounting the wires. The deformation was held by an external structure that kept the frame roughly in shape throughout the wire installation. Finally, the assembled electrode was dismounted from the station.

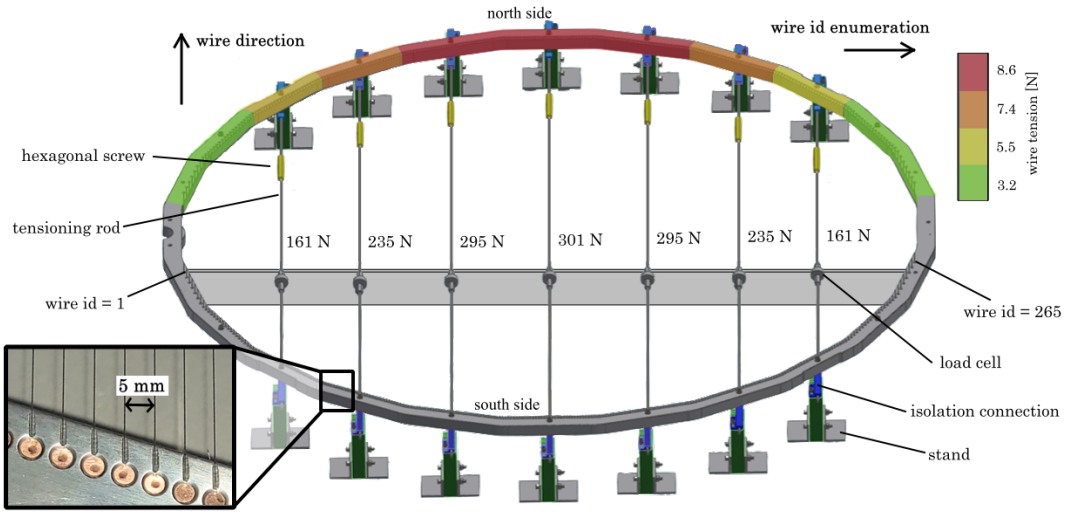

Figure 5.8: Schematic drawing of the wire electrode frame mounted onto the tensioning system. The colour on the electrode frame indicates the target tension of the wires in each section. The tensioning system underneath the frame consists of the tensioning rods that hold the ring, with the hexagonal screw changing the length and the load cells that measure the axial tension on the respective tensioning rods. The band underneath the load cells limits the lateral load on the load cells. The stand supports the whole structure, and the isolation connections allow movements and relaxations of the ring and the tensioning rods relative to external anchors. The indicated coordinate system was used during the assembly for clarity and to reduce errors and documentation. The inset shows the picture of the assembled electrode, where individual wires are separated in 5 mm and fixed by copper pins.

The more detailed procedure is as follows. First, during preparation, we assembled seven tensioning rods to deform the electrode frame. Each tensioning rod consisted of three 5 mm-diameter SS rods, sandwiching a brass hexagonal screw and a load cell. The hexagonal screw adjusted the length and thus the tension on the tensioning rod. The load cell then measured the tension on the rods. Each tensioning rod was mounted onto two stands on each side through an isolation connection, such that the stands had the freedom to move in a relative longitudinal direction. Secondly, seven sets of tensioning rods and stands were prepared on a table with a rough relative po-

sition of the electrode frame, parallel to the wire direction. The stands, apart from the central one, could move in longitudinal and lateral directions. Thirdly, the electrode frame was mechanically coupled to the tensioning rods with screws. Since the stands could move freely on the table, the frame and the tensioning rod were decoupled from external anchors. Therefore, by reducing the length of the tensioning rods with the hexagonal screw, the electrode frame was pulled into the final equilibrium shape as if all the wires were mounted. The required tension on each rod is calculated by FEA, as shown in Figure 5.8.

When tuning one rod, the tension on the other rods also changed non-linearly. Therefore, it is still an iterative process, which took around half a day to reach the required values within $\pm 10\,\mathrm{N}$ altogether. Compared to the previously known procedure, this reduces the complexity of optimising the tension on the 265 wires and the ring to only seven tensioning rods. After tensioning the frame and before installing wires, we waited a few days for the whole system to relax.

During installation, the shape of the electrode frame has limited change from wire installation due to the stiffness of the tensioning rods. The wires are installed with their target tension values as indicated in Figure 5.8. With custom-made tools, we tensioned the wire on both ends through the pin hole and fixed the wire using copper pins.

A laser measurement system pioneered in [169], updated and fabricated by [170] was used to measured the axial tension. The working principle is as follows: A laser[1] is shone onto a tensioned target wire, where the tension is to be determined. For each measurement, a wire vibrates as GN2 is blown from a nozzle. A photodiode subsequently measures the scattered laser on the wire to determine the normal modes of the vibration. The frequency of the first harmonics ν_f can then be related to the axial tension of the wire by [19]:

$$\nu_f = \frac{1}{2L_0}\sqrt{\frac{F_{ax}}{A_0 \cdot \rho_{ss}}}, \tag{5.6}$$

where L_0 is the undeformed length of the wire, F_{ax} is the axial tension on the wire, A_0 is the undeformed area of the wire, and ρ_{ss} was taken at $8000\,\mathrm{kg/m^3}$ for the density of the SS316 [112, 157]. Given the large number of wires, to monitor tension more efficiently and reduce human error, I further developed an automatic scanning algorithm for the system, which was equipped with a motor rail, enabling it to scan a continuous array of wires. From the axial tension, we could obtain the expected wire deflection during the detector operation using Equation 5.4.

If we assume the tensioning rods are perfect rigid bodies, after all the wires are installed, all the load on the tensioning rod will be transferred to the tensioned wire to hold the frame in the final shape in equilibrium. In reality, there was some net force

[1] Laserfuchs spot laser. 650 nm, class II with 0.75 mW, 3 V DC, dimension 10×22 mm, focus adjustable. Adjustable focus is useful to obtain a sharper signal.

component remaining between the tensioning rods and the frame. Therefore, there were screws at the end of each rod to release the remaining tension and decouple the tensioning system and the frame. The frame was removed from the tensioning system.

5.4 Quality Assurance

In the following section, the electrode, that is, the wires, the frame, and the copper pins, together with the assembly procedures, were tested to assure the quality of the final assembled anode that can satisfy our scientific requirements:

- maximum of 0.5 mm wire deflection
- limited frame deformation as predicted
- sturdy wire fixation that does not lead to wire breakage

5.4.1 Test Assembly

The test assembly took place at Karlsruhe Institute of Technology (KIT) in a non-cleanroom environment, with the procedure described in section 5.3. No parts were cleaned or degreased beforehand except for the copper pins, as will be discussed further later.

We monitored the tension of all mounted wires using the mentioned laser measurement system during and after the assembly. The force on the tensioning rods was also monitored using the load cell attached to them (see Fig. Figure 5.8). Figure 5.9 shows the results from this test installation, including the tension values, the estimated deflection after all the wires, and the time trends of selected wires. From the plot, the final tension is centred around the target value both before and after dismounting the electrode from the tensioning system. The maximum deflection of each wire is mostly less than 0.5 mm in this test installation.

In the lower plot of Figure 5.9 between the long time gap between 2023-11-22 and 2023-12-01, the electrode was transported forth to Johannes Gutenberg University Mainz (JGU) and back to KIT, showing that the axial tension of the selected wires remained steady after transportation. In fact, all measured wires retained their tension within the measurement error after the transportation.

Frame Deformation

The deformation of the frame was measured by a FaroArm® (4-meter long 7-axis Quantum^{M}) [171, 172] during the test installation as listed in Table 5.4. Note that the deformation was referenced to the measurements before deformation, but compared to the CAD drawing. This is because the actual geometry of the manufactured frame also deviated slightly from the CAD drawing, and it is highly affected by how the frame was placed in the laboratory for measurements.

After all the wires were installed, the frame deformed slightly upward along the wire direction and slightly downward across it. The unevenness of the frame increased from 0.43 mm, with no wires installed, to 0.73 mm, with all wires installed and the

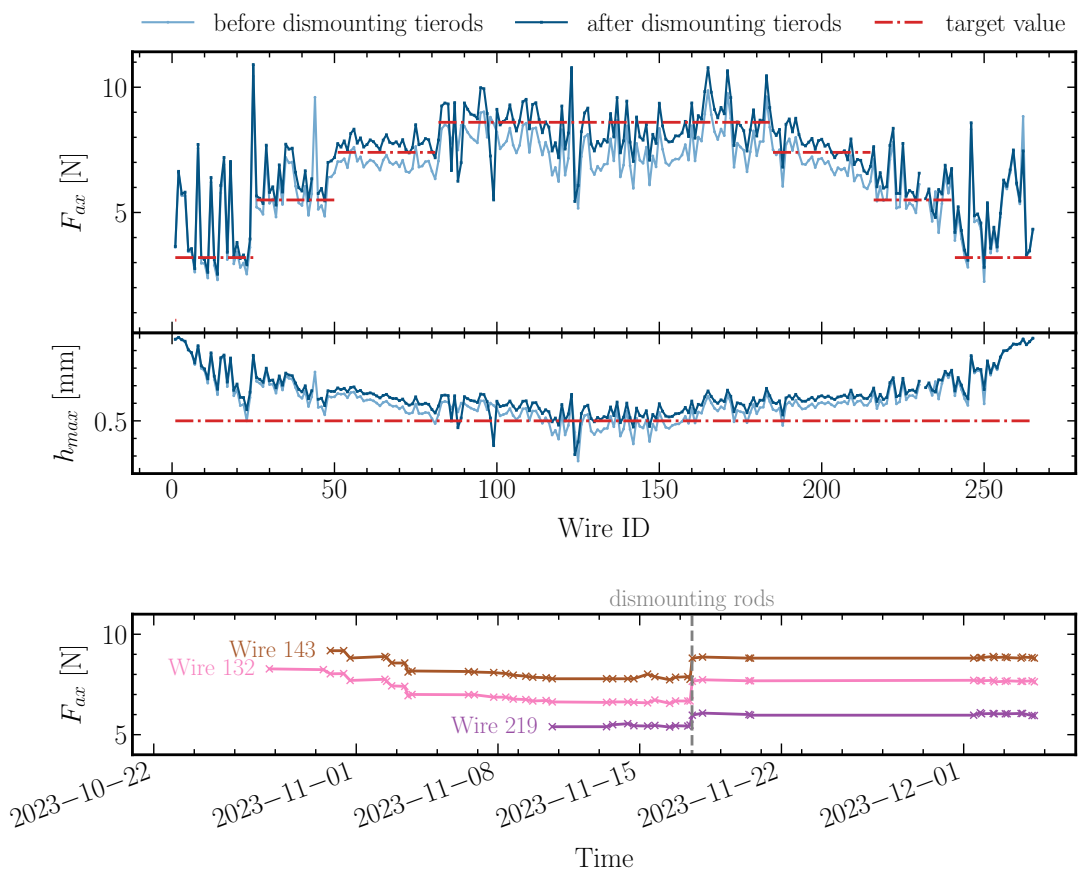

Figure 5.9: Top panel: Wire tension and resulting expected wire deflection across all wire IDs before and after dismounting of the tensioning rods. The wire ID notation is defined in Figure 5.8. The red dashed lines indicate the target tension of the wires. Bottom panel: Wire tension over time of selected wires. The black dashed line indicates the time when the tensioning rods were dismounted. Figure adapted from [1].

Table 5.4: Deformation of the electrode frame derived by FEA simulation and from measurement with FaroArm® at different stages of the assembly. The deformation parallel and perpendicular to the wires is shown in the second and third columns, respectively. All measurements with the Faro Arm have an uncertainty of 0.24 mm.

	Deformation [mm]	
Status of the Frame	$\parallel$ to wires	$\perp$ to wires
Only Tensioning Rods installed		
simulation	4.46	-4.48
measurement	4.26	-4.34
diff. (simulation - measurement)	0.20	-0.14
Fully assembled and rods dismounted		
simulation	4.44	-4.41
measurement	4.48	-4.35
diff. (simulation - measurement)	-0.04	-0.06

rods were dismounted. Concerning the planar deformation, as shown in Table 5.4, the measured values were in good agreement with the FEA simulation in subsection 5.2.1

within an error of 0.24 mm. This error originates from discrepancies between measurements taken on the bore of the hole and on the side surface of the frame. In principle, both methods should yield identical deformation values; however, the use of uneven and non-identical surfaces led to small differences. Thus, the error is attributed to the measurement surfaces rather than to the FaroArm® itself.

It is not listed in the table in Table 5.4, but the transportation to JGU and back to KIT results in sub-mm changes in the geometry in all directions, which is negligible compared to measurement uncertainties. This again demonstrated that the electrode remained sturdy against vibrations and forces due to inertia.

Discussion

There are a few additional observations. First, halfway through the installation, we realised the copper oxide layer of the copper pin unpredictably increased the wire tension values when we pressed the copper pins into the pin hole. This explains the wide range of wire tension deviating from the target value in Figure 5.9. Later trials with cleaned pins significantly reduce the difference between the installed tension and the target tension.

In addition, since the tensioning rods are not perfectly rigid, the tension on the wires reduced as we inserted more wires. Examples are shown in Figure 5.9. The earlier the wire was installed, the greater the reduction, with the maximum drop of $\sim$2 N. Since the installation started from the middle of the electrode towards the sides, the tension of most wires in the middle sections fell below the target value. To mitigate this, we increased the target axial tension of the central 3 sections of the 24-gon from 8.6 N to 9.2 N for the final installation to ensure that the maximum wire deflection can be kept below 0.5 mm after dismounting the tierods. The safety factor from 0.01% permanent deformation becomes 1.5 compare to Figure 5.4 The increase in frame deformation would be increased by 0.2 mm from the FEA simulation, which is still within tolerance to be compatible with the rest of the TPC components. For the future generation parallel-wire electrode, one can use thicker tensioning rods to increase the stiffness of the tensioning system and mount the wires from the outermost wires towards the centre.

Another observation is that the tension for all wires increased after dismounting the electrode from the tensioning system, with the maximum of 1.1 N. One possible contribution is from the non-zero pulling tension remaining on the tensioning rods, of around 300 N. After dismounting, the electrode frame extended backwards and stretched the wires. We also monitored the total tension gained by the installed wires, ΔF_{wires}, and the total reduction in tension in all tensioning rods, ΔF_{rods}, which should be the same in an ideal case.

5.4.2 Pull Test

As mentioned, the stress acting on the wire from the groove tip and copper pin fixation was not quantified and was potentially significant. During the test installation, wires in certain holes were more susceptible to breakage, likely due to sharp edges at the

groove tip. To quantitatively and systematically assess and measure this, a “pull test” was performed after shipping back from Mainz. Based on the result of the test, we further polished the frame and repeated the test.

To perform the test, all the installed wires were first cut in the middle. A wire was then tied to a force gauge[2] while it was still fixed by the pins on one side. The wire was then pulled at the force gauge along its length until it broke. At the same time, the force gauge was recording the maximum force from the wire, with the instrumental error of 0.1 N. The test was repeated for all the wires and holes.

From the results, most wires broke at around 30 N, consistent with the UTS in subsection 5.1.3. However, some wires broke at a lower force and broke at the groove tip. This is likely due to the plastic deformation and damage done by the groove tip on the wire during the pin installation. Figure 5.10 shows the different fractures on the wires as they broke, captured using a digital microscope[3]. The ductile fracture happened at the groove tip, indicating additional damage to the wire, creating a weak point for fracturing. The wires that did not break at the groove tip exhibited necking fracture.

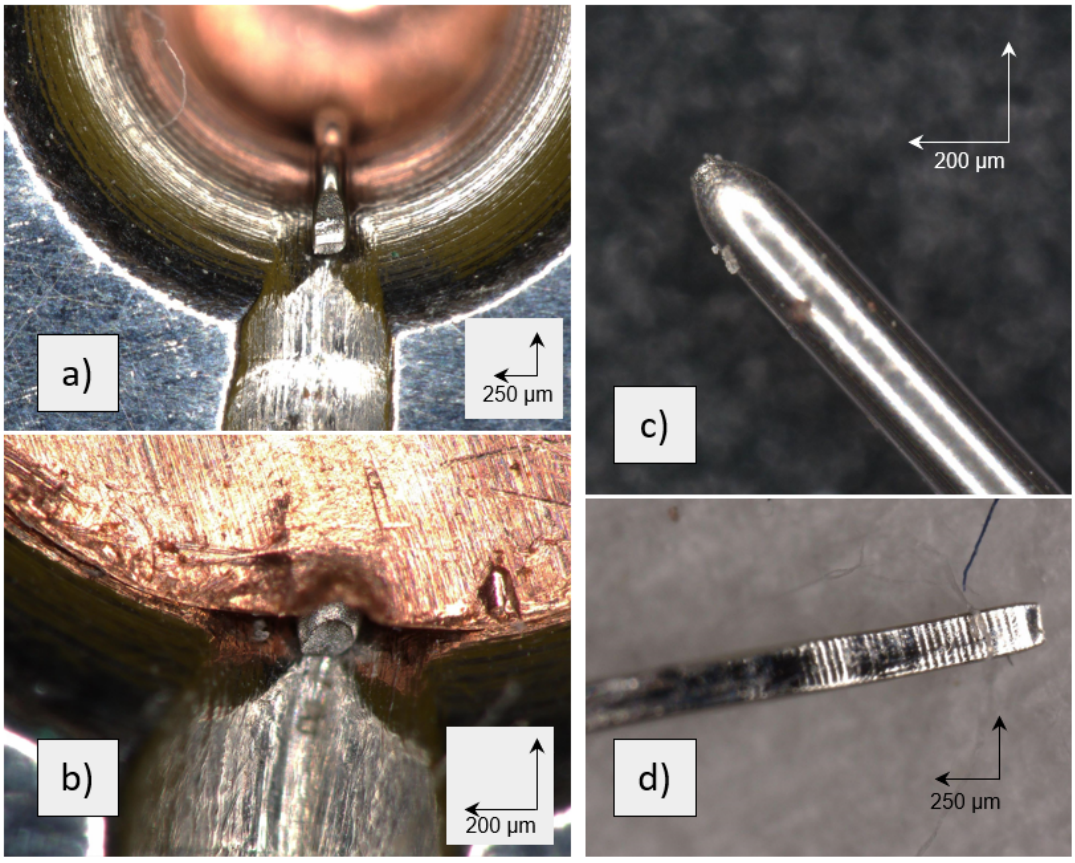

Figure 5.10: Photos of wire breakage. Photos (a) and (b) show two examples where the wires broke at the groove tip. (a) was installed with a headless pin, while (b) was installed with a pin with a head. (c) is a necking fracture on the wire, and (d) is a ductile fracture.

[2]Brand: Sauter. Model: FK 100.

[3]Brand: KEYENCE. Model: VHX-7000 digital microscope. Lenses: VHX-E20 / VHX-E100 / VHX-E500. Mobile camera: VHX- Z20R.

To reduce the stress on the wires, we manually polished the edge of some of the groove tips with a grinding cord the second time, especially where the wires broke at the groove edge or at a stress much lower than 20 N. Since the grinding introduced rough surfaces and possibly degraded the HV performance of the electrode, the frame subsequently underwent the second electropolishing. The pull test was then partially repeated for a subset of holes, with the result shown in Figure 5.11. For simplicity, only the data points with the maximum force less than 21 N before treatment are shown. Some data points have large uncertainties because the values were not properly recorded and had to be estimated qualitatively based on the force experienced while pulling. From the result, most of the wires reinstalled showed the UTS back to beyond 30 N after the treatment. One of them had a lower value, but it was likely due to measurement error. Repeated measurement with new wires on the same hole showed the UTS greater than 30 N. This indicates that the frame after the treatment is more reliable against overloading the wires and early wire breakage compared to before the treatment.

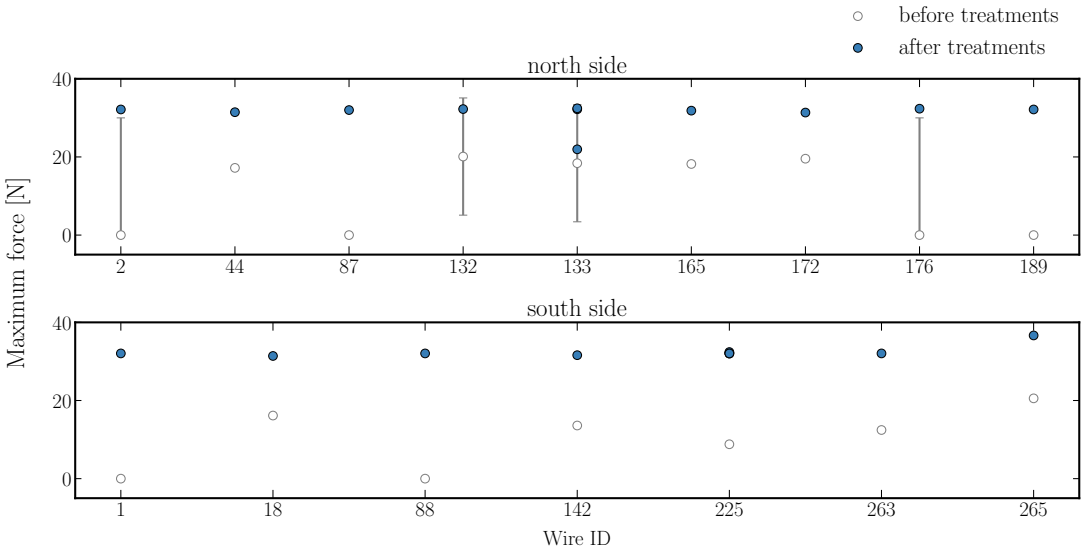

Figure 5.11: Results from the pull test. The top and the bottom plots correspond to the north and south sides, as indicated in Figure 5.8. The data points indicate the maximum force recorded for the wire ID. The hollowed points were the measurements before the grinding and electropolishing treatments, while the filled blue points were the measurements after the treatments.

5.5 Final Assembly and Handling

As the requirements were met after a few iterations and improvements, all parts were ready for the final assembly. All parts of the electrode (the wire, the frame, and the copper pins), as well as the tools, were extensively cleaned.

For the wire, a new spool of wire from the same batch, which had been extensively tested and certified for use, was prepared for the final installation. They were wound onto a frame specially designed for cleaning and standby. A fresh batch of copper pins with different sizes and geometries, as in Figure 5.7, was also prepared for the final installation.

For the frame, the following summarises all the treatments performed on it from manufacturing up until the final installation in a cleanroom environment at Laboratori Nazionali del Gran Sasso (LNGS):

- manually grinding all the grooves of the frame at MPS
- first electropolishing at MPS
- test assembly and quality assurance (transportation and HV test)
- manually grinding some grooves, given the result of the pull test
- second electropolishing at MPS
- localized and manual electropolishing
- cryogenically treated the frame with LN_2
- cleaning

Note that we cryogenically treated the frame with LN_2 before installation. This was to further relax the mechanical stress built up during the machining and handling of the frame before wire installation [173]. Otherwise, if the mechanical stress is only released after wire installation, the axial tensions of the wire might reduce, as is the case for the original XENONnT electrodes. It was done by immersing the frame segment by segment in the LN_2 bath, and subsequently left to warm back to room temperature. There will be more discussion on this in section 5.7.

Cleaning Electrodes

Proper cleaning of all components introduced into the TPC is crucial, since impurities increase the background rate and absorb signals, thereby degrading the detector's sensitivity. This requirement is particularly stringent for electrodes, where surface contaminants such as dust can also trigger unwanted electron emissions and even electrical breakdowns.

Passivation improves the electrical performance of electrodes and suppresses electron emissions, which otherwise contribute to the background events of the detector [96, 97, 110] (see also section 3.2). A common passivation method is to immerse degreased SS samples in a nitric or citric acid bath. The acid removes impurities, the native oxide layer, and corrosive compounds, enabling the formation of a new oxide layer under controlled and clean conditions. This regenerated layer exhibits an enhanced chromium-to-iron ratio, which is more chemically stable.

Since citric acid also has demonstrated promising results in suppressing electron emission [97, 110] and is easier to handle than nitric acid, we adopted citric acid for passivating all SS electrode components. However, based on internal experience, operating an ultrasonic bath with citric acid was found to increase the surface roughness of the SS wires. To mitigate this effect, the ultrasonic bath was used only during the initial 10-minute acid cleaning and switched off for the subsequent passivation step.

The overall cleaning procedure for the SS parts of the anode is briefly summarised below. They were first degreased with HARO soaps and then rinsed with deionised water. This was followed by a 10-minute acid cleaning (with ultrasonic bath) and a 50-minute passivation using 7% citric acid at around 40°C. Finally, the SS parts were

thoroughly rinsed and dried by blowing nitrogen. Similarly, for the copper pins, they went through steps of degreasing with Decon® acid rinse, passivation for 15 minutes, rinsing, and drying.

Wire Tension

The final wire tension after the installation is shown in Figure 5.12. As in the case discussed in subsection 5.4.1, the wire tension increased by around 1 N after releasing the tierods.

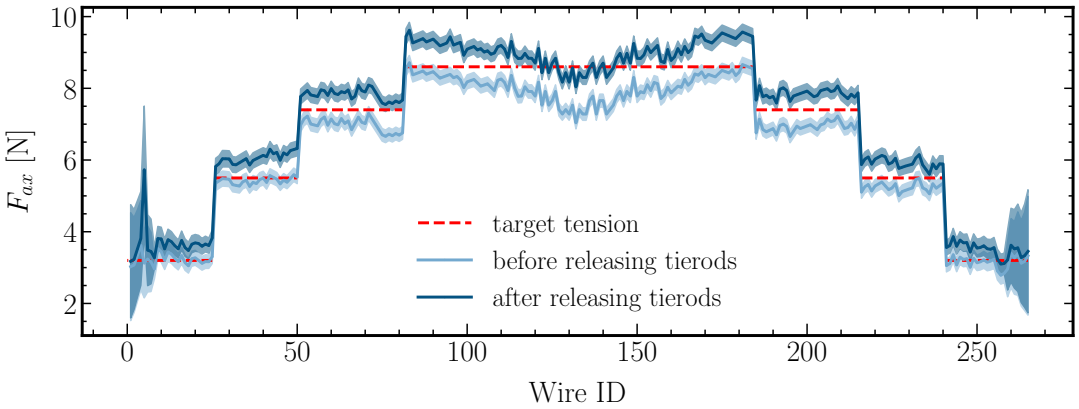

Figure 5.12: The wire tension after installation in the cleanroom.

Frame Deformation

As mentioned, the axial tension of wires on the centre 3 sections increased from 8.6 to 9.2 N. Therefore, the nominal value of deformation from the FEA calculation is −4.62 mm (4.64 mm) for the direction parallel (perpendicular) to the wire direction. The average values measured were −4.57 mm (4.54 mm) ±0.24mm. The error is due to the geometrical uncertainty of different surfaces used to evaluate the deformation, as mentioned in subsection 5.4.1.

The ring also deforms in the z-direction from the FaroArm® measurement. Due to this z-direction deformation, the overall unevenness increased from 0.39 mm to 0.86 mm. Note that the unevenness of the surface that the ring is lying on was not calibrated; nevertheless, the difference between the two numbers should cancel out the effect. The changes in the unevenness were slightly greater than the one quoted in subsection 5.4.1 (from 0.3 mm to 0.47 mm), which was expected due to the increased axial tension of the wires in the central segments.

Discussion

During installation, we encountered a problem when mounting the cleaned wires onto the cleaned frame. Initially, the wires could not be tensioned beyond 6 N, a limitation not observed in previous generations of detector since the wires had never been tensioned to this level. After a series of tests, we hypothesised that the issue arose from attractive forces between two clean metal surfaces of the same material at the atomic

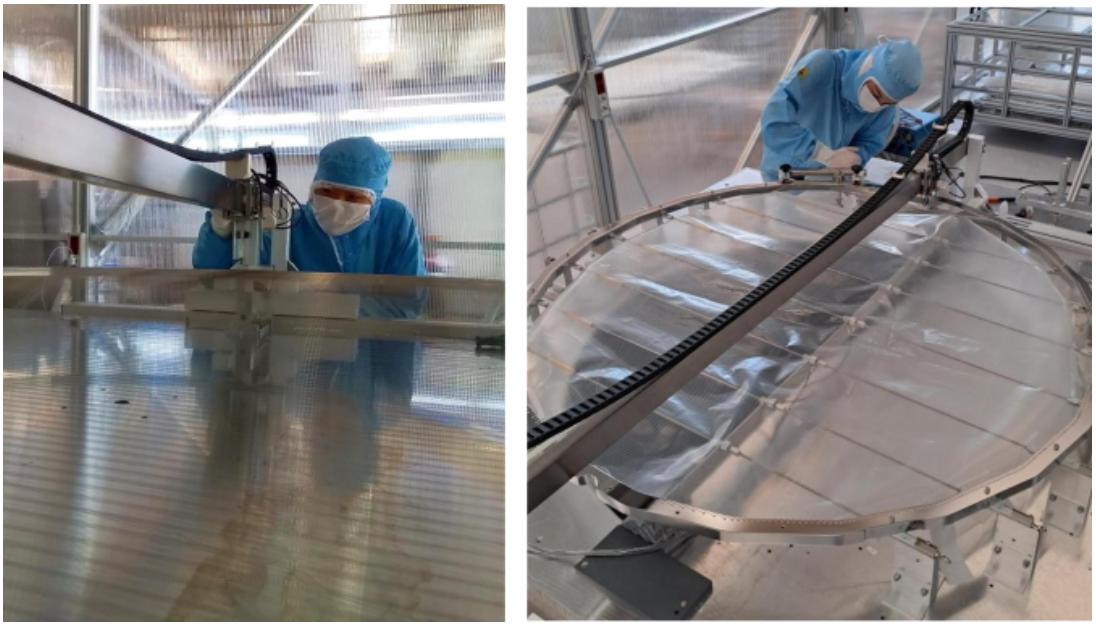

Figure 5.13: Photos of assembly. Left: adjusting the laser measurement system for the gate electrode. Right: installing the wire and inserting the pin for the anode electrode. Plastic cover on top of the tierods to prevent wire damage or kinks during installation.

level. This effect, also exploited in cold welding, occurs once a certain pressure threshold is exceeded. This effect, occurring only after a certain pressure threshold, is also the working principle used in the cold welding technique.

The problem posed two challenges for installation: first, the wire could become stuck and fail to reach the target tension; second, conventional lubricants such as grease could not be used due to radiopurity and cleanliness requirements. To address this onsite, we dripped ethanol into the grooves to act as a temporary lubricant. In addition, the wires were slightly tensioned and released to help them slide more smoothly into the desired tension. This combined method proved effective and was systematically applied throughout the entire installation campaign.

For future parallel-wire electrodes, it was suggested to use different SS grades for the wires and the frame to mitigate this issue. For example, using SS316 wires for their lower electron emission rate, and SS304 frames, which are already covered by PTFE insulators.

5.6 Quanlity Control

After completing the full installation of the electrodes in the cleanroom, they underwent the final quality control step to ensure the quality of the final production.

5.6.1 The PANCAKE test

An XLZD-scale testing facility at the University of Freiburg, PANCAKE, was adapted to test the XENONnT upgrade electrodes at 173 K [174]. The campaign aimed to emulate the relevant operating conditions of XENONnT to assess the reliability of

the electrodes. The assembled anode, gate, and cathode were all tested together in the PANCAKE setup, placed in an open-topped vessel with a flat floor. The gate and cathode (excluding the frame) were separated by only 3 cm, compared to about 1460 cm in the actual TPC. The temperature difference between the wires and the electrode frame was limited to 20 K, as the open-topped container was filled with LXe. The liquid level was positioned between the anode and gate electrodes. High voltage was applied such that the resulting fields between the electrodes were comparable to those in XENONnT. By the end of the test, the electrodes had undergone a complete thermal cycle, including cooling, submersion, and warming back to room temperature. Further details of the setup and results are provided in [174].

5.6.2 Gate Electrode

Before discussing the result, the following summarises the gate electrode properties and assembly for completeness and for later comparisons.

The gate electrode was assembled in the summer of 2021 and was essentially a replica of the original XENONnT design, with a few minor modifications. To minimise wire tension loss after cooling cycles, the frame was annealed and mechanically relaxed during manufacturing, just as the anode electrode was. In addition, the axial tension of the central segments was increased by 1 N, so that any reduction after cooling would still limit deflection to an acceptable level. The choice of 1 N was based on previous experience, where the tension was reduced by around 1 N after the cooling cycle [19]. This adjustment was further motivated by the fact that relaxation effects diminish with successive cooling cycles and that the TPC would undergo only a limited number, if any, of such cycles.

After the assembly, the gate electrode was stored in a custom-made storage box purged by gaseous nitrogen for years to avoid accumulation of ^{222}Rn. The wire tension was measured again in early 2024 to see if the tension had reduced during the few years of storage using the laser measurement system described in section 5.3. No significant deviations were observed. Then it was shipped together with the assembled anode and cathode to the University of Freiburg for the PANCAKE test. The results together with the anode electrode will be discussed in the following subsection.

As shown in Table 5.2, the total load on the gate electrode wires is around a third of that for the anode electrode. That was because the field is lower in the liquid phase, and the downward gravitational force on the wires partially cancels out the upward electrostatic force. In addition, the wire deformation of the gate electrode has a lesser effect on S2 signal amplification and signal shape. Therefore, the deflection requirement was less stringent for the gate than for the anode, resulting in lower axial tension. This also justified the less extensive tests on the gate electrode.

5.6.3 Final Result

The difference in the axial tension before and after the PANCAKE test of both the anode and the gate is shown in Figure 5.14. The significant deviation for Wire ID 1 for the gate was likely due to measurement error, due to the short length of the wire,

and the limited space for the laser measurement. While the anode wires did not show any significant reduction in the axial tension, the tension of the gate wire significantly reduced, with a maximum of 1.4 N for the wire at the centre segment. This translates to around 0.2 mm increase in the deflection. The expected maximum wire deflection, given the load in Table 5.2, amounted to 0.6 ± 0.3mm. Nevertheless, the amount of tension reduction is close to expectation, and the expected wire deflection is still within tolerance.

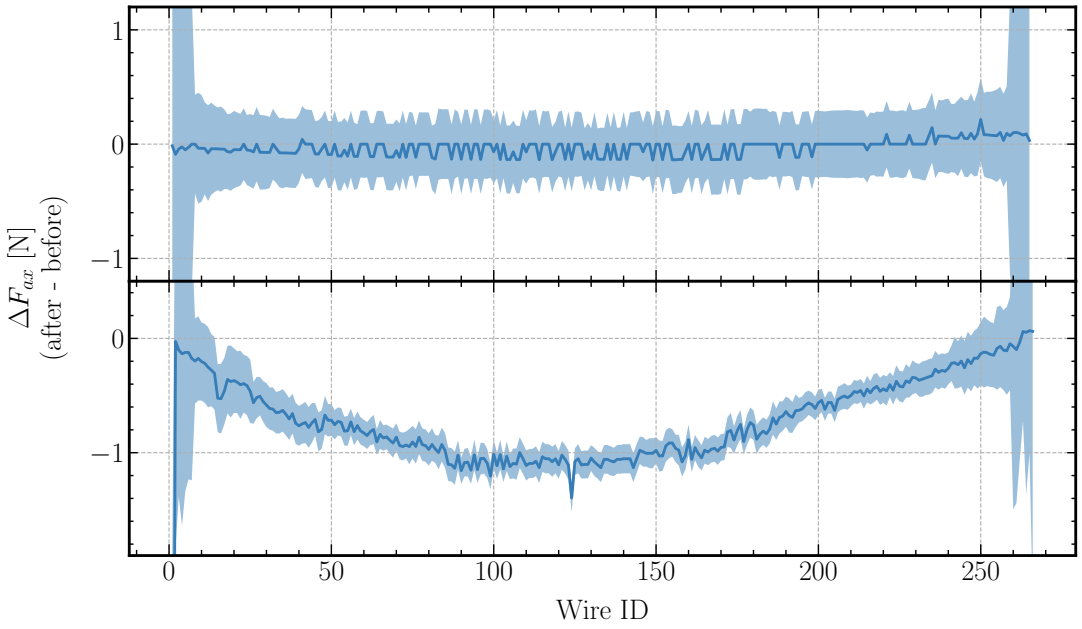

Figure 5.14: The difference in wire tension before and after the PANCAKE test in LXe temperature. The top is for the anode, while the bottom is for the gate electrode.

Relaxation after the cooling cycle could be problematic for the TPC as the tension on the electrode might be significantly reduced, increasing the sagging and thus affecting the signal response, like the original XENONnT electrodes. From this result, the difference in results between the anode and gate may provide insight into how to effectively limit the relaxation of the electrode after cooling cycles. Several possible explanations were considered.

Both frames were fabricated from SS316L slabs supplied by Nironit and machined by MPS [167], and both sets of wires were SS316 manufactured by CFW. Although the materials were not from the same batch and their properties (e.g., YTS) may differ slightly, this can hardly account for the observed discrepancy. The specific YTS of the gate wires was not measured, but general values for annealed SS316 wires are ∼241 MPa [165]. With a pretension of 4 N, the stress should remain well below this limit. Moreover, if the wire tensions or frame stresses had exceeded the YTS, a reduction would already have been observed after long-term storage. Likewise, the differences in stress due to the differences in frame dimensions also seem insufficient to explain the results.

Localised overstress at the groove tips of the gate electrode is similarly unlikely, as this would produce isolated deviations, as seen during the test assembly, rather than

the systematic trend shown in Figure 5.14. Long-term storage of the gate is also an unlikely cause, since tension measurements before and after storage showed no significant change. Additionally, their installation procedures differed slightly: the gate frame underwent iterative deformation during wiring, while the anode was pre-deformed to its equilibrium geometry during installation. However, the connection between this difference and the observed relaxation remains unclear.

A more plausible explanation lies in the additional relaxation step applied only to the anode frame. Both frames were annealed before the final machining step to reduce internal stresses, though some residual stress likely remained. Prior to the wire installation, the anode frame was cryogenically treated by immersing small segments sequentially in liquid nitrogen and then allowing the entire ring to warm to room temperature overnight. The gate frame did not undergo this process. This treatment likely released residual stresses in the anode frame, thereby minimising relaxation during cooling cycles, similar to the standard cryogenic treatment for metals [173].

For future-generation electrodes, particularly if monolithic or large mechanical support frames are adopted, comparable relaxation procedures should be applied after manufacturing and before installation to ensure stable electrode tension through cooling cycles.

After all manipulations, the wire tension of both the anode and the gate was measured again. From the measured values, the final expected wire deflection for the anode and the gate is shown in Figure 5.15. Note that no feedback effect was considered, as it was expected to be small given the higher wire tension.

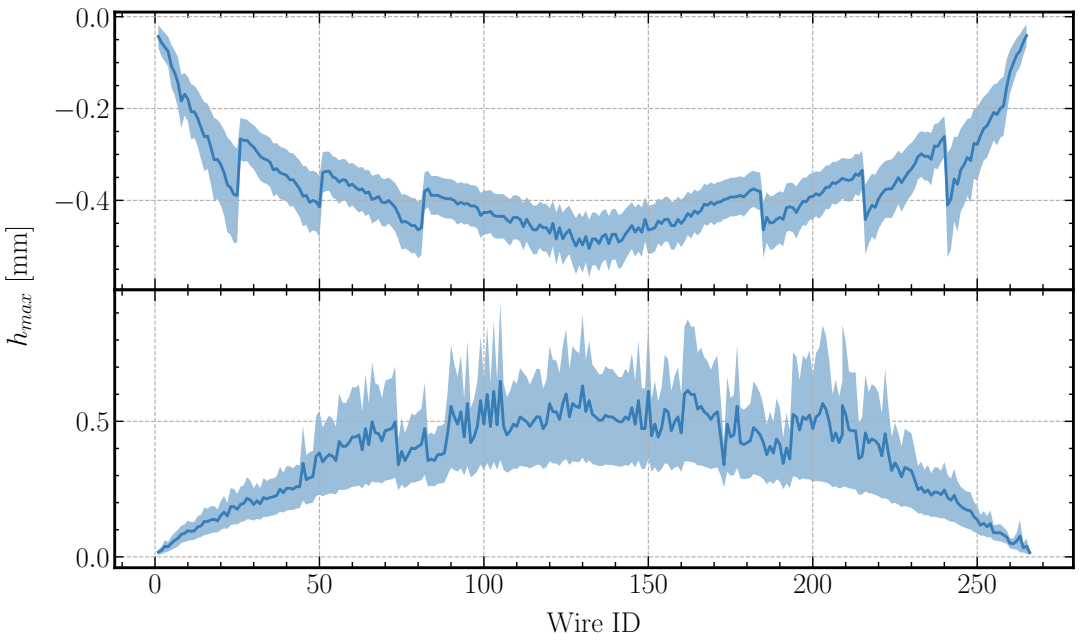

Figure 5.15: The estimated wire deflection of the anode and the gate electrode based on the final wire tension measurement. The top is for the anode, while the bottom is for the gate electrode.

5.7 Lessons Learned from the XENONnT Parallel-Wire Electrode

We have conducted a series of simulations and tests to ensure a reliable electrode design with sufficient safety margins. Our new installation method also reduces the complexity of installing the parallel-wire electrode while remaining reliable. Nevertheless, there are additional challenges or further R&D needed to realise the next-generation electrode with 2.6–3m, should a parallel-wire design be considered.

One problem that would be common to the existing design of future generation electrodes would be the relaxation of the internal tension in the electrode frame after a cooling cycle, which reduces the wire tension and increases the sagging as mentioned in subsection 5.6.3 and [19]. This effect should be more apparent for a larger monolithic electrode frame, which might explain why it was not reported before, and more severe for parallel-wire electrodes than for woven-mesh or etched mesh electrodes. It is expected to affect the future generation electrode as well, not just the parallel wire electrodes. In addition to annealing the frame during the manufacturing process, we also found that cryogenically cold cycling the frame before wire installation might help to further release the tension. Further investigation into the causal relationship and tests with additional samples could confirm this observation. Regardless of the method, future generation electrodes should ensure that they release this internal tension before wire installation. After the installation, a test with a full cooling cycle should be carried out.

Another issue common to the existing design of parallel wire frames is the saddle shape of the frame, as pointed out in [109]. The design with the wires on top of the frame (both for XENONnT and PandaX-4T electrode [107]) would inevitably create a z-component of force to the frame, resulting in a chip or saddle shape profile after full installation. Although a thicker frame can alleviate the effect, it increases the difficulty of manufacturing and the radioactive background due to the additional material. For future detectors, a ”counter-frame” can be fixed on top of the assembly electrode to reduce the saddle shape formation. Such an equipotential cover can also remove the high localised field from grooves in general or the welding spots in the case of PandaX-4T.

An elliptical ring, as the one demonstrated by PandaX-4T, could be a good solution to further reduce the material of the electrode frame. With the capability for an accurate FEA simulation, the geometry can be designed such that the final equilibrium shape of the electrode is close to a perfect circle. The advantage is that the stress on the frame is more distributed, rather than having a localised weak point or stress hotspot. In this case, the electrode frame can be made thinner.

As mentioned in subsection 5.2.2 and Appendix C, the groove edges would be a limiting factor to lowering the field on the electrode frame. In case of future design, if an equipotential cover or insulators do not cover the grooves on the electrode frame, the frame should be designed such that the groove edges are smoother or rounded to reduce localised high fields. Note that if only insulators are used, such as PTFE, there

is still a risk that a strong breakdown could establish a permanent path through the PTFE or insulating material. The risk of breakdown scales with the stress area of the electrode [97], so it would become a higher risk in the future. Therefore, adding an equipotential cover with smooth surfaces should also be considered.

One of the advantages of the parallel-wire electrode, often mentioned, is the ease of repair and manufacturing feasibility. However, from the endeavour described in this work, one often neglected factor is the challenge brought by the monolithic electrode frame. Compared to the etched mesh, the parallel-wire electrode frame involves more substructures at a sub-millimetre scale within the meter-scale frame, such as the wire grooves. Specifically, in the case of XENONnT, the faulty machining of the pin holes was severely lengthening the testing and fabrication time. On the other hand, a monolithic electrode frame is favourable for reducing mechanical complexity and risks to structural integrity. Possible solutions to this dilemma could include designing with a thinner frame or conducting R&D for sturdy composite rings.

Concerning the wires, the current safety margin for annealed SS316 does not accommodate significantly larger electrodes. Therefore, if we use the same type of material, a thicker wire is anticipated, which means a reduction in optical transparency, see section 5.8 for more discussion. Another possibility is to have a new wire fixation mechanism that avoids bending the wire by $90°$, allowing the design to accommodate harder but more brittle wire candidates. For example, PandaX-4T fixes the wire by glueing it with epoxy or clamping the wires using copper plates.

On a related note, experiences suggest that the copper pin fixation should be avoided. First, it creates unpredictable, non-linear stress on the wire as it was bent and pressed at 90°. Second, it requires delicate craftsmanship, making it difficult to automate.

Additionally, it was suggested to use different SS grades for the wires and the frame to mitigate this issue. For example, using SS316 wires for their lower electron emission rate, and SS304 frames, which are already covered by PTFE insulators. This is expected to be specific to the copper pin fixation, or a similar kind. In the case of an installation method like PandaX with epoxy, this should be less of an issue.

5.8 Parallel-wire Anode for XLZD

This section evaluates the feasibility of using parallel-wire electrodes for XLZD, with particular emphasis on the anode, which has the most stringent requirements in terms of optical transparency and mechanical sagging. At present, no final decision has been made regarding the electrode design for XLZD. Possible options include parallel-wire arrays, hexagonal-etched meshes, or woven-wire meshes, with the final choice driven by both performance and feasibility considerations. The study presented in this section provides a fundamental input to the electrode design of the XLZD project.

When considering the optimal anode wire diameter, one might expect that thinner wires are better to maximise LCE. However, reality is more complex. First of all, the thinner the wire, the less axial tension can be applied, and the more it will sag.

The more the sagging, the less uniform the single electron gain (SEG) (see subsection 5.1.2 for more) over the horizontal plane. Thinner wires can sustain less axial tension, increasing the sagging under electrostatic force: this reduces the uniformity of the SEG (subsection 2.1.3) in the (x,y) plane. Secondly, the more the wires sag, the stronger the field between the wire and the liquid-gas interface, which increases the electroluminescence yield. Meanwhile, the shorter drift path reduces the creation of electroluminescence. Thirdly, the thinner the wire, the less light would be blocked by the wire itself. Therefore, the direct effect on the S2 signal is also unclear. If all of these factors are considered, it is hard to tell which wire diameter is preferred and what sagging level is acceptable.

It boils down to the question, what is a feasible wire diameter, and correspondingly, the relation to the S2 signal or the SEG. Then, we can also inquire about the reduction in LCE in case we need to use thicker wires. To address these questions, I identified the one parameter that cannot be arbitrarily changed and is the same for all wire diameters. It is the material strength of the wire. In subsection 5.1.3, I performed the tensile test measurements for different wire candidates. Weighing in factors such as surface quality and ductility, we preferred the annealed SS316 from CFW over the harder wires. The minimum measured YTS at 0.01% offset was 445 MPa, which is independent of wire diameter (see also Table 5.3). Consider this value, and a safety factor of 1.5 from plastic deformation, as well as subtracting the thermal stress of 75 MPa assuming a temperature difference to be 25 K, then a maximum allowed axial stress on the wire was calculated to be 222 MPa, valid for wire of different diameters. This value is the premise for the whole study.

Then, for different wire diameter, the applied axial tension applied to the wire varies due to the changing cross-sectional area. On the other hand, the load from the electrostatic force, weight, and buoyancy also changes according to equations in subsection 5.1.2. From the two information, the maximum sagging was determined for each wire diameter, including the feedback effect from the electrostatic force. Subsequently, for each wire diameter with different sagging values, I estimated the amount of photons produced by a single electron using empirical formulas, defined as the SEG. The shadowing effect was also estimated by neglecting all the reflection and secondary photon propagation effects. Eventually, I obtained the estimate SEG as a function of wire diameter.

Several assumptions were made to simplify the model. Here I only considered the longest wire of the anode, which was set at 2.6 m, with the lowest point of sagging in the middle (i.e., the centre of the horizontal plane). I also kept the gate wire diameter constant at 0.3 mm. This is assumed because the gate wires have less effect on the SEG compared to the anode wires. The load on them is also smaller than that of the anode, so thinner wires are likely still a viable option for the gate wires. Also, the pitch of both the anode and gate wires is not changing. For a final design, this parameter should be optimised. However, for a fair comparison, this number remains unchanged.

The anode and the gate are assumed to be biased at $+6.5$ kV and -1.0 kV, respectively, same as the XENONnT designed values. And the initial gap length between the anode and the liquid-gas interface was set at 4.04 mm. For the feedback effect, I assumed

the electrostatic force to be uniform along the whole wire, and considered the entire wire to sink by h_{max} amount instead of having the sag profile. This overestimated the electrostatic force, resulting in sagging, but it can be treated as a conservative value. The deflection of the gate wires also contributes to the feedback effect of the anode wires [19], but it is also not considered for this study.

Additionally, for the shadowing effect, I assumed that the SS wire is 100% opaque. It is likely to be lower, but the exact number from the literature is inconclusive in the cold xenon environment. Also, the ring deformation caused by the wire tension was not considered, because it was shown that there are ways to mitigate it.

5.8.1 The Feedback Effect

The initial sagging for all wire diameters was assumed to be zero, and the central axis of the wires was kept the same. Then, a 2D axially symmetric COMSOL simulation, same as in subsection 5.1.2, was used to calculate the electrostatic force on the wires. The load, ω_{el}, was obtained by averaging the force measured on three wires at different radial positions r away from the centre – more details in subsection 5.1.2. This is defined as the *0th iteration* of ω_{el}. The load from weight and buoyancy, ω_g and ω_b respectively, was also calculated for each wire diameter, but they do not change with sagging. As mentioned, the maximum stress allowed on the wires was calculated at 222 MPa. The stress multiplied by the cross-sectional area of the wire yielded the maximum axial tension force on the wire. Then, using Equation 5.4, the *0th iteration sagging* was calculated, as shown in Figure 5.16.

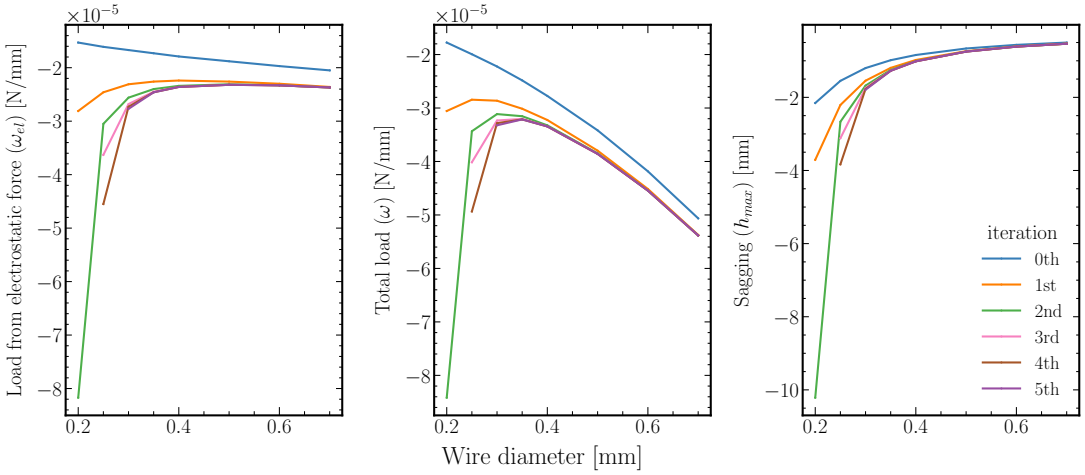

Figure 5.16: Iterations to obtain the converged sagging values for different wire diameters. Left: load from only the electrostatic force (ω_{el}). Middle: the total load from the electrostatic force, the weight and the buoyancy (ω). Right: maximum sagging (h_{max}) using the assumed F_{ax} and the load from the middle figure. There are a total of 5 iterations as labelled.

The calculated sagging was used to update the simulation geometry in the COMSOL simulation and recalculate the new ω_{el} for the subsequent iterations. For wire diameters of 0.2 and 0.25 mm, the sagging diverged after a few iterations, indicating they are would snap under the electrostatic force and are unlikely to be viable options for the XLZD-scale parallel-wire anode. So they are not considered for the remaining

steps of this study. Subsequently, field maps for each wire diameter and the associated sagging were produced by the same 2D axial simulation from COMSOL.

5.8.2 Electron Path

As explained in chapter 2, when the extracted electron propagates through GXe towards the anode, it excites the xenon atoms, which subsequently emit electroluminescence photons along the drift path. The number of photons emitted along the path can be estimated by the empirical formula [59, 75, 175]:

$$\frac{dN_{ph}}{dl} = A \cdot N_e(l) \cdot \left(\frac{E(l)}{p} - B \right) p, \tag{5.7}$$

where N_{ph} is the number of photons produced, l is the position along the drift path, dl denotes the differential path length, $N_e(l)$ is the number of electrons, E is the field strength that changes along the path, p is the pressure in atm (or bar), and both A and B are empirical parameters determined by experiments. Physically, A can be interpreted as the amplification factor, and B can be the threshold of the reduced field E/p to produce proportional electroluminescent photons [75]. I am using the result from the measurement of $A = 151 \pm 19$ photons/e$^-$/kV and $B = 0.97 \pm 0.13$ kV/cm/bar [59, 176].

To estimate the SEG, the number of electrons extracted from the liquid-gas interface $N_e(l = 0) = 1$, without loss of generality. As the electron drifts along its path, it may have sufficient energy to ionise atoms, releasing more electrons. This happens only in high field regions, typically beyond 14 kV/cm in GXe in our operating conditions [59]. Accumulatively, the number of electrons produced at a certain point l' along the path is given by:

$$N_e(l) = \int_0^l \alpha(l')\, dl', \tag{5.8}$$

where $l = 0$ denote the location of the liquid-gas interface, and α is the first townsend coefficient of ionisation. This coefficient is parametrised by the reduced field, which depends on the pressure [177]. Given the pressure at around 2 atm and temperature at 180 K, the coefficient can be simplified to [177, 178]:

$$\alpha(l) \left[\mathrm{cm}^{-1}\right] = 1.39 \times 10^4 \times \exp\left(-\frac{53.2}{\sqrt{E(l') \left[\mathrm{kV/cm}\right]}} \right), \tag{5.9}$$

For the numerical integration, the step sizes $dl \rightarrow \Delta l$ were chosen at 0.0001 mm, as it was checked that the discretisation error becomes negligible from this step size. For the first-order estimation, the field line was used as the drift path of the extracted electron, meaning the diffusive motion was not considered. The field line started from the same lateral position as the wire ($r = 336.25$ mm), as shown by the example in Figure 5.17 (right). This is because the anode and the gate are off by half of the pitch, so the extracted electrons are focused by the gate wires to the position right below the anode position, spanning a radius of 0.1 mm (Figure 4.7). Electrons propagated

from 0.1 mm away from $r = 336.25$ mm resulted in reduced light production, but the difference caused by this was found to be smaller than the difference caused by the wire diameter. Therefore, the following only consider the electron started at $r = 336.25$ mm, right below the anode wire.

Note that in the example in Figure 5.17, the field close to the wire is above 40 kV/cm, which is well beyond the ionisation threshold of gaseous xenon [179, 180]. However, since the high field region is very localised, the additional number of electrons produced on average due to ionisation (Equation 5.8) is only 0.03 in this example, far less than 1. This means that the number of electrons cannot be effectively multiplied, let alone causing a breakdown. More will be discussed in subsection 6.4.2.

For comparison, the same calculations were performed for the wires without any wire sagging, with all wires centred 4.04 mm from the liquid-gas interface. The numerical differential photon production per unit length, $\Delta N_{ph}/\Delta l$ (see Equation 5.7), is shown in Figure 5.17 for illustration. The plot also shows the calculation with the consideration of the shadowing effect, which is explained in the following subsection.

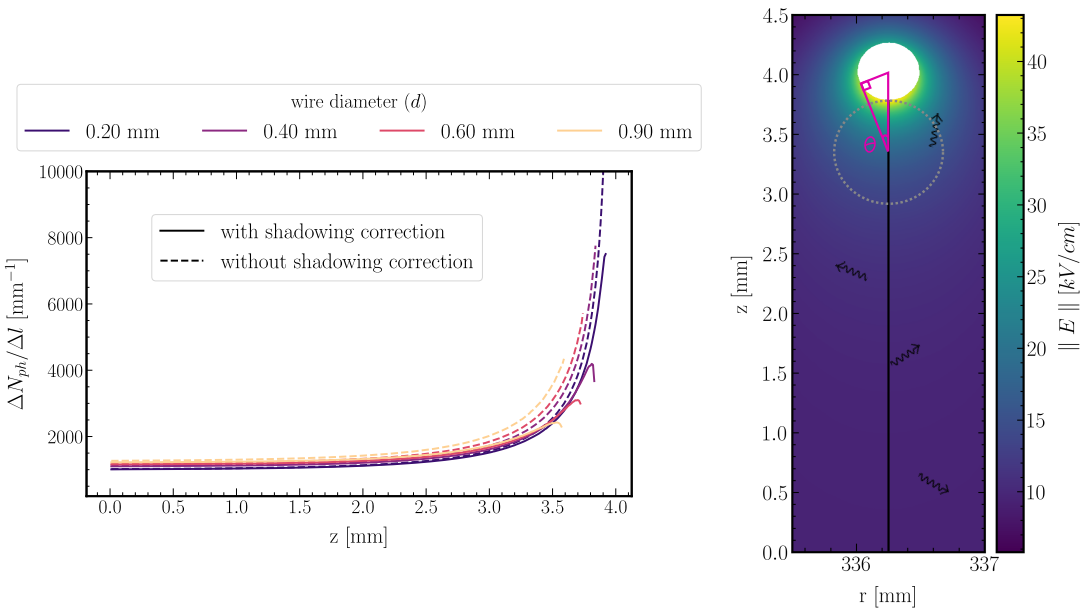

Figure 5.17: EL production calculation for the case without wire sagging. Left: differential photon production. Right: field map and the field line for the path integral, with wire diameter of 0.5 mm. The liquid level is right at the bottom of the domain. The trigonometric calculation of the solid angle is drawn in magenta lines.

5.8.3 Shadowing Effect

One can observe in Figure 5.17 (dashed lines) that the majority of the light is produced beneath the wire where the electric field is the highest. However, the closer the photon is produced near the wire, the more the light is obstructed by the wire. The reflectivity of SS wire at LXe temperature was not directly measured, but it showed a quick drop below room temperature in vacuum, down to 35% at 0 °C [82]. The current best guess and value used in simulation is at 30% [83]. To simplify the calculation, it was assumed that the SS wire is not reflective at the LXe temperature.

Given that the drift path is a straight line below the anode wire, the light blockage by the wire was calculated as follows. Let the distance between the photon emission position, l, and the bottom edge of the wire be denoted as r_{ph}. This distance also defines the minimum distance at which a photon emitted at position l can intersect the wire. Assuming isotropic photon emission at position l, a photon propagation sphere of radius r_{ph} can be defined. For each step in l, the angle θ between the line connecting the emission point to the tangential edge of the wire and the line connecting the centre of the photon propagation sphere to the centre of the wire was calculated, as illustrated in Figure 5.17 (right). Photons contained within the spherical wedge span by an angle 2θ were assumed to be completely blocked by the wire. The corresponding solid angle fraction of the spherical wedge is given by θ/π. The shadowing correction factor $S(l)$ at each position l was therefore defined as the fraction of photons not blocked by the wire, namely $S(l) = 1 - \theta(l)/\pi$. This factor can be applied as a multiplicative correction to the right-hand side of Equation 5.7. In reality, photon propagation also involves reflection and other microphysical processes. A full optical simulation, for example, using the GEANT4 package, would be required to account for these higher-order effects.

5.8.4 Result

The final form for the total number of photons produced, also known as the the EL photon yield, with numerical integration is:

$$N_{ph} = \sum_{i=1}^{n} A \cdot N_e(l_i) \cdot \left(\frac{E(l_i)}{p} - B \right) p \cdot S(l_i) \cdot (l_{i+1} - l_i), \tag{5.10}$$

where n is the n^{th} segment of the path length when the field line reaches the wire.

To compare this amplification factor with experimental data, other detector effects were added to account for the number of photons detected by the photosensors [19, Chapter 6]. Since the produced photons might escape or transmit away instead of reaching the PMTs, the factor LCE obtained from optical simulation was used to correct this effect. In GXe it is around 23% [19], which is usually lower than that in LXe due to the absence of total internal reflection. Note that the LCE should also depend on the wire diameter, but the dependence is expected to be small as it is dominated by other factors, such as the photosensor coverage, the geometry of the TPC and the coverage of the PTFE reflectors. For those photons reaching the PMTs, there is a certain probability that a photoelectron is emitted at the photocathode inside the PMT, named the QE. In the LXe temperature, the QE of the PMTs is around 30% [35, 84]. Around 20% of the time, known as the double photoelectron emission (DPE) probability, two photoelectrons are created at the photocathode instead of one [181]. Among them, around 90% of them can reach the first dynode for the signal multiplication in a PMT [86]. This is called the collection efficiency (CE). For this simplified model, the EL photon yield N_{ph} is multiplied by all these correction factors to obtain the estimated SEG:

$$\text{SEG} = N_{ph} \times \text{LCE} \times \text{QE} \times (1 + \text{DPE}) \times \text{CE}. \tag{5.11}$$

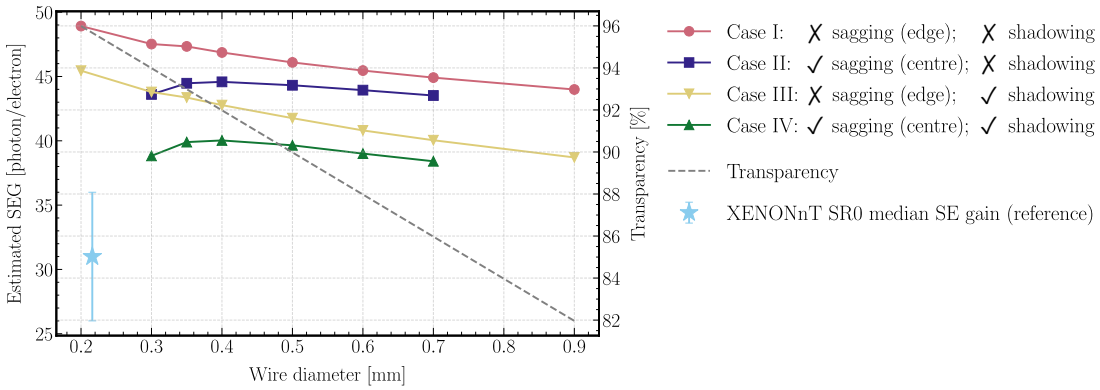

Figure 5.18: Estimated single electron gain (SEG) vs wire diameter for different cases. The corresponding optical transparency was marked with a dashed line. The XENONnT reference point was the median of the SEG map, taken from [99, Figure 13], where the error bar corresponds to the range of the colour map.

The results with and without sagging, and with and without shadowing corrections, were calculated and shown in Figure 5.18. The SEG from XENONnT science run 0 data [99] was added to the plot for comparison. Due to the slightly different field configuration (subsection 2.2.1), the value from XENONnT is not directly comparable to this study for the case of XLZD. Still, the compatible result demonstrates the validity of this simplified model.

Generally, the SEG drop with thicker wires, but not by a substantial amount. At the same time, in Cases II and IV, the SEG dropped if the wire diameter is thinner than 0.35 mm due to more sagging. When comparing Case I and Case III without sagging, the difference is due to the correction of the shadowing effect. The difference due to the correction is more significant for thicker wires, as expected.

In addition, consider the cases ”without sagging” (i.e., Cases I and III) as the wires at the *edge* of the electrode, where sagging is minimal. The cases “with sagging” (i.e., Cases II and IV) indicate the place with the strongest sagging, that is, the *centre* of the electrode. The difference in the values between the centre and the edge can be understood as the measure of SEG non-uniformity across the horizontal plane. From Figure 5.18, the difference in SEG between the edge and centre is larger for thinner wires. The same conclusion can be drawn whether or not the shadowing correction is applied. This is expected, because the thicker the wire, the less sagging, as shown in Figure 5.16, and thus a more uniform SEG across the horizontal plane.

When the sagging effect and the approximated shadowing corrections are taken into account, that is Case IV, the wire with a diameter of 0.4 mm achieves an SEG of 40.0, which is the highest among the considered wire diameters. The relative difference between the centre and the edge is 6.9%, which is lower than that of a 0.35 mm diameter wire at 12.8%, indicating improved signal response uniformity. The optical transparency is 92.0%, which is comparable to the values reported for the XENONnT [35] and LZ electrodes [110]. These results also show that the sagging of the wire has a major impact on the SEG. The dependence of the shadowing effect correction on the wire diameter is relatively minor.

5.8.5 Conclusion

Although assumptions and simplifications were made for this study, they are justified. The results were also in the correct order compared to experimental data. Therefore, the conclusion from this study can provide a first-order assessment on the feasibility of a parallel-wire electrode for XLZD.

The key idea of this study is that material strength is a parameter that is difficult to alter or optimise, unlike wire diameter, bias voltage or the pitch. At the same time, the material strength is independent of the wire diameter, unless the difference is by orders of magnitude. Meaning that the maximum axial tension one can apply to a thinner wire is less than that on a thicker wire, leading to different wire deflection. Therefore, for a fair comparison between wires of different diameters, I set the material strength at a fixed value as the premise, and use the estimated SEG as the final metric to assess the performance. The shadowing effect was also approximated in this study.

From this study, we first observed that wires with 0.2 mm and 0.25 mm diameters are likely to snap under electrostatic force due to the limited axial tension they can withstand. The exact limit of wire diameter also depends on the hardness and strength of the particular wire used, but the range is limited. Therefore, thicker wires and a more relaxed sagging limit should be considered if a parallel-wire electrode is pursued for XLZD.

On the other hand, there was concern that using thicker wires might result in worse SEG and LCE, which could degrade the performance of the TPC. The result of this study generally follows this trend, but it also shows that the wire sagging plays a significant role in the SEG. Thinner wires sag more due to the limited axial tension, resulting in lower SEG. At the same time, the SEG for thicker wires is still comparable to that for thinner wires. And the transparency of the thicker-wire electrode can be comparable to the current generation experiments. Therefore, *the use of thicker wires should be positively considered for the parallel-wire electrode of XLZD-scale*.

The major concern for a parallel-wire electrode is the structural integrity. A single breakage of a wire would result in a detrimental effect on the operation of the electrode. Note that in this study, the safety factor from plastic deformation was fixed at 1.5, and the safety factor from fracture was close to 3. Additionally, future designs should avoid fixing the wires using copper pins, as pointed out in section 5.7, due to the unaccountable non-linear stress from the pin acting on the wires. With future R&D for alternative wire fixing techniques, such as the use of epoxy or other methods, the structural integrity can be further ensured.

From this study, wires with 0.4 mm diameter seem to be the best option. However, this cannot be concluded from this study, as it might be subject to change due to factors such as material strength, wire pitch, field strength, gate wire diameter, and the gap distance between the anode and the liquid-gas interface, among others. Future studies should be performed to optimise these factors in addition.

Last but not least, with thicker wires, higher axial tension, and a larger number of

wires, the force exerted by the wires onto the electrode frame will increase by at least a factor of two compared to the XENONnT upgrade electrode. In the case of the wire with 0.4 mm diameter, the force can increase by a factor of 6. Therefore, the electrode frame should be carefully designed and optimised to withstand the load from the wires. Possible mitigation might be the use of an elliptical ring, as in PandaX-4T [107], together with a counter frame as mentioned in section 5.7.

Chapter 6

Etched-mesh Electrode

From section 2.1, we can see the importance of electrodes and their effect on the signal. From there, we learned the criteria needed for the electrodes. In chapter 3, an overview of different types of electrode designs was presented and extended to the latest developments in electrodes across various experiments and observations, specifically regarding HV stability and electrode backgrounds. In subsection 2.2.1, section 3.4, and section 4.4, details specific to the XENONnT current and upgrade electrodes were introduced, which set the context for this and the next chapter. Note that this chapter and the previous chapter are complementary to [1].

The previous chapter provided an in-depth discussion of the QA/QC and assembly for a parallel-wire electrode. This chapter focuses on fabricating a hexagonal etched-mesh electrode, with particular attention to ensuring high-voltage performance, supported by quantitative measurements for QA/QC. The reason is that the etched mesh is more prone to abnormal features and asperities than wires, which can lead to electrode-induced backgrounds or even earlier breakdown, with the latter potentially being detrimental to TPC operation. The manufacturing and repair processes for large-scale hexagonal etched-mesh electrodes are also known to be difficult, if possible at all, so overcoming this disadvantage of an etched mesh is another key focus of this chapter. Meshes have a lower risk of structural failure and exhibit less grid deformation, making these positive aspects less of a focus in this chapter.

The chapter is organised as follows. I will first discuss the design and manufacturing of the meshes (section 6.1). The assembly procedure for the mesh electrode is then described in section 6.2 to provide more context for subsequent sections. The quality of the mesh was ensured through iterative testing and repairs (section 6.3). Among the quality assurance steps, the extensive HV test was treated as a separate section for clarity (section 6.4). After quality assurance, the cathode electrode was assembled in a cleanroom, and its final quality was controlled (section 6.5).

While the concepts presented in this chapter are relevant to the next-generation detector, namely the XLZD project, the work was performed on the upgrade electrodes for

XENONnT, which have a diameter of approximately 1.3 m. Experiences and insights were obtained and summarised from the production of the XENONnT cathode for future XLZD mesh electrodes (i.e., approximately $2.6-3$ m in diameter).

6.1 Design and Manufacturing

The hexagonal etched mesh discussed here was produced by photochemical etching of a 0.3 mm thick SS sheet manufactured by PCM Products, Inc. [182]. As mentioned in chapter 3, photochemical etching is a subtractive manufacturing process commonly used for thin SS sheets. It allows the manufacturing of complex-patterned stainless steel sheets with high precision depending on the thickness of the SS sheet. It has been used in various experiments for producing electrode meshes [114, 115].

The general procedures for photochemical etching are described here in the following [183]. The surface of the SS sheet is first cleaned and coated with a photoresist. Then, the photoresist is exposed to UV light through a mask of the desired geometry. Depending on the type of photoresist, the exposed part becomes more soluble or harder. Then an alkaline solution can wash away the softer or more soluble part of the photoresist, while the remaining part adheres to the SS sheet. Since the photoresist is resistant to the acidic etching chemicals, the non-covered part of the SS sheet is subsequently etched away upon the application of the etching chemicals, and the protected areas remain intact. In the end, the photoresist is removed from the SS sheet. There might be a final etching step (or post-etching step) to reduce sharp edges from the initial etch [114]. It is well known that no mechanical stresses are introduced during photochemical etching [111].

In our case, hexagonal openings 7.5 mm in size were etched to allow light to penetrate. The drawing and photos of the mesh are shown in Figure 6.1. The edges of each hexagon will subsequently be referred to as the *legs*. The cross-section of the legs is $0.3 \times 0.3\,\mathrm{mm}^2$. Meshes with thinner legs with the dimension of $0.2 \times 0.2\,\mathrm{mm}^2$ were found to be too fragile. These meshes had apparent broken legs and could not withstand the subsequent electropolishing[1] and tensioning. These broken legs can induce a high field and potentially an electrical breakdown due to their sharp ends. Therefore, to gain mechanical robustness, the thicker leg width (0.3 mm) was chosen, despite sacrificing slightly the LCE. Later in [114], it was reported that a mechanically robust electrode with the leg cross-section of $0.127 \times 0.127\,\mathrm{mm}^2$ was manufactured by the same company (see also section 3.3), by using thicker photoresist and skipping the final etching step. Note that no test against electropolishing was reported.

The material used for the hexagonal etched mesh is SS304, as the manufacturer indicated that greater hardness than SS316 was required to withstand manufacturing stresses. While SS304 was shown to have a higher electron emission rate compared to SS316 [96], it was compromised to reduce the risk of having broken legs, which can induce significant electrode backgrounds and potentially cause breakdowns. Note that the etched mesh reported in [114] was made of SS316Ti, with a small titanium content

[1] As mentioned in section 3.2, electropolishing can help smooth the surface and has been shown to reduce the electrode background [96].

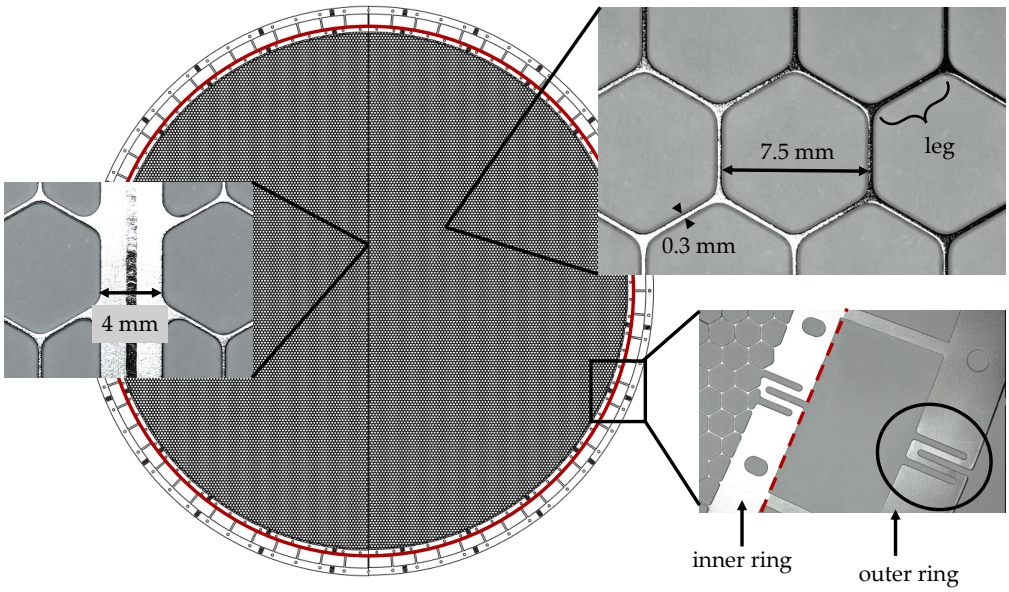

Figure 6.1: Illustration of the hexagon mesh with insets showing close-up images of several locations on an electropolished mesh. The leftmost inset shows the 4 mm wide laser-welded strip and the welding seam in its middle. The upper-right inset displays the dimensions of an individual hexagon in the mesh, with a leg thickness of 0.3 mm and an opening of 7.5 mm. The bottom-right inset illustrates the outer edge of the mesh, with the inner and outer rings designed for stretching and fixation on the electrode frame, respectively. An omega-shaped section on the outer ring is circled in black. The red line indicates the boundary beyond which the structure is intended to be mechanically cut after the installation of the mesh onto the electrode frame (see Figure 6.2 and section 6.2).

that is absent in SS316, which may be worth considering for the XLZD project.

6.1.1 Welded Strip

At the time of design and fabrication, an etched mesh in a single piece with a diameter $D{\approx}1.3$ m was not commercially available (see section 3.3 and [114]). To overcome this issue, two half-meshes were laser-welded together at the centre. The joining edge on each half-mesh is 2 mm wide to facilitate welding and to ensure mechanical stability. After welding two meshes together with a butt joint, a SS central strip 4 mm wide is formed, which will be referred to as the *central welded strip*.

Other methods of joining two half-meshes, such as spot-welding and soldering, were not desired, as they might introduce additional material with high radioactive backgrounds. They were also tested to provide insufficient mechanical stability [114]. The laser-welding technique does not require additional material, minimising the risk of decreasing radiopurity. The ultimate tensile strength of the joint was later tested and found to be well beyond the load exerted on the mesh (see subsection 6.3.4).

It was later reported that PCM Products, Inc. [182] managed to produce etched meshes with the size of 1.5 m [114]. For the XLZD cathode electrode of $D{\approx}2.6$ m, a similar design could be feasible by welding 4 quarter-meshes together with laser-welded strips, at least from a manufacturing point of view.

The effect of the central welded strip on the field uniformity was addressed in subsection 4.4.1. To summarise, the strip enhanced the field in the nearby regions as expected. For the cathode, the field above the welded strip was found to increase moderately, without entering the active volume of the TPC. However, the enhancement makes such a design unsuitable for the anode or the gate due to the $\mathcal{O}(1\,\mathrm{kV/cm})$ field strength and the narrow gap between the electrodes.

According to the CAD drawing, the etched mesh with the welded strip has an optical transparency of 91.42%. Compared to a parallel-wire electrode with 0.3 mm diameter wires and the same pitch of 7.5 mm, the transparent area ratio is reduced by 4.6%, which is still within the requirements and does not significantly reduce the sensitivity for WIMP detection.

6.1.2 Deflection of the Cathode

One of the most significant advantages of the hexagonal mesh is that it distributes load in all directions [114], despite the limited strength of SS sheets being typically lower than that of cold-drawn SS wires (see section 3.1). The deflection of the mesh during detector operation is therefore expected to be moderate even with a limited applied tension.

The deflection and the stress on the cathode mesh were estimated using ANSYS Workbench 2021 [184]. To reduce the computational time, a 2-fold mirror symmetry was applied. Additionally, the leg width and opening were scaled by a factor of 2, whereas the leg height was not. With this scaling factor, the increased mass from the wider leg was offset by the wider opening, thereby keeping the load from the weight constant. A comparison model with a smaller mesh size but higher complexity verified that the mentioned scale factor did not affect the results.

Various loads acting on the mesh were considered for the simulation. The electrostatic force acting on the cathode was estimated (see subsection 4.4.2), where the value of 1.5 N/m^2 was used as the input for the mechanical calculation. The load from the electrostatic force is comparable to the gravitational load, which is determined in the simulation at 1.9 N/m^2. The gravitational loads, thermal shrinkage, and an assumed tensioning stress on the mesh were also accounted for.

Since it was non-trivial to measure and control the tension applied to the mesh [114], the sagging of the mesh under gravitational force h_g was controlled instead. Using the mechanical simulation, the measured h_g was given as the input to calculate the tension applied on the mesh, as well as the mesh deflection h_o during the operation of the detector. If h_g is controlled at 0.6 mm, h_o was calculated at 1.1 mm, which is within the TPC detector requirement.

In this case, the maximum stress in the mesh was found to be 167 MPa, with a 25 K temperature difference between the mesh and the frame. This corresponds to a safety factor of 1.4, assuming the YTS of the material of 240 MPa [112, page 29]. The UTS of the mesh, which is the maximum recorded force measured by a force gauge[2]

[2]Brand: Sauter. Model: FK 100.

until breakage, divided by the cross-sectional area of 0.09 mm^2, was measured to be 600 MPa.

6.2 Tensioning and Assembly Procedure

The details of the assembly procedure are described in [1]. For completeness, the essence of the assembly is mentioned here for the subsequent discussion.

The frame for the etched mesh is an SS ring with a major radius of 1.395 m and width of 20 mm. It was produced and electropolished by Mühlbauer Parts & System (MPS) [167]. The top of the frame is flat, allowing the etched and laser-welded mesh to be placed, stretched by external holders, and secured with SS clamps. A schematic diagram of the frame and the tensioning method is illustrated in Figure 6.2.

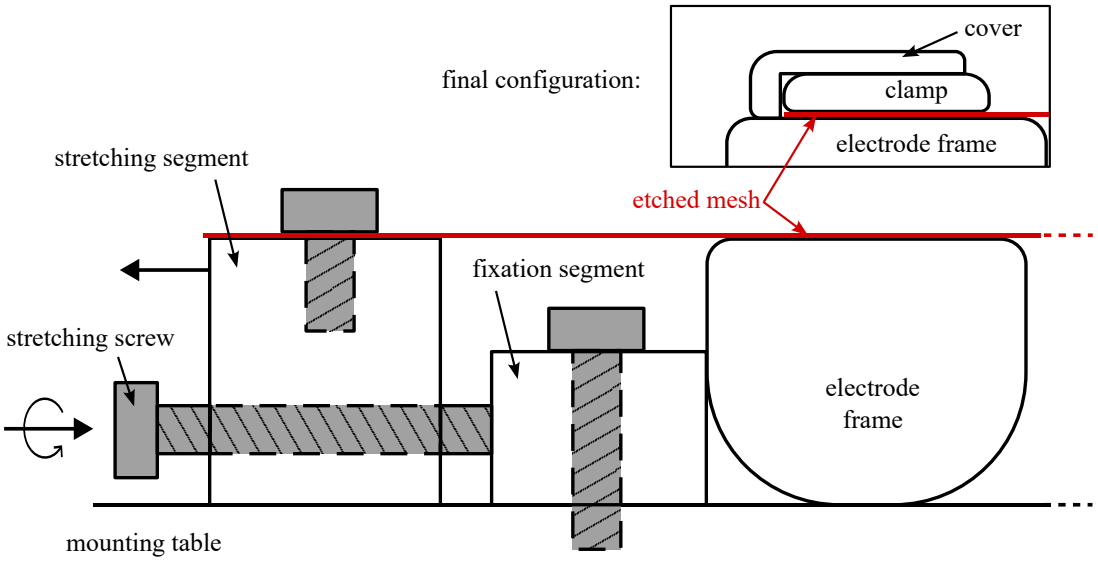

Figure 6.2: Schematic diagram of the electrode frame and the tensioning method. The view shows the cross-section of the setup at the edge of the electrode. The inner part of the electrode is located on the right-hand side and is not shown. The etched mesh is highlighted in red. The objects in shaded grey are screws. The final configuration after assembly is shown in the upper-right inset diagram. The large arrows on the left of the figure indicate the direction of motion. The *stretching screw* was turned inward (towards the right of the figure) such that the stretching segment, together with the etched mesh, moved outward (towards the left of the figure) relative to the electrode frame, which was fixed by the fixation segment.

The laser-welded mesh has an outer and an inner ring for stretching and fixing the mesh to the electrode frame, respectively, as shown in Figure 6.1. During the assembly, the inner ring was lying right on top of the electrode frame, while the outer ring was fixed right on top of the stretching segment in Figure 6.2. The position of the electrode frame was also fixed by the fixation segments, which are secured to the mounting table. During the final assembly, cleaning cloths were placed between the fixation segment and the frame to protect the frame from scratches by the segments.

To tension the mesh, a torque wrench was used to screw the *stretching screw* inward, with the torque of $0.1-0.15$ Nm, such that the stretching segment, together with the

outer ring of the mesh, moves outwards relative to the electrode frame. The 72 stretching screws were screwed inward sequentially for several rounds until the mesh reached the target sagging h_g. Then, the etched mesh was secured to the electrode frame using 24 SS *clamps* and 96 coated SS screws (M4). Initially, silver-coated screws were used, but later replaced by gold-coated screw, explained in section 6.5. Finally, the outer ring is removed by cutting at the connection point to the inner ring (see Figure 6.1). In total, 24 SS *covers* were placed on top of the clamps to cover the sharp edges from the cuttings, fixed by 72 coated screws (M2.5).

The assembly process was first tested at KIT in non-cleanroom conditions, without removing the outer ring. Then, the mesh was stress-tested in an HV environment (section 6.4) before the final assembly in a cleanroom at LNGS (section 6.5).

6.3 Quality Assurance

Two complete etched meshes were laser-welded: one was used as a *sample mesh* and not used in the TPC, the other one was installed in the TPC for the XENONnT upgrade, named the *TPC mesh*. The sample mesh was electropolished before any handling and QA/QC, while the other one was electropolished at a later stage.

For the mesh deflection, the assembled electrode was monitored after the test assembly. Regarding HV performance, the metric used to assess electrode quality was the resistance to electrical breakdown until the desired bias voltage of the TPC was reached. The quality assurance was done in four steps:

1. identifying the imperfections or abnormal *features* that might induce early breakdowns (subsection 6.3.3),
2. repairing the imperfections using the laser-welding technique (subsection 6.3.4),
3. testing the mesh in an HV setup (section 6.4),
4. repeating Step 1-3 to verify the quality of the repaired mesh (section 6.4).

6.3.1 Deflection of the Etched Mesh

As mentioned in subsection 6.1.2, to achieve the sagging during operation h_o of 1.1 mm, the deflection after installation h_g should be less than 0.6 mm. The torque set on the torque wrench affects the final tension and deflection of the etched mesh, which should not be overstretched. As noted, no analytical calculations or simulations were performed to predict the required applied torque for the target deflection. Therefore, it was tested on the sample mesh before the actual assembly.

The h_g was measured by inserting a screw on the mounting table until it just touched the middle of the central welded strip from below (see the right photo of Figure 6.10). Then, the FaroArm® probed the position of the mesh on top of the screw relative to the frame to give the sagging magnitude. With the sample mesh, we used a torque of 0.1 Nm and 3 rounds of tensioning, resulting in approximately 0.5 mm of sag under the gravitational load, corresponding to approximately 1 mm of sag during operation. Under such tension and sagging, no leg breakage was observed, unlike in the etched

mesh with a leg cross-sectional area of $0.2 \times 0.2\,\mathrm{mm}^2$.

6.3.2 Cross-sectional profile and surface roughness

The cross-section of a leg of the mesh was profiled using a KEYENCE microscope[3]. A cutout from the non-electropolished mesh was positioned vertically on the microscope platform with the side of the leg facing upwards. The 3D profile was acquired by scanning the sample in the z-direction, constructing the profile from the focused regions of each image. The profile obtained with the microscope head tilted by 15° is shown in Figure 6.3. The results indicate that the sides of the leg are convex, suggesting a cross-sectional shape more consistent with a hexagon than a square profile. The former shape results in a lower surface field, which is desirable although unintended. The profile also showed substantial corner rounding. However, the degree of rounding appeared to depend on the measurement angle, limiting confidence in the measured curvature of the corners.

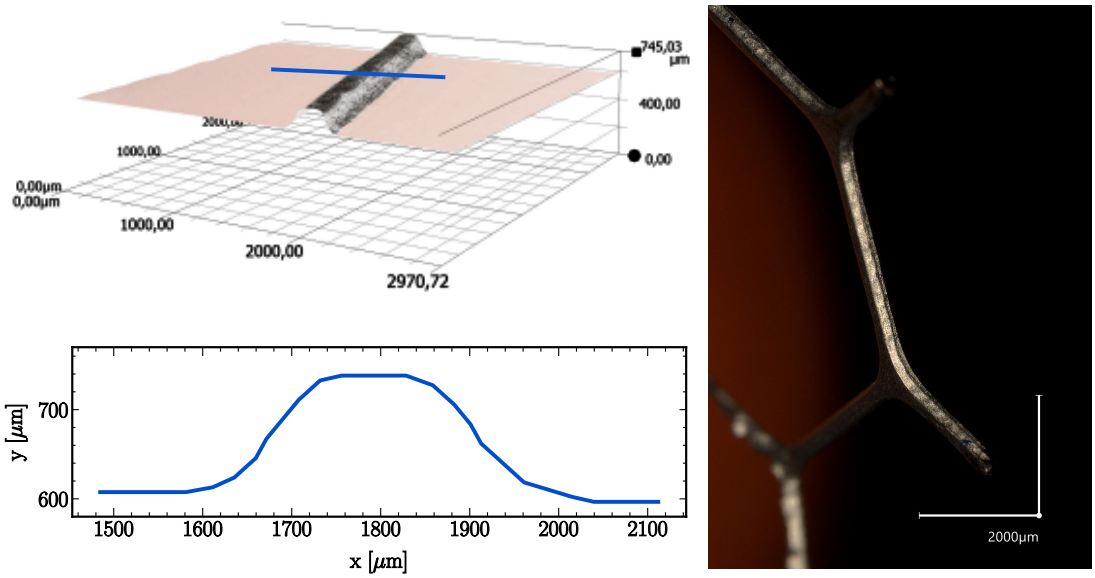

Figure 6.3: Cross-sectional profile of a hexagonal etched mesh leg. Right: zoomed-out view of the measurement sample inclined at the angle used for 3D profiling. Upper-left: high-magnification 3D profile of a leg. The blue line, drawn perpendicular to the leg, defines the cutline for the cross-sectional profile, as shown in the lower-left plot. Lower-left: 1D profile perpendicular to the leg. The x-axis is the distance along the blue line in the upper-left plot. The y-axis represents the profile's height.

The thickness of the mesh legs was measured using a microscope on both electropolished and non-polished etched mesh. The measurements were compared to estimate the change in leg width resulting from electropolishing. The measured values are summarised in Table 6.1. It is important to note that measurements for the electropolished mesh were taken only at the outer region, whereas those for the non-electropolished mesh were scattered throughout the mesh. Due to resistance effects during electropolishing, more material is removed from the outer region than from the inner region. This sampling of measurement points likely introduced an upward bias in the difference between the two mesh types, which was found to be $106 \pm 8\,\mu\mathrm{m}$. Nevertheless,

[3]Brand: KEYENCE; Model: VHX-7000 digital microscope; Mobile camera: VHX-Z20R.

Table 6.1: The thickness of the mesh legs was measured using a microscope on both electropolished and non-polished etched mesh. The measurement error was the standard error of the measurements.

Mesh	No. of legs measured	Average leg width [μm]
Electropolished	6	239 +/- 8
Non-electropolished	19	345 +/- 2
Difference		106 +/- 8

from the trial tensioning, we observed that the reduction in thickness did not compromise the structural integrity of the mesh.

The surface roughness, R_a, was measured using a stylus-type profilometer. Since the profilometer could damage the surface, measurements were taken only at the edge. Along an $800\,\mu$m path, R_a was found to be $0.35\,\mu$m and $0.51\,\mu$m for the electropolished and non-electropolished mesh, respectively. Although the results were not directly comparable, the electropolished mesh was expected to have a smoother surface, as indicated by the measurement.

6.3.3 Defect Identification and Evaluation

Two methods were used to identify abnormal features that could potentially enhance the field and induce electrode-induced backgrounds or breakdowns. The first method was thorough human inspections. The second utilised a machine learning algorithm trained on photos taken of the entire mesh [1]. Human inspection offers greater flexibility for viewing the mesh from different angles and under varying lighting conditions, whereas the machine learning method is constrained by limited input data. On the other hand, human inspection is time-consuming and impractical for inspecting the entire mesh of XLZD-scale electrodes. Machine learning methods provide a more systematic approach that yields consistent results across different operators and comparable results across different mesh samples.

In either case, once the features were identified, a handheld microscope was used to capture their geometry. A list of all identified features on the TPC mesh, whether found by humans or machines, and their coordinates is summarised in Appendix D, see also [1, Figure 10]. A physical coordinate system was laid below the mesh to systematically locate and trace the features with a resolution of $\sim$5 cm. For future work, the coordinate system can be incorporated into a 2D robot arm or profiling system, thereby improving tracking accuracy and coordinate resolution.

The geometries of several defects were measured with microscope images and modelled for electrostatic field simulations. An example of a broken leg on the sample mesh is shown in Figure 6.4. Because the tips of the broken leg exhibit sharp geometry, inducing a rapidly varying field, the result was highly dependent on the geometry. Two models with slightly different geometries were built for comparison. Only Model 2 is shown in the figure, as it best resembles the real geometry. For Model 1, a different numerical discretisation was used for the simulation, labelled as "Mesh" in Figure 6.4. The different parameters are summarised in Table 6.2.

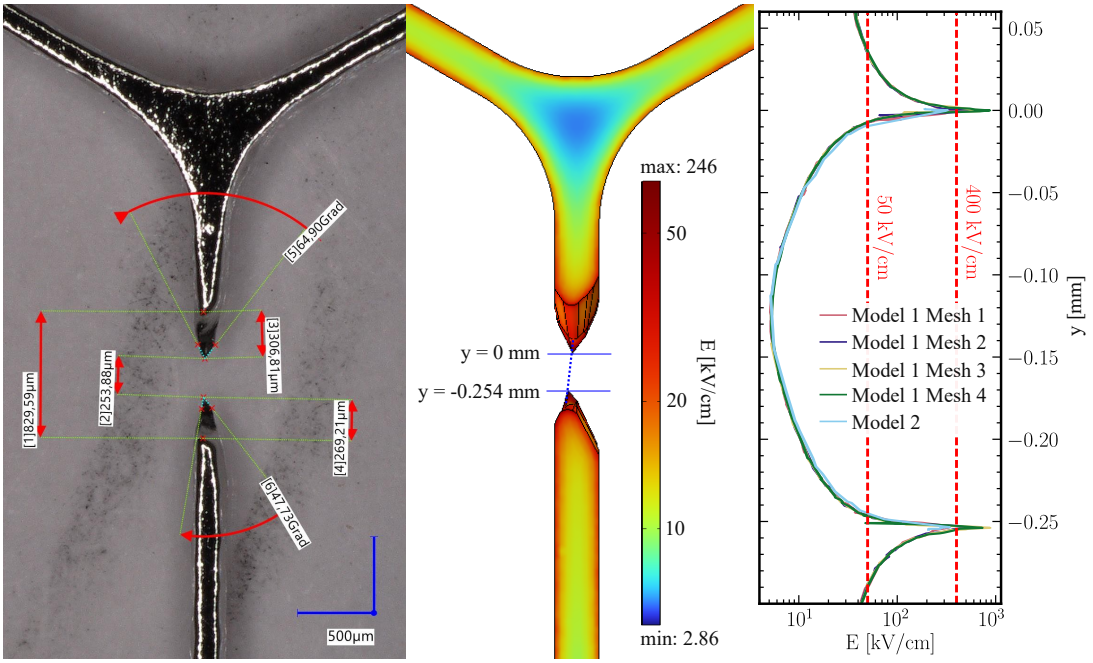

Figure 6.4: Local 3D field simulation for the broken leg feature on the sample mesh. Left: microscopic image and dimensional measurements. Middle: implemented simulation (Model 2) geometry together with the surface field shown. The blue lines indicate the coordinate system, and the blue dotted line passing through the tips indicates the line where the field is plotted in the right plot. Right: the field along the blue dotted line in the middle figure. The different discretisations (Meshes) used are summarised in Table 6.2. The red dashed line indicates the empirical breakdown limit of 50 kV/cm [96, 109, 121], and the electroluminescence thresholds of 400 kV/cm in liquid xenon [124].

Table 6.2: Parameters for the discretisation used for the simulation for Model 1 shown in Figure 6.4 (right). The minimum element size refers to the minimum length of the edge of a discretised element. The growth rate is the ratio of the sizes of adjacent elements.

Discretisation	Min. element size	Growth rate
Mesh 1	0.002	1.5
Mesh 2	0.002	1.3
Mesh 3	0.001	1.3
Mesh 4	0.002	1.1

While modelling these features in simulations might provide some quantitative risk assessment, the simulations are subjected to significant uncertainty due to the sharp geometry and the difficulty of obtaining the exact 3D profile of each feature. In reality, the tip should have a finite curvature. However, this curvature could not be resolved by the microscope. In the simulation models, the tip was treated as an ideal sharp point (i.e. with infinite curvature). The curvature was subsequently lowered due to the numerical discretisation of the simulation domain. In other words, the maximum field obtained at the tip is highly sensitive to the numerical discretisation and does not provide meaningful absolute values. Slightly away from the tip, however, simulations with different discretisations (Mesh) and geometry (Model 1 vs Model 2) yielded consistent results. The field near the tip of the broken leg exceeds the empirical breakdown limit of approximately 50 kV/cm [96, 109, 121], and potentially reaches

the electroluminescence and charge-multiplication thresholds of roughly 400 kV/cm and 700 kV/cm in LXe, respectively [124]. Such features can readily induce electrode backgrounds and even cause breakdown events. The result highly underlines that such a feature cannot be left unrepaired or exchanged.

Removing these features by cutting the entire leg away and mechanically smoothing the surface was also considered. However, tests and simulations showed that such a method could create mechanical weak points and non-uniform fields. The removed region would result in a larger charge-insensitive volume, i.e., the regions where ionisation electrons would not drift towards the gas phase. This is particularly problematic for some extended defects. This motivated the use of a laser-welding repair technique, as described in the next section.

6.3.4 Repair via Laser Welding

Protruding features on the TPC mesh were repaired using laser welding, the same technique used to join the two half-meshes. The repair procedure consisted of the following steps. First, the defective parts were removed from the mesh legs by a cutter. A replacement part of the same size was also cropped from a spare mesh. The replacement part was then positioned into the removed part. The legs were subsequently rejoined by laser welding. After the repair, the mesh underwent electropolishing to further smooth the surfaces. Figure 6.5 shows the image before and after the treatment.

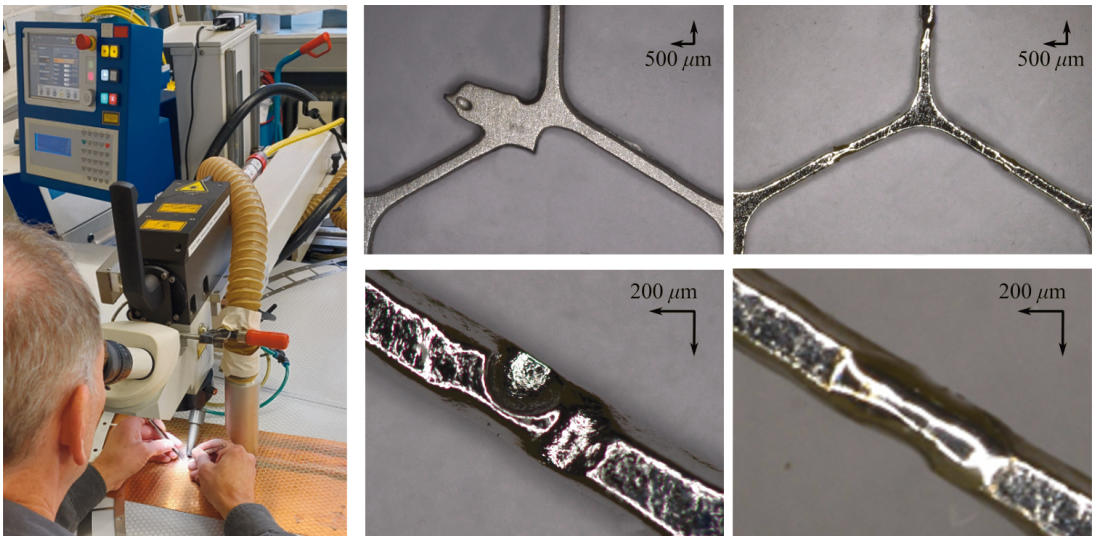

Figure 6.5: Photos of laser-welding repairing. Left: photo of the laser-welding process. Middle (right): close-up of the features before (after) laser welding. The feature at the top was repaired by removing the defective part and replacing it with a new piece featuring an etched mesh. The feature at the bottom was found after electropolishing and was repaired using the filling technique.

The robustness of the laser-welded connections was verified using tensile tests. Small segments with and without a welding connection were pulled in opposite directions until breaking. The UTS, which is the maximum recorded force[4] divided by the cross-

[4]Brand: Sauter. Model: FK 100.

sectional area (0.09 mm^2), was measured at 454 MPa and 600 MPa for the samples with and without the welding connection, respectively. In the laser-welded segment, the break occurred at the joint.

Despite the reduction in the UTS after laser welding, the measured UTS values lie well beyond the maximum load expected on the tensioned etched mesh, which is 167 MPa discussed in subsection 6.1.2. Also, the cross-sectional area of the laser-welded spots became slightly narrower and non-uniform, and therefore was not well-defined. Due to this reason, the measured UTS might be underestimated. Therefore, this test suggested that the laser-welding repair technique will not compromise the structural integrity of the etched mesh, which was also verified by the mock and the final assemblies.

Note that not all features were repaired by the laser-welding technique, as the associated risk of additional damage due to each operation was weighted against the marginal benefit. Therefore, all large protruding features and those with sharp edges were repaired, and the repaired mesh was subsequently stress-tested in an HV environment, as described in the next section.

6.4 High-Voltage Test in Argon Environment

Each of the aforementioned assurance techniques has limitations: the survey of abnormal features may be incomplete; field simulation is subject to significant uncertainty due to inaccurate geometry and discretisation errors; and the novel laser-welding reparation has an unknown HV response and performance. Therefore, an ultimate HV test was required to verify the overall HV performance of the repaired mesh.

The HV test was performed in a gaseous argon (GAr) environment at atmospheric pressure. Argon was used because of its properties and response to high fields that are similar to those of xenon [49], while being more cost-effective. The aim is to directly observe light signals in argon induced by the enhanced local field, such as by electroluminescence, corona discharge, or breakdown events. This test concept was proposed in [90, 185] and adapted for the hexagonal-mesh electrode, as discussed in this chapter. The charge signal can also be observed in instabilities in the power supply, such as current surges or voltage drops, despite limited sensitivity. The HV instabilities from the multiple tests were also used to predict the overall performance of the electrodes in LXe.

This test in GAr was also intended to be quick and to serve as an initial diagnosis, such that if problems were identified, the mesh could be repaired and treated again. Therefore, for the test, the repaired mesh was mounted on the electrode frame in a non-cleanroom environment, and the outer ring was left in place for re-mounting and final assembly.

6.4.1 High-Voltage Test Setup

The test setup was built inside the Faraday cage. The hexagonal mesh under test was negatively biased by the power supply, with the maximum rating to 200 kV. The bottom of the mesh was 4.97 cm above a grounded aluminium plate with a diameter of 1.2 m. The electrodes were placed inside a box that contained the GAr environment. The lid of the box transmits visible and NIR light. While the power supply measured the current, commercial cameras were used to record the light signal. The cameras were positioned at a vertical distance of ∼1.4 m above the mesh, ensuring the entire mesh was in the field of view. The setup is shown schematically in Figure 6.6. The following paragraphs provide details on each component of the setup, largely overlapping with ref. [1].

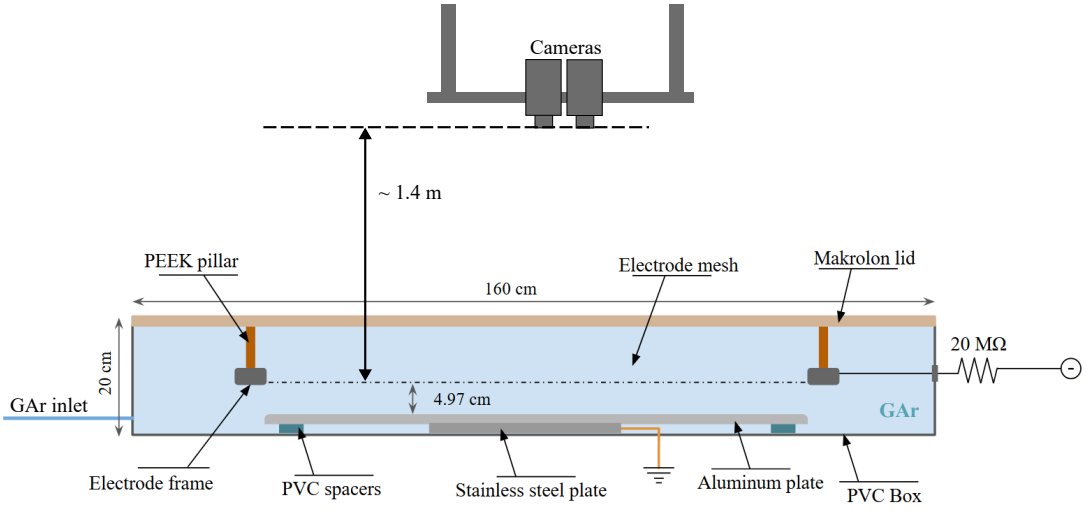

Figure 6.6: Schematic diagram of the HV test setup in GAr (not to scale). The drawing depicts the final test configuration, in which 4 PEEK pillars suspended the electrode under test. Figure adapted from [1].

The tests were conducted in a light-tight human-accessible Faraday cage, using an FuG Elektronik HCP 140 power supply which provides DC voltage up to 200 kV (negative polarity) with a maximum current of 0.7 mA. The HV was fed from the power supply into the Faraday cage via a shielded cable, which connected to a custom-developed ground terminator with an aluminium toroid at its top. A LabVIEW-based software controlled the power supply parameters, such as current limit and set voltage, and provided data readout at frequencies of the order of 1 Hz.

Inside the Faraday cage was the square PVC box measuring 1.6 m in length and 20 cm in depth, which housed the electrode. To maintain a GAr atmosphere and to protect the electrode under test from environmental contaminants, the box was covered by a 1.1 cm thick lid made of Makroclear® polycarbonate sheet [186], which transmits ∼ 90% of the light with the wavelength in the visible and near-infrared range [187, 188]. Strips of Armaflex® tape were added to the side of the lid for partial sealing. Grade 5.0 argon was fed into the box via a GAr tube inlet, and the flow was controlled via a flow meter connected to the bottle containers. Since the PVC box was not leak-tight, the pressure inside the box was assumed to be close to the atmospheric pressure, and thus not monitored. The lid's weight added only 0.13% to the pressure. Additionally,

a humidity and temperature sensor[5] was placed at the farthest corner from the GAr inlet, as these parameters can affect the HV behaviour. This will be explained in subsection 6.4.3. In short, the box was filled with GAr at 1 atm and room temperature $\sim$293 K.

An unpolished aluminium plate (1.2 m in diameter and 5 mm thick) with a rounded edge was placed at the bottom of the box, acting as the ground plate in the setup. It was raised by 1 cm using a smaller metal plate and PVC spacers, so that the grounding connection could be placed below the ground plate to avoid exposure to the high electrostatic field. In such a configuration, the unevenness of the ground plate was measured to be 6.4 mm. Throughout the test campaign, the alignment between the ground plate and the electrode under test was not controlled. With the maximum gap distance between the mesh electrode and the ground plate to be 4.97 cm, the uncertainty of the bulk field due to the unevenness of the ground plate was derived to be at most 15%.

An electropolished hexagonal mesh was mounted on the electrode frame in a non-cleanroom environment, with the procedure described in section 6.2. However, the non-electropolished outer ring was not removed, as explained at the beginning of this section, and the SS covers were consequently also not installed. The electrode was positioned so that the bottom of the mesh was at a maximum distance of 4.97 mm from the ground plate, without accounting for sagging or unevenness. The electrode frame, as shown in Figure 6.6, faces away from the ground plate to reduce field strength at the edge, a configuration different from the final one in the TPC where the hexagonal mesh is above the cathode frame. The hexagonal frame was connected to a metallic connection, which was connected to the toroid of HV. The mesh was negatively biased and cathodic in this test. For most tests, 20 M Ωresistors were added to the HV line from the test box to the toroid, limiting the transient current into the system in the event of a breakdown.

During commissioning of the test setup, we tested various insulating materials to separate the mesh from the grounding plate, including PVC, POM, and a 3D-printed insulator made of ASA plastic. There were also insulators in various geometries designed to provide a long creepage path between the electrodes. Nevertheless, electrical breakdown persisted near the insulator and at the edge of the ground plate. This phenomenon may be caused by field enhancement at the fillet profiles of the insulator's corners. Such profiles around the electrodes can introduce a narrow gap filled with gaseous argon (GAr) between the conductor and the insulator. Because GAr has a lower dielectric constant than the insulator materials, the electric field becomes intensified within these fine gaps at the edges of the ground plate, in which the field was already higher than in other regions [132]. A similar behaviour was observed for insulators with chamfered corners [110].

To mitigate electrical breakdown, the electrode under test was suspended from the lid of the box using PEEK cylinders, so that the insulators were not exposed to a high electric field. As a result, the field around the edge of the ground plate was not

[5] Infactory NC-7004-675.

enhanced. In addition, in this configuration, the substantially longer creepage path between the electrode and the ground plate further reduced the leakage current. The lid was mechanically strengthened with four SS profiles, not shown in Figure 6.6, to reduce lid sagging from the weight of the electrode.

Since the entire electrode was ramped under high voltage, the light signal could be induced from anywhere on the mesh. Two cameras were installed $\sim$1.4 m above the electrode, roughly at the centre, so that each camera's field of view covered the entire electrode. Commercial cameras and lenses were used[6] with the advantage of wide field of views and easy position reconstruction, but at the expense of low customisability and light collection efficiency due to the low coverage. To improve the signal-to-noise ratio, the Faraday cage is wrapped in light-tight covers to reduce background light. In addition, most images were captured with long exposure times ($5-10$ s) to increase the light collected from potential signals. The camera ISO was mainly set to 800 to balance gain and thermal noise from the sensor[7]. In a subset of tests, a third camera captured videos with higher temporal resolution, albeit with reduced exposure.

For electrical safety reasons, no cables were allowed to enter or exit the Faraday cage except the HV power supply. The cameras were triggered by a trigger control with a timer function, such that their exposures overlapped with each other's dead times. Data from the cameras and the humidity sensor were stored internally and read out after each test.

The procedure for each HV test is outlined as follows. After assembling the setup and closing the lid of the PVC box, the closed PVC box was continuously flushed with GAr at a rate of 20 NL/min until the end of the test. Due to the high Reynolds number of the injected GAr of 5×10^5, the gas mixture was considered reasonably well mixed, and no additional mixing mechanism was used. The cameras were then installed and calibrated as described in subsection 6.4.3. Each HV test consisted of multiple ramps. During each ramp, the electrode bias voltage was increased in steps, with the ramping speed gradually reduced at higher voltages. The current limit was set to below 5 μA to prevent potential electrode ageing effects as a result of discharges [189]. At the same time, the current and voltage fluctuations from the power supply were monitored. The cameras also transmitted live views for monitoring, but with some time delay. In the event of an HV breakdown or persistent current fluctuations[8], the HV was manually ramped down. The toroid was grounded to discharge the remaining capacitance in the circuit. We subsequently inspected visually the electrode with the lid closed to ensure no significant disruption or damage had occurred to the electrode or within the setup.

6.4.2 Working Principle of the Test Setup

In the aforementioned argon environment under HV, various processes occur under different conditions, resulting in distinct outcomes. To simplify the complicated ensemble of phenomena involved, I divide the processes into three main stages. First,

[6] A Nikon Z50 mirrorless camera, a Canon EOS 90D, and a Canon EOS 700D, with the NIKKOR DX 18-140mm f/3.5-6.3, Canon EF-S 18-135mm f/3.5-5.6 IS USM and STM lenses, respectively.

[7] Higher the ISO, higher the gain and higher the thermal noise, vice versa.

[8] It has been reported as early indications of a potential breakdown [97]

free electrons (sometimes called seed electrons) are generated by various mechanisms. Secondly, the electrons accelerate in the electric field and deposit energy into the argon atoms, which is subsequently released either as light or as ionisation energy. Thirdly, depending on the field strength, an electron avalanche might develop. In the presence of a feedback effect, this can lead to a discharge or breakdown.

Each of these stages can involve different physical processes that depend primarily on the material, the local field E, the atom density (or the pressure p), and the gap distance d_G between the anode and the cathode. The material, in our case with SS and GAr, changes the work function and the ionisation energy. The local field accelerates the electrons. The atom density affects the mean free path of the free electrons, thereby influencing their recoil energy. The gap distance determines the total drift length, which favours certain processes over others. A commonly used parameter to characterise gas discharge is the pressure-distance pd_G [131], and the reduced field E/N, defined as the field per atomic density [49], which encapsulates the effects of both the field and the atom density or pressure. A common unit used for the reduced field is Townsend, which $1\,\mathrm{Td} = 1 \times 10^{-17}\,\mathrm{Vcm^2 atom^{-1}}$ [49]. In the GAr environment in our setup at 1 atm and 293 K, the conversion becomes 1 Td=0.256 kV/cm. In the following, the description focuses on argon, but xenon also undergoes similar processes [49].

Seed Electrons

The initial or seed electrons can come from, for example, background radiation and field emission [131, Chapter 4]. Although the number of initial electrons generated may be insufficient to produce a detectable light or current signal in our setup, these processes are essential for providing seed electrons that can be amplified in the presence of high fields.

Regardless of the field between the electrodes, there are constant background radiations from cosmic rays or radioactivity on the electrode that ionises the surrounding gas, creating free electrons and a dark current of $\mathcal{O}(10^{-15}\,\mathrm{A})$[131, 132]. If these seed electrons are amplified into a detectable signal, the location of the light signal will be independent of any features or defects.

In case the local field on a cathodic surface is considerably high, for example, due to a pointy feature, the potential well for electrons at the surface becomes a potential barrier with a finite width, allowing electrons to escape the surface through quantum tunnelling [131, 190]. This is called field emission, which can also contribute to seed electrons [131]. The typical field needed for a detectable current is of the order of 1 MV/cm to 10 MV/cm [131, Page 69] (see also section 3.2). If these seed electrons are amplified into a detectable signal, the location of the light signal should correlate with the location of the features or defects, as the normal grid surface does not have such a high field (see Figure 6.4).

Photoionisation (PI) also produces electrons, as explained in section 3.2. However, this should not be the primary source of seed electrons in this setup, which is in a light-tight environment; PI can, however, lead to secondary electron emission. Thermionic

emission is unlikely to occur in our setup at room temperature and with the current limit. Ultimately, if the current limits are high, the arc discharge might generate sufficient energy to induce thermionic emission and damage the electrodes [131].

Energy Deposition through Light

Once the initial electrons are present, they accelerate in the electrostatic field before interacting with the argon atoms. The electrons may scatter and excite the argon atoms, which subsequently emit photons called electroluminescence (EL). EL can be futher divided into three types [49]: starting at the lowest field below 4 Td is the Neutral bremsstrahlung (NBrS), in which the electron is scattered by the dipole field of neutral atoms and emits bremsstrahlung light [191]. The emitted light spans a wide spectrum, ranging from 200 to 1000 nm. Starting from 4 Td, some electrons also gain enough energy to excite the argon atom, which is called the *ordinary EL*. It is the same signal observed as the S2 in a TPC with the wavelength in the VUV range (128 nm for argon). At an even higher field beyond 8 Td [49], higher excited states are also involved, emitting photons in the near-infrared range ($700 - 850$nm). The light yield as a function of the reduced field, as well as its spectrum, is shown in Figure 6.7. From the spectrum, it is clear that the setup was sensitive to only the EL from NBrS.

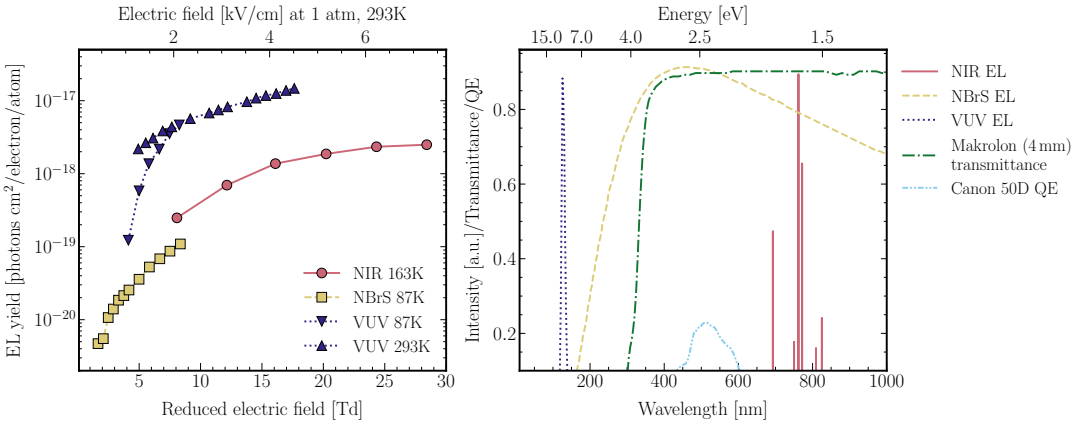

Figure 6.7: Light yield and spectrum of the argon electroluminescence (EL), adapted from [49]. Left: the EL response as a function of the reduced field. The corresponding field at the operating condition of this test (1 atm, 293 K) is shown in the top axis. Measurements include the near-infrared (NIR) EL, the EL due to neutral bremsstrahlung (NBrS), and the ordinary EL at the VUV range (VUV). The temperature of the corresponding measurements is listed in the legend. Right: the argon EL spectrum. The transmittance of the Makrolon lid at 4 mm thick is also shown as a reference [187], while the thickness of the lid in this test is 1.1 cm. The quantum efficiency of the CMOS sensor in the Canon 50D camera, a similar model to one of the cameras we used, is shown in the same plot [192, Figure 2 (left)].

Electron Multiplication and Feedback

As the field further increases, some electrons can gain enough energy (>15 eV) [131, Table 4.3] to overcome the ionisation potential of the argon atoms, resulting in electron multiplication. The ionisation can be parametrised by Townsend's first ionisation coefficient $\alpha(E)$ [179].

Additionally, some mechanisms compete with the multiplication process [131]. The

electrons lose energy as they propagate and deposit energy to other atoms and molecules, slowing down the development of the avalanche. Additionally, the electrons produced are removed by the electrodes and attached to impurities. In order to achieve a self-sustaining discharge[9], a secondary feedback mechanism is needed [132], in other words, the *multiplication of avalanche* [131].

There are various feedback mechanisms that induce discharge, such as ion- or photon-induced electron emission from the cathode. Like primary electrons, electrons from these secondary emissions can also deposit energy into argon atoms, resulting in light emission. For a small value of the product of pressure-distance, the feedback can be provided by the presence of ions close to the cathode [131, 132]. While the impact ionisation of ions on the cathode is inefficient at knocking out electrons, the field provided by the ions can cause increased electron emission from the surface, leading to secondary emissions [131]. At large pressure-distance, the slow-drifting ions cannot explain the time-scale of observed breakdowns, and the threshold voltage no longer depends on the cathode material [132]. The streamer mechanism is commonly used to explain the phenomenon instead [179], in which the multiplication of avalanches is attributed to the thin channel of high-density ions that enhances the field, inducing secondary electrons by ionisation and photoionisation [131, 132]. The pressure-distance value for the transition from the Townsend mechanism to the streamer mechanism is ambiguous, ranging from $5\,\mathrm{bar}\cdot\mathrm{mm}$ [132] to $50\,\mathrm{bar}\cdot\mathrm{mm}$ [179]. The test setup described here operated in this transition region, with a pressure-distance of $50\,\mathrm{bar}\cdot\mathrm{mm}$. Ref. [179] introduced augmented empirical models to bridge the two breakdown mechanisms, and was found to offer a better match with the data in the wide range from $1\,\mathrm{bar}\cdot\mathrm{mm}$ to $100\,\mathrm{bar}\cdot\mathrm{mm}$.

Self-sustaining electrical discharges can occur under various conditions, and are generally classified as follows: glow discharge occurs at a range of currents from 10^{-6} A to 10^{-1} A, typically in low-pressure environments below 10 Torr or 0.013 bar, and is thus not applicable to this setup. Arc discharge occurs at a high-current regime ($>$1 A), which is precluded in this experiment due to the set current limitations. Corona discharge occurs at sharp features and typically initiates at currents of the order of 10^{-6}A. It is a type of partial discharge that does not connect the anode and cathode electrodes. In contrast, a breakdown or spark leads to short-circuiting, a surge in current, and a drop in voltage [131, Chapter 12]. Spark discharge typically occurs at larger gap lengths and at ambient pressure. Corona discharge can precede a spark if the gap length d_G is much greater than the length-scale of the sharp feature l_f, for example, at a threshold of $d_G > 6 \times l_f$ times in air [131]. Otherwise, a spark can occur directly without initiating a corona discharge.

Expected Light Yield

The HV setup at KIT is far less sensitive than the underground TPC experiments for observing faint scintillation light. The LCE is much lower. While the lid has approximately 90% transmittance, there are no reflective panels between the box and the camera to collect more light. The camera observed the entire electrode at a distance

[9] It is a type of discharge or flow of current that, even when the source of seed electron is removed, the discharge can be sustained.

of $\sim$1.4 m. Given that the camera's aperture is 67 mm, the solid angle is 0.06%, which can serve as a proxy for the LCE. Note that the camera lens also comprises multiple optical elements, which further reduce the light reaching the camera sensor; however, this effect is not accounted for.

Due to the commercial camera's filter cutoff, the cameras have limited sensitivity to both VUV and NIR light from the argon emission, leaving the NBrS signal detectable. Consider the light yield for NBrS at around 10^{-19} photons $\cdot$ cm^2/electron/atom at the field above 8 Td or 2 kV/cm, as shown in Figure 6.7. The operating condition yields an argon atom number density of 2.56×10^{19} atom/cm^{-3}, resulting in a specific light yield of $\mathcal{O}(1\,\mathrm{photon/electron})$. Given the solid angle of a camera, the light collected by an emitted electron will be of $\mathcal{O}(10^{-3}\,\mathrm{photons/electron})$. Note that the efficiency and the baseline noise level of the camera sensor are not even taken into account, which could be $20 - 60\%$ [192–194], but no literature values from the used camera model can be found to the best of our knowledge.

Consider the ionisation due to cosmic radiation, producing around 10 electrons at sea level per cm^3 per second [131]. With the volume sandwiched by the electrodes, there are $\mathcal{O}(10^5)$ seed electrons per second on average. However, they are sparse and likely insufficient to produce detectable light, unless a seed electron triggers a discharge or breakdown. Note that radioactivity on the surface of the electrodes were not taken into account, which is expected to be lower than the cosmic ray induced ionisation. The ionisation inside the electrode have to overcome the potential barrier, to contribute as the seed electron, thus going into the case of the field emission in the following.

For field emission, a significantly enhanced local field is required to produce a detectable signal when the bulk field is insufficient to sustain feedback effects. Using the formulation in section 2.1 from [130], assuming a highly enhanced local field at 12 MV/cm (enhancement factor $\beta \sim 100$) on a relatively large surface of 0.01 mm^2, the current is of $\mathcal{O}(10^{-16}\,\mathrm{A})$, leading to around 600 electrons and less than 1 photon possibly reaching the camera sensor. The larger the area, the higher the current, but the area also anticorrelates with the enhancement factor. Features with an extremely large enhancement factor that could produce a detectable light signal were unlikely, as they should have been identified in the extensive survey of abnormal features. To achieve a measurable light signal, the charge from field emission should be amplified by the bulk field, entering the corona or spark discharge regime.

6.4.3 Calibrations

Camera Calibration

We calibrated the time, noise levels, and electrode position for each camera. Since the internal clocks of the cameras were not synchronised, the time difference between the internal clocks and GPS time was recorded before each HV test. For noise calibration, images were taken with the cap covering the camera lens and the camera placed in a dark environment. The obtained images were used to infer which pixels had a relatively higher noise level on the day of measurement. Position calibration images were taken while the electrode was illuminated, allowing us to subsequently correlate the

glow or breakdown location in the photos with its position on the tested electrode.

Argon Calibration

Breakdown voltage or HV instability depends, among other factors, on the gas composition of the environment as well as the water content in it [132, 195, 196]. As mentioned, the PVC box of the setup was not leak-tight and could not withstand vacuum pressure. Before and during the test, the GAr, which is heavier than air, was constantly flushed and displaced the air inside the box, albeit partially mixed with the remaining air. The breakdown voltage in pure argon gas is lower than that in air at our operating conditions [131]. The mixture of gases thus introduces uncertainty into the interpretation of HV instability.

To indirectly infer the concentration of the GAr environment, the relative humidity inside the box measured by the humidity sensor and the GAr flush time were recorded. The longer the flush time, the more argon displaces the air inside the box, resulting in lower relative humidity. Since argon has a lower breakdown voltage, the breakdown voltage should decrease with increasing flush time. As a result, the humidity should correlate with the breakdown voltage in our setup. A calibration run was performed to verify the correlation between GAr flush time, humidity, and the HV instability of the setup.

The calibration setup consists of one biased and one grounded SS plate, with outer diameters of 29.5 cm and 16.5 cm, respectively. The HV was connected to the setup via the $20\,\mathrm{M}\Omega$ resistor as in the actual tests. The biased electrode was supported by three PEEK pillars mounted on an external platform. The gap distance was measured to be 35 ± 1 mm without alignment control. The setup was assembled in a non-cleanroom environment, but wiped with ethanol and subsequently positioned at the farthest corner from the gas inlet. A humidity sensor was placed about 10 cm from the biased plate, farther from the gas inlet, to measure humidity inside the box. During calibration, as the argon was flushing into the box at 20 NL/min, and the electrode was repeatedly ramped up until the power supply current limit of 5 µA was reached. The voltage V_c is defined as the voltage one time-step, which is 0.2 s, before the current limit was reached, as shown in the inset plot in Figure 6.8. V_c is plotted as a function of the effective GAr flush time, as shown in the same figure. Voltage drop can also be used to indicate HV instability, giving similar results.

In this calibration run, most ramps have a ramp-up speed of 500 V/s. Ramps with ramp-up speeds of 100 V/s and 250 V/s were used a few times, but no systematic deviations from the overall trend were observed, so they are not shown in the figure. The HV system was grounded from time to time in between ramps, but no systematic differences were observed. At the beginning of the calibration campaign (time $t < 0$ in Figure 6.8), many ramps were performed to condition the system, removing the remaining dust and impurities [197, 198], resulting in a gradual increase in V_c. At time $t = 0$, the GAr valve was opened, and both the humidity and V_c decreased. Since there was an overnight break during the test, the argon escaped from the box, causing V_c to increase. Therefore, an additional flush time was required to restore V_c to its pre-pause level. The dashed line in Figure 6.8 marks the time window that was

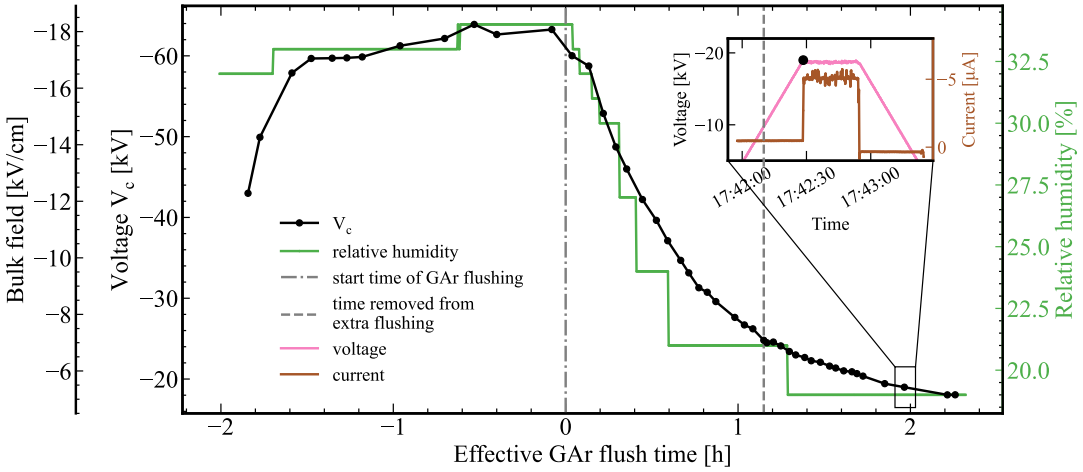

Figure 6.8: Evolution of V_c with respect to the effective GAr flush time. The inset shows an example of one ramp of V_c, the voltage just before the current reached 5 µA. The y-axis (inner left) shows the voltage V_c. The y-axis (outer left) shows the reference bulk field, deduced as V_c divided by the maximum electrode gap. The x-axis is the effective elapsed time of the GAr flush. At time $t = 0$ (marked by the dash-dotted line), the GAr started flushing at 20 NL/min. After around one hour of flushing (marked by the dashed line), there was a 20-hour pause on flushing, where some GAr escaped. The additional flush time needed to reduce V_c again was removed from the above plot. The right y-axis indicates the humidity level measured by the sensor at the synchronised time.

eliminated. The argon flow was intermittently turned off to confirm that the change in GAr concentration caused the reduction in V_c. Those periods were also removed from the plot, yielding the effective flush time.

The V_c and humidity profiles show a correlation throughout the test, with the humidity limited by the sensitivity of its sensor. From the result, a flush time at 20 NL/min of slightly more than 2 h resulted in a relatively stable V_c. This implied that the uncertainty in HV instability with respect to GAr concentration became subdominant. Quantitatively, at a flush time beyond 0.5 h, V_c follows an exponential decay $V_c \propto e^{-t/\tau}$ with the time constant $\tau \approx 1.817$ s. From 1.5 h on until the end of the measurement, the relative change in V_c was 16.4%. The absolute breakdown voltage $|V_c|$ plateaued at 18.0 kV after 2.26 h of flushing, corresponding to a bulk field of 5.1 ±0.1 kV/cm. The breakdown voltage between polished spheres in gaseous argon parameterised by the PyBoltz-Townsend model mentioned in the previous section, at a pressure of 1 atm and a gap distance of 3.5 cm, was reported at 21.7 kV [179], resulting in a bulk field of 6.2 kV/cm. The measured breakdown voltage from this calibration was expected to be lower, as the plate surfaces were not mirror-polished.

6.4.4 Test with Sample Mesh

As a preliminary test and proof of concept, the sample mesh with a broken leg defect, shown in Figure 6.4, was tested. As the HV ramps up, we observe glow at the outer edge of the etched mesh, which was not electropolished, as well as at the broken leg. Note that the outer edge is not electropolished and was later bent slightly upward to reduce the surface field, as it is not the region of interest in these tests.

A third camera zoomed in on the broken leg and recorded a video as we ramped up the HV. Figure 6.9 shows the synchronised current and voltage profiles, along with the video taken during the measurements, which captures the corona discharge before spark discharge (breakdown) occurs. This figure indicates that the current profile is in good agreement with the brightness profile and demonstrates adequate sensitivity to pre-breakdown discharge. At the same time, we observed the same signal with long-exposure images from the overhead camera. This indicates that the overhead cameras were sufficiently sensitive to capture the dim light signal before the breakdown.

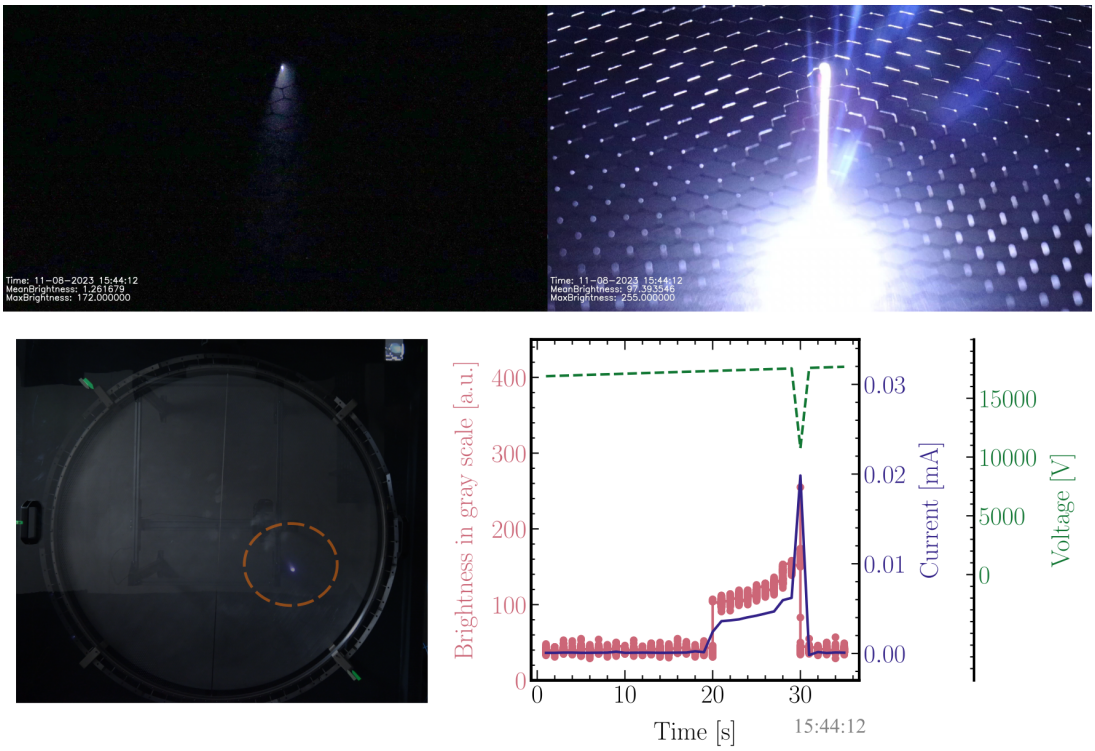

Figure 6.9: Example of the test with the sample mesh. The top images are from the video camera, zoomed in on the region with the broken leg. The video was captured at 100 frames per second, with each frame's time rounded to the nearest second. The bottom-left image is from the overview camera at the same time, with a 10-second exposure and ISO 800. The region of the broken leg is highlighted with a circle, showing the glow before the breakdown. The bottom-right plot shows the data from the video frames and the power supply. The pink line with markers is the maximum brightness over all pixels for each frame. The blue solid line and green dashed line are the current and voltage readings from the power supply, respectively. The x-axis represents an arbitrary elapsed time, with 30 s corresponding to 15:44:12, as shown in the top video frame.

Due to the sharp geometry, the field at the tip can reach a local field of $\mathcal{O}(1\text{-}10\,\mathrm{MV/cm})$ (Figure 6.4), possibly leading to field emission. The field emission provided the seed electrons, together with the high field, the electron avalanche produced an observable light signal as shown in Figure 6.9. The jump in current could also be understood as the transition from the non-self-sustaining background discharge (e.g. dark discharge) to self-sustaining discharge like corona discharge, with a typical current of $\mathcal{O}(10^{-6}\mathrm{A})$ [131, Chapter 12], in agreement with our observation (Figure 6.9 top left). As the avalanche multiplied, as clearly evidenced by the light and current profiles, the corona discharge developed into a complete breakdown. Therefore, an abnormal feature or

defect of a similar level of field enhancement should be detectable from this setup.

6.4.5 High-Voltage Performance

Concerning the mesh that was eventually installed in the XENONnT TPC, the results from this HV test setup were reported in section 4.3 of [1]. A few key observations can be highlighted from the test results. First, no glow other than breakdowns was found above the light signal threshold in the images, unlike in the case of the sample mesh. Secondly, the three recorded breakdown events on the mesh cannot be correlated with known defects or features, including the places with the repaired laser-welding joints. The mesh was carefully inspected afterwards. A few new features were identified, but their coordinates did not match the locations of the breakdowns. A similar observation was made by [114]. Some of these newly identified features were repaired to ensure the mesh's mechanical robustness. They were labelled as *Stage 2* repair to distinguish them from the previous repair, which was labelled *Stage 1*. Subsequent tests did not record any breakdown on the mesh, but only with a smaller number of ramps. Statistically, the overall result suggested that the TPC mesh can withstand a bulk field of 3.1 kV/cm at 95% survival probability in GAr, with upper and lower bounds of 2.8 kV/cm and 3.4 kV/cm, respectively [1].

The observed breakdown events were not preceded by glow or corona discharge, likely indicating that there are no sharp features at the location of breakdown. The observation that the breakdown events do not correlate with any known features and are non-repeating might be explained by seed electrons from background radiation, which develop into an avalanche and breakdown due to the high field at the surface and between the electrodes. Another explanation that cannot be ruled out is filament-like dust particles, given that the test was conducted in a non-cleanroom environment. The filament might trigger field emission at the cathode surface, leading to breakdown due to the high field.

While the result does not directly infer the performance of the electrode in LXe, the GAr result can serve as a proxy and be extrapolated to assess performance in LXe. First, the extrapolation from GAr and GXe was made by comparing literature values of the breakdown field using Paschen's curve. Paschen's curve is an empirical formula for the breakdown voltage in a uniform field, given the pressure and gap length. The empirical values from ref. [179] and [180] to perform this extrapolation as given in Table 6.3: the former considers both the Townsend and the streamer mechanism, and the latter accounts for the temperature dependence. The quoted breakdown field values from these references were measured using uniform fields. In contrast, the field between the electrodes of this measurement is close to, but not uniform, which is expected to result in a lower breakdown field. Note, however, that the local field scales with the bulk field, enabling a naive conversion based on the ratio from GAr to GXe.

In a second step, the ratios were extrapolated from GXe to LXe. Although the ionisation threshold of LXe was found at around 700 kV/cm [124], breakdowns were recorded at fields lower than this threshold. In a configuration of large electrodes, a breakdown field of less than 100 kV/cm was reported [108, 109]. Various theories

Table 6.3: Extrapolation of breakdown from the GAr environment in the HV setup to LXe in the XENONnT TPC environment. Empirical values in [179, 180] are used. (**): gas Xe bubbles in the liquid phase.

	Ref. [179]	Ref. [180]
Condition 1: HV test condition (GAr, 1.0 bar, 293 K, gap 4.97 cm)	5.7 kV/cm	12.5 kV/cm
Condition 2: XENONnT condition (GXe**, 1.9 bar, 177 K, gap 5.44 cm)	14.4 kV/cm	21.1 kV/cm
Ratio (Condition 1 $\rightarrow$ 2)	2.5	1.7
Ratio$\times$1.18 (Condition 1 $\rightarrow$ 2 in LXe)	3.0	2.0

have been proposed to account for this, such as an earlier breakdown due to the presence of GXe bubbles at the size of the order of 1 mm. The field enhancement inside such a bubble cavity is calculated as 1.18 times, using the dielectric sphere equation [132] with the dielectric constant of 1.88 for LXe [71, 72]. With reference to the operating condition in XENONnT Table 2.1, the conversions are tabulated in the table below:

Two conversion factors were derived. For the conservative case, using the lower conversion factor of 2.00 and the 95% survival rate at 3.1 kV/cm, the TPC mesh might withstand a field of 6.2 kV/cm before inducing electrical breakdown. This limits the field between the cathode and the bottom screen[10], which was designed to be around 5 kV/cm. It should be noted that these results do not provide information on other electrode-induced backgrounds discussed in section 3.2 and [96]. Nevertheless, this process demonstrates a quick test that can be incorporated into quality assurance procedures, enabling timely interventions and repairs.

6.4.6 Discussion and Future Work

Several factors limited the test results and can be improved for future tests. First, during testing, the electrode frame with the screws and clamps faced the high-field side, whereas in the XENONnT TPC, they will face the low-field side. This test configuration, intended to reduce the field between the unpolished ground plate and the electrode frame, left the unpolished, uncovered screws exposed to a high electric field. As a result, most electrical breakdowns occurred at the frame and the edge of the ground plate, limiting the ability to stress-test the mesh itself under realistic conditions.

The quality of the ground plate further constrained the HV setup. Electrodes used in HV tests are typically mirror-polished and have edges shaped according to the Rogowski profile for optimal field grading. The flatness and alignment to the cathode

[10] In the actual upgrade, this limits the field between the cathode and the bottom PMT array from a purely electrical point of view.

should also be controlled. While a movable grounding probe can improve the resolution and accuracy of detecting regions of field enhancement, a sufficiently large ground plate remains essential for a comprehensive assessment of HV stability of the entire electrodes.

Furthermore, all tests were conducted outside a cleanroom environment. Despite cleaning the electrode surfaces with ethanol before testing, dust particles inevitably remained, potentially influencing the results.

To improve future tests, several enhancements should be considered, which have been partially implemented in [199]. Implementing a more sensitive, dedicated current probe in the circuit could improve the detection sensitivity of charge signals, which are more sensitive than light-based diagnostics but lack position information. Employing wavelength shifters or placing a broadband photosensor closer to a movable probe could also enhance light collection. Finally, the testing methodology described here could be generalised and applied to a range of electrode types.

6.5 Assembly and Quality Control

As an overview, the TPC mesh underwent the following steps of treatments and tests before the final assembly:

- inspection for abnormal features and defects
- Stage 1 repair
- electropolishing
- HV test with 17 ramps
- Stage 2 repair
- HV test with 5 ramps
- cleaning and passivation

The frame was electropolished twice for a shiny surface and cold-treated before installation, as in the case of the anode frame described in section 5.5. The frame was partially immersed in the liquid nitrogen puddle at a time and rotated until the entire frame was cooled. The frame was subsequently left to warm up overnight.

The cleaning for all SS parts is the same as that described in section 5.5. The silver-coated screws were qualified for vacuum applications and were thoroughly cleaned before shipment. They were cleaned in an ultrasonic bath in ethanol at 50 °C right before installation.

The final assembly in the cleanroom at LNGS took two days, including the wait for the tensioned electrode to relax. During assembly, to sufficiently tension the mesh, 7 rounds of tensioning were performed using 0.1 Nm torque on the stretching screw (see Figure 6.2), followed by an additional round using 0.15 Nm torque (Figure 6.10 left). As mentioned in subsection 6.3.1, the sagging was measured by placing a screw beneath the middle of the welded strip, and the FaroArm was used to measure the sagging from the electrode frame, also shown in Figure 6.10 (right). After dismounting

all fixations, the final sagging under gravity was measured to be h_g=0.6 mm, which is expected to result in h_o=1.1 mm downward during the operation of the TPC.

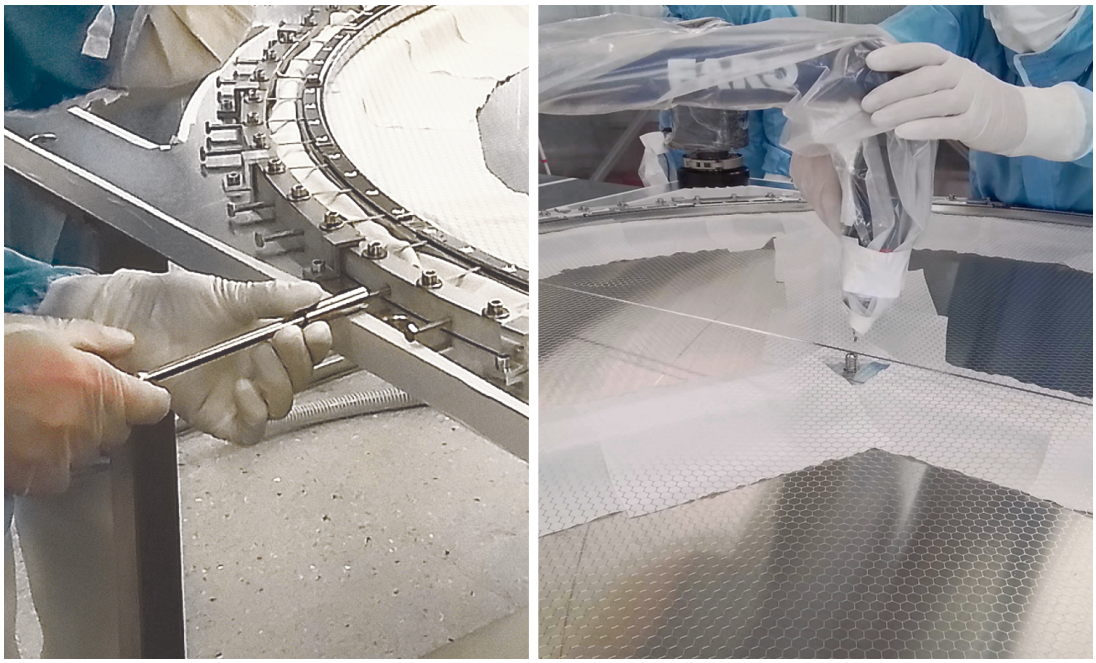

Figure 6.10: Installation in the LNGS cleanroom. Left: tensioning the etched mesh by screwing the stretching screws using a torque wrench, as explained in Figure 6.2. Right: measuring the gravitational sagging of the etched mesh, with the screw underneath the central welded strip.

As mentioned in subsection 5.6.1, the assembled cathode electrode was also tested in an LXe environment together with the anode and the gate. After the PANCAKE test, discolouration was observed on the silver-coated screws of the frame covers, likely caused by the formation of silver compounds with sulphide, chloride, and oxygen from ambient air [200]. Although likely only a minor surface problem, the contaminated screws were later replaced by gold-coated screws[11] inside the cleanroom. Note that these screws fix the cover of the electrode frame, which was used to cover sharp edges from the etched mesh (see section 6.2), but are not responsible for the tension of the mesh. Therefore, no change in mesh tension due to the replacement is expected, as shown by the measurement described below.

Instead of using the FaroArm as shown in Figure 6.10, a laser setup was used to measure deflection before and after replacing the screws. The etched mesh was placed on a metallic slab on an optical table, with the etched mesh on top of the electrode frame. A laser distance measurement device[12] with the repeatability of 70 µm was installed on a rail system perpendicular to the central welded strip above the electrode. The distances from the device to the top of the cathode mesh and to the table in the immediate vicinity were measured. The difference, Δy, along the rail system is shown in Figure 6.11. Since the etched mesh should sag naturally under gravity, it was expected that $\Delta y \leq$20.3 mm (yellow dashed line), accounting for the thickness of the electrode frame (20 mm) and the thickness of the etched mesh (0.3 mm). However, Δy was also

[11] Manufactured by VOC - Vacuum Optimizing Components GmbH.
[12] WayCon laser (type LAR-70-5V).

measured greater than 20.3 mm, with a maximum difference of 0.7 mm, meaning that there is an unaccounted systematic error in the measurement. It may be due to unevenness of the metallic slab, diffuse reflection from protective clothing placed beneath the electrode, or vibration from the rail system.

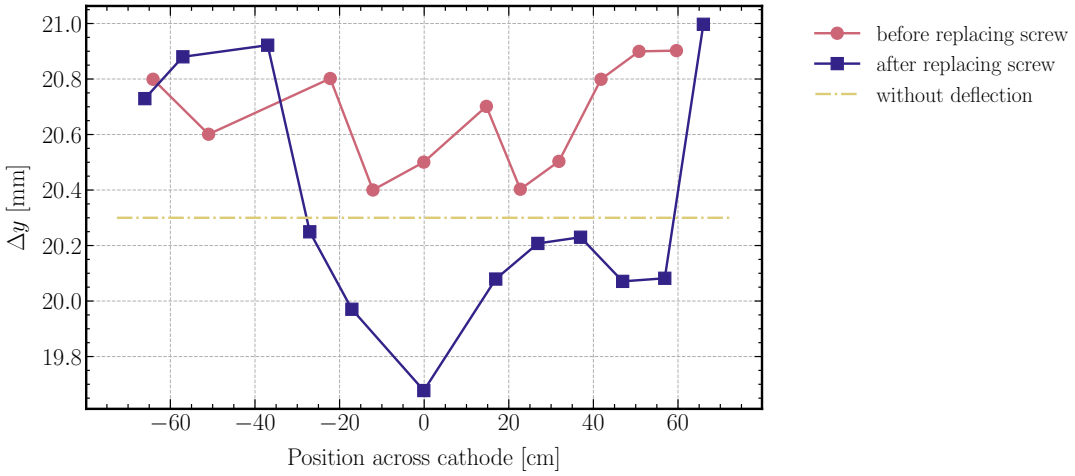

Figure 6.11: Deflection after the PANCAKE test, and before and after replacing the cover screws. The y-axis Δy is the distance from the table to the top of the mesh. The yellow-dashed line indicates the expected maximum Δy, or the position of the mesh if there is no deflection or sagging.

From Figure 6.11, the sagging profile before the replacement was also the first measurement after the electrode went through a complete cooling cycle in LXe in PANCAKE. All data points were above the maximum expected values, meaning the systematic error of 0.7 mm was greater than the sagging under gravity, which was measured at 0.6 mm by the FaroArm before the PANCAKE test.

The sagging profile after the replacement was consistently lower than before. However, if taking the 0.7 mm systematic error into account, the significance of the observation is questionable. Therefore, we concluded that there was no significant change in sagging following the replacement operation.

To improve future measurements, it should be performed directly on an optical table, with typical unevenness of less than 0.1 mm, and the frame has to be carefully fixed to the optical table. The precision of the longitudinal distance measurement should be calibrated against an external reference as well.

6.6 Discussion and Outlook

The hexagonal etched mesh has a central welded strip 4 mm wide, which was shown to have a moderate effect on field homogeneity and transparency. The cathode was calculated to deflect downward by 1.1 mm during operation under the nominal field configuration. Some sharp, protruding features were observed on the etched mesh, which were repaired using laser welding. The repaired mesh underwent extensive HV tests; the cathode can withstand a bulk field of 3.1 kV/cm at 95% survival probability in GAr, which was extrapolated to 6.2 kV/cm between the cathode and the bottom

screen in LXe. To further reduce the electrode backgrounds from the cathode, the mesh underwent electropolishing and passivation treatments.

For the XLZD project, if a hexagonal mesh is chosen, the use of the welded strip is foreseen, as current manufacturing limitations allow. While this strip makes the mesh unsuitable for anode and gate electrodes, it remains a viable option for the cathode and screening electrodes.

Although the etched mesh allows a quicker and more robust installation than parallel-wire electrodes, its main disadvantages include unprofiled, uneven surfaces; abnormal features; and difficulty in repair due to its relatively monolithic configuration. Nevertheless, this chapter has described and demonstrated a set of QA/QC procedures for identifying and addressing these issues, making the etched mesh a feasible option for constructing a reliable cathode in future TPC experiments.

Future R&D should further investigate the electrode background originating specifically from laser-welded joints, and seek to integrate all surveillance techniques using a consistent, automated, and accurate coordinate system.

Chapter 7

SiPM Characterisation in Liquid Xenon

SiPMs have grown in attention for their application in rare-event search experiments in the past years, as proved by their use in the DarkSide-20k experiment[1] [85, 201], the NEXT experiment[2] [68], the nEXO experiment [202, 203], the DUNE experiment [204, 205] and the JUNO-TAO [206] among others. Despite the relatively higher dark count rate (DCR) compared to its PMT counterpart, SiPMs offer a comparable gain and additional benefits such as lower radioactivity level [207], robustness [208, 209], and a lower operating potential[147]. While the baseline design for XLZD consists only of PMTs [34], SiPMs remain an open option as photosensors owing to the advantages they provide, presented later in this chapter.

Local setups, like NUXE-3 at the University of California, San Diego, also made use of SiPMs and serve as a test-bed for these photosensors. NUXE-3 is a single-phase LXe detector for low-energy studies and an R&D effort for future dark matter and neutrino experiments, first proposed in [210]. It aims at demonstrating the feasibility and performance of single-phase TPCs, which avoid problems typical of dual-phase TPCs such as the trapped electrons at the liquid-gas interface, total internal reflections, and non-uniform extraction field due to the non-uniform gas gap [211]. Unlike the design of the dual-phase TPC as introduced in section 2.1, the anode wire is along the vertical central axis of the upright cylindrical TPC, the cathode grids are on the side enclosing the LXe volume, and the concentric field shaping rings are on the top and bottom sides of the TPC. For the photosensors, 96 Hamamatsu VUV4 (S13371) SiPMs were installed behind the cathodes in an octagonal configuration.

This chapter presents the commissioning results with the NUXE-3 SiPM array and the performances of the SiPMs in both GXe and LXe. Section 7.1 introduces the working principle and properties of SiPMs. Section 7.2 describes the NUXE-3 detector and its subsystems. Section 7.3 to Section 7.5 outlines the data-taking, analysis and results for the gain calibrations and dataset with calibration sources.

[1] The DarkSide-20k experiment is using >260,000 FBK NUV-HD-cryo SiPM, $11.7\times7.9\,\mathrm{mm}^2$ [85].
[2] The NEXT experiment is using 3,584 SiPM of Hamamatsu S13372-1350TE, $1.3\times1.3\,\mathrm{mm}^2$

7.1 Introduction to Silicon Photomultiplier

SiPM is a type of semiconductor device sensitive to single photons with a wide range of applications [147]. The typical size of a SiPM is around $\mathcal{O}(1)\text{mm}^2$ [208]. It is a pixelated device, typically featuring 100 to 10,000 pixels [212].

Each pixel, also named microcell, consists of an avalanche photodiode (APD) and a quenching resistor, R_Q, connected in series [212]. Each pixel is then connected in parallel within a SiPM to the bias voltage V_{bias}, which is typically at 50 V. An illustrative diagram and circuit diagram are shown in Figure 7.1.

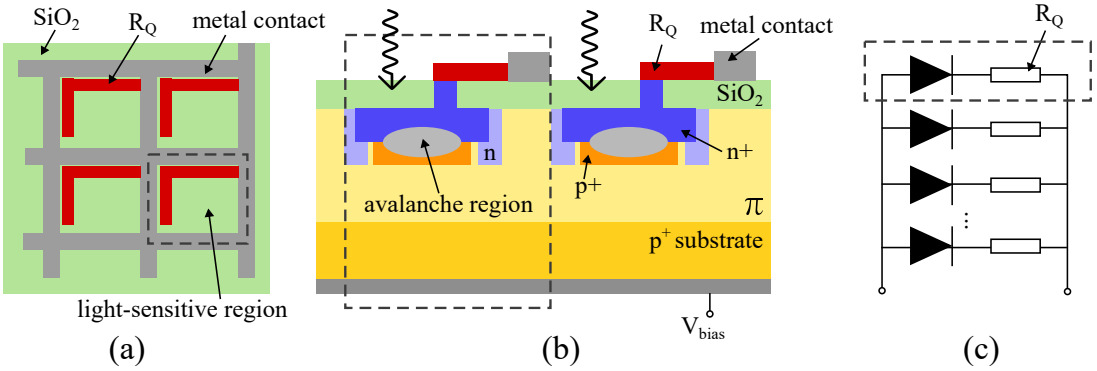

Figure 7.1: Typical structure of a SiPM. The dashed line encloses a single pixel (or microcell). (a) Top view of the SiPM pixels. (b) Side view of the SiPM pixels. (c) Simplified circuit diagram of the SiPM. Figure adapted from [59, 212, 213].

The following will summarise the operation principle of a SiPM and the comparison to PMT in terms of rare-event search experiments. A more complete overview of SiPM can be found in [59, 147, 208, 212–216]

7.1.1 Operation Principle

The working principle of an APD is primarily based on the presence of a p-n junction [212, 216]. Consider a p-n junction, where the p-region has a higher concentration of holes in the valence band and the n-region has a higher concentration of electrons in the conduction band. As the mobile charge carriers (the valence holes and the conduction electrons) diffuse and recombine at the junction, a region with no mobile charge carriers is formed, called the depletion layer. The p-side and the n-side of the depletion layer are left with negative and positive ions, respectively. The ions create an electric field in the depletion layer directing towards the p-region. When an incident photon with an energy greater than the band gap energy is absorbed in the depletion layer, an electron-hole pair is created due to photoelectric effect. The created electron is called single photoelectron (SPE). Due to the presence of the electric field in the depletion layer, the electron and hole do not recombine [212], but drift towards the n- and p-region, respectively. This creates a current pulse in the circuit.

Suppose a reverse bias voltage, V_{bias}, is applied to the p-n junction, that is, connecting the cathode to the p-region and the anode to the n-region. In this case, the depletion region is further widened, and the electric field inside the depletion layer becomes

stronger [216]. Therefore, the electric field inside the depletion region is tuned by V_{bias}.

A schematic diagram of a typical p^+-p-n junction of an APD and the corresponding electric field is shown in Figure 7.2. Similar to the p-n junction, the incident photon generates an electron-hole pair in the p-region. Since an electric field is also present in the p-region, the electron drifts towards the depletion region.

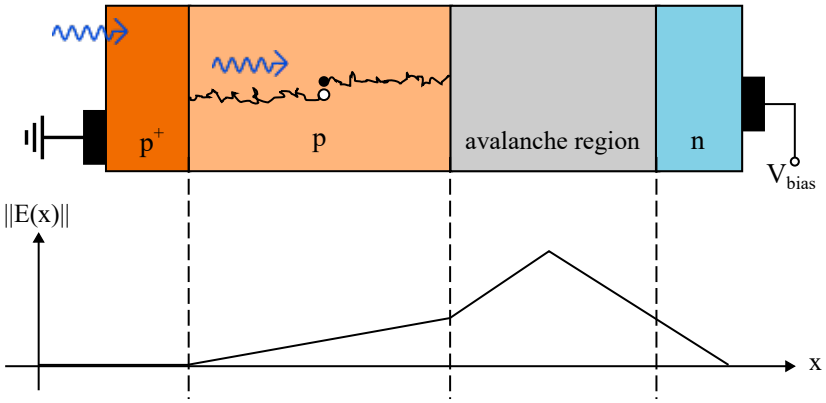

Figure 7.2: Top: schematic diagram of an avalanche photodiode (APD). The incoming photo (blue arrow) enters the p-region and creates an electron-hole pair as indicated by the filled and hollowed circles, respectively. The electron drifts towards the n-side, while the hole drifts towards the p-side. Bottom: corresponding electric field inside the APD. The field inside the avalanche region is enhanced by the presence of the reversed bias voltage V_{bias}. Figure adapted from[212].

When the field in the depletion region is high enough such that the energy of the accelerated electron exceeds the band gap energy ($\sim$1.15 eV for silicon at 175 K [217, 218]). The electron can ionise the atoms upon collision and create an avalanche of electron-hole pairs, thus providing signal amplification [216]. Therefore, the depletion region is also known as the avalanche region.

The additional charge induced by the SPE is defined as the gain. Figure 7.3 illustrates the relationship between the bias voltage and the gain in the different modes of signal amplification [59, 212]. At a low V_{bias}, the charge carriers are not energetic enough to ionise more atoms, resulting in no signal gain. In the linear mode, the avalanche starts to develop. However, the ionisation rate is lower than the extraction rate of the charge carriers, i.e., the rate of the charge carriers being collected by the electrodes, so the avalanche eventually stops. In this mode, the gain increases linearly with V_{bias}. If V_{bias} continues to increase, the ionisation rate eventually surpasses the extraction rate of electrons from the APD. Then, the avalanche becomes self-sustaining, creating an exponential amount of electrons. This phase is called the Geiger mode, and the bias voltage separating the two modes is defined as the breakdown voltage, V_{bd}. The difference between the bias voltage and the breakdown voltage is defined as the overvoltage, $\Delta V = V_{bias} - V_{bd}$.

Due to the avalanche in the APD, the current surges [216]. To protect the APD [59] and allow subsequent measurements [216], a quenching resistor R_Q is connected in series to the APD to quench the current. A typical rating of R_Q is 150 kΩ [212]. A

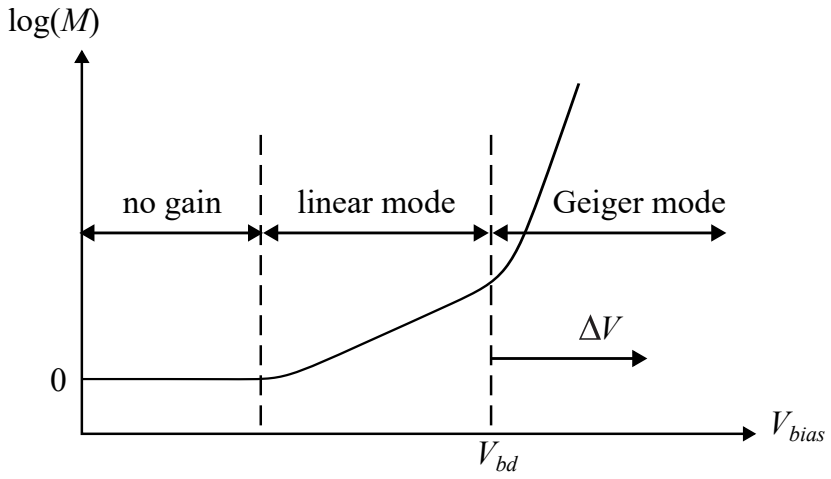

Figure 7.3: Illustration of the relationship between the bias voltage and the gain of an avalanche photodiode (APD). As the bias voltage V_{bias} increases, the APD switches into different modes: the mode with no signal gain, the linear mode, and the Geiger mode. Figure adapted from [212].

single pixel on SiPM is defined as an APD connected to a quenching resistor [212], see also Figure 7.1(c).

The working principle of each pixel is as follows [59, 212]: before the avalanche, consider the APD as being a capacitor, C_j, which is called the junction capacitance. The capacitor is charged up and has the potential difference of V_{bias}. During the avalanche, the APD becomes conducting and has a resistance with a typical value of $\mathcal{O}(100\,\Omega)$ [59, 208]. Therefore, as the current surges, the potential difference across R_Q increases, whereas that across C_j decreases. As the potential difference across C_j drops below V_{bd}, the avalanche is ceased as previously explained. This results in a drop in current back to the value before the avalanche, and C_j is recharged. The resulting signal is a current pulse with the rise time of approximately 1 ns, and the recovery time of $\mathcal{O}(10\,\mathrm{ns})$. The maximum current is proportional to $\Delta V/R_Q$. A more detailed explanation, including the circuit diagram, can be found in [59, 219].

From the above explanation, we can infer the following [212]: when a pixel (an APD connected in series with the quenching resistor) absorbs 2 or more photons at the same time, the resulting current signal always has the same amplitude and duration as the signal induced by an SPE due to the presence of the quenching resistor. On the other hand, if distinct pixels absorb photons simultaneously, the resulting pulse is a superposition of the single-photon pulses, as the pixels are connected in parallel. Therefore, multiple photoelectrons (PEs) correspond to the SPE from multiple pixels. This property also implies a reduction in performance when the SiPMs are illuminated with high photon flux or a localised photon source, as discussed in more detail in [59]. This can be improved by increasing the number of pixels per area [212], but it is also not a major concern for low background experiments like XLZD and when using low energy calibration sources.

The gain M in the Geiger mode is formulated as [147, 212, 216]:

$$M = \frac{Q}{q_e} = \frac{C_j \times (V_{bias} - V_{bd})}{q_e} = \frac{C_j \times \Delta V}{q_e}, \tag{7.1}$$

where Q are the charges produced during the avalanche, q_e is charge of an electron and C_j is the junction capacitance. The typical gain in the Geiger mode is around 10^5-10^7 [147, 213]. The junction capacitance typically depends on surface area [216], the built-in voltage of the p-n junction [212], and the depths of the depletion layer, which are fixed by the architecture of the SiPM [213, 216]. Therefore, the overvoltage ΔV is the determining parameter affecting the gain [212]. Additionally, to achieve a stable gain, an power supply with stable voltage output is required, for example an ultralow-ripple power supply [216].

A subtlety in Equation 7.1 is the temperature dependence in C_j and V_{bd} [214, 215]. While C_j was found to have less temperature dependence, V_{bd} has a linear and significant dependence on temperature [220]. This could be understood as follows: the higher the temperature, the more the atoms within the crystal lattice vibrate, and the lower the mean-free-path of the charge carriers [214]. Therefore, a higher applied voltage is needed to accelerate the charge carriers beyond the band gap energy and initiate the avalanche, resulting in a higher V_{bd}. In short, the higher the temperature, the higher the V_{bd}, or the lower the gain at the same V_{bias}.

In situations where the temperature may vary, to reduce the temperature dependence of the gain M, the change in V_{bd} should be compensated by a change in V_{bias} to maintain the same ΔV. A biasing correction circuit or temperature-compensation circuitry can be used to maintain a stable gain value [219]. Temperature also affects other aspects of the performance of the SiPM, which are less relevant to this work and nicely summarised in [214].

As a summary, when $V_{bias} > V_{bd}$, the avalanche induced from an SPE in a APD is self-sustaining and achieves the signal gain of 10^5-10^7. The avalanche is subsequently quenched by the quenching resistor R_Q, and then the pixel is ready to capture the next signal again. The final output signal from the SiPM is the superposition of the SPE signal from pixels where an avalanche happened [212]. The stability of the gain can be maintained given a stable overvoltage ΔV, even when the temperature varies [215].

7.1.2 SiPM vs PMT

As previously mentioned, SiPM is considered an alternative to the traditional PMT for a rare-event search experiment. The following will compare different factors discussed in [208], but in the context of a rare-event search experiment. This section is complementary to the summary in [221, Section 3.6].

The factors that are comparable between SiPM and PMT are the gain, the jitter, and the detection efficiency. Both photo detectors have a gain of 10^5–10^7. Jitter, as referring to the uncertainty in the arrival time, is generally comparable between the two types, around $\mathcal{O}(100\,\mathrm{ps})$[3] [208]. The detection efficiency of a PMT is known as the

[3] Specifically, the jitter for the VUV4 SiPM was measured at 24 ps with square pulses [222]. That

QE, which is the probability of the photon being absorbed in the active region of the photocathode. That for a SiPM is the PDE, which is the product of the quantum efficiency, geometrical fill factor, and the probability of initiating an avalanche. The two values are comparable between PMT and SiPM.

On the other hand, SiPM and PMT perform differently for the following factors:

- **Dark count rate**: Dark counts are uncorrelated thermal noise. The dark count rate of SiPM was found to be $\mathcal{O}(10-80)$ times higher than the PMT counterpart at LXe temperature [207, 223]. The higher the dark count rate, the higher the accidental coincidence rate in the detector, which becomes a non-negligible contribution to the background in high-sensitivity experiments. For future detectors with even more photodetectors, this becomes a critical problem when considering SiPM [59]. However, with the recent development of a new SiPM reported in [224], the dark count rate was further suppressed down to only 3.5-6.9 times that of its PMT counterpart. Specifically, the dark count rate recorded for the SiPM (MPPC-VUV-LDC-050UM-SPL) at 162 K is 0.035–0.069 Hz/mm^2 [224], while that for PMT (R11410-21) at 173 K is 0.009 Hz/mm^2 [86]. This demonstrated that SiPM can still be a strong candidate for photodetection in future dark matter experiments.

- **Operating voltage**: The operating voltage of SiPM is $\sim$50 V, while that for PMT is $\sim$1500 V [224], making SiPM easier and safer to operate. The low operating voltage can be attributed to the narrow band gap and the avalanche effect within a micrometer-scale semiconductor, as opposed to the voltage divider design of a PMT. Another factor to consider is the performance under an external field around the photosensors. Electrode screens are usually placed in front of the PMT array to protect them from the high field of the electrodes [35, 109, 118]. On the other hand, a study showed that a strong external field (up to 30 kV/cm) perpendicular to the SiPM does not significantly alter the performance of their SiPM samples [225]. A bulk field at or higher than 30 kV/cm is not anticipated for the XLZD, given the cathode potential is $\sim$−70 kV in the baseline design [34], and $\sim$ +10 kV for the anode. Therefore, if the SiPM array is used, the protective electrode screens is not needed. This is beneficial for increasing light collection efficiency, reducing material background, and reducing the risk of failure. Note that the author of [225] suggests doing further testing to confirm the result in long-term stability under HV. Futhermore, the measurement was not performed in a high-sensitivity low-background experiment, so the result might not be a direct indication of their performances in that environment.

- **Robustness**: As a delicate instrument, PMT is prone to failure in a large-scale LXe experiment during years of operation [226, Chapter 5]. One of the causes is the leakage of xenon into the vacuum tube of PMTs [118], which is not a problem for SiPM. On the other hand, SiPM is also known for its mechanical stability and sturdiness, thanks to the semiconductor nature [208].

for the R11410-21 PMT for XENONnT was measured at 9 ns, which is larger than other types of PMTs [84].

- **Area Coverage**: SiPM is more compact and pixelated compare to PMT. Therefore, SiPM offers a better spatial resolution, which might be beneficial for the x-y position reconstruction of an event [59]. However, due to the compact nature of a solid-state sensor, the photosensor itself and the entire sensor array are more challenging to scale up in area coverage compared to PMT. This increases the cost and the burden on readout electronics [219]. A possible solution is to bundle the tiles together to reduce the number of readout cables and feedthroughs [201, 219, 227].

- **SPE resolution**: The SPE resolution of SiPM is better than that of PMT, which is beneficial for photon counting for low-energy search [147] and for the neutrinoless double-beta decay search. It was found that although a bundled readout can reduce the number of electronics, the SPE resolution increases, albeit still lower than that of PMT [147].

- **Signal noise (afterpulse)**: Both types of photosensors have afterpulse, which is the delayed signal induced by the actual signal, though with different origins [59]. In the case of PMT, the initial PEs might ionise some residual gas particles in the vacuum tube; then the positively charged ions will induce more PEs at the photocathode [84]. In the case of SiPM, some electrons might be trapped inside the band gap during the avalanche process due to the presence of impurities [59]. The trapped electrons will later induce either a signal that is indistinguishable from an actual signal, or a smaller signal in the tail of the primary signal, depending on the time of release [59]. In either case, after-pulsing increases dead time and accidental coincidence. From [59], the afterpulse of the SiPM by Hamamatsu that is sensitive to the xenon scintillation light (Hamamatsu VUV4) was measured at around $5-20\%$. The afterpulse rate of a specialised model can be suppressed to $< 1\%$ probability [208, 216].

- **Signal noise (crosstalk)**: SiPMs have an additional noise contribution called *crosstalk*, which is the correlated signal induced by neighbouring pixels. The crosstalk signals have different causes and time scale, but typically at $\mathcal{O}(10)$ns [202, 213]. Although it has been reduced due to recent developments, it is unlikely to reach zero, as individual pixels cannot be fully optically isolated [208].

- **Radioactivity**: The radioactivity of unoptimised SiPMs has shown lower levels compared to that of PMTs that have undergone dedicated low-radioactivity optimisation [91, 207, 228]. SiPMs might have the potential to have even better radiopurity [207], which is critical for a high-sensitivity low-background experiment.

In addition, SiPM is insensitive to magnetic fields but can be damaged by high neutron radiation, while PMT is the opposite [147, 208, 229, 230]. However, these are less of an issue for experiments such as XLZD, where magnetic field and strong neutron sources are absent. The work from [230] suggested that the SiPM may withstand a neutron flux up to 6×10^{12} n/cm^2.

7.1.3 Hamamatsu VUV4 S13371

For the photosensor, the NUXE-3 detector is equipped with 96 Hamamatsu VUV4 *SiPM tiles* (model S13371-6050CQ-02) [231]. This model is a preconfigured array of 2×2 *SiPM units* with ceramic package and quartz window, which can be read out independently or in combinations (see Figure 7.5 top right) [59]. Note that the casing is not hermetically sealed to allow LXe to enter [231]. Each SiPM unit has an area of $5.95 \times 5.85\,\mathrm{mm}^2$, 13,923 pixels, and 50 µm pitch resulting in a fill factor of 60% for the tile [222, 231].

The VUV4 SiPMs were first designed for the MEG-II experiment [232]. Other experiments also tested this model extensively, including the nEXO experiment [202, 203, 233], the LoLX experiment [222], and Prof. Baudis' group [147, 207, 209, 221].

The PDE at 175 nm in vacuum conditions was measured at 24% by Hamamatse Photonics K.K. [231] and at $20.5 \pm 1.1\%$ measured by nEXO collaboration [202]. This is lower than the QE of on average 35% of the PMTs (Hamamatsu R11410) used in XENON1T and XENONnT [228]. With a lower detection efficiency, the detector detects fewer light signals, thereby increasing the detection threshold for energy deposition. Nevertheless, as mentioned, the radiopurity of this SiPM model is comparatively lower than the PMT counterpart [207]. This would reduce the detection dead time of the detector, and thus increase the exposure and sensitivity for rare signals.

7.2 The NUXE-3 Detector

The NUXE-3 detector, which is the successor of the Liquid Xenon Proportional Scintillation Counter [211], can house $\sim$10 kg of LXe and utilises 96 Hamamatsu VUV4 S13371 SiPM tiles as the photosensors, as shown in Figure 7.4 [234]. The array of SiPMs is arranged around an octagonal cylinder. The detector also consists of three electrodes and four field shaping rings to provide an axially symmetric (i.e., from the center of the cylindrical detector out to the walls) drift field and multiplication field for 3D event reconstruction. The cathode is right in front of the SiPM array and defines the active volume of the detector. However, the electrodes were not used in this test campaign, as they were not required for the gain calibration or determining the LCE in this detector. A PTFE case encloses the detector volume to increase the reflectivity, but it is not hermetic. The following will introduce each subsystem in more detail.

The entire detector is contained within a vacuum-sealed inner vessel with feedthroughs for voltage biasing and signal readout. A turbo pump, either a turbo pump from Pfeiffer Vacuum (model HiCube) or the TPS-compact pump from Apilent Technologies, was used to provide vacuum insulation between the inner and outer vessels. Note that the insulation layer at the bottom of the cryostat is thinner due to the HV feedthroughs for the electrodes.

The cooling power was provided by the cryocooler from Sumitomo Cryogenics (model CH-100LT). The cold-head temperature was regulated by a PID temperature controller from Lakeshore (model 336), which received input from a temperature sensor located near the cold-head. The controller regulated the power of the resistive heaters, which

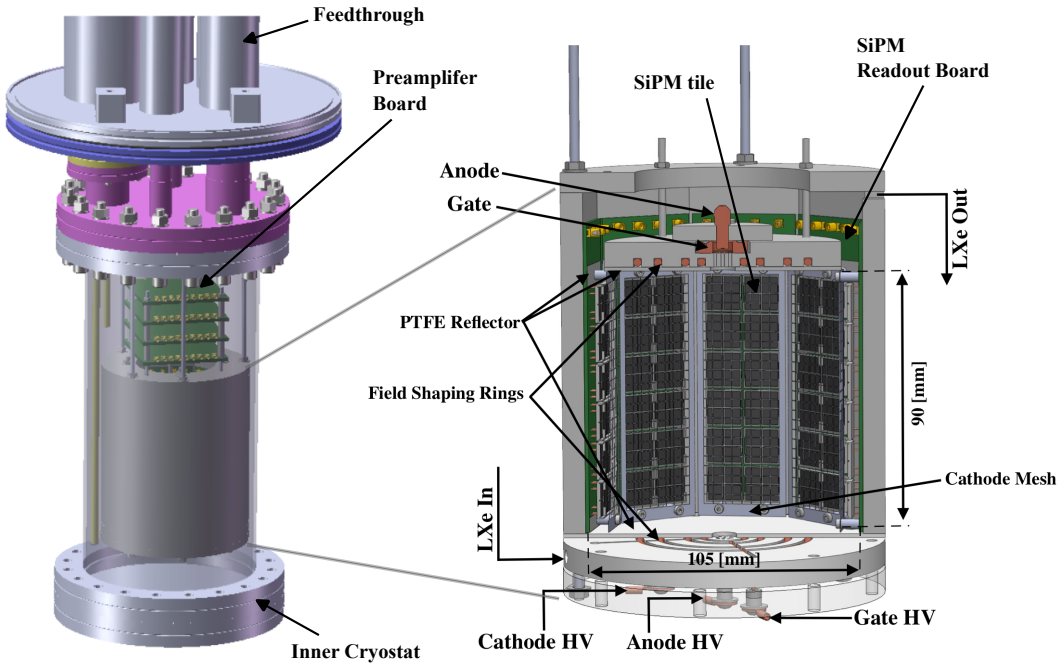

Figure 7.4: CAD drawing of the NUXE-3 detector. Left: the NUXE-3 detector with the inner cryostat. Right: cut-out of the NUXE-3 detector, showing the interior with the silicon photomultiplier (SiPM) array.

surrounded the cold-head, to stabilise the temperature around the setpoint. After filling, the pressure changes according to the set temperature for the saturated xenon fluid system inside the closed gas system. The temperature reading was stable with $\mathcal{O}(0.1)$K fluctuation, while the pressure sensor was not sensitive enough to register any fluctuation. The amount of xenon inside the detector was estimated with the weight cells of the xenon storage bottles.

As briefly mentioned in subsection 7.1.2, to reduce the amount of electronics and cabling, experiments usually bundle the SiPM array together, i.e., combining several channels into a single channel [201, 219, 227]. Possible bundling methods include connecting in parallel, in series, or a hybrid form [219]. With the parallel connection, the input capacitance increases with the number of SiPM and therefore reduces the time response, and the noise level also increases [219, 227]. This potentially reduces the signal discrimination capability and increases the energy threshold. In addition, the connection in parallel should ideally be accompanied with a biasing correction circuit, as explained in subsection 7.1.1, in case the intrinsic breakdown voltage of the connected SiPM is inhomogeneous [219]. Otherwise, the SPE resolution can be worsened due to the different response from the SiPM combined into a single output. On the other hand, while a series connection can avoid these issues, the connection introduces time differences between the connected SiPM [227]. In the hybrid mode, 2 or more SiPM connected in series are connected in parallel [219], as demonstrated in [235].

In the NUXE-3 detector, custom-made baseboards bundle every 4 SiPM tiles in paral-

lel to readout as a single *SiPM channel*. Therefore, there are in total 24 SiPM channels, corresponding to the total of 96 S13371 SiPM tiles, and corresponding to a total of 384 SiPM units. To further reduce the amount of electronics and cabling, each baseboard accommodates 3 SiPM channels, arranged vertically but electronically separated. Therefore, there are in total 8 baseboards, each with 3 SiPM signal outputs, as illustrated in the lower part of Figure 7.5. The baseboards also distribute the V_{bias} to the 3 channels on the board in parallel, but without the biasing correction circuit. The 8 baseboards form the octagonal cylinder surrounding the active volume behind the cathode electrode inside the NUXE-3 detector.

The output signal of each SiPM channel from the baseboards is then connected to the preamplifier board, which is designed and provided by the nEXO collaboration. The preamplifier boards amplify the output signals and also distribute V_{bias} to the baseboards. Note that in some cases, the baseboard and the preamplifier board were combined into a single circuit board [147, 209]; they are separate boards in the NUXE-3 experiment, each with a different number of connection channels.

There are in total 5 preamplifier boards to provide signal amplification and distribute the bias voltages, as shown in Figure 7.4 (left). Each preamplifier board receives signals from 4-5 SiPM channels, while distributing the V_{bias} to 1-2 baseboards. Note that the connections for an SiPM channel to the V_{bias} and signal amplification might be on different preamplifier boards. The connections of the SiPM channels to the respective V_{bias} and signal amplification on the preamplifier boards are summarised in Figure 7.5.

Each preamplifier board consists of operational amplifiers which require $+5$ and -5 V input voltage. They were either powered by a KEYSIGHT E3630A Triple Output DC Power Supply, which outputs a fixed ratio between the voltage source, or two GW Instek GPS-1850D power supplies with a common ground. The five V_{bias} to the preamplifier boards were initially provided by CAEN SY4527LC and CAEN A7038STN 32 Channels 1 kV/100 µA power supply board before a power failure. It was then changed to a combination of four channels from CAEN DT5533N and one channel from CAEN N1471 power supplies.

To read out the signal from the 24 channels, we used two CAEN V1725 analog-to-digital converter (ADC) boards, each of which has 16 channels, with a sampling rate of 250 MS/s, 14-bit, and 2 V_{pp} range [236]. They are subsequently referred to as *ADC board-0* and *board-1*. All connections from the detector to power supplies and the ADC board are summarised in Figure 7.6.

Since the noise level for individual channels varies, the trigger threshold was predetermined before data taking. 3000 events were taken for each channel, where the standard deviation (σ) of the baseline was measured. Then, the threshold was set at multiples of σ, ranging from 3 to 10, away from the baseline.

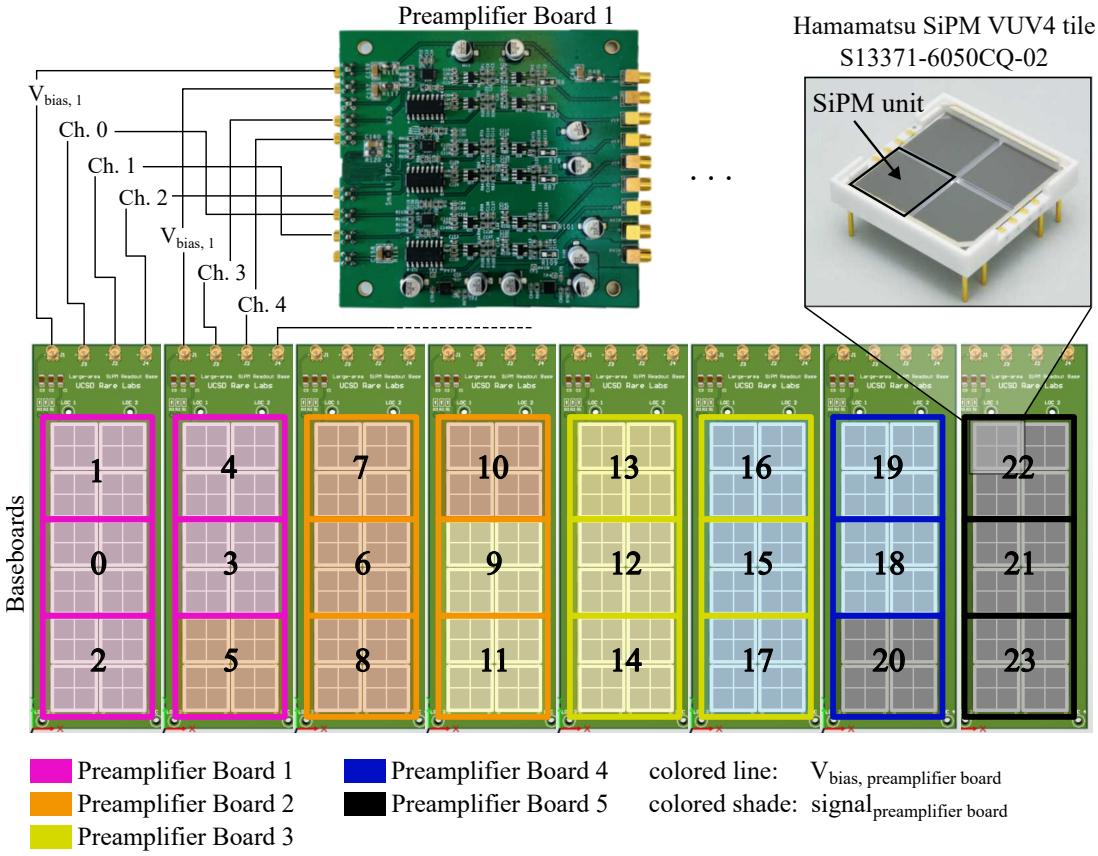

Figure 7.5: Illustration of the SiPM readout arrangements. The lower part of the image shows the 8 baseboards, unwrapped from the cylindrical configuration in the detector (see Figure 7.4 right). Each baseboard contains 3 SiPM channels, and each channel contains 4 SiPM tiles. A numerical identifier is marked on each SiPM channel. Each baseboard has 3 signal outputs for the 3 channels, and a V_{bias} input. Therefore, there are in total 24 signal outputs and 8 V_{bias} input connections from all the baseboards. They are distributed to 5 preamplifier boards. Note that the V_{bias} and the signal output from the baseboard may connect to different preamplifier boards. An example of the preamplifier board is shown on the top-left side, together with the schematic connections to the baseboards. Each preamplifier board receives signals from 4-5 SiPM channels, while distributing the V_{bias} to 1-2 baseboards. Shaded boxes show the corresponding preamplifier board connected to each SiPM channel: each color indicates the preamplifier board as shown in the legend, the outline corresponds to the V_{bias} connection, and the shade corresponds to the signal output connection. The top-right side shows the image of the VUV4 SiPM tile [231] used in NUXE-3.

7.3 Datasets and Operations

There were in total 3 runs in this measurement campaign, 2 in which the detector was filled with GXe only, and 1 in which the detector was fully filled with LXe. They are subsequently named *GXe-1*, *GXe-2*, and *LXe-1*. Between the runs, the detector was warmed back up to room temperature.

During the GXe runs, the detector was filled with $\sim$300 g GXe and the controllor set-point was set to $\{167, 169, 171, 173, 175\}$K. Note that the temperature on the preamplifier board or next to the SiPM array was not measured, but is likely to be higher than the mentioned set values due to the heat dissipation on the readout electronics.

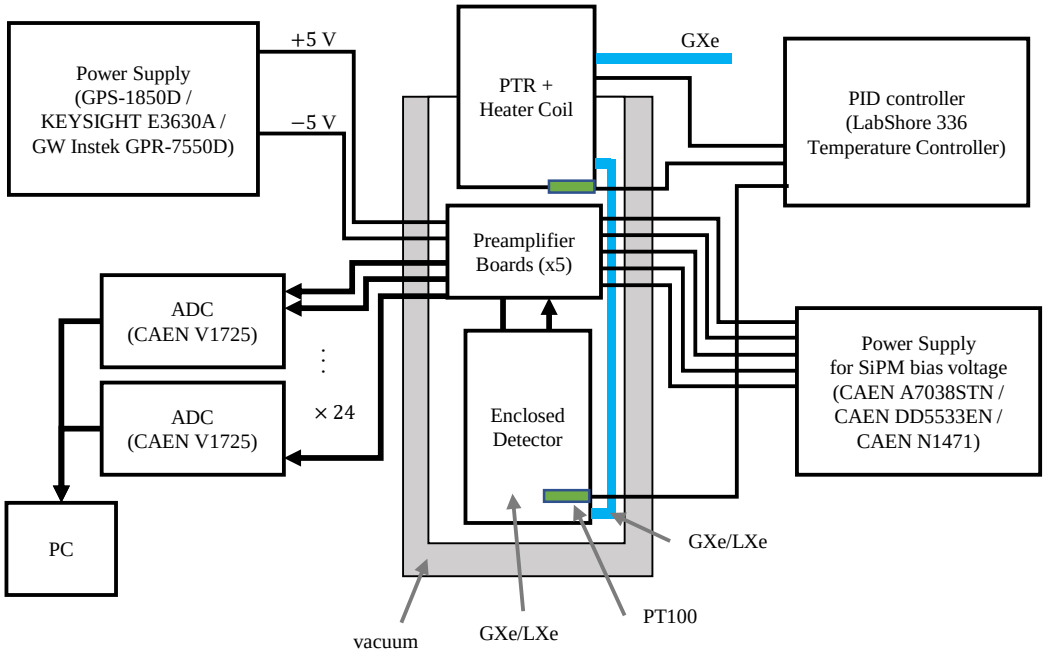

Figure 7.6: Schematic diagram of the setup. The circulation and purification system is omitted for simplicity. The blue lines indicate the piping for GXe or LXe inlet. The green boxes indicate the PT100 temperature sensor. The arrows indicate the signal output connection. Solid lines without arrows indicate connections in general.

The temperature range in this measurement was narrower compared to other existing measurements. This is because the insulation layer at the bottom of the cryostat is thinner due to the HV feedthroughs, reducing the insulation power. At these temperatures, part of the GXe was liquified and formed a buffer to isolate the heat from the bottom of the cryostat. This allowed the system to reach an equilibrium state before any data-taking began.

During LXe run, the detector was filled with $\sim$10 kg LXe at 175 K. The liquid level was estimated by the difference in the weight of the xenon bottles, as well as the light signal measured by the SiPM photosensors. It was observed that when the liquid was not fully covering all SiPM, the bottom SiPM channels observed more light as expected. From the CAD model of the detector, it is estimated that after filling the xenon, the liquid surface barely touched the lowest preamplifier board, as shown in Figure 7.4 (left), meaning that all the SiPMs were covered by LXe.

After filling, the xenon gas was circulated by a pump through the MonoTorr Heated Getter Purifiers by SAES Pure Gas [237]. The flow meter regulated the flow rate at around setpoint, which will be discussed in section 7.5. The cooling power of the cryogenic system compensated for the heat loss during circulation and transfer.

For the data-taking, we used the self-triggering mode with the Waveform Recording firmware. Appendix E explains the details of the self-triggering scheme. In particular, with the configuration of 24 SiPM output signal channels and two v1725 boards, it

is not possible to achieve channel-level coincidence. Therefore, in this study, no coincidence was configured for the data-taking. The clock was synchronised across the boards, with a time delay of around 0.04 s. This enables offline software trigger and channel-level coincidence across the boards.

With the Waveform Recording firmware, the ADC board records the waveforms of all enabled channels within a fixed acquisition window upon receiving a trigger. This firmware simplifies the processing when utilising NumPy array slicing to analyze waveforms across all channels. On the other hand, while the Dynamic Acquisition Window firmware may offer improved analysis efficiency when performing pulse-level analysis, the firmware can result in excessive dead time at high data rates or with a high-activity source for energy calibrations.

Each dataset, in binary format, contains metadata of the detection configuration and information for data selection and cuts, including the operating temperature, the applied V_{bias}, run tag, data-taking mode, triggering threshold for each channel, the ADC board used, and other relevant configurations. Each dataset contains only one entry for the operating temperature and V_{bias}, as the five V_{bias} inputs were set at the same value.

There are two data-taking modes: *single-channel mode*, where only a single channel was enabled for the ADC boards, and *all-channels mode*, where all channels were enabled. The single-channel mode was used for single-channel triggering, which is presumably desirable for the gain calibration, especially for noisier channels. It was later found that, due to the high dark count rate, the all-channels data-taking mode also allows for the identification of SPE pulses and subsequently the gain calibration, as explained later.

7.4 Characterisation of the SiPM Array and the Readout

This section presents the results of the gain calibration and an observation on the noise level. The dark count rate, which is highly temperature-dependent, was not measured due to limitations. In order to measure the dark count rate at low temperature, noble gases cannot be used due to the intrinsic scintillation light. In addition, the detector could not reach thermal equilibrium during the time of the operation for other common inert gases like N_2. Similarly, the cross-talk probability was not measured, as it requires the dark count measurement.

Data was taken at different bias voltages and different temperatures. The temperature variation was narrow and did not account for heat dissipation from the electronics, as mentioned in section 7.3. The temperature T was set at $\{167, 169, 171, 173, 175\}$K. The bias voltage V_{bias} was set at $\{-46, -47, -48, -49, -50, -51, -52\}$V. The data at V_{bias} at −46 V was excluded from the calibration as the SPE positions were easily misidentified.

7.4.1 Gain Calibration

The gain calibration was performed for each channel in all datasets separately. The standard procedure of determining the gain is by looking at the integral voltage distribution, known as the *finger plot*, as shown in Figure 7.7. The finger plot was obtained by integrating the area of each waveform above baseline within a time window around the trigger. The peak at around zero is the noise pedestal, the first peak above zero corresponds to the signal from SPEs, and the subsequent peaks correspond to multiple PEs.

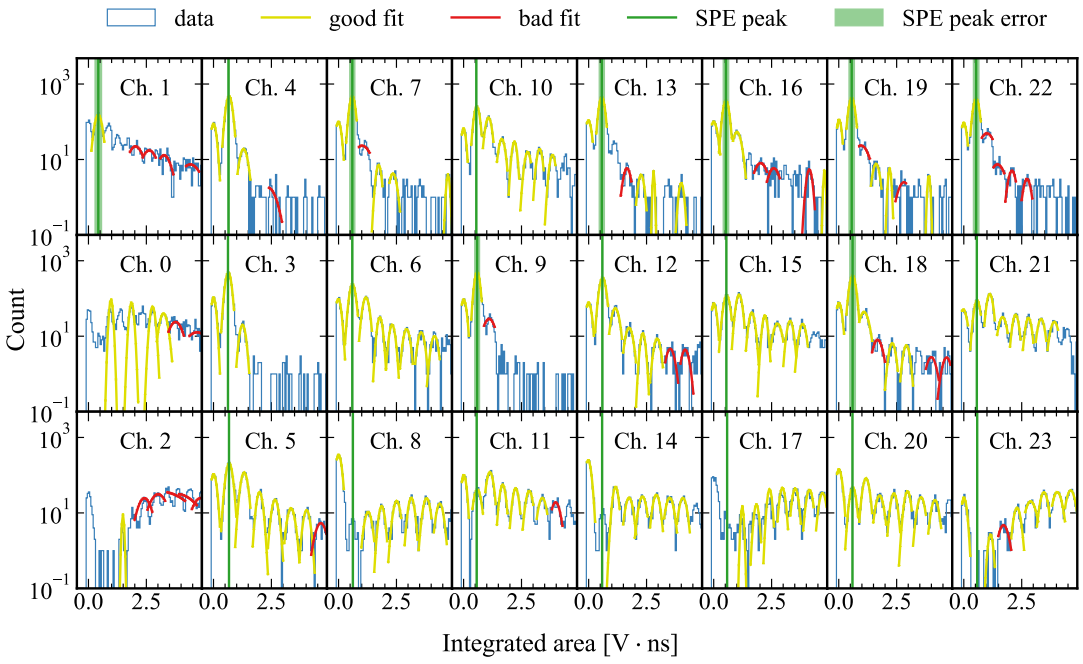

Figure 7.7: Example for determining the SPE location for all SiPM channels from one of the datasets. The numbers on each subplot indicate the SiPM channel, consistent with the relative position as shown in Figure 7.5. The blue histogram shows the integral area of all events in a dataset. The yellow and the red lines indicate the Gaussian fits for multiple PEs, while yellow and red represent a good fit and a bad fit, respectively. The green vertical line indicates the final determined SPE position and the corresponding error.

As explained in subsection 7.1.1, the additional peaks or "fingers" correspond to multiple SPE, and consecutive peaks are separated by one SPE. Therefore, to robustly determine the SPE position in our measurement, multiple peaks with a rough initial guess were fitted with a Gaussian function $G(\mu, \sigma)$, where μ is the mean and σ is the standard deviation. The fits were classified as either a good or a bad fit with an arbitrary choice of the fitting error of $\mu > 0.03$. The average distance between consecutive well-fitted peaks was determined as the SPE position. The error of the SPE is the standard error. The SPE resolution is defined as $\sigma_{\text{SPE}}/\mu_{\text{SPE}}$ of the SPE peak [238]. If the number of well-fitted peaks is less than 3 or without consecutive well-fitted peaks, the algorithm checks if the highest well-fitted peak is around the rough initial guess position, accompanied by the uncertainty of σ, such as the plot for SiPM channel 1, 18, 19, and 22 in Figure 7.7.

The SPE position of each channel at each V_{bias} across all the runs, that is, both in GXe

and LXe, is shown in Figure 7.8. We can observe the expected strong dependence of SPE position on the applied V_{bias}. The error bar represents the standard deviation across all included datasets for each channel and V_{bias}, accounting for variations in temperature and the different power supply used during maintenance. On average, the percentage error on the SPE position per channel per bias voltage is 7.4% and a maximum of 13.6%. These non-negligible systematic errors will contribute to the uncertainty of the energy reconstruction if only the average SPE position is used. Therefore, one should perform the gain calibration regularly to reduce the systematic variations.

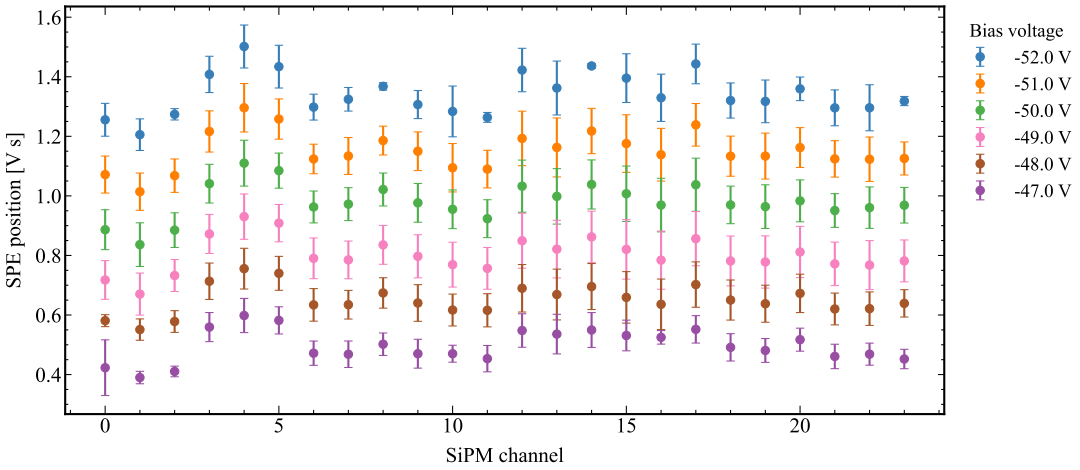

Figure 7.8: SPE position for all the channels at different bias voltages. The x-axis indicates the SiPM channel, consistent with the numbering in Figure 7.5. Each color represents a bias voltage V_{bias}. The error bar represents the standard deviation across all datasets for each channel and V_{bias}.

The variation of the SPE position across channels is significant. At $|V_{bias}|$ =47 V, the percentage difference between the highest and the lowest SPE position across channels is 52.5%, gradually reduced to 25.0% as $|V_{bias}|$ increases to 52 V. Nevertheless, this does not affect the energy or signal reconstruction as the calibration should always be performed independently between channels.

The majority of the SPE resolution was measured to be less than 20% for the gain greater than 1×10^6 and has a negative correlation with the gain. The result of the SPE resolution is consistent with the values reported in [147], where they also bundled the SiPM units in a group of four. However, without the LED and external trigger, the SPE peak is less prominent and induces a significant fitting uncertainty to the σ of the Gaussian function. Therefore, the result is noisier compared to the mentioned measurement, making it difficult to draw a more quantitative conclusion.

The gain M is obtained by the following formula:

$$M = \frac{\text{SPE}\,[\text{V s}]}{R_{imp}\,[\Omega] \times q_e\,[\text{C}]}, \tag{7.2}$$

where SPE is the SPE position, R_{imp} is the input impedance, which is 50 Ω, and q_e is

the charge of an electron. Note that the measured gain here is the gain from a single SiPM channel combined with the gain from the preamplifier.

From Equation 7.1, to correlate the gain M and the overvoltage ΔV, the breakdown voltage V_{bd} has to be determined. One way to determine V_{bd} is the following [213]: extrapolate the linear relation between M and V_{bias} down to $M = 0$. The interception on V_{bias} at $M = 0$ is the V_{bd}. Then $\Delta V = V_{bias} - V_{bd}$. As mentioned, since each dataset contains only one V_{bias}, all datasets were grouped approximately every 10 days to contain different values of V_{bias} for the fit. Only the groups with more than 3 different V_{bias} values were fitted with the linear function to determine V_{bd}, as shown in the example of Figure 7.9.

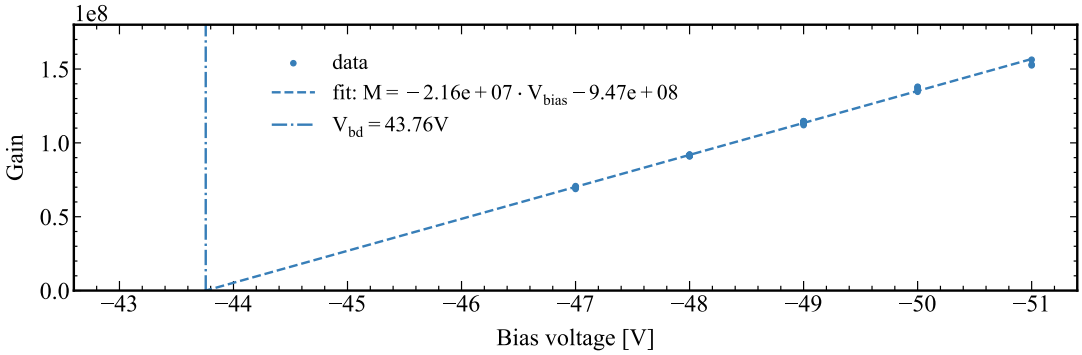

Figure 7.9: Example of determination of the breakdown voltage V_{bd}. The data points shown are from several datasets, spanning approximately 10 days. The data points were fitted with a linear function, with the parameter annotated in the legend. The breakdown voltage V_{bd} was given by the x-interception of the linear function.

Figure 7.10 shows the gain vs ΔV from all the runs at different temperatures and with different power supplies. Note that the gain in this plot was divided by the gain from the preamplifier, which is around 33 [239], therefore showing approximately the gain of the SiPMs. Results from other experiments were also shown in comparison.

From Equation 7.1, the junction capacitance C_j can be obtained by the slope in Figure 7.10 multiplied by the charge of an electron. The variation across SiPM channels and at various temperatures is shown in Figure 7.11. The result aligns with the existing literature, as shown in the same plot. The lower subplot shows the standard deviation of the channel divided by the mean value. The overall variation of C_j for all the runs is within 4.1% for an individual channel. The same plot for breakdown voltage V_{bd} is shown in Figure 7.12, with the overall variation of each channel less than 1.0%.

7.4.2 Noise Level

Ideally, with the mentioned procedure, the gain calibration can be performed for all the datasets. However, occasionally, the noise level increased substantially throughout the runs, limiting the analysis pipeline's capability to identify the SPE position for all the datasets.

While the noise occasionally fluctuated as some cables were reconnected between the power supplies, hinting at a connection issue, there were also occasions where the

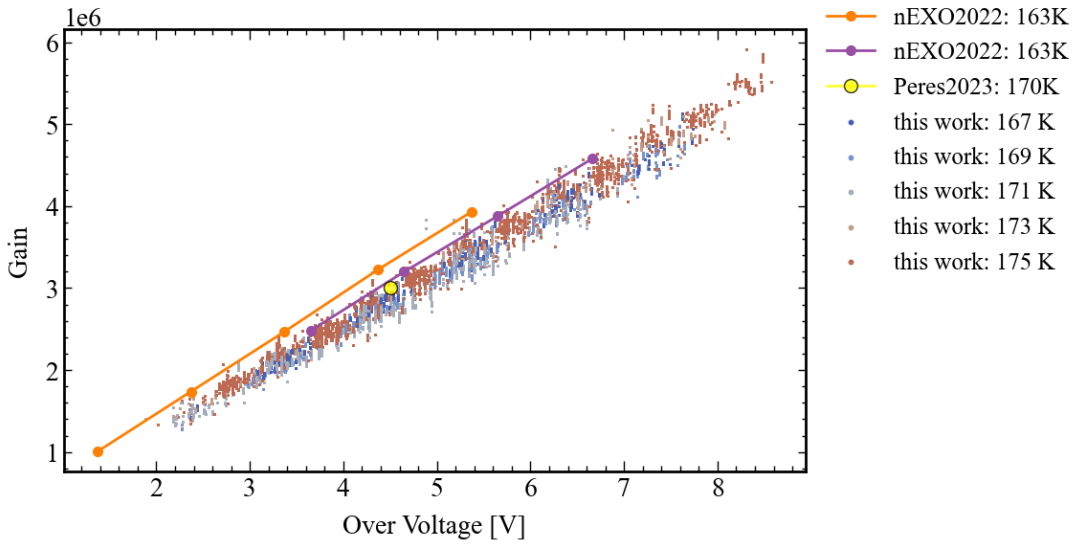

Figure 7.10: SiPM gain against overvoltage at different temperatures for all the calibration runs and the science run. The results from [202] is labelled as *nEXO2022*. The result from [240] is labelled as *Peres2023*. The legend also annotates the (reported) temperature of the measurements.

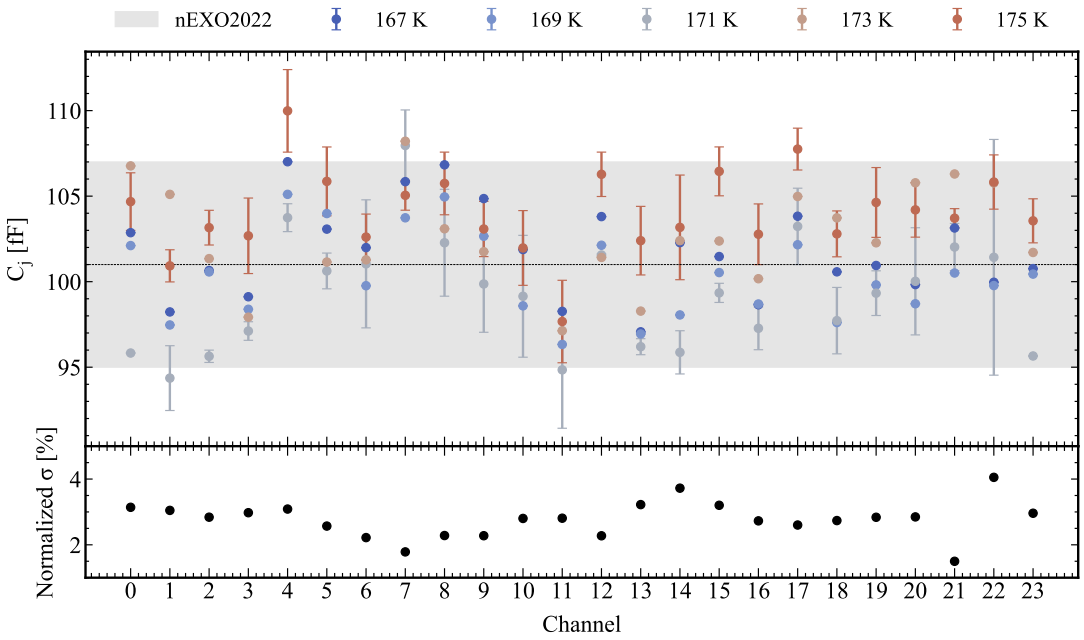

Figure 7.11: Upper plot: junction capacitance C_j across all the SiPM channels at different temperatures. The results from [202] (dashed line) are shown for comparison. The gray band corresponds to the error reported. Lower plot: the standard deviation of the channel divided by the mean value.

noise level fluctuated without any manipulation or handling. The exact cause of the fluctuation of the noise level was inconclusive due to limited statistics or information.

Apart from the fluctuation of the noise level, Figure 7.13 shows the averaged noise level for all the datasets for each channel. The noise for each dataset was obtained

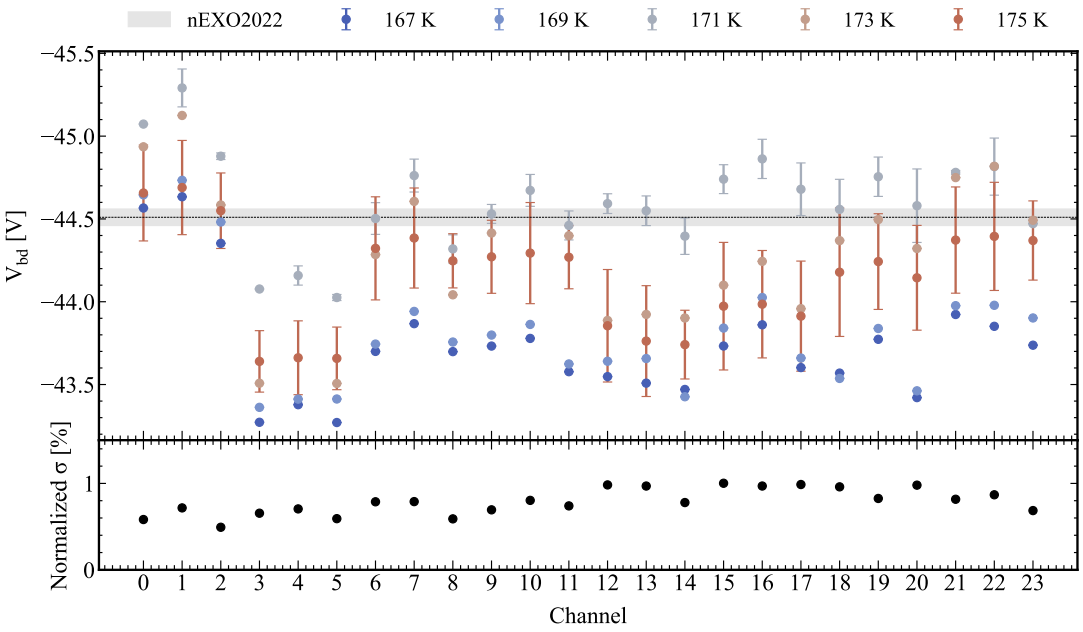

Figure 7.12: Upper plot: breakdown voltage V_{bd} across all the SiPM channels at different temperatures. The results from [202] (dashed line) are shown for comparison. The gray band corresponds to the error reported. Lower plot: the standard deviation of the channel divided by the mean value.

by the standard deviation of the raw waveform around the baseline before the triggering. The channels are arranged according to their relative physical location on the baseboard, as shown in Figure 7.5. From the figure, the lower the layer of the SiPM channels, the relatively higher the noise level. This suggests that the noise is partly due to electronic noise from the baseboard, where the circuit path is longer.

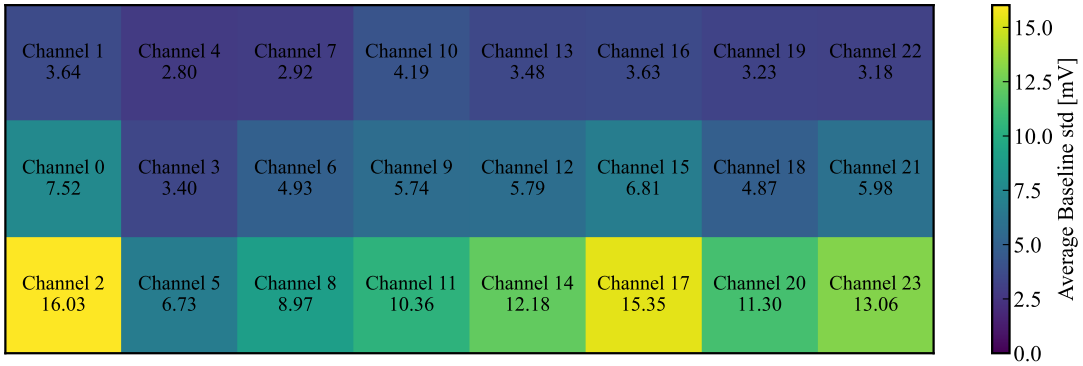

Figure 7.13: Average standard deviations around baseline for each SiPM channel. The numbers on each subplot indicate the SiPM channel, consistent with the relative position as shown in Figure 7.5. Both the numbers on the tile plot and the color bar indicate the value for each SiPM channel.

As mentioned in section 7.2, the trigger threshold was therefore pre-determined individually for each channel before data taking. 3000 events were taken for each channel, where the standard deviation (σ) of the baseline was measured. Then, the threshold was set at multiples of σ, ranging from 3 to 10, away from the baseline.

7.5 Pulse-level Analysis

As described in section 7.3, we configured a board-based global trigger without coincidence and utilised the Waveform Recording firmware for data acquisition. Therefore, a dedicated offline pulse-finding algorithm was implemented to identify and process the pulses in each waveform. This analysis is subsequently called the pulse-level analysis, which enabled studies for afterpulsing and event selection with coincidence, and more.

A pulse finding algorithm was implemented to identify pulses and determine the basic parameters such as the *pulse start time*, the *pulse area*, the pulse height, and the pulse width. The following summarises the procedure:

1. Smooth the waveform using a *rolling average window*.

2. Identify pairs of samples where the ADC counts exceed the *pulse-finding threshold* as the start and end point of the pulse candidates. The difference between the two samples in each pair defines the *naive width* of the pulse candidate.

3. Discard pulse candidates whose naive width is smaller than the *minimum allowed width*.

4. Note that the start and end samples are currently defined with respect to the pulse-finding threshold, not the baseline. Shift the start and end positions to the baseline (i.e., the first sample above baseline) to form updated pulse candidate pairs.

5. Merge any overlapping pulse candidates.

6. Calculate all pulse parameters.

After trials, the parameters of the rolling average window, pulse-finding threshold, and the minimum allowed width were set at 6 samples, 3 root mean square of the baseline, and 18 samples, respectively. With these settings, an example of a processed waveform is shown in Figure 7.14, where the pulses above the thresholds were correctly identified, and the respective pulse area was listed in the figure.

As a cross-check, the area spectrum with the pulse area within a dataset was compared to the integral window area of each channel (i.e. Figure 7.7). While they are in good agreement, the pulse-level analysis is far more computationally expensive.

From the same example in Figure 7.14, we can also see the signal undershooting below the baseline after the main pulse, which is an undesired electronic artifact that would induce a downward bias of the obtained pulse area. The larger the pulse, the more the signal undershoots. In addition, we can observe that there are small pulses following the main pulse. These smaller pulses are probably caused by afterpulsing originating from the same event.

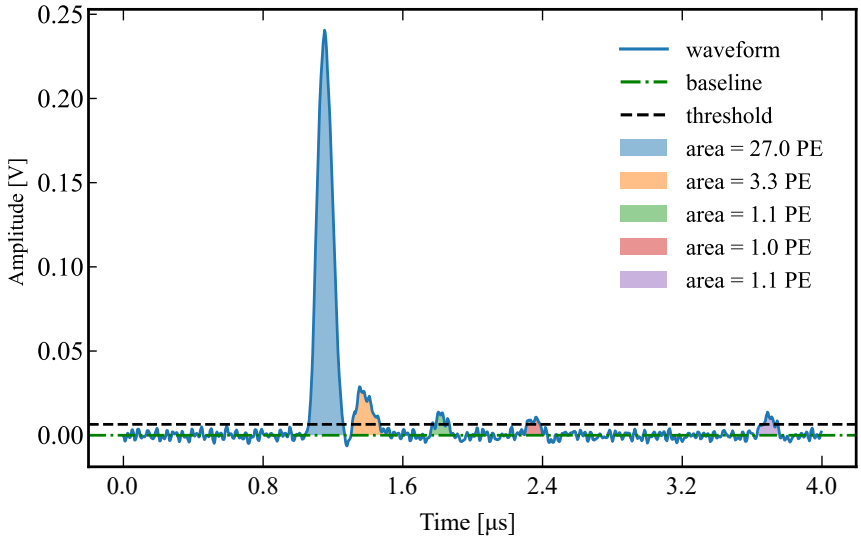

Figure 7.14: Example waveform with the identified pulses and the respective areas. The blue solid line is the waveform with a low-pass filter applied and baseline subtracted. The dashed-dotted line, which is the baseline, is therefore at 0 V. The dashed line indicates the threshold of pulse finding at 3σ away from the baseline. The found pulses are shaded with colors, and their respective areas above the baseline are listed in the legend.

All the results shown in the following were taken where the SiPMs were all covered by LXe at 175 K with around 0.1 K uncertainty from the sensor readout. The LXe was purified continuously by the circulation system. Figure 7.15 shows the example distribution of the pulse area and the pulse start time within a recording window for **a single dataset**. The trigger was set at 1 µs of the 4 µs recording window, where the majority and the large area pulses (main pulses) were located. The position of SPE slightly reduces after around 2.25 s. Although the exact cause is unclear, it is worth for future investigation.

Another observation is that a large population of pulses was identified after the main pulse, in contrast to the insignificant distribution of pulses located before the trigger time. This strongly suggests that the smaller pulses after the trigger time were correlated with the main pulses. Typical timescales of delayed cross-talk are around $\mathcal{O}(10)$ns [202, 213]. Therefore, the main contribution to these correlated pulses should be due to afterpulses.

The time difference between the first pulse and the subsequent pulses was determined for each event in a dataset. This histogram of the time difference is shown in Figure 7.16, where the main pulse is at 0.0 µs and an exponential decay can be observed between the time 1.0 and 2.5 µs. The distribution before 1.0 µs was diminished due to the presence of the main pulse.

The same procedure was repeated for 52 datasets, partly with injected tritium and purification circulation, at different bias voltages between −47 and −51 V with 613,449 events in total. The triggering position is all at 1 µs and in LXe. On average, the decay time scale is 4.2 ± 0.7µs, where the standard deviations give the error for all the

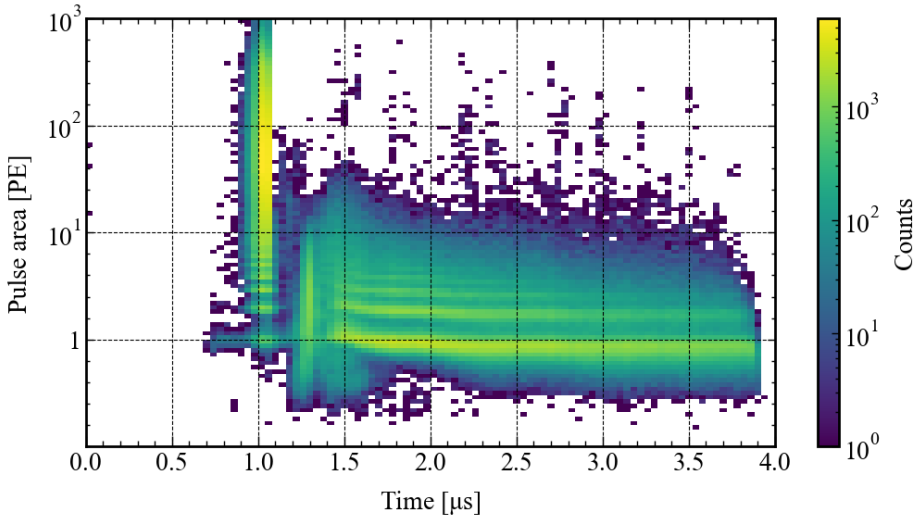

Figure 7.15: Pulse area against the pulse start time within the recording time window, stacked for all channels. Both the color-axis and the y-axis are in log scale for better visualisation. The single photoelectron (SPE) position is at y = 1.

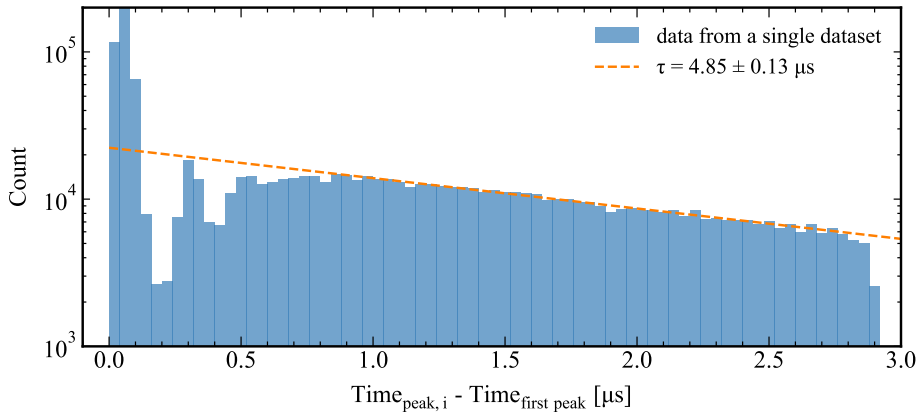

Figure 7.16: Histogram of the time difference between the pulse start time ($\text{Time}_{\text{peak, i}}$) and the start time of the first pulse ($\text{Time}_{\text{first peak}}$) in the recording window for a single dataset with 18,499 processed events. After around 1 us, the rate of pulses reduced exponentially, with a decay time constant of 4.85 ± 0.13µs. The reported error was from the fitting error. The fit was performed on 1,073,153 identified pulses.

datasets. Therefore, the recording time window after the trigger should be longer than 4 µs for a more accurate energy reconstruction.

In addition, as shown in Figure 7.17, the decay time of these correlated pulses positively correlates with the date of measurement and the absolute bias voltage V_{bias} in the span of 10 days. The power supplies for the preamplifier were changed in between, but this does not affect the result. This correlation might be reasoned by the following: as more electrons were produced, more electrons were cumulatively trapped in the impurities in the depletion layer of the APD, and therefore, more were released upon a main pulse. A longer-term study should be performed in the future to verify this behaviour.

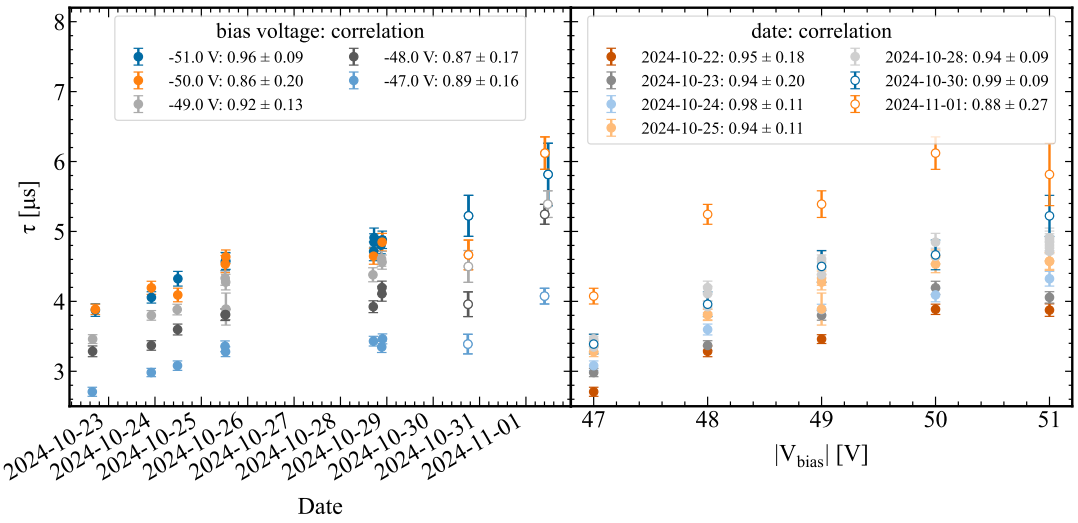

Figure 7.17: Afterpulse dependence on date and bias voltage. The hollowed points are data with injected tritiated methane and a purification circulation. Left: the decay time against the date of measurement. Right, decay time against the absolute bias voltage V_{bias}.

An additional undesired electronic artifact identified was the distorted waveforms due to saturation, which were prominent in the tests with LXe and irrelevant for the gain calibrations. Figure 7.18 shows the superimposed waveforms. On the left, the waveforms saturated at around 1.25 V, while the ADC board readout range was configured at –0.2 to 1.8 V. On the right shows the waveforms when the readout range was purposefully configured such that most events saturated the ADC board. The waveform shapes are noticeably different from each other, suggesting a different cause of the issue. It was postulated that the distortion was due to the saturation of the operational amplifiers on the preamplifier boards [234].

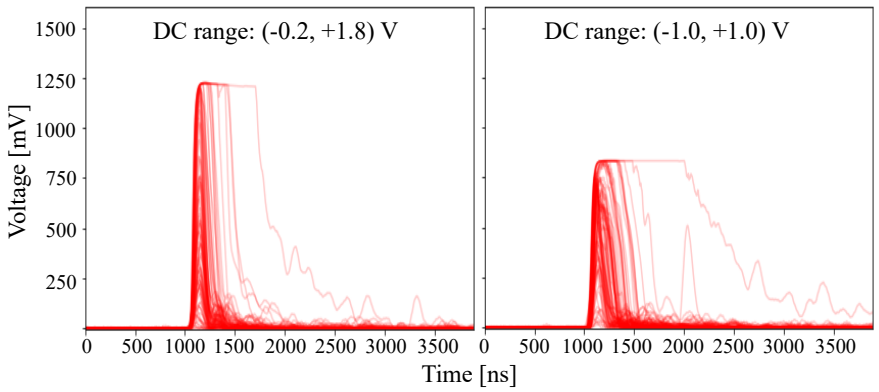

Figure 7.18: Superimposed waveforms at different DC offset, data-taking in LXe. The corresponding DC ranges are listed in the figures. The baseline of the waveforms was subtracted, which was ∼120 mV. Left: the ADC board was not saturated. The saturation was presumably on the operational amplifier in the preamplifier boards. Right: the ADC board was saturated. Since the baseline was subtrated, therefore the saturation was not exactly at 1 V. From these figures, we can see the different waveform shapes between saturations on different electronic components.

For a low bias voltage at –47 V, most of the pulses start saturating at a pulse height of

1.25 V with the pulse area between 300 to 600 PE, as shown in Figure 7.19. Assuming a gamma ray source of 662 keV and with no electric field around, the electronic recoil interaction in LXe emits around 43,700 photons [241]. From an optical simulation [234], the LCE was estimated at around 80%, meaning on average 1460 photons reaching each SiPM. As mentioned, the PDE of this SiPM model was measured to be $20.5 \pm 1.1\%$ [202], resulting in around 300 PE. This is right at the border where most of the SiPM channels saturate, referring to Figure 7.19. Therefore, with such a source, the saturation has to be corrected for a more accurate energy reconstruction.

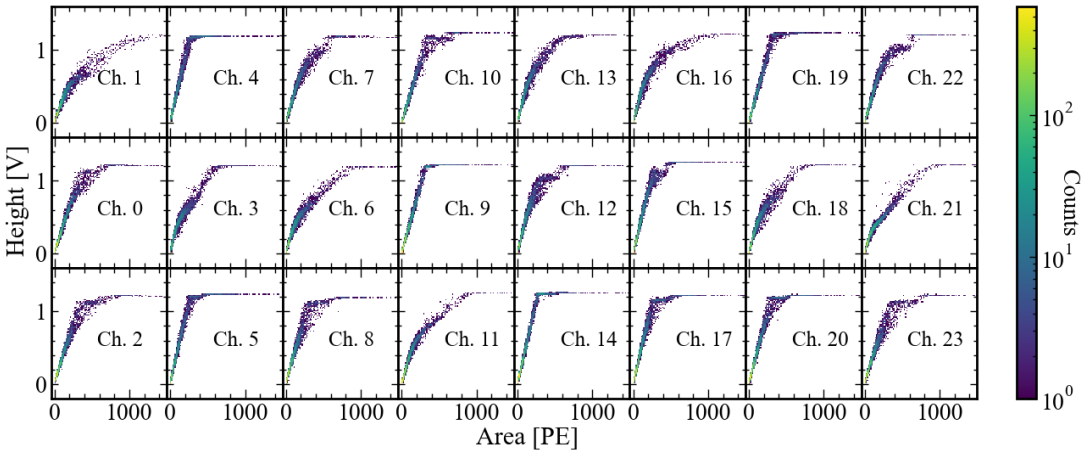

Figure 7.19: Pulse height against pulse area across all the channels at the bias voltage of –47 V. The numbers on each subplot indicate the SiPM channel, consistent with the relative position as shown in Figure 7.5. Most signal start to saturate at around 1.25 V.

From Figure 7.19, we also observe that each SiPM channels have a slightly different response for the saturation. For example, the pulses from Channel 1 and 16 reach saturation a higher pulse area compare to the rest of the channels, meaning they have relatively broader pulses for large pulses. The difference in pulse shapes does not match the connection to the preamplifier board summarised in Figure 7.5. Therefore, the difference in pulse shapes should be caused by the intrinsic difference in each SiPM channel.

7.6 Discussion

The recorded dependence of the gain of SiPM on temperature is not linear as reported by other experiments [59, 147, 221]. Several factors might be contributing. First, the power supplies for the SiPM array and the preamplifier were switched between the experiment, which might induce unknown systematic errors in the result. To perform a correction on the supply voltage, the output from the power supply was probed by a multimeter for the actual V_{bias}. However, the result was still non-linear. Another contribution is the uncertainty of the temperature measurement. In this work, the stated temperatures corresponded to the setpoint of the temperature controller, where the sensor was close to the cold-head, not to the actual temperature of the SiPM array. Due to the heat generated by the system's electronics, and the temperature around the cold-head might be a few degrees lower, the proper operating temperature at the sensor boards was likely higher than the reported temperatures. To mitigate this effect, a temperature sensor can be placed close to the SiPM baseboards, allowing for

direct measurement of the local temperature. Additionally, from [202, Table 3], the difference in the breakdown voltage V_{bd} due to the 8 K temperature difference is 0.4 V, which is comparable to the recorded errors.

The gain calibration procedure used in this study demonstrated that it is possible to perform calibration without the use of an LED light source. This is advantageous in situations where LED coupling is impractical or when minimising hardware complexity is desirable. Nevertheless, the inclusion of an LED could yield more robust results, as it can externally trigger the ADC board and result in a prominent finger plot. An LED-based calibration would also reduce statistical uncertainties and allow for more efficient data processing.

The radioactive sources ^{137}Cs and ^{57}Co, which emit monoenergetic gammas, were placed separately in the vicinity of the detector for energy calibration. However, the energy spectrum could not be correctly reconstructed due to the reason mentioned in the previous section, especially the signal distortion due to saturation. Without a correction, the reconstructed energy would be largely underestimated for events near the saturation limit. Additionally, the data acquisition time window of 4 µs is insufficient to capture the long afterpulsing tail from high-energy events. Extending the recording window would ensure complete signal integration, thereby improving both the accuracy of the energy calibration at higher energies.

Finally, tritiated methane was also injected into the detector volume and subsequently removed by the getter and the circulation system. The event rate was checked, where the rate was gradually reduced when the circulation system was turned on with a flow rate of 1.3 SLPM. However, after some time, the event rate surged and then steadily increased. The time of the surge was in close coincidence with the time when the flow rate was manually set to a higher flow rate. The cause is unclear as this work was written.

7.7 Conclusion and Outlook

Due to several advantages offered by SiPM, such as robustness, better SPE resolution, and low operating potential, it has gained attention in the field of rare-event search experiments. One of a local R&D project, the NUXE-3 detector at University of California San Diego, utilises an array of 96 Hamamatsu VUV4 SiPMs (model S13371-6050CQ-02) to explore the potential of a novel TPC design.

From this work, all SiPMs in the NUXE-3 detector were successfully commissioned and operated with the gain consistent with literature values. The normalised standard deviation of the breakdown voltage and junction capacitance for each channel for all the runs is within 1.0% and 4.1%, respectively.

From this commissioning campaign, possible improvements or caveats were identified for further data-taking and analysis, which could be mitigated by additional work on the analysis level or the hardware level. In particular, it was found that the signal was saturating the readout system even at low bias voltage and with low energy source.

This hinders the energy reconstruction for calibrations. In addition, the afterpulsing rate showed a dependence on the operation time and bias voltage. More in-depth and longer measurement campaigns should be performed to confirm this behaviour as well as to determine the optimal record time window.

For future upgrades, an LED calibration source can be installed for a more efficient SiPM calibration as well as a temperature sensor next to the SiPM array for more accurate temperature measurements. A different preamplifier board can also be tested to see if the waveform distortion at the reported range persists. Such a test would eliminate the possibility that the SiPM was the saturating component. The future design of the baseboard should also minimise the difference in path length between the readout channels to equalise the noise level in each channel.

Chapter 8

Conclusion and Outlook

Despite abundant cosmological and astrophysical evidence for dark matter, its fundamental nature remains unknown. In case dark matter is a particle, which is well motivated, one of the most promising candidates is weakly interactive massive particles (WIMPs). The XENONnT detector, a dual-phase time projection chamber (TPC) with an active mass of 5.9 tonnes, is one of the world's most sensitive direct dark matter detection experiments, at the time of writing, dedicated to detecting WIMPs. The search for dark matter will continue with next-generation experiments, such as the XLZD project, which aims to extend the sensitivity of liquid xenon detectors further.

Dual-phase xenon TPC with liquid xenon targets have led the search for WIMPs. Xenon is chosen for both physical and technological reasons, offering high sensitivity to WIMP interactions due to its large atomic mass and to neutrinoless double beta decay ($0\nu\beta\beta$). Its favourable detector properties include a high scintillation yield, strong self-shielding, and low intrinsic background, enabling high event rates and efficient signal collection. In a dual-phase TPC, both scintillation and ionisation signals are measured, named S1 and S2 signals respectively, allowing position reconstruction and discrimination between electronic recoil (ER) and nuclear recoil (NR) interactions.

Throughout this work, the critical role of the electrostatic field configuration and the electrodes has been emphasised. Electrodes are essential for the operation of a dual-phase TPC on multiple levels. Most importantly, they establish fields in the detectors, enabling the production of the S2 signal, which is crucial for effective ER/NR discrimination and position reconstruction. The homogeneity of the drift and extraction field is critical for achieving a uniform detector response and reducing signal loss.

The XENONnT experiment experienced performance issues related to its electrodes, namely the introduction of perpendicular wires to mitigate electrode sagging and the occurrence of a short circuits between the cathode and the bottom screen. The former introduced a strong inhomogeneity in the extraction field, and the latter limited the achievable drift field. To improve the detector performance, a new set of upgraded electrodes was prepared. For the upgraded electrodes, parallel-wire electrodes, based

on previous designs, are used for the anode and the gate, and a welded hexagonal etched mesh for the cathode.

During this PhD project, I was directly involved in the realisation of robust upgrade electrodes, primarily the anode and cathode. The work centres on ensuring the structural integrity and HV stability of the electrodes, as malfunctions in either could be detrimental to the detector's operation. This work also included detailed field simulations to understand and quantify the resulting electrostatic field properties. Throughout the study, particular attention was given to developing methods and design principles that can be scaled to future experiments at the XLZD scale.

As shown in Chapter 4, electrostatic field simulations were performed using three complementary modelling approaches to evaluate the field uniformity in the TPC as well as key electrode parameters such as surface fields and electrostatic forces. These approaches consist of a full 3D simulation, a 2D axisymmetric model and local 3D simulations. The full 3D simulation employed the boundary element method (BEM) implemented in the KEMField module of the open-source software *Kassiopeia*, developed by the KATRIN collaboration. The 2D axisymmetric and local 3D simulations were carried out using the finite element method (FEM) in the commercial software COMSOL®.

Each modelling approach and software tool has distinct strengths and limitations. When used together, they provide a complementary framework that allows cross-verification of results, thereby increasing confidence in the correctness of the implementations and reducing the risk of systematic effects associated with any single model or simulation package.

Among the models, the full 3D BEM model was implemented and verified against the well-validated 2D axisymmetric model developed in [19]. The full 3D model was then used to study extended and intrinsically three-dimensional structures, including the high-voltage feedthrough (HVFT), perpendicular wires, and the upgraded electrode designs.

Concerning the upgrade electrodes, the key conclusion from the simulations is that firstly, the central welded strip of the new cathode introduces the expected local field non-uniformity, but this distortion does not extend into the region of interest of the TPC. Secondly, the surface field of the hexagonal mesh was also estimated to remain below the empirical breakdown threshold of 50 kV/cm in liquid xenon [121]. In addition, electrostatic forces acting on the electrodes were quantified and provided inputs to the electrode deflection studies. Last but not least, the removal of the top and bottom screens was found not to substantially affect the bulk field and the electrostatic force.

Looking ahead to future-generation experiments, such as XLZD, a similar multi-tiered field simulation approach can be adopted, combining models of varying accuracy and computational efficiency. Furthermore, additional tools, such as the BEM module in COMSOL, may be explored to further enhance simulation capabilities and the versatility of the model.

With the simulation framework being set up, the next step was to realise the upgrade electrodes. Since the electrode system is a central component of the detector, it must be highly robust, exhibiting minimal mechanical deflection and limited field leakage to provide a homogeneous electric field. At the same time, its contributions to the radioactive background and its impact on light collection must be minimised. These competing requirements impose stringent constraints and pose challenges for electrode design and fabrication, particularly for next-generation experiments with larger electrodes. Methods are needed to quantify the reliability and robustness of these electrodes and reduce the risk of failure during year-long operation at cryogenic temperatures.

In addition, there are specific requirements for each electrode. For the anode, the grid deflection requirement is the most stringent among all electrodes, as it significantly affects the S2 response. Similarly, the alignment between the anode and the gate electrodes also affects the width of the S2 signal. Both the gate and the cathode are cathodic electrodes, which can induce electrode backgrounds and trigger electrical breakdown. Therefore, their surface field and smoothness are also important quantities of interest for the electrode fabrication.

In general, parallel-wire grids have a more well-defined surface field and are easier to scale up. However, they have a higher risk of structural failure and greater grid deformation. In contrast, the hexagonal etched mesh likely has a more difficult-to-profile surface field; the grid itself is more complex to scale up; and it is difficult to repair in the event of imperfections identified after fabrication. However, they have a lower risk of structural failure and grid deformation.

Concerning the parallel-wire anode, as presented in Chapter 5, a series of simulations and experimental tests were carried out to ensure a reliable electrode design with adequate safety margins. A new installation method was developed, which reduces the complexity of assembling the parallel-wire electrode while maintaining reliability. During this campaign, evidence was also found that cryogenic cold shocking of the electrode frame may effectively relieve residual mechanical stress. If left unmitigated, this stress would significantly reduce the wire tension after cool-down and increase grid deflection, as observed in the XENONnT electrodes prior to the upgrade.

For XLZD with electrodes of $2.6-3$m diameter, if a parallel-wire design is considered, there are additional challenges or further R&D needed, such as the design for a mosaic frame or a more robust and efficient method to fix the wire onto the frame than the use of copper pins. In addition, the material strength of the wires limits the maximum axial tension that can be applied, which in turn determines the electrode deflection for a given field configuration. Since electrode deflection is particularly critical for anodes, a simplified calculation was performed to estimate feasible wire diameters for next-generation electrodes. This study accounts for the limited axial tension, electrostatic forces, feedback effects, and optical shadowing. It was found that wires with a diameter of 0.2 mm, as used for the XENONnT anode, are no longer feasible for an XLZD-scale anode. Thicker wires, for example with a diameter of 0.4 mm, should therefore be considered, at the cost of a modest reduction in light collection efficiency.

Chapter 6 presents the quality assurance and quality control for the electropolished hexagonal etched mesh. A significant drawback of the monolithic etched-mesh electrode was that it could not be repaired if abnormal features were detected, and such features on cathodic electrodes tend to contribute to electron-emission backgrounds. Sharp and protruding features were also sought and identified on the fabricated etched mesh using dedicated methods. Nevertheless, the technique of laser welding was used to repair these features. The repaired mesh subsequently underwent extensive HV tests. It was concluded that the cathode can withstand a bulk field of 3.1 kV/cm at 95% survival probability in GAr, which was extrapolated to 6.2 kV/cm between the cathode and the bottom screen in LXe, without causing breakdowns, thus principally allowing to reach drift fiels of ~ 200 V/cm.

For the XENON-LUX-ZEPLIN-DARWIN (XLZD) project, if a hexagonal mesh is chosen for the electrode design, the use of a composite mesh seems to be applicable, as this is compatible with current manufacturing capabilities. While the presence of a welded strip makes such a mesh unsuitable for anode and gate electrodes due to the resulting strong field inhomogeneities, it remains a viable option for the cathode. As for the anode, a mosaic frame design will likely be required to accommodate the larger detector size. Future R&D should further investigate electrode-related backgrounds. In addition, a dedicated testing facility should integrate optical inspection and high-voltage testing using a consistent, automated, and accurate coordinate system to ensure reliable quality assurance of large-scale electrodes.

As a final remark on electrode options for the XLZD project, there is currently no clear preference between parallel-wire and hexagonal-mesh designs. Neither electrode design decisively outperforms the other at the projected three-metre scale. Significant R&D would be required for either approach to address their respective limitations and challenges before a reliable electrode with a diameter of approximately 3 m can be realised.

Besides electrodes, Photosensors are also a primary component of the experiments, as they collect light from the scintillation and ionisation signals. As a consequence, I also contributed to testing photosensors in LXe in the context for future-generation experiments.

While photomultipliers (PMTs) have traditionally been used in xenon TPCs, silicon photomultipliers (SiPMs) have attracted attention due to their robustness, better single-photon resolution, and low operating voltage. As part of a local R&D effort, the NUXE-3 detector at the University of California, San Diego, employs an array of 96 Hamamatsu VUV4 SiPMs to explore the feasibility of a novel TPC design.

As shown in chapter 7, all SiPMs in the NUXE-3 detector were successfully commissioned and operated within this thesis, with gains consistent with literature values. The normalised standard deviations of the breakdown voltage and junction capacitance for each channel across all runs are 1.0% and 4.1%, respectively.

During commissioning, it was observed that the signal saturated the readout system even at low bias voltages and with low-energy sources, limiting accurate energy recon-

struction during calibration. Additionally, the afterpulsing rate showed dependence on both operating time and bias voltage. Longer and more detailed measurement campaigns are needed to confirm this behavior and identify the optimal recording time window. For future upgrades, a redesigned preamplifier board may be required to mitigate signal saturation if the SiPM is not the limiting factor. The baseboard design should also minimise differences in readout path lengths to equalise noise levels across all channels.

In closing, the search for dark matter remains a dynamic and rapidly advancing field. Although dedicated experiments have probed a large fraction of the parameter space without having found dark matter particles, substantial regions remain unexplored. Looking further ahead, the XLZD project brings together the XENON, LZ, and DARWIN collaborations to pursue a next-generation liquid xenon observatory for dark matter and neutrino physics, aiming to achieve sensitivities that no single collaboration can attain. The presented work focused on the design, optimisation, construction and quality control of electrodes of different type, being one of the essential R&D steps needed for the ambitious goal of the next-generation dual-phase xenon TPC experiments, the XLZD project, to reach the irreducible background from the neutrino fog.

Appendix A

Mesh Refinements for the Field Shaping Rings

As mentioned, in general, the element aspect ratio should not be too large to ensure accurate results and efficient computation. However, given the geometry of the field-shaping rings (implements as toroidal wires in KEMField) with a diameter $\mathcal{O}(10^{-4}\,\mathrm{m})$ and length $\mathcal{O}(1\,\mathrm{m})$, the aspect ratio $\mathcal{O}(1)$ would easily correspond to $\mathcal{O}(10^6)$ or more mesh elements just for a single wire. To effectively reduce the computational time and maximise the accuracy, various sizes of the discretisation elements were tried. I identified that a sensitive quantity for quantifying discretisation error in KEMField is the field inside the wire, which should be zero.

To refine the discretisation, the number of discretisation elements in the axial and toroidal directions was varied. The results are shown in Figure A.1. The figure shows that the field began to flatten as the axial number of elements exceeded 10.

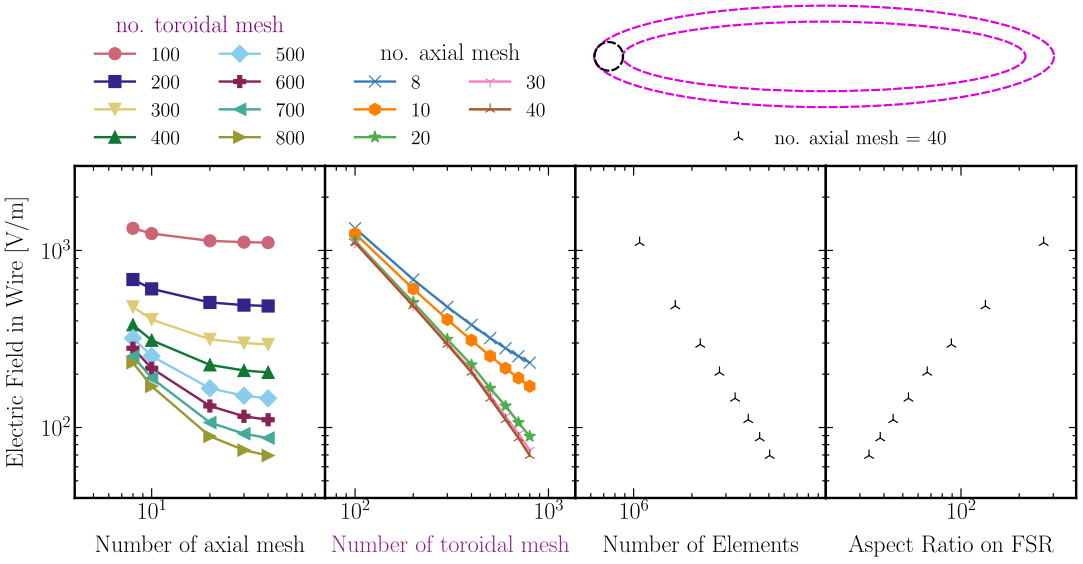

Figure A.1: Mesh refinement study of the field shaping rings.

The computational times of these simulations are shown in Figure A.2. The computation time increases linearly with the number of elements, as expected. It also shows that for the aspect ratio greater than 100, the computational time per element increases. For aspect ratios below 100, the dependence of computational time per element on aspect ratio is small, possibly indicating that other limiting factors are overriding the aspect ratio of the field-shaping rings (note that there are also other components in the simulation). Therefore, the toroidal number of elements was set to 200, such that the aspect ratio was less than 100. Subsequently, for computing the XENONnT field map, I have been using 10 elements around the ring and 200 elements along the ring.

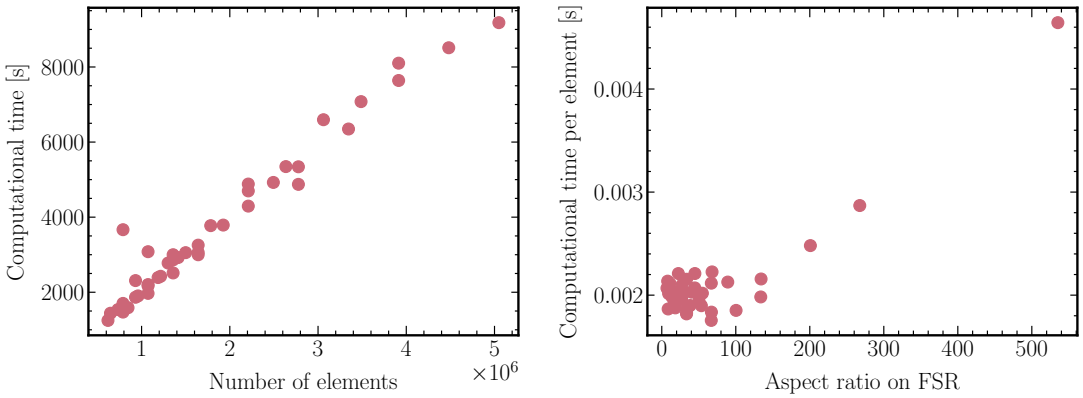

Figure A.2: Computational time of simulations with different discretisations of the rings.

The comparison of the field strength across the field shaping rings between KEMField and COMSOL is shown in Figure A.3. The figure shows that, with the refined mesh, the error in the overall field is reduced relative to the COMSOL 2D simulation. The figure also shows a nonzero field in the wires in KEMField, whereas it was set to zero in the COMSOL 2D simulation.

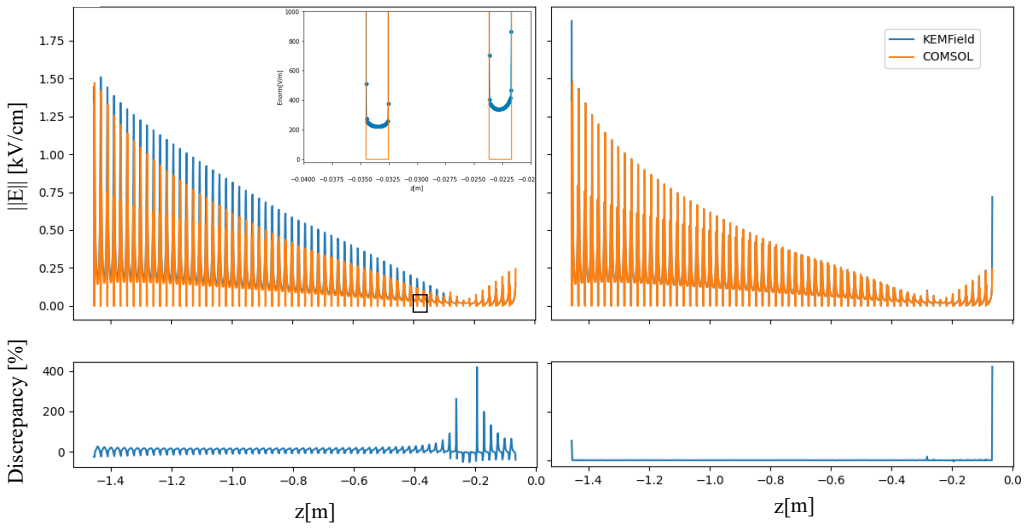

Figure A.3: Field strength across the field shaping rings. Left: from the simulation before refinement. Right: from simulation with refined discretisation elements.

Appendix B

Settings for the Krylov Solvers

Given the mirror symmetry of the detector, the x and y components of the electric field at $x = y = 0$ should be zero. However, initially it was found that $E_{x/y} \neq 0$ from the KEMField field map, but at max around 0.14 V/cm. This is infinitely big compared to the expectation, which is 0 V/cm. Hence, I increased the accuracy of the field map by changing the FFTM parameters in KEMField. For future reference, the parameters are as follows:

FFTM parameters in KEMField	Fast	Accurate
`degree`	7	12
`zero_mask`	0	3
Computational time (res = 5 mm)	332 s	2.97 hr

Table B.1: Two settings for the field solver.

where `degree` means the maximum degree of the multipole and local expansions, and `zero_mask` defines the number of the neighbouring cubes where multipole expansion is not valid [144]. The values were chosen as they were recommended and written in the documentation. With the increase in accuracy, the computational time is longer by $\sim$32 times. However, the computation time was also not affordable in this specific case.

The increase in accuracy is manifested in the following. For the line at the centre along the z direction (i.e. x = y = 0), the electric field components with the two settings in Table B.1 are shown in Figure B.1.

There are still negligible but noticeable residuals at the top and bottom, i.e. very close to the cathode and top screen. So a comparison was also made between direct field calculation and the accurate FFTM. The direct calculation did not improve the accuracy much. Hence, the effect is likely due to the discretisation error from these electrodes. We decided to live with this for the moment, and the accurate FFTM will be used, since the FFTM reduce the computational time by 5 times with similar accuracy. Other Krylov solver parameters are shown in Table B.2.

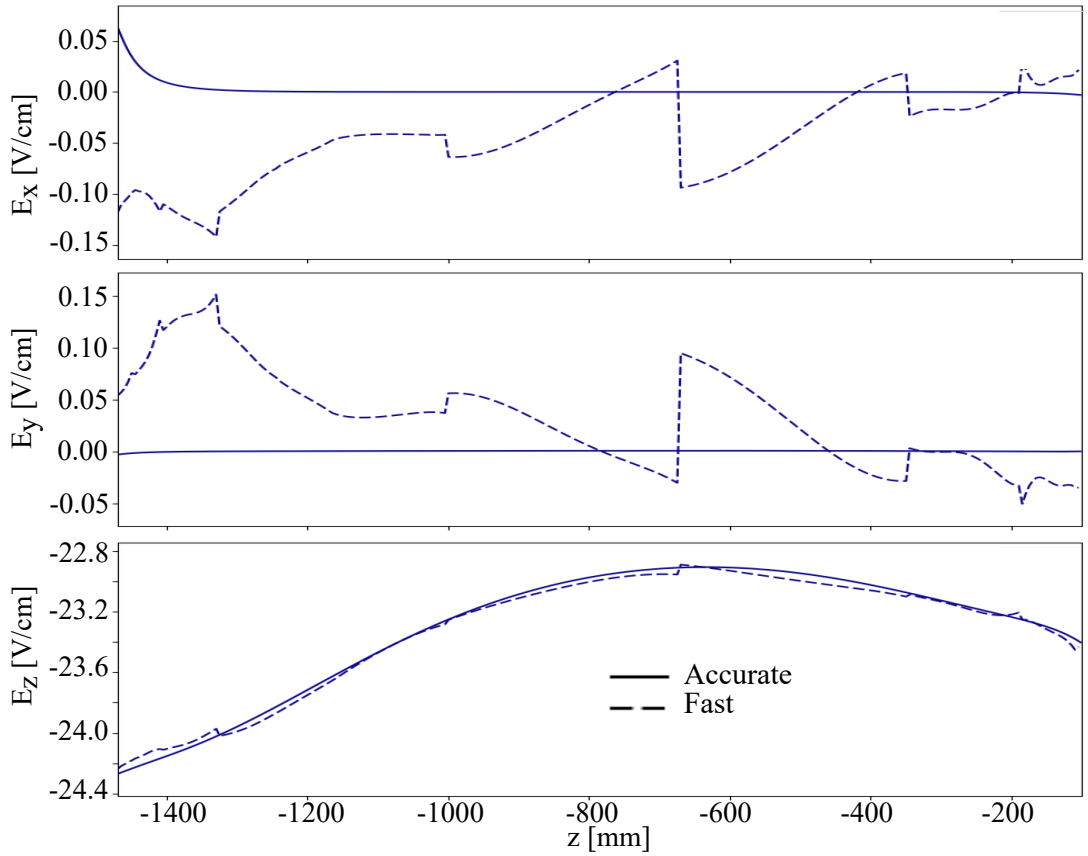

Figure B.1: Field at $x = y = 0$ with the two settings of the field solver.

Table B.2: Solver configuration and numerical parameters used in the KEMField simulation.

Parameter	**Value**
Krylov Solver	
Krylov type	GMRES
Tolerance	1×10^{-6}
Maximum iterations	1000
Iterations between restarts	50
Fast Multipole Method Parameters	
Top-level divisions	4
Tree-level divisions	2
Polynomial degree	7
Zeromask size	1
Maximum tree depth	8
Verbosity	3
Use region estimation	true
Region expansion factor	1.1
Use caching	true
Preconditioner Parameters	
Preconditioner type	implicit_krylov
Tolerance	0.1
Maximum iterations	30
Iterations between restarts	50
Polynomial degree	2

Appendix C

Copper Pin Simulation

Copper pins with different shapes were used for the upgrade anode electrode, with the drawing shown in Figure C.1. While it was expected that the absence of a head would also reduce the electrostatic field around the pin, a 3D local field simulation was performed to confirm the effect of the pins on the field. The following describes techniques for setting boundary conditions, defining the region of interest, improving meshing for efficiency and accuracy, and verifying the results.

The simulation tools were introduced in chapter 4. To recap, the local 3D simulation was performed using COMSOL Multiphysics® [142] to solve the electrostatic equations using the FEM. The boundary conditions (BCs) of the simulation domain was either taken from the global 2D axial symmetric model described in subsection 4.3.1 or from symmetry planes. The latter BCs are commonly used to truncate the simulation domain, enabling more efficient and accurate localised simulations while preserving the global field configurations.

Figure C.2 shows the simulation geometry and the BCs. The anode pins in question are highlighted in pink in the figure. Two types of pins were simulated, namely "H−" and "H−". Since the electric field inside conductors is zero, all conductors except the anode pins are excluded from the simulation domain to reduce computational cost: the anode electrode on top, the gate electrode at the bottom, and the gate pins. Between the gate and the anode electrode frames, a PTFE block was installed to obstruct the line of sight between the frames, thereby reducing the risk of breakdown. The gate electrode was submerged in liquid xenon (LXe). Wires for the electrodes were also added for completeness, although they did not contribute significantly in this simulation.

The top and bottom boundaries were set to the interpolated function given by the 2D simulation mentioned in subsection 4.3.1. The front side was set to a symmetry BC, as it is sufficiently far away from the region of interest, that is, around the copper pins. The back side was grounded as it is the position of the bell, which regulates the liquid level in XENONnT [35]. The two sides were set to periodic BC for the infinite array of wires and the electrode frame to reduce computational time when using the actual

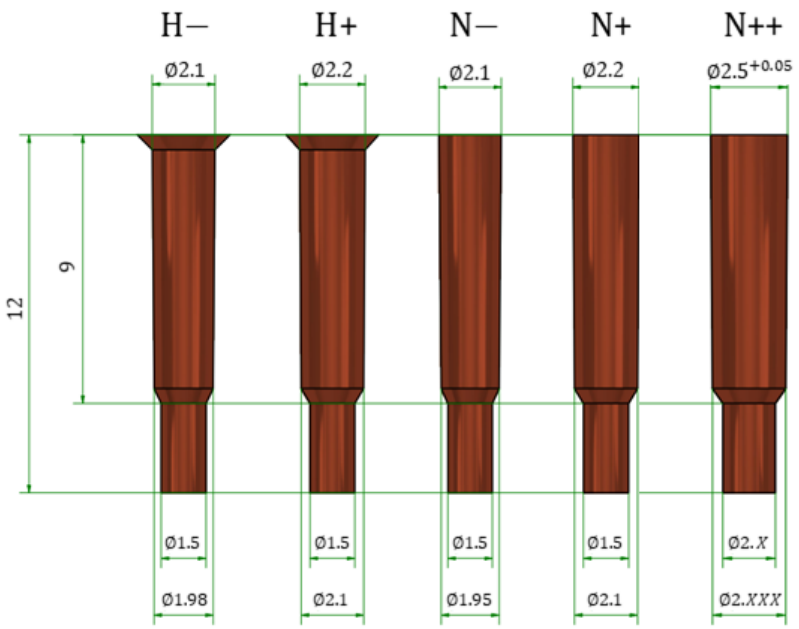

Figure C.1: Different types of pins used for the anode electrode. All dimensions are in mm. Pins labeled "H" have a head, while those labeled "N" do not. The clipping parts of the pin, which exerted most of the force to fix the wire in place, were approximately 9 mm in length and had a conical shape. The "++", "+" and "-" signs indicate the maximum diameter of clipping part of the pin to be 2.5, 2.2 and 2.1 mm respectively. The remaining part of the pin, which had a thinner diameter, was the extension that held the pin in place just before the insertion process.

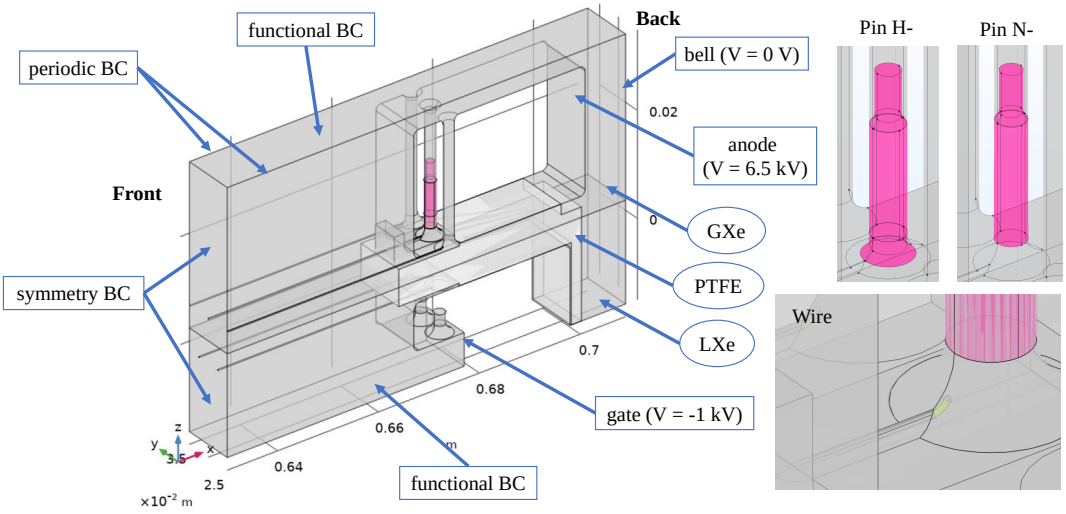

Figure C.2: Geometry and boundary conditions (BCs) of the simulation. The rectangular boxes label the BC. The ellipses label the material. The inset on the top-right-hand side shows the geometry of the pins used in the simulation. The inset on the bottom-right-hand side shows the geometry of the simplified wire.

geometry.

Figure C.3 shows the region of interest and the discretisations in the region. Other re-

gions were adaptively discretised accordingly. For more simulation details, including the verification with the 2D model and the discretisation.

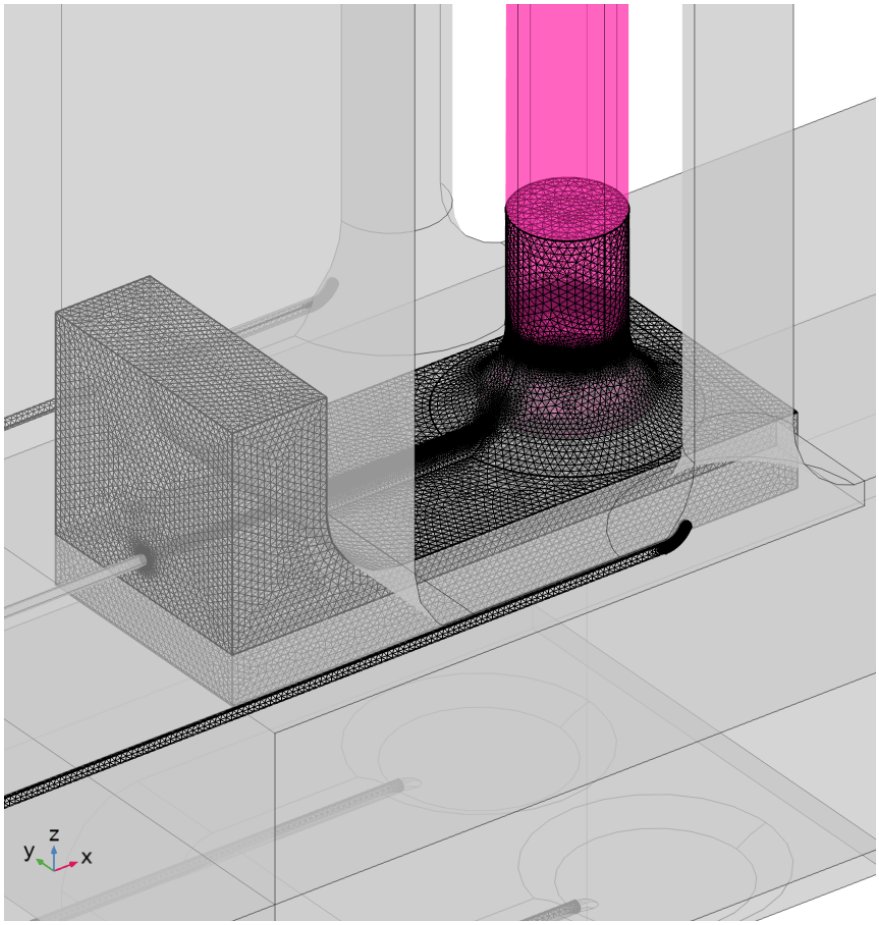

Figure C.3: Discretisation of the region of interest

Results

Figure C.4 shows the resulting field lines in the case with the "H−" pin. The field between the anode frame and the polytetrafluoroethylene (PTFE) block is higher than other regions due to the difference in dielectric constant between PTFE and gaseous xenon (GXe). With the PTFE block, there were no field lines connecting the anode and gate frame. The maximum field in the region of interest is on the anode wire. However, the field on the wire is locally high but non-hazardous. The field right below the copper pin is also below the EL threshold for GXe, which is 25 kV/cm.

Figure C.5 shows the difference in E_{norm} between the result with and without the head on the xz-plane. The field above the copper pin head was around 4 kV/cm higher than the case with "H−" pin. Therefore, solely from the electrostatic point of view, "H−" pin is more favorable.

From the results, the edge of the wire groove and the wires exhibited the highest field. Figure C.6 shows a sample of the field profile across the grooves. In other words, the edge of the groove is the limiting factor of achieving a low electrostatic field in this design, but not the pins. Nevertheless, the actual value is likely to be lower than

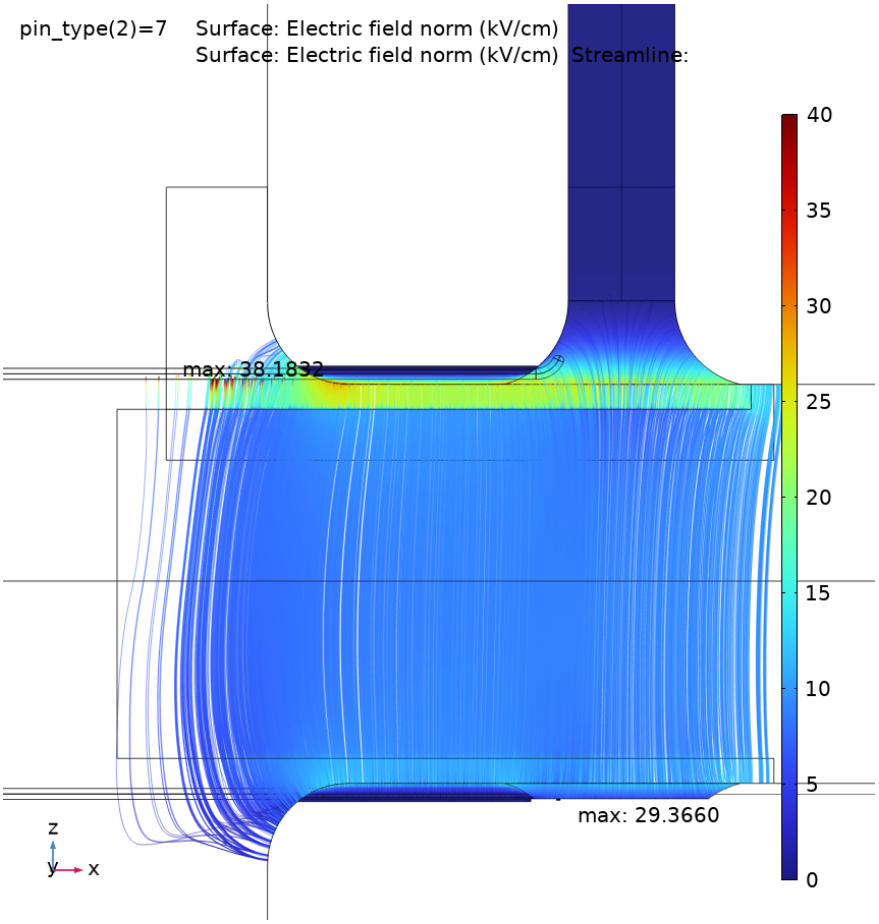

Figure C.4: Field lines in the case of the “H−” pin.

the value in the simulation due to the additional rounding from polishing. The exact values of the field highly depend on the precise geometry, which is unobtainable.

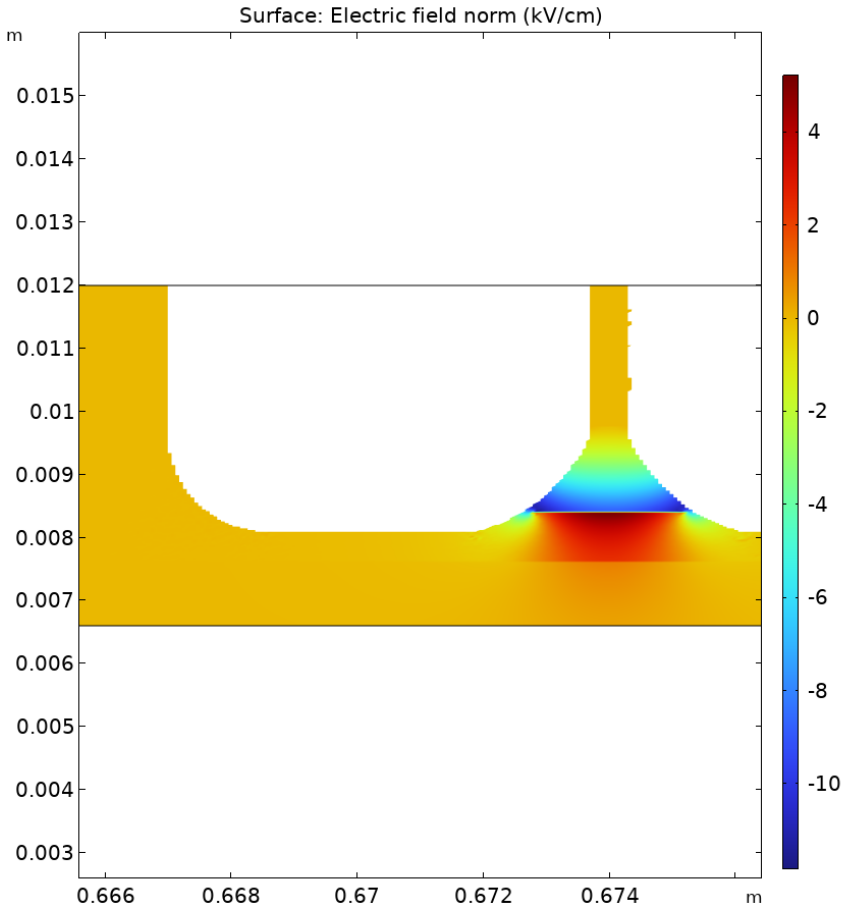

Figure C.5: Difference of E_{norm} ("H−" - "H−") on the xz-plane.

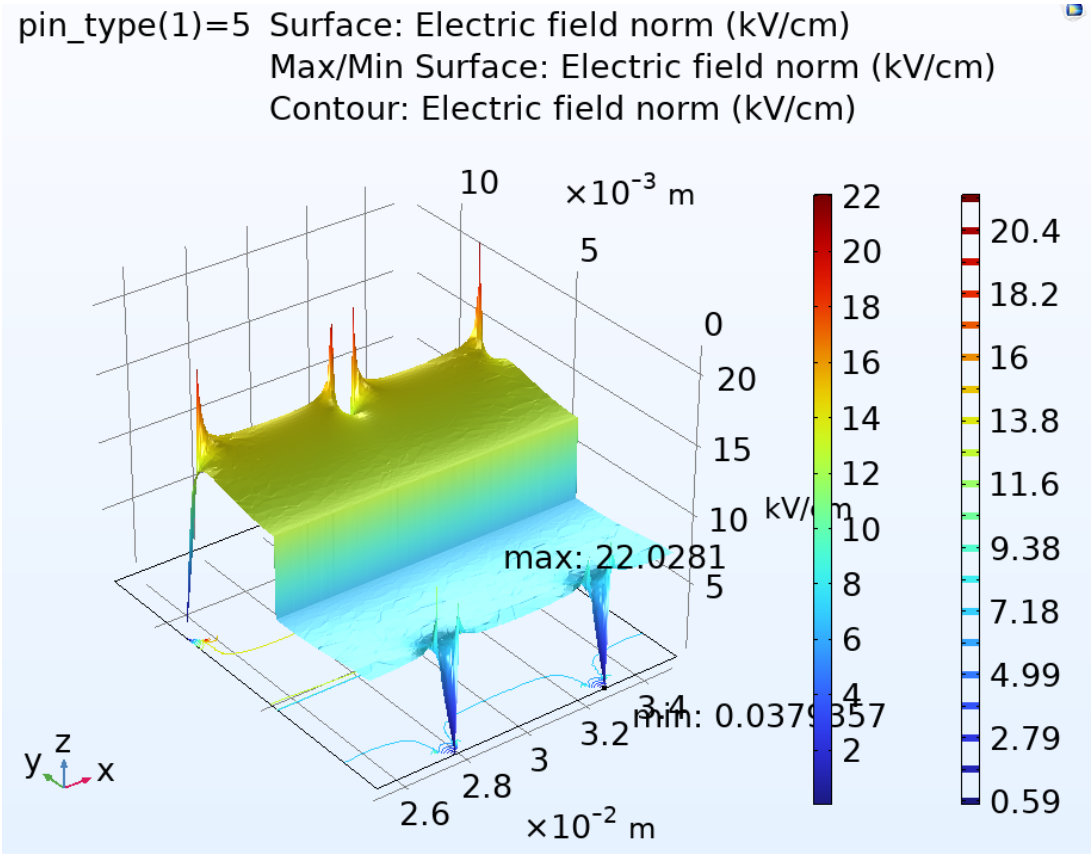

Figure C.6: Field profile across the groove in the yz-plane.

Appendix D

List of Features on the Cathode

The coordinates of the identified features, with an error of $\pm$ 1 cm, are shown in Figure D.1.

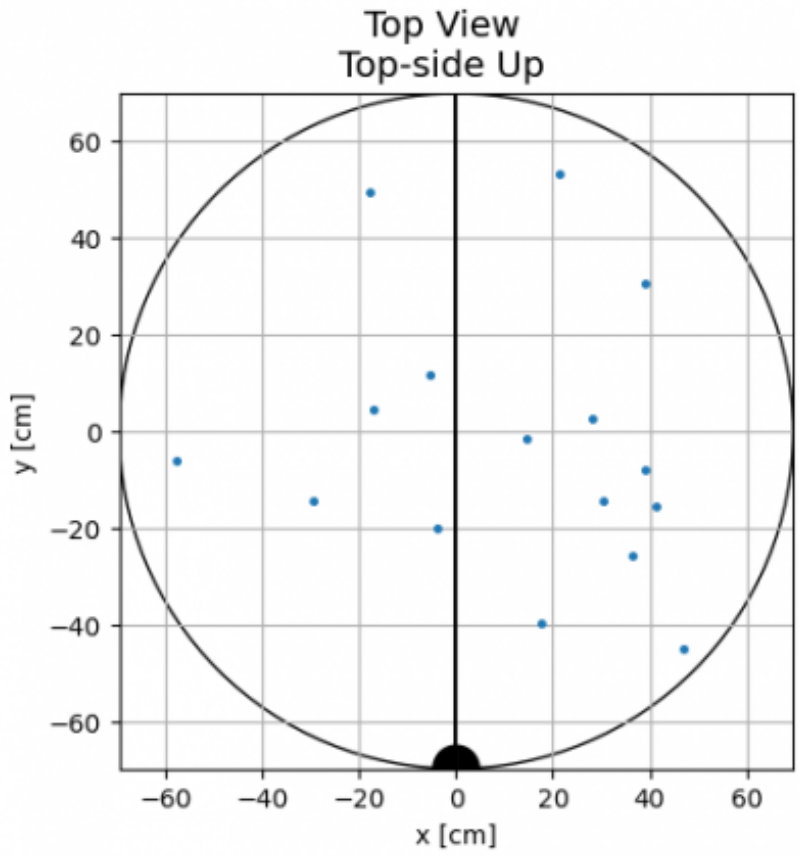

Figure D.1: Locations of all the identified defects.

The final status of all the identified features is shown in Figure D.2. The label on top of each figure shows the (x, y) coordinates, which side of the cathode, and the repaired method, if any. The (x, y) coordinates are consistent with Figure D.1. The top side refers to the side of the cathode facing the drift region, and the bottom side refers to

the side facing the bottom PMT array. Images of the features were mainly captured by a hand-held microscope[1], apart from extended features.

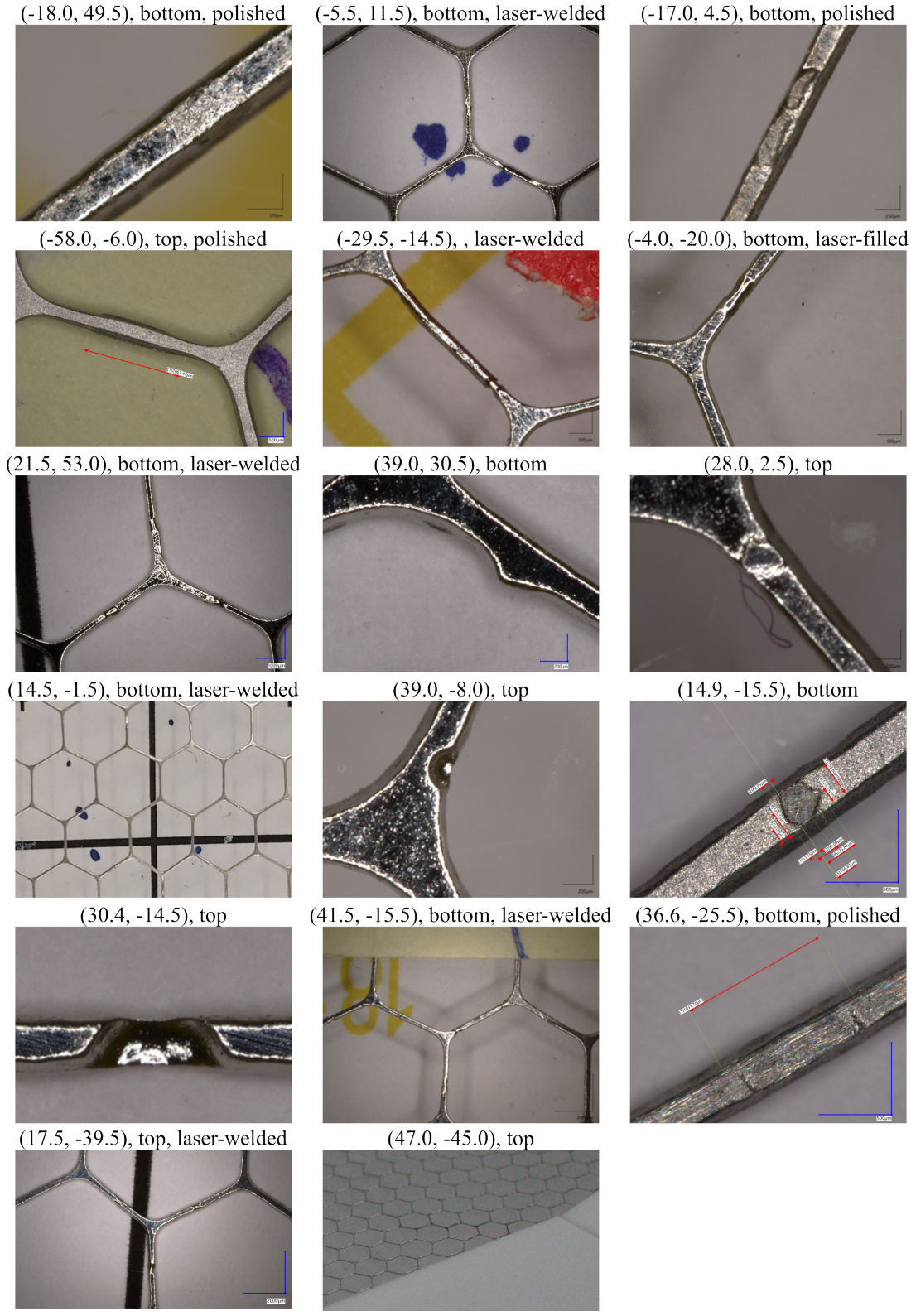

Figure D.2: List of all identified features. The label on top of each figure shows the (x, y) coordinates, which side of the cathode, and the repaired method, if any.

[1]Brand: KEYENCE. Model: VHX-7000 digital microscope. Mobile camera: VHX- Z20R.

Appendix E

Self Triggering Mode of v1725 DAQ Board

The schematic diagram of the self-triggering scheme of v1725 is shown in E.1. Each channel, equipped with a digital discriminator, generates trigger signals when the digitised input signal surpasses the threshold. The threshold can be configured individually for each channel. The trigger signals are processed in adjacent pairs (i.e. channel 0 and channel 1 are paired, and so on), referred to as ”groups”, to generate trigger requests to the motherboard. Possible processing operations are ”AND”, ”OR”, ”ONLY 0”, or ”ONLY 1”. In this experiment, the ”OR” operation was used, also illustrated in E.1. Then, the trigger requests from all groups, which at most 8 groups for 16 enabled channels, are ORed to form a board common trigger, distributed back to all channels for event acquisition.

In case coincidence is enabled by configuring the majority level > 0, the coincidence is formed on the group level, but not on the channel level, within a specified time window. For example, when the majority level $= 1$, at least two trigger requests in coincidence within the time window are required to trigger the event acquisition. Consider the trigger signals shaded in green in E.1, these signals are in coincidence on channel level, but not in group level. To have channel-level coincidence, only half of the v1725 board (i.e., 8 channels) can be enabled.

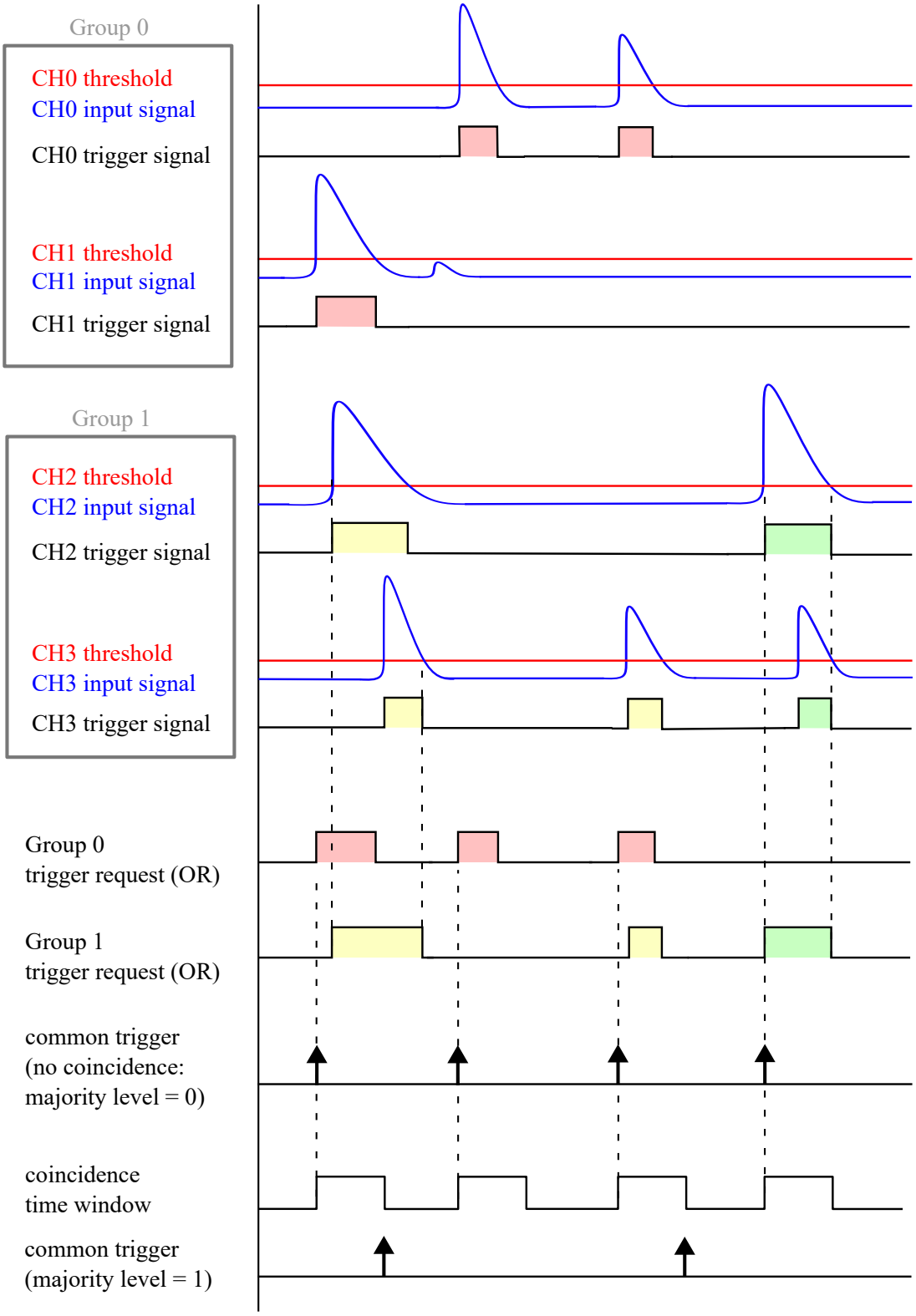

Figure E.1: Schematic diagram of the self-triggering mode of v1725 DAQ board. Channel 4-15 is omitted without loss of generality. Blue solid lines represent the input signal, red solid lines represent the triggering threshold set for individual channels, black solid lines represent the logic signal, and vertical dashed lines serve as visual guides. Group 0 logic signals are shaded in red, and those of Group 1 are shaded in yellow or green. Similarly, Group 2-7 are omitted in this diagram. In this particular example, the trigger requests from each group are formed by the OR operation between channels within the group. Arrows mark the final common triggers. Figure inspired by [236].

Bibliography

[1] A. Elykov et al. “Development & Characterization of Electrodes for large-scale Xenon Time Projection Chambers”. In: (Nov. 2025).

[2] M. Cirelli, A. Strumia, and J. Zupan. “Dark Matter”. In: (June 2024).

[3] M. Schumann. “Direct Detection of WIMP Dark Matter: Concepts and Status”. In: *J. Phys. G* 46.10 (2019), p. 103003. DOI: 10.1088/1361-6471/ab2ea5.

[4] J. L. Feng. “Dark Matter Candidates from Particle Physics and Methods of Detection”. In: *Ann. Rev. Astron. Astrophys.* 48 (2010), pp. 495–545. DOI: 10.1146/annurev-astro-082708-101659.

[5] R. A. Sunyaev. “The Thermal History of the Universe and the Spectrum of Relic Radiation”. In: *Confrontation of Cosmological Theories with Observational Data*. Ed. by M. S. Longair. Dordrecht: Springer Netherlands, 1974, pp. 167–173. DOI: 10.1007/978-94-010-2220-0_14. URL: https://doi.org/10.1007/978-94-010-2220-0_14.

[6] D. J. Fixsen. “The Temperature of the Cosmic Microwave Background”. In: *Astrophys. J.* 707 (2009), pp. 916–920. DOI: 10.1088/0004-637X/707/2/916.

[7] N. Aghanim et al. “Planck 2018 results. I. Overview and the cosmological legacy of Planck”. In: *Astron. Astrophys.* 641 (2020), A1. DOI: 10.1051/0004-6361/201833880.

[8] D. Perkins. *Particle Astrophysics*. New York: Oxford University Press, 2011.

[9] B. D. Fields. “The primordial lithium problem”. In: *Ann. Rev. Nucl. Part. Sci.* 61 (2011), pp. 47–68. DOI: 10.1146/annurev-nucl-102010-130445.

[10] S. Navas et al. “Review of particle physics”. In: *Phys. Rev. D* 110.3 (2024), p. 030001. DOI: 10.1103/PhysRevD.110.030001.

[11] D. N. Schramm. “Primordial nucleosynthesis”. In: *Proceedings of the National Academy of Sciences* 95.1 (1998), pp. 42–46. DOI: 10.1073/pnas.95.1.42. URL: https://www.pnas.org/doi/abs/10.1073/pnas.95.1.42.

[12] D. Clowe et al. “A Direct Empirical Proof of the Existence of Dark Matter*”. In: *The Astrophysical Journal* 648.2 (Aug. 2006), p. L109. DOI: 10.1086/508162.

[13] M. Lisanti. *Lectures on Dark Matter Physics*. 2016. DOI: 10.48550/arXiv.1603.03797.

[14] V. C. Rubin and W. K. Ford Jr. “Rotation of the Andromeda Nebula from a Spectroscopic Survey of Emission Regions”. In: *Astrophys. J.* 159 (1970), pp. 379–403. DOI: 10.1086/150317.

[15] V. C. Rubin, N. Thonnard, and W. K. Ford Jr. “Rotational properties of 21 SC galaxies with a large range of luminosities and radii, from NGC 4605 /R = 4kpc/ to UGC 2885 /R = 122 kpc/”. In: *Astrophys. J.* 238 (1980), p. 471. DOI: 10.1086/158003.

[16] A. Bosma. “21-cm line studies of spiral galaxies. 2. The distribution and kinematics of neutral hydrogen in spiral galaxies of various morphological types.” In: *Astron. J.* 86 (1981), p. 1825. DOI: 10.1086/113063.

[17] M. Persic, P. Salucci, and F. Stel. “The Universal rotation curve of spiral galaxies: 1. The Dark matter connection”. In: *Mon. Not. Roy. Astron. Soc.* 281 (1996), p. 27. DOI: 10.1093/mnras/278.1.27.

[18] J. F. Navarro, C. S. Frenk, and S. D. M. White. “The Structure of cold dark matter halos”. In: *Astrophys. J.* 462 (1996), pp. 563–575. DOI: 10.1086/177173.

[19] F. Toschi. “Design of the field cage and charge response of the XENONnT dark matter experiment”. PhD thesis. Albert-Ludwigs-Universität Freiburg im Breisgau, 2022.

[20] M. Milgrom. “A Modification of the Newtonian dynamics as a possible alternative to the hidden mass hypothesis”. In: *Astrophys. J.* 270 (1983), pp. 365–370. DOI: 10.1086/161130.

[21] F. Kühnel and B. Carr. “Primordial Black Holes as Dark Matter: Recent Developments”. In: *Annual Review Nuclear and Particle Science* 70 (2020), pp. 355–394. DOI: 10.1146/annurev-nucl-050520-125911.

[22] M. Martínez. “Dark Matter searches via direct detection”. In: *PoS* CORFU2018 (2019). Ed. by K. Anagnostopoulos et al., p. 037. DOI: 10.22323/1.347.0037.

[23] N. Craig. “Naturalness: past, present, and future”. In: *Eur. Phys. J. C* 83.9 (2023), p. 825. DOI: 10.1140/epjc/s10052-023-11928-7.

[24] I. J. R. Aitchison. *Supersymmetry in Particle Physics. An Elementary Introduction*. Cambridge: Cambridge University Press, 2007. DOI: 10.1017/CBO9780511619250.

[25] R. D. Peccei and H. R. Quinn. "CP Conservation in the Presence of Instantons". In: *Phys. Rev. Lett.* 38 (1977), pp. 1440–1443. DOI: 10.1103/PhysRevLett.38.1440.

[26] L. Di Luzio, M. Giannotti, E. Nardi, and L. Visinelli. "The landscape of QCD axion models". In: *Phys. Rept.* 870 (2020), pp. 1–117. DOI: 10.1016/j.physrep.2020.06.002.

[27] S. Profumo. "Astrophysical Probes of Dark Matter". In: *Theoretical Advanced Study Institute in Elementary Particle Physics: Searching for New Physics at Small and Large Scales*. 2013, pp. 143–189. DOI: 10.1142/9789814525220_0004.

[28] C. A. J. O'Hare. "New Definition of the Neutrino Floor for Direct Dark Matter Searches". In: *Phys. Rev. Lett.* 127.25 (2021), p. 251802. DOI: 10.1103/PhysRevLett.127.251802.

[29] F. D. Amaro et al. "The CYGNO Experiment". In: *Instruments* 6.1 (2022), p. 6. DOI: 10.3390/instruments6010006.

[30] R. Hammann. "Probing the Invisible – From Dark Matter and Neutrinos in XENONnT to Infrared Scintillation for Future Xenon Detectors". PhD thesis. Heidelberg University, 2025.

[31] K. D. Morøa, I. Olcina, X. Chen, and Y. Ma. *dd_limit_plot: Repository to plot Dark Matter Direct Detection Limits.* https://github.com/kdund/dd_limit_plot. 2024.

[32] A. Bolozdynya, V. Egorov, B. Rodionov, and V. Miroshnichenko. "Emission detectors". In: *IEEE Transactions on Nuclear Science* 42.4Pt1 (Aug. 1995). DOI: 10.1109/23.467913. URL: https://www.osti.gov/biblio/129185.

[33] L. Baudis. "DARWIN/XLZD: A future xenon observatory for dark matter and other rare interactions". In: *Nucl. Phys. B* 1003 (2024), p. 116473. DOI: 10.1016/j.nuclphysb.2024.116473.

[34] J. Aalbers et al. "The XLZD Design Book: Towards the Next-Generation Liquid Xenon Observatory for Dark Matter and Neutrino Physics". Oct. 2024.

[35] E. Aprile et al. "The XENONnT dark matter experiment". In: *Eur. Phys. J. C* 84.8 (2024), p. 784. DOI: 10.1140/epjc/s10052-024-12982-5. URL: https://doi.org/10.1140/epjc/s10052-024-12982-5.

[36] Y. Meng et al. "Dark Matter Search Results from the PandaX-4T Commissioning Run". In: *Phys. Rev. Lett.* 127.26 (2021), p. 261802. DOI: 10.1103/PhysRevLett.127.261802.

[37] D. S. Akerib et al. “The LUX-ZEPLIN (LZ) Experiment”. In: *Nucl. Instrum. Meth. A* 953 (2020), p. 163047. DOI: 10.1016/j.nima.2019.163047.

[38] C. E. Aalseth et al. “DarkSide-20k: A 20 tonne two-phase LAr TPC for direct dark matter detection at LNGS”. In: *Eur. Phys. J. Plus* 133 (2018), p. 131. DOI: 10.1140/epjp/i2018-11973-4.

[39] U.S. Secretary of Commerce. *Saturation Properties for Xenon — Temperature Increments*. URL: https://webbook.nist.gov/cgi/fluid.cgi?TLow=161&THigh=289&TInc=&Digits=5&ID=C7440633&Action=Load&Type=SatP&TUnit=K&PUnit=bar&DUnit=kg%2Fm3&HUnit=kJ%2Fmol&WUnit=m%2Fs&VisUnit=uPa*s&STUnit=N%2Fm&RefState=DEF#Vapor (visited on Sept. 4, 2025).

[40] E. Aprile et al. “Search for Light Dark Matter in Low-Energy Ionization Signals from XENONnT”. In: *Phys. Rev. Lett.* 134.16 (2025), p. 161004. DOI: 10.1103/PhysRevLett.134.161004.

[41] E. Aprile et al. “Light Dark Matter Search with Ionization Signals in XENON1T”. In: *Phys. Rev. Lett.* 123.25 (2019), p. 251801. DOI: 10.1103/PhysRevLett.123.251801.

[42] E. Aprile, A. E. Bolotnikov, A. I. Bolozdynya, and T. Doke. *Noble Gas Detectors*. Wiley-VCH, 2006.

[43] V. Gehman. “Direct Search for Dark Matter with Two-Phase XENON Detectors: Current Status of Lux and Plans for LZ”. In: *Frascati Phys. Ser.* 58 (2014). Ed. by R. Fusco Femiano and G. Mannocchi, p. 51.

[44] E. Aprile et al. “Scintillation response of liquid xenon to low energy nuclear recoils”. In: *Phys. Rev. D* 72 (2005), p. 072006. DOI: 10.1103/PhysRevD.72.072006.

[45] E. Aprile and T. Doke. “Liquid Xenon Detectors for Particle Physics and Astrophysics”. In: *Rev. Mod. Phys.* 82 (2010), pp. 2053–2097. DOI: 10.1103/RevModPhys.82.2053.

[46] L. Baudis, P. Sanchez-Lucas, and K. Thieme. “A measurement of the mean electronic excitation energy of liquid xenon”. In: *Eur. Phys. J. C* 81.12 (2021), p. 1060. DOI: 10.1140/epjc/s10052-021-09834-x.

[47] T. Doke, A. Hitachi, J. Kikuchi, K. Masuda, H. Okada, and E. Shibamura. “Absolute Scintillation Yields in Liquid Argon and Xenon for Various Particles”. In: *Jap. J. Appl. Phys.* 41 (2002), pp. 1538–1545. DOI: 10.1143/JJAP.41.1538.

[48] K. Fujii et al. “High-accuracy measurement of the emission spectrum of liquid xenon in the vacuum ultraviolet region”. In: *Nuclear Instruments and Methods in Physics Research Section A: Accelerators, Spectrometers, Detectors and Associated Equipment* 795 (2015), pp. 293–297. DOI: https://doi.org/10.1016/j.nima.2015.05.065. URL: https:

/ / www . sciencedirect . com / science / article / pii / S016890021500724X.

[49] A. Buzulutskov. "Electroluminescence and Electron Avalanching in Two-Phase Detectors". In: *Instruments* 4.2 (2020). URL: https://www.mdpi.com/2410-390X/4/2/16.

[50] G. R. Araujo, L. Baudis, N. McFadden, P. Krause, S. Schönert, and V. H. S. Wu. "R &D of wavelength-shifting reflectors and characterization of the quantum efficiency of tetraphenyl butadiene and polyethylene naphthalate in liquid argon". In: *Eur. Phys. J. C* 82.5 (2022), p. 442. DOI: 10.1140/epjc/s10052-022-10383-0.

[51] T. Heindl et al. "The scintillation of liquid argon". In: *EPL* 91.6 (2010), p. 62002. DOI: 10.1209/0295-5075/91/62002.

[52] E. Aprile et al. "Observation of two-neutrino double electron capture in ^{124}Xe with XENON1T". In: *Nature* 568.7753 (2019), pp. 532–535. DOI: 10.1038/s41586-01C9-1124-4.

[53] E. Aprile et al. "Double-Weak Decays of ^{124}Xe and ^{136}Xe in the XENON1T and XENONnT Experiments". In: *Phys. Rev. C* 106.2 (2022), p. 024328. DOI: 10.1103/PhysRevC.106.024328.

[54] J. Aalbers et al. "Neutrinoless double beta decay sensitivity of the XLZD rare event observatory". In: *J. Phys. G* 52.4 (2025), p. 045102. DOI: 10.1088/1361-6471/adb900.

[55] C. Adams et al. "Sensitivity of a tonne-scale NEXT detector for neutrinoless double beta decay searches". In: *JHEP* 2021.08 (2021), p. 164. DOI: 10.1007/JHEP08(2021)164.

[56] M. J. Dolinski, A. W. P. Poon, and W. Rodejohann. "Neutrinoless Double-Beta Decay: Status and Prospects". In: *Ann. Rev. Nucl. Part. Sci.* 69 (2019), pp. 219–251. DOI: 10.1146/annurev-nucl-101918-023407.

[57] J. W. Kingston et al. "Gas Electroluminescence in a Dual Phase Xenon-Doped Argon Detector". In: (Oct. 2025).

[58] M. Suzuki, J.-z. Ruan(Gen), and S. Kubota. "Time dependence of the recombination luminescence from high-pressure argon, krypton and xenon excited by alpha particles". In: *Nuclear Instruments and Methods in Physics Research* 192.2 (1982), pp. 565–574. DOI: https://doi.org/10.1016/0029-554X(82)90874-6. URL: https://www.sciencedirect.com/science/article/pii/0029554X82908746.

[59] J. Wulf. "Direct Dark Matter Search with XENON1T and Developments for Multi-Ton Liquid Xenon Detectors". PhD thesis. University of Zurich, 2018.

[60] A. Bailey. "Dark Matter Searches and Study of Electrode Design in LUX and LZ". PhD thesis. Imperial College London, 2016.

[61] J. Aalbers. “Dark Matter Search with XENON1T”. PhD thesis. University of Amsterdam, 2018.

[62] M. Elwan. “SuperCDMS Experiment at SNOLAB: Current Status and Recent CUTE Results”. In: *PoS* ICRC2025 (2025), p. 482. DOI: 10.22323/1.501.0482.

[63] C. Amsler et al. “Luminescence quenching of the triplet excimer state by air traces in gaseous argon”. In: *Journal of Instrumentation* 3.02 (Feb. 2008), P02001. DOI: 10.1088/1748-0221/3/02/P02001.

[64] A. Hitachi, T. Takahashi, N. Funayama, K. Masuda, J. Kikuchi, and T. Doke. “Effect of ionization density on the time dependence of luminescence from liquid argon and xenon”. In: *Phys. Rev. B* 27 (1983), pp. 5279–5285. DOI: 10.1103/PhysRevB.27.5279.

[65] J. Lindhard, M. Scharff, and H. Schiøtt. *Range concepts and heavy ion ranges: (notes on atomic collisions, 2)*. Matematisk-fysiske meddelelser. Munksgaard, 1963. URL: https://books.google.de/books?id=M2yrnQEACAAJ.

[66] A. Hitachi, T. Doke, and A. Mozumder. “Luminescence quenching in liquid argon under charged-particle impact: Relative scintillation yield at different linear energy transfers”. In: *Phys. Rev. B* 46 (18 Nov. 1992), pp. 11463–11470. DOI: 10.1103/PhysRevB.46.11463. URL: https://link.aps.org/doi/10.1103/PhysRevB.46.11463.

[67] K. Abe et al. “Direct dark matter searches with the full data set of XMASS-I”. In: *Phys. Rev. D* 108.8 (2023), p. 083022. DOI: 10.1103/PhysRevD.108.083022.

[68] C. Adams et al. “The NEXT-100 Detector”. May 2025.

[69] D. S. Akerib et al. “Discrimination of electronic recoils from nuclear recoils in two-phase xenon time projection chambers”. In: *Phys. Rev. D* 102.11 (2020), p. 112002. DOI: 10.1103/PhysRevD.102.112002.

[70] E. Aprile et al. “Design and performance of the field cage for the XENONnT experiment”. In: *Eur. Phys. J. C* 84.2 (2024), p. 138. DOI: 10.1140/epjc/s10052-023-12296-y.

[71] W. M. Haynes, ed. *CRC Handbook of Chemistry and Physics*. 97th ed. Taylor and Francis Group, 2017.

[72] R. L. Amey and R. H. Cole. “Dielectric Constants of Liquidied Noble Gases and Methane”. In: *Journal of Chemical Physics* (1964). DOI: https://doi.org/10.1063/1.1724850.

[73] D. S. Akerib et al. “Investigation of background electron emission in the LUX detector”. In: *Phys. Rev. D* 102.9 (2020), p. 092004. DOI: 10.1103/PhysRevD.102.092004.

[74] A. Michel. “Analysis & Characterization of the anomalous e^--burst background in the XENONnT Dark Matter detector”. MA thesis. Karlsruhe Institute of Technology, 2025.

[75] E. Aprile, K. Giboni, P. Majewski, K. Ni, and M. Yamashita. “Proportional light in a dual-phase xenon chamber”. In: *IEEE Transactions on Nuclear Science* 51.5 (2004), pp. 1986–1990. DOI: 10.1109/TNS.2004.832690.

[76] J. Xu et al. “Electron extraction efficiency study for dual-phase xenon dark matter experiments”. In: *Phys. Rev. D* 99.10 (2019), p. 103024. DOI: 10.1103/PhysRevD.99.103024.

[77] B. N. V. Edwards et al. “Extraction efficiency of drifting electrons in a two-phase xenon time projection chamber”. In: *JINST* 13.01 (2018), P01005. DOI: 10.1088/1748-0221/13/01/P01005.

[78] A. Bolozdynya. “Two-phase emission detectors and their applications”. In: *Nuclear Instruments and Methods in Physics Research Section A: Accelerators, Spectrometers, Detectors and Associated Equipment* 422.1 (1999), pp. 314–320. DOI: https://doi.org/10.1016/S0168-9002(98)00965-6. URL: https://www.sciencedirect.com/science/article/pii/S0168900298009656.

[79] National Institute of Standards and Technology. *NIST Chemistry WebBook, SRD 69*. 2025. URL: https://webbook.nist.gov/cgi/cbook.cgi?ID=C7440633&Mask=28 (visited on Oct. 28, 2025).

[80] S. Vetter. “Optimization of the DARWIN TPC geometry in regard to the S1 signal efficiency”. MA thesis. Karlsruhe Institute of Technology, 2022.

[81] F. Neves et al. “Measurement of the absolute reflectance of polytetrafluoroethylene (PTFE) immersed in liquid xenon”. In: *JINST* 12.01 (2017), P01017. DOI: 10.1088/1748-0221/12/01/P01017.

[82] C. Louis De Canonville et al. “Optical properties, surface composition and desorption of Stainless Steel (316L) studied from ambient temperature to 1000 K in vacuum”. In: *Materials Today Communications* 36 (2023), p. 106865. DOI: https://doi.org/10.1016/j.mtcomm.2023.106865. URL: https://www.sciencedirect.com/science/article/pii/S2352492823015568.

[83] L. Althueser et al. “GPU-based optical simulation of the DARWIN detector”. In: *JINST* 17.07 (2022), P07018. DOI: 10.1088/1748-0221/17/07/P07018.

[84] V. C. Antochi et al. “Improved quality tests of R11410-21 photomultiplier tubes for the XENONnT experiment”. In: *JINST* 16.08 (2021), P08033. DOI: 10.1088/1748-0221/16/08/P08033.

[85] F. Acerbi et al. “Quality assurance and quality control of the 26 m^2 SiPM production for the DarkSide-20k dark matter experiment”. In: *Eur. Phys. J. C* 85.5 (2025), p. 534. DOI: 10.1140/epjc/s10052-025-14196-9.

[86] P. Barrow et al. “Qualification Tests of the R11410-21 Photomultiplier Tubes for the XENON1T Detector”. In: *JINST* 12.01 (2017), P01024. DOI: 10.1088/1748-0221/12/01/P01024.

[87] D. S. Akerib et al. “Study of few-electron backgrounds in the LUX-ZEPLIN detector”. In: (Oct. 2025).

[88] N. Kato. “Novel technique to purify liquid xenon for the XENONnT dark matter search experiment”. PhD thesis. The University of Tokyo, 2021. URL: https://www-sk.icrr.u-tokyo.ac.jp/paper/list/.

[89] E. Aprile et al. “The neutron veto of the XENONnT experiment: results with demineralized water”. In: *Eur. Phys. J. C* 85.6 (2025), p. 695. DOI: 10.1140/epjc/s10052-025-14105-0.

[90] D. Wenz. “Commissioning of the world’s first water Cherenkov neutron veto and first WIMP dark matter search results of the XENONnT experiment”. PhD thesis. Johannes Gutenberg-Universität in Mainz, 2023.

[91] E. Aprile et al. “Material radiopurity control in the XENONnT experiment”. In: *Eur. Phys. J. C* 82.7 (2022), p. 599. DOI: 10.1140/epjc/s10052-022-10345-6.

[92] D. S. Akerib et al. “Improving sensitivity to low-mass dark matter in LUX using a novel electrode background mitigation technique”. In: *Phys. Rev. D* 104.1 (2021), p. 012011. DOI: 10.1103/PhysRevD.104.012011.

[93] E. Aprile et al. “Radon Removal in XENONnT down to the Solar Neutrino Level”. In: *Phys. Rev. X* 15.3 (2025), p. 031079. DOI: 10.1103/zc1w-88p6.

[94] D. S. Akerib et al. “Searches for Light Dark Matter and Evidence of Coherent Elastic Neutrino-Nucleus Scattering of Solar Neutrinos with the LUX-ZEPLIN (LZ) Experiment”. In: (Dec. 2025).

[95] E. Aprile et al. “Search for New Physics in Electronic Recoil Data from XENONnT”. In: *Phys. Rev. Lett.* 129.16 (2022), p. 161805. DOI: 10.1103/PhysRevLett.129.161805.

[96] A. Tomás et al. “Study and mitigation of spurious electron emission from cathodic wires in noble liquid time projection chambers”. en. In: *Astroparticle Physics* 103 (Dec. 2018), pp. 49–61. DOI: 10.1016/j.astropartphys.2018.07.001.

[97] J. Watson et al. “Study of dielectric breakdown in liquid xenon with the XeBrA experiment”. en. In: *Review of Scientific Instruments* 94.1 (Jan. 2023). arXiv:2206.07854 [hep-ex, physics:nucl-ex, physics:physics], p. 015112. DOI: 10.1063/5.0107082.

[98] M. Agostini et al. "Final Results of GERDA on the Search for Neutrinoless Double-β Decay". In: *Phys. Rev. Lett.* 125 (25 Dec. 2020), p. 252502. DOI: 10.1103/PhysRevLett.125.252502. URL: https://link.aps.org/doi/10.1103/PhysRevLett.125.252502.

[99] E. Aprile et al. "XENONnT analysis: Signal reconstruction, calibration, and event selection". In: *Phys. Rev. D* 111.6 (2025), p. 062006. DOI: 10.1103/PhysRevD.111.062006.

[100] E. Aprile et al. "Projected WIMP sensitivity of the XENONnT dark matter experiment". In: *JCAP* 11 (2020), p. 031. DOI: 10.1088/1475-7516/2020/11/031.

[101] E. Aprile et al. "WIMP Dark Matter Search Using a 3.1 Tonne-Year Exposure of the XENONnT Experiment". In: *Phys. Rev. Lett.* 135.22 (2025), p. 221003. DOI: 10.1103/msw4-t342.

[102] E. Aprile et al. "First Indication of Solar B8 Neutrinos via Coherent Elastic Neutrino-Nucleus Scattering with XENONnT". In: *Phys. Rev. Lett.* 133.19 (2024), p. 191002. DOI: 10.1103/PhysRevLett.133.191002.

[103] E. Aprile et al. "First Search for Light Dark Matter in the Neutrino Fog with XENONnT". In: *Phys. Rev. Lett.* 134.11 (2025), p. 111802. DOI: 10.1103/PhysRevLett.134.111802.

[104] J. Aalbers et al. "Dark Matter Search Results from 4.2 Tonne-Years of Exposure of the LUX-ZEPLIN (LZ) Experiment". In: *Phys. Rev. Lett.* 135.1 (2025), p. 011802. DOI: 10.1103/4dyc-z8zf.

[105] J. Aalbers et al. "A Next-Generation Liquid Xenon Observatory for Dark Matter and Neutrino Physics". In: *arXiv* (2022). DOI: https://doi.org/10.48550/arXiv.2203.02309.

[106] D. S. Akerib et al. "The LUX-ZEPLIN (LZ) Experiment". In: *Nucl. Instrum. Meth. A* 953 (2020), p. 163047. DOI: 10.1016/j.nima.2019.163047.

[107] Z. Huang. "A Search for Spin-independent and Spin-dependent Dark Matter using PandaX-4T Detector". PhD thesis. Shanghai Jiao Tong University, 2023.

[108] L. Tvrznikova et al. "Direct comparison of high voltage breakdown measurements in liquid argon and liquid xenon". In: *JINST* 14.12 (2019), P12018. DOI: 10.1088/1748-0221/14/12/P12018.

[109] R. Linehan, R. L. Mannino, A. Fan, C. M. Ignarra, S. Luitz, and K. Skarpaas. "Design and production of the high voltage electrode grids and electron extraction region for the LZ dual-phase xenon time projection chamber". In: *Nuclear Instruments and Methods in Physics Research Section A: Accelerators, Spectrometers, Detectors and Associated Equipment* 1031 (May 2022), p. 165955. URL: https://www.sciencedirect.com/science/article/pii/S0168900221009062.

[110] R. Linehan. “High Voltage Electrode Development and the LZ Experiment’s WIMP Search”. PhD thesis. Stanford University, 2022.

[111] V. Ruhela et al. “An experimental investigation of photo chemical machining process for stainless-steel material by using different etchants”. In: *Materials Today: Proceedings* (2023). DOI: https://doi.org/10.1016/j.matpr.2023.03.324. URL: https://www.sciencedirect.com/science/article/pii/S2214785323013706.

[112] J. R. Davis. *Alloy digest sourcebook: stainless steels*. ASM International, 2000.

[113] Kian Huat Metal Pte Ltd. *Exploring the Differences: Hot Rolled vs. Cold Rolled vs. Cold Drawn Steel*. URL: https://kianhuatmetal.com/blog/2023/12/26/hot-rolled-vs-cold-rolled-vs-cold-drawn-steel/ (visited on Nov. 23, 2025).

[114] K. Mistry et al. “Design, characterization and installation of the NEXT-100 cathode and electroluminescence regions”. In: *JINST* 19.02 (2024), P02007. DOI: 10.1088/1748-0221/19/02/P02007.

[115] E. Aprile et al. “The XENON100 Dark Matter Experiment”. In: *Astropart. Phys.* 35 (2012), pp. 573–590. DOI: 10.1016/j.astropartphys.2012.01.003.

[116] D. S. Akerib et al. “First results from the LUX dark matter experiment at the Sanford Underground Research Facility”. In: *Phys. Rev. Lett.* 112 (2014), p. 091303. DOI: 10.1103/PhysRevLett.112.091303.

[117] D. S. Akerib et al. “The Large Underground Xenon (LUX) Experiment”. In: *Nucl. Instrum. Meth. A* 704 (2013), pp. 111–126. DOI: 10.1016/j.nima.2012.11.135.

[118] E. Aprile et al. “The XENON1T dark matter experiment”. In: *Eur. Phys. J. C* 77.12 (2017), p. 881. DOI: 10.1140/epjc/s10052-017-5326-3.

[119] E. Aprile et al. “Physics reach of the XENON1T dark matter experiment”. In: *JCAP* 04 (2016), p. 027. DOI: 10.1088/1475-7516/2016/04/027.

[120] H. Zhang et al. “Dark matter direct search sensitivity of the PandaX-4T experiment”. In: *Sci. China Phys. Mech. Astron.* 62.3 (2019), p. 31011. DOI: 10.1007/s11433-018-9259-0.

[121] D. S. Akerib et al. “LUX-ZEPLIN (LZ) Conceptual Design Report”. In: (Sept. 2015).

[122] B. Rebel et al. “High Voltage in Noble Liquids for High Energy Physics”. In: *JINST* 9 (2014), T08004. DOI: 10.1088/1748-0221/9/08/T08004.

[123] L. Tvrznikova et al. “Direct comparison of high voltage breakdown measurements in liquid argon and liquid xenon”. In: *JINST* 14.12 (2019), P12018. DOI: 10.1088/1748-0221/14/12/P12018.

[124] E. Aprile et al. “Measurements of proportional scintillation and electron multiplication in liquid xenon using thin wires”. In: *JINST* 9.11 (2014), P11012. DOI: 10.1088/1748-0221/9/11/P11012.

[125] L. Malter. “Thin Film Field Emission”. In: *Phys. Rev.* 50 (1 July 1936), pp. 48–58. DOI: 10.1103/PhysRev.50.48. URL: https://link.aps.org/doi/10.1103/PhysRev.50.48.

[126] J. Va’Vra. “Review of wire chamber aging”. In: *Nuclear Instruments and Methods in Physics Research Section A: Accelerators, Spectrometers, Detectors and Associated Equipment* 252.2 (1986), pp. 547–563. DOI: https://doi.org/10.1016/0168-9002(86)91239-8. URL: https://www.sciencedirect.com/science/article/pii/0168900286912398.

[127] M. Y. Dong et al. “Aging phenomenon in BESIII drift chamber”. In: *Nucl. Instrum. Meth. A* 1066 (2024), p. 169582. DOI: 10.1016/j.nima.2024.169582.

[128] Tampa Steel & Supply. *316 vs. 316L Stainless Steel: What’s the Difference?* 202506052025. URL: https://tampasteel.com/316-vs-316l/.

[129] China SS Hydraulic Fittings & Adapters Manufacturer. *SS 316 Vs. SS316L: Difference and Application*. 202506052025. URL: https://www.qchydraulics.com/ss-316-vs-ss316l.html.

[130] R. G. Forbes. “Refining the application of Fowler–Nordheim theory”. In: *Ultramicroscopy* 79.1 (1999), pp. 11–23. DOI: https://doi.org/10.1016/S0304-3991(99)00097-2. URL: https://www.sciencedirect.com/science/article/pii/S0304399199000972.

[131] Y. P. Raizer. *Gas Discharge Physics*. Springer-Verlag, 1991.

[132] F. H. Kreuger. *Industrial High Voltage*. Delft University Press, 1991.

[133] D. Y. Akimov et al. “The ZEPLIN-III dark matter detector: Instrument design, manufacture and commissioning”. In: *Astroparticle Physics* 27.1 (2007), pp. 46–60. DOI: https://doi.org/10.1016/j.astropartphys.2006.09.005. URL: https://www.sciencedirect.com/science/article/pii/S0927650506001289.

[134] X. Xiao. “Design and Performance of Time Projection Chambers for the PandaX Dark Matter Detector”. PhD thesis. Shanghai Jiao Tong University, 2015.

[135] X. Cao et al. “PandaX: A Liquid Xenon Dark Matter Experiment at CJPL”. In: *Sci. China Phys. Mech. Astron.* 57 (2014), pp. 1476–1494. DOI: 10.1007/s11433-014-5521-2.

[136] L. Gu. “Search for Fermionic Dark Matter Absorption Signal with PandaX-4T Detector”. PhD thesis. Shanghai Jiao Tong University, 2022.

[137] A. H.-D. Cheng and D. T. Cheng. “Heritage and early history of the boundary element method”. In: *Engineering Analysis with Boundary Elements* 29.3 (2005), pp. 268–302. DOI: https://doi.org/10.1016/j.enganabound.2004.12.001. URL: https://www.sciencedirect.com/science/article/pii/S0955799705000020.

[138] D. Poljak, C. A. Brebbia, and J. Zhu. *Boundary element methods for electrical engineers, volume 4*. WIT Press, 2005.

[139] Altair Engineering Inc. *Mesh Growth Rate*. 2021. URL: https://2021.help.altair.com/2021.2/hwsolvers/acusolve/topics/acusolve/mesh_growth_rate_global_mesh.htm?utm_source=chatgpt.com.

[140] O. C. Zienkiewicz and R. L. Taylor. *The Finite Element Method: Its Basis and Fundamentals*. Butterworth-Heinemann, 2013.

[141] J. P. Barrett. “A Spatially Resolved Study of the KATRIN Main Spectrometer Using a Novel Fast Multipole Method”. PhD thesis. Massachusetts Institute of Technology, 2017. URL: https://dspace.mit.edu/handle/1721.1/114314.

[142] COMSOL AB, Stockholm, Sweden. *COMSOL Multiphysics® v. 6.1*. http://www.comsol.com.

[143] M. Aker et al. “Direct neutrino-mass measurement based on 259 days of KATRIN data”. In: *Science* 388.6743 (2025), adq9592. DOI: 10.1126/science.adq9592.

[144] D. Furse et al. “Kassiopeia: A Modern, Extensible C++ Particle Tracking Package”. In: *New J. Phys.* 19.5 (2017), p. 053012. DOI: 10.1088/1367-2630/aa6950.

[145] T. Corona. “METHODOLOGY AND APPLICATION OF HIGH PERFORMANCE ELECTROSTATIC FIELD SIMULATION IN THE KATRIN EXPERIMENT”. PhD thesis. University of North Carolina, 2014.

[146] J. A. Formaggio, P. Lazic, T. J. Corona, H. Stefancic, H. Abraham, and F. Glück. “Solving for Micro- and Macro-scale Electrostatic Configurations Using the Robin Hood Algorithm”. In: *Progress In Electromagnetics Research B* 39 (2012).

[147] R. Peres. “Advancing Multi-Messenger Astrophysics and Dark Matter Searches with XENONnT and the Top SiPM Array of Xenoscope”. PhD thesis. University of Zurich, 2023.

[148] D. F. R. Hilk. “Electric Field Simulations and Electric Dipole Investigations at the KATRIN Main Spectrometer”. PhD thesis. Karlsruhe Institute of Technology, 2017.

[149] M. H. Gutknecht. “A Brief Introduction to Krylov Space Methods for Solving Linear Systems”. In: *Frontiers of Computational Science*. 2007. DOI: 10.1007/978-3-540-46375-7_5.

[150] F. Glück. internal discussion. Feb. 2022.

[151] R. Schramm, A. Clark, and R. Reed. *A Compilation and Evaluation of Mechanical, Thermal, and Electrical Properties of Selected Polymers*. National Institute of Standards and Technology, Gaithersburg, MD, 1973. DOI: 10.6028/NBS.MONO.132. URL: https://nvlpubs.nist.gov/nistpubs/Legacy/MONO/nbsmonograph132.pdf.

[152] Y. Ma. internal discussion. Result may be found in Ma’s thesis. Feb. 2022.

[153] F. Toschi. *PyCOMes*. https://github.com/ftoschi/PyCOMes. 2022.

[154] California Fine Wire Co. *California Fine Wire Co. Website*. 2025. URL: https://calfinewire.com/.

[155] Vogelsang-Edelstähle. *Vogelsang-Edelstähle Website*. 2025. URL: https://www.vogelsang-edelstaehle.de/en/home/.

[156] J. G. Dahmen GmbH & Co. KG. *dahmen - experts in wire. trakus - experts in fine wire.* 2025. URL: http://www.dahmen-draht.de/en/.

[157] R. K. Adhitan and N. Raghavan. “Transient Thermo-mechanical Modeling of stress Evolution and Re-melt Volume Fraction in Electron Beam Additive Manufacturing Process”. In: *Procedia Manufacturing* 11 (2017). 27th International Conference on Flexible Automation and Intelligent Manufacturing, FAIM2017, 27-30 June 2017, Modena, Italy, pp. 571–583. DOI: https://doi.org/10.1016/j.promfg.2017.07.151. URL: https://www.sciencedirect.com/science/article/pii/S2351978917303554.

[158] L. Bauer. *Electrostatic Force Calculations for dual-phase Time Projection Chambers*. B.Sc. Thesis. 2023.

[159] W. C. Young and R. G. Budynas. *Roark’s Formulas for Stress and Strain*. Seventh. New York: McGraw-Hill, 2002.

[160] National Institute of Standards and Technology. *Cryogenic Material Properties Calculators*. URL: https://trc.nist.gov/cryogenics/calculators/propcalc.html (visited on Sept. 4, 2025).

[161] J. Choi, J. Choi, K. Lee, N. Hur, and N. Kim. “Fatigue Life Prediction Methodology of Hot Work Tool Steel Dies for High-Pressure Die Casting Based on Thermal Stress Analysis”. In: *Metals* 12.10 (2022). DOI: 10.3390/met12101744. URL: https://www.mdpi.com/2075-4701/12/10/1744.

[162] NATIONAL INSTRUMENTS CORP. *National Instruments Website*. 2025. URL: https://www.ni.com/.

[163] tribology-abc. *Coefficient of friction, Rolling resistance and Aerodynamics*. URL: https://www.tribology-abc.com/abc/cof.htm#rolweerstand (visited on Sept. 15, 2025).

[164] M. Huang, Y. Fu, X. Qiao, and P. Chen. *Investigation into friction and wear characteristics of 316l stainless-steel wire at high temperature*. Dec. 2022. URL: https://pmc.ncbi.nlm.nih.gov/articles/PMC9822317/.

[165] California Fine Wire Co. *Item No. 100194, Stainless Steel 316 Wire*. 2025. URL: https://calfinewire.com/item/alloys/all-alloys/100194-stainless-steel-316-wire.

[166] E. Cadoni, L. Fenu, and D. Forni. "Strain rate behaviour in tension of austenitic stainless steel used for reinforcing bars". In: *Construction and Building Materials* 35 (2012), pp. 399–407. DOI: https://doi.org/10.1016/j.conbuildmat.2012.04.081. URL: https://www.sciencedirect.com/science/article/pii/S0950061812002838.

[167] Mühlbauer Parts & System. *Mühlbauer Parts & Systems Website*. 2025. URL: https://www.mps-muehlbauer.com/parstsystems/.

[168] R. L. Mannino. "Measuring Backgrounds From 85Kr and 210Bi to Improve Sensitivity of Dark Matter Detectors". PhD thesis. Texas A&M University, 2017.

[169] M. Prall, V. Hannen, R. Johren, H. W. Ortjohann, M. Reinhardt, and C. Weinheimer. "Contactless 2-dimensional laser sensor for 3-dimensional wire position and tension measurements". In: *IEEE Trans. Nucl. Sci.* 57 (2010), p. 787. DOI: 10.1109/TNS.2010.2042612.

[170] J. Reininghaus. "Tension Measurement System for TPC electrode wires". B.S. Thesis. Albert-Ludwigs-Universität Freiburg, 2023.

[171] FARO. *FARO*. 2025. URL: https://www.faro.com/.

[172] FARO. *FARO® Quantum M FAROARM® Tech Sheet*. 2018. URL: https://euromarket.bg/js/tiny_mce/plugins/ajaxfilemanager/upload/Machine-Tools/TechSheet_QuantumM_FM_AM_EN.PDF (visited on Apr. 28, 2025).

[173] T. Sonar, S. Lomte, and C. Gogte. "Cryogenic Treatment of Metal – A Review". In: *Materials Today: Proceedings* 5.11, Part 3 (2018), pp. 25219–25228. DOI: https://doi.org/10.1016/j.matpr.2018.10.324. URL: https://www.sciencedirect.com/science/article/pii/S2214785318326282.

[174] A. Brown et al. “PANCAKE: a large-diameter cryogenic test platform with a flat floor for next generation multi-tonne liquid xenon detectors”. In: *JINST* 19.05 (2024), P05018. DOI: 10.1088/1748-0221/19/05/P05018.

[175] A. Fonseca, R. Meleiro, V. Chepel, A. Pereira, V. Solovov, and M. Lopes. “Study of secondary scintillation in xenon vapour”. In: *IEEE Symposium Conference Record Nuclear Science 2004.* Vol. 1. 2004, 572–576 Vol. 1. DOI: 10.1109/NSSMIC.2004.1462260.

[176] E. Aprile et al. “Observation and applications of single-electron charge signals in the XENON100 experiment”. In: *Journal of Physics G: Nuclear and Particle Physics* 41.3 (Feb. 2014), p. 035201. DOI: 10.1088/0954-3899/41/3/035201.

[177] L. Jacques, W. Bruynooghe, R. Boucique, and W. Wieme. “Experimental determination of the primary and secondary ionisation coefficients in krypton and xenon”. In: *Journal of Physics D: Applied Physics* 19.9 (Sept. 1986), p. 1731. DOI: 10.1088/0022-3727/19/9/017.

[178] F. Toschi. internal discussion. June 2020.

[179] L. Norman et al. “Dielectric strength of noble and quenched gases for high pressure time projection chambers”. In: *Eur. Phys. J. C* 82.1 (2022), p. 52. DOI: 10.1140/epjc/s10052-021-09894-z.

[180] R. Massarczyk et al. “Paschen’s law studies in cold gases”. In: *JINST* 12.06 (2017), P06019. DOI: 10.1088/1748-0221/12/06/P06019.

[181] C. H. Faham, V. M. Gehman, A. Currie, A. Dobi, P. Sorensen, and R. J. Gaitskell. “Measurements of wavelength-dependent double photoelectron emission from single photons in VUV-sensitive photomultiplier tubes”. In: *JINST* 10.09 (2015), P09010. DOI: 10.1088/1748-0221/10/09/P09010.

[182] PCM Products Inc. *Photo chemical etching & machining.* 2025. URL: https://www.pcmproducts.com.

[183] E. P. DeGarmo, J. T. Black, and R. A. Kohser. *DeGarmo’s Materials and Processes in Manufacturing*. 12th ed. Hoboken, NJ: Wiley, 2018.

[184] ANSYS, Inc. *Ansys® Workbench 21.2*. https://www.ansys.com/products/ansys-workbench.

[185] S. Mitra. *Corona Discharge as a Tool for Identifying Thin Wire Surface Irregularities*. B.Sc. Thesis. available at https://cms.zdv.uni-mainz.de/fb08-xenon-physik/wp-content/uploads/sites/107/2025/07/oberlack-group-thesis_2023_BSc_Mitra-Shumit.pdf. 2023.

[186] Arla Plast AB. *MAKROCLEAR™*. 2025.

[187] Bayer MaterialScience AG. *optical properties of Makrolon® and apec® for non-imaging optics*. 2025.

[188] Y. Li et al. "Review on the Role of Polymers in Luminescent Solar Concentrators". en. In: *Journal of Polymer Science Part A: Polymer Chemistry* 57 (3 Feb. 2018), pp. 201–215. DOI: 10.1002/pola.29192.

[189] G. F. Steib and E. Moll. "High-voltage conditioning at large gaps in industrial vacuum". en. In: *Journal of Physics D: Applied Physics* 6.2 (Jan. 1973), pp. 243–255. DOI: 10.1088/0022-3727/6/2/311.

[190] R. H. Fowler and L. Nordheim. "Electron emission in intense electric fields". In: *Proc. Roy. Soc. Lond. A* 119 (1928), pp. 173–181. DOI: 10.1098/rspa.1928.0091.

[191] P. Amedo, D. González-Díaz, and B. J. P. Jones. "Neutral bremsstrahlung in TPCs". In: *JINST* 17.02 (2022), p. C02017. DOI: 10.1088/1748-0221/17/02/C02017.

[192] C. Buil. *Comparison of the Canon 40D, 50D, 5D and 5D Mark II*. 2024. URL: https://buil.astrosurf.com/50d/test.htm (visited on Nov. 10, 2025).

[193] Ibsen Photonics. *Spectrometer detectors*. 2025. URL: https://ibsen.com/products/oem-spectrometers/spectrometer-detectors/ (visited on Nov. 8, 2025).

[194] K. Martišek and H. Druckmüllerová. *A NUMERICAL METHOD FOR THE VISUALIZATION OF THE Fe xiv EMISSION IN THE SOLAR CORONA USING BROADBAND FILTERS*. 2011. DOI: 10.1088/0067-0049/197/2/23.

[195] H. R. Lin et al. "Experimental study of discharge voltage of air gap with high humidity". In: *2012 11th International Conference on Environment and Electrical Engineering*. 2012, pp. 1028–1031. DOI: 10.1109/EEEIC.2012.6221529.

[196] M. Radmilović-Radjenović et al. "The humidity effect on the breakdown voltage characteristics and the transport parameters of air". In: *Nuclear Instruments and Methods in Physics Research Section B: Beam Interactions with Materials and Atoms* 279 (2012). Proceedings of the Fifth International Conference on Elementary Processes in Atomic Systems Belgrade, Serbia, 21-25 June 2011, pp. 103–105. DOI: https://doi.org/10.1016/j.nimb.2011.10.053. URL: https://www.sciencedirect.com/science/article/pii/S0168583X11010135.

[197] L. Tvrznikova. "Sub-GeV Dark Matter Searches and Electric Field Studies for the LUX and LZ Experiments". PhD thesis. Yale University, Apr. 2019. URL: http://arxiv.org/abs/1904.08979.

[198] C. Olivier. “Electrode conditioning effects in liquid helium”. In: *1982 IEEE International Conference on Electrical Insulation*. 1982, pp. 268–271. DOI: 10.1109/EIC.1982.7464486.

[199] A. Götz. “Development of a Prototype for an Automated HV Scanning System for XLZD Electrodes”. MA thesis. Karlsruhe Institute of Technology, 2025.

[200] A. Elykov. internal discussion. June 2025.

[201] G. Matteucci. “Cryogenic SiPMs for the Optical Readout of DarkSide-20k”. In: *6th International Workshop on New Photon-Detectors*. Feb. 2025.

[202] G. Gallina et al. “Performance of novel VUV-sensitive Silicon Photo-Multipliers for nEXO”. In: *Eur. Phys. J. C* 82.12 (2022), p. 1125. DOI: 10.1140/epjc/s10052-022-11072-8.

[203] G. Gallina et al. “Characterization of the Hamamatsu VUV4 MPPCs for nEXO”. In: *Nucl. Instrum. Meth. A* 940 (2019), pp. 371–379. DOI: 10.1016/j.nima.2019.05.096.

[204] C. Brizzolari et al. “Cryogenic front-end amplifier design for large SiPM arrays in the DUNE FD1-HD photon detection system”. In: *JINST* 17.11 (2022), P11017. DOI: 10.1088/1748-0221/17/11/P11017.

[205] A. Falcone et al. “Cryogenic SiPM arrays for the DUNE photon detection system”. In: *Nucl. Instrum. Meth. A* 985 (2021), p. 164648. DOI: 10.1016/j.nima.2020.164648.

[206] X. Chen et al. “Burn-in test and thermal performance evaluation of Silicon Photomultipliers for the JUNO-TAO experiment”. In: *JINST* 19.07 (2024), P07028. DOI: 10.1088/1748-0221/19/07/P07028.

[207] L. Baudis, M. Galloway, A. Kish, C. Marentini, and J. Wulf. “Characterisation of Silicon Photomultipliers for liquid xenon detectors”. en. In: *Journal of Instrumentation* 13.10 (Oct. 2018), P10022–P10022. DOI: 10.1088/1748-0221/13/10/P10022.

[208] S. Piatek. *Low light detection: PMT v. SiPM*. 2016. URL: https://www.hamamatsu.com/eu/en/resources/webinars/detectors/low-light-detection-pmt-sipm.html (visited on June 3, 2025).

[209] L. Baudis et al. “The first dual-phase xenon TPC equipped with silicon photomultipliers and characterisation with ^{37}Ar”. In: *Eur. Phys. J. C* 80.5 (2020), p. 477. DOI: 10.1140/epjc/s10052-020-8031-6.

[210] Q. Lin. “Proposal of a Geiger-geometry single-phase liquid xenon Time Projection Chamber as potential detector technique for dark matter direct search”. In: *JINST* 16.08 (2021), P08011. DOI: 10.1088/1748-0221/16/08/P08011.

[211] J. Qi, H. Xu, Y. Ma, Y. Liu, and K. Ni. “Feasibility of liquid-phase xenon proportional scintillation for low-energy physics”. In: *Phys. Rev. D* 111.1 (2025), p. 012005. DOI: 10.1103/PhysRevD.111.012005.

[212] S. Piatek. *Physics and operation of the MPPC silicon photomultiplier*. 2014. URL: https://hub.hamamatsu.com/us/en/technical-notes/mppc-sipms/physics-and-operation-of-the-MPPC-silicon-photomultiplier.html (visited on June 3, 2025).

[213] S. Piatek. *What is a silicon photomultiplier?* 2016. URL: https://hub.hamamatsu.com/us/en/technical-notes/mppc-sipms/what-is-an-SiPM-and-how-does-it-work.html (visited on June 3, 2025).

[214] S. Piatek. *How does temperature affect the performance of an SiPM?* 2017. URL: https://hub.hamamatsu.com/us/en/technical-notes/mppc-sipms/how-does-temperature-affect-the-performance-of-an-SiPM.html (visited on June 6, 2025).

[215] S. Piatek. *How does temperature affect the gain of an SiPM?* 2016. URL: https://hub.hamamatsu.com/us/en/technical-notes/mppc-sipms/how-does-temperature-affect-the-gain-of-an-SiPM.html (visited on June 6, 2025).

[216] A. Ghassemi, K. Sato, and K. Kobayashi. *A technical guide to silicon photomultipliers (MPPC)*. Tech. rep. Hamamatsu Photonics K. K., 2022.

[217] V. Alex, S. Finkbeiner, and J. Weber. “Temperature dependence of the indirect energy gap in crystalline silicon”. In: *Journal of Applied Physics* 79.9 (May 1996), pp. 6943–6946. DOI: 10.1063/1.362447. URL: https://doi.org/10.1063/1.362447.

[218] K. P. O’Donnell and X. Chen. “Temperature dependence of semiconductor band gaps”. In: *Applied Physics Letters* 58.25 (June 1991), pp. 2924–2926. DOI: 10.1063/1.104723. URL: https://doi.org/10.1063/1.104723.

[219] F. Arneodo et al. “Cryogenic readout for multiple VUV4 Multi-Pixel Photon Counters in liquid xenon”. In: *Nucl. Instrum. Meth. A* 893 (2018), pp. 117–123. DOI: 10.1016/j.nima.2018.03.022.

[220] N. Otte et al. “Characterization of Three High Efficiency and Blue Sensitive Silicon Photomultipliers”. In: *Nucl. Instrum. Meth. A* 846 (2017), pp. 106–125. DOI: 10.1016/j.nima.2016.09.053.

[221] C. Marentini. “Characterization of Novel VUV-Silicon Photomultipliers and their Application in Xenon-Based Dual-Phase TPCs”. Master Thesis. University of Zurich, 2018.

[222] A. d. S. Croix. "The Light only Liquid Xenon Experiment Signal Production, Data Acquisition and Commissioning". Master's Thesis. The University of British Columbia, 2020.

[223] K. Ozaki, S. Kazama, M. Yamashita, Y. Itow, and S. Moriyama. "Characterization of New Silicon Photomultipliers with Low Dark Noise at Low Temperature". In: *JINST* 16.03 (2021), P03014. DOI: 10.1088/1748-0221/16/03/P03014.

[224] S. Sakamoto, T. Hasegawa, Y. Itow, S. Kazama, M. Kobayashi, and M. Yamashita. "Development of a low-noise SiPM for the DARWIN experiment". In: *PoS* ICRC2023 (2023), p. 1435. DOI: 10.22323/1.444.1435.

[225] X. L. Sun et al. "Study of Silicon Photomultiplier Performance in External Electric Fields". In: *JINST* 13.09 (2018). Ed. by Z.-A. Liu, T09006. DOI: 10.1088/1748-0221/13/09/T09006.

[226] A. Brown. "Search for Elastic and Inelastic Dark Matter Interactions in XENON1T and Light Detection for XENONnT". PhD thesis. University of Zurich, 2020.

[227] W. Zhi et al. "Front-end electronics development of large-area SiPM arrays for high-precision single-photon time measurement". In: *JINST* 19.06 (2024), P06011. DOI: 10.1088/1748-0221/19/06/P06011.

[228] E. Aprile et al. "Lowering the radioactivity of the photomultiplier tubes for the XENON1T dark matter experiment". In: *Eur. Phys. J. C* 75.11 (2015), p. 546. DOI: 10.1140/epjc/s10052-015-3657-5.

[229] D. Durini et al. "Evaluation of the dark signal performance of different SiPM-technologies under irradiation with cold neutrons". In: *Nucl. Instrum. Meth. A* 835 (2016), pp. 99–109. DOI: 10.1016/j.nima.2016.08.016.

[230] S. Kumar, D. Durini, C. Degenhardt, and S. van Waasen. "Photodetection Characterization of SiPM Technologies for their Application in Scintillator based Neutron Detectors". In: *JINST* 13.01 (2018), p. C01042. DOI: 10.1088/1748-0221/13/01/C01042.

[231] Hamamatsu Photonics K. K. *VUV-MPPC 4th generation (VUV4)*. URL: https://hamamatsu.su/files/uploads/pdf/3_mppc/s13370_vuv4-mppc_b_(1).pdf (visited on July 16, 2025).

[232] S. Ogawa. "Liquid xenon calorimeter for MEG II experiment with VUV-sensitive MPPCs". In: *Nucl. Instrum. Meth. A* 845 (2017). Ed. by G. Badurek et al., pp. 528–532. DOI: 10.1016/j.nima.2016.06.085.

[233] P. Nakarmi et al. "Reflectivity and PDE of VUV4 Hamamatsu SiPMs in Liquid Xenon". In: *JINST* 15.01 (2020), P01019. DOI: 10.1088/1748-0221/15/01/P01019.

[234] K. Ni, Y. Ma, H. Xu, J. Qi, and N. Hood. private communication. Oct. 31, 2024.

[235] T. Cervi et al. “Characterization of SiPM arrays in different series and parallel configurations”. In: *Nucl. Instrum. Meth. A* 912 (2018), pp. 209–212. DOI: 10.1016/j.nima.2017.11.038.

[236] CAEN S.p.A. *CAEN V1725 / V1725S 16/8 Channel 14-bit 250 MS/s Digitizer*. 2025. URL: https://www.caen.it/products/v1725/ (visited on July 15, 2025).

[237] SAES Pure Gas. *MonoTorr Heated Getter Gas Purifiers*. 2016. URL: http://www.saespuregas.com/Library/specifications-brochures/MonoTorr_Brochure.pdf (visited on July 15, 2025).

[238] C. Zhong et al. “Study on SiPM performance at low temperatures between -60°C and -20°C”. In: *JINST* 17.11 (2022), T11003. DOI: 10.1088/1748-0221/17/11/T11003.

[239] G. Cao. private communication. Sept. 24, 2024.

[240] R. Peres. “SiPM array of Xenoscope, a full-scale DARWIN vertical demonstrator”. In: *JINST* 18.03 (2023), p. C03027. DOI: 10.1088/1748-0221/18/03/C03027.

[241] NEST collaboration. *Calculator*. 2025. URL: https://nest.physics.ucdavis.edu/download/calculator (visited on Aug. 16, 2025).